Doctoral Thesis

Spatiotemporal Control of Terahertz Waves in Random Media via Nonlinear Ghost Imaging

Vittorio Cecconi

Emergent Photonics (EP*ic*) Laboratory

Submitted for the degree of Doctor of Philosophy

University of Sussex

31st August 2022

Supervisors:

Prof Marco Peccianti

Prof Alessia Pasquazi

Dr Juan Sebastian Totero Gongora

Candidate:

Vittorio Cecconi

Declaration

I hereby declare that this thesis has not been and will not be submitted in whole or in part to another University for the award of any other degree.

Signature: Vittorio Cecconi

'…the Whole is Something Beside the Parts'

Aristotle, 980a Metaphysics

(Translated by W.D. Ross)

UNIVERSITY OF SUSSEX

VITTORIO CECCONI
DOCTOR OF PHILOSOPHY

SPATIOTEMPORAL CONTROL OF TERAHERTZ WAVES IN RANDOM MEDIA VIA NONLINEAR GHOST IMAGING

Abstract

Harnessing the spatiotemporal control of complex fields is a critical challenge in a plethora of scientific domains, from photonics to ultrasound imaging. The demand for engineering field manipulation techniques is crucial in many disciplines, for instance, the investigation of imaging methodologies in disordered environments. The control of fields through complex media is an established application domain in microwave and ultrasound imaging. In the last two decades, scientists have developed similar approaches for optical waves. There is a great interest in extending this study to the state-of-the-art at Terahertz (THz) frequencies, particularly in the spatiotemporal field manipulation of ultrafast THz pulses, given the significant difference in methodologies and technologies compared to optical frequencies, for instance. Also, this study would be of great interest in telecom applications at THz frequencies, as communications in this band are expected to be more susceptible to scattering when compared to microwaves.

This thesis contains the results obtained in the Emergent Photonics Laboratory, where I have been developing novel field manipulation techniques in random systems. I will illustrate a new route for harnessing the spatiotemporal properties of THz waves by exploiting scattering media as space-time combinatory elements. The state-of-the-art of THz TDS allows approaching wave scattering as a deterministic spatiotemporal event to be used as complex and inexpensive pulse shapers. As a specific case study, I will show the possibility of spatiotemporal superfocusing of ultrafast THz pulse propagating in complex media, corresponding to a simultaneous focusing in space and pulse re-compression in time. It is worth mentioning that the methodology behind the study of field manipulation in complex media is based on the Time-Resolved Nonlinear Ghost Imaging, a novel correlation-based near-field THz imaging that I have contributed to developing throughout my PhD. In this methodology, an electromagnetic image is reconstructed by correlating the known spatial THz patterns

projected on the target object with the scattered field measured by a standard time-domain spectroscopy (TDS) detection, a mature approach in the field.

The work is mainly presented in the form of a collection of publications (paper-style) but also includes very recent developments that are still unpublished. In its deployment, this thesis offers a general overview of the topic to introduce the subject field to a general Photonics physicist, presents published materials aggregated per topic, and discusses novel material and results in the final chapter. All the material presented has been generated by myself individually or within teamwork unless otherwise specified. Teamwork outputs are presented in full, with my specific contribution clearly highlighted at the beginning of each chapter. This project has received funding from the European Research Council (ERC) under the European Union's Horizon 2020 research and innovation programme Grant agreement n° 725046.

Acknowledgements

I would like to express my special thanks to my supervisors, Prof Marco Peccianti, Prof Alessia Pasquazi, and Dr Juan Sebastian Totero Gongora, for allowing me to join this exciting PhD project and providing me with guidance throughout my research. Moreover, I would like to thank Dr Luke Peter and Dr Luana Olivieri for their support during these years. Finally, I would like to thank the group for allowing me to serve as president of the University of Sussex OPTICA Student Chapter for the last two years. I had a great time, and I especially want to thank my PhD colleagues and members of the chapter, particularly Antonio Cutrona (with whom I had the pleasure to collaborate on many exciting projects), Vivek Kumar, and Christophe Valahu. Remarkably, the Chapter was awarded for its outreach activities at the OPTICA-IONS 2021 conference and this year organised a global poster conference (SCPS 2022) to interact with young researchers worldwide. It was an extraordinary experience, and I hope to organise similar events in the future.

Content

Declaration 4

Abstract 6

Acknowledgements 8

Content 9

List of Figures 12

List of Abbreviations 15

Chapter 1: Introduction 16

1.1 Spatiotemporal Control of Light through Scattering Media at Optical Frequencies 18

1.1.1 Light Propagation in Random Systems 18

1.1.2 A Random System as a Lens 20

1.1.3 Time and Frequency Control 21

1.2 Brief overview of Terahertz Radiation 23

1.2.1 Terahertz Time-Domain Spectroscopy 24

1.3 Broadband Terahertz Propagation in Random Media 27

1.3.1 Light Propagation in Random Media 29

1.3.2 Ultrafast Terahertz Imaging in Complex Media 32

1.3.3 Ultrafast Terahertz Radiation and their Applications for Ghost Imaging 33

1.4 The Structure of the Thesis 34

Chapter 2: Terahertz Time-Resolved Nonlinear Ghost Imaging 36

About the paper: Route to Intelligent Imaging Reconstruction via Terahertz Ghost Imaging 41

Impact 41

Link 41

About the paper: Hyperspectral Terahertz Microscopy via Nonlinear Ghost Imaging 41

Impact 42

2.1 Route to Intelligent Imaging Reconstruction via Terahertz Ghost Imaging 43

2.2 Hyperspectral Terahertz Microscopy via Nonlinear Ghost Imaging 59

Chapter 3: Terahertz Spatiotemporal Superfocusing - Theoretical Framework 70
About the paper: Nonlinear Field-Control of Terahertz Waves in Random Media for Spatiotemporal Focusing 71
Impact 71
Link 71
About the paper: Deterministic Terahertz Wave Control in Scattering Media .. 71
Impact 72
Link 72
3.1 Nonlinear Field-Control of Terahertz Waves in Random Media for Spatiotemporal Focusing 73
3.2 Deterministic Terahertz Wave Control in Scattering Media 85
Chapter 4: Experimental Spatiotemporal Superfocusing of Ultrafast Terahertz Pulses through Scattering Media 99
4.1 Introduction 99
4.2 Discussion 101
4.3 Experimental Setup 105
4.4 Conclusions 106
Chapter 5: Conclusions & Future Perspectives 107
Final Reflections 108
Chapter 6: List of Publications, Conferences & Awards 109
Papers (Published) 109
Papers (Work in Progress) 109
Patents 109
Conferences 109
Peer-Reviews 110
Awards and Grants 110
Bibliography 111
Appendix A: All-Optical Two-Colour Terahertz Emission from Quasi-2D Nonlinear Surfaces 127
A.1 About the paper: All-Optical Two-Colour Terahertz Emission from Quasi-2D Nonlinear Surfaces 127

A.1.1 Impact 129

A.1.2 Link 129

A.2 Journal Article 130

Appendix B: Generation and Detection in Terahertz Photonics 137

B.1 Nonlinear Optics in Terahertz Photonics 137

B.2 Optical Rectification 137

B.3 Electro-Optical Sampling 140

Appendix C: MATLAB Code for the Pulse-Retrieval 141

C.1 GA Flowchart 141

C.2 MATLAB code 141

List of Figures

FIGURE 1.1 (A) ILLUSTRATIVE FIGURE THAT SHOWS WAVEFRONT SHAPING THROUGH A DISORDERED MEDIUM IS ABLE TO CREATE A SMALLER FOCUS COMPARED TO THE LIMITED NUMERICAL APERTURE OF THE LENS THANKS TO THE HIGHER NUMERICAL APERTURE OF THE MEDIUM, $\lambda f2 / D2$. (B) SCHEMATIC OF A REFOCUSING EXPERIMENT. WHEN THE INPUT PHASE PROFILE IS OPTIMIZED, THE INTENSITY AT THE TARGET POINT IS ENHANCED MORE THAN 103 TIMES. FIGURES ADAPTED WITH PERMISSION FROM [9]. 20

FIGURE 1.2 (A) THE FIGURE SHOWS A MONOCHROMATIC BEAM OF LIGHT IMPINGING AT DIFFERENT POSITIONS ON A SCATTERING MEDIUM, AND AT THE OUTPUT, THE UNCORRELATED TRANSMITTED FIELD PATTERNS (AKA SPECKLES) ARE OBSERVED. HOWEVER, A PARTICULARLY SHAPED WAVEFRONT CAN GIVE RISE TO A BRIGHT TRANSMITTED FOCUS AT THE OUTPUT OF THE SAMPLE. (B) THE FIGURE SHOWS THAT TUNING THE LASER FREQUENCY BY MORE THAN THE CORRELATION FREQUENCY $\delta\omega$ OF THE MEDIUM PROVIDES AN UNCORRELATED SPECKLE PATTERN. BY SENDING ALL THE FREQUENCIES, WE CAN CREATE A FOCUS IN SPACE AND TIME BY ADJUSTING THE PHASES AND AMPLITUDES. THE SPECKLE CORRELATIONS ARE LOST WHEN MOVING THE BEAM IN SPACE OR TUNED IN FREQUENCY. FIGURES ADAPTED WITH PERMISSION FROM [9].. 22

FIGURE 1.3 (A) ILLUSTRATIVE FIGURE SHOWING THE FOCUSING AND COMPRESSION OF ULTRASHORT PULSES THROUGH SCATTERING MEDIA. FIGURE ADAPTED WITH PERMISSION FROM [47]. (B) TYPICAL SCHEMATIC OF A SETUP FOR REFOCUSING THROUGH AN ITERATIVE FEEDBACK METHODOLOGY. FIGURE ADAPTED WITH PERMISSION FROM [9]. (C) EXPERIMENTAL DEMONSTRATION OF SPATIAL AND TEMPORAL CONTROL OF LIGHT THROUGH OPAQUE MEDIA. THE CONTROL IS ACHIEVED BY SPATIAL MANIPULATION OF THE INCIDENT WAVEFRONT. FIGURE ADAPTED WITH PERMISSION FROM [55]. 23

FIGURE 1.4 THE ELECTROMAGNETIC SPECTRUM WITH APPLICATIONS ASSOCIATED WITH EACH BAND. NOTICE THAT THE TERAHERTZ BAND THAT RANGES FROM $0.1 - 10\,THz$ IS LOCATED IN BETWEEN ELECTRONICS AND PHOTONICS. 24

FIGURE 1.5 THE EXPERIMENTAL SETUP FOR A TYPICAL THZ-TDS EXPLOITING OR AND EOS FROM ZNTE <110> CRYSTALS FOR GENERATION AND DETECTION, RESPECTIVELY. BS: BEAM SPLITTER. 25

FIGURE 1.6 (A) EXAMPLE OF THE EXPERIMENTAL THZ ELECTRIC FIELD FROM A <110> $ZnTe$ AND (B) ITS SPECTRUM AS MEASURED WITH THE THZ TDS SHOWN IN FIG. 1.5. 26

FIGURE 1.7 (A) ILLUSTRATIVE FIGURE OF THE SETUP OF THE TRANSMISSION EXPERIMENT. (B) THE FIRST PULSE IS THE REFERENCE, TRANSMITTED THROUGH AN EMPTY CELL. THE FOUR WAVEFORMS ARE DESCRIBED AND DELAYED IN TIME DUE TO THE INCREASING PATH LENGTH (1.59, 7.94, 14.29, 20.64) MM. (C) THE SCATTERING COEFFICIENT AS A FUNCTION OF WAVELENGTH, EXTRACTED FROM THE TIME-DOMAIN WAVEFORMS. NOTICE THAT THE SOLID CURVE REPRESENTS A PREDICTION OF THE QUASI-CRYSTALLINE APPROXIMATION. FIGURE ADAPTED WITH PERMISSION FROM [67].. 28

FIGURE 1.8 AN INCIDENT PLANE WAVE $Einc$ SCATTERED BY A SINGLE OBJECT PRODUCING A SPHERICAL WAVE Es.. 29

FIGURE 1.9 INFINITE SAMPLE OF THICKNESS L WITH RANDOMLY DISTRIBUTED SCATTERING PARTICLES EMBEDDED IN A HOMOGENEOUS MEDIUM. 30
FIGURE 1.10 THE THREE MAIN SCATTERING REGIMES. WE NOTE AN EXPONENTIAL DECAY OF THE TRANSMISSION COEFFICIENT, WHEREAS THE DIFFUSION REGIME DECAYS AS $1/L$. FIGURE ADAPTED FROM [87]. 30
FIGURE 1.12 (A) THE SCHEMATIC OF THE IMAGING SETUP FOR MEASURING THE DIFFUSED THZ FIELD. THE MEASUREMENT SHOWS THE ANGULAR DISTRIBUTION OF THE SCATTERED THZ SPECTRAL POWER. THE SAMPLE IS MADE OF THREE DIFFERENT MATERIALS: HDPE, α-LACTOSE, AND PABA. (B) THE CHEMICAL THZ MAPS. FIGURES WERE ADAPTED FROM [102] AND RE-USED UNDER THE CREATIVE COMMONS ATTRIBUTION 4.0 (CC-BY ARTICLES). 33
FIGURE 1.13 (A) SCHEMATIC DIAGRAM OF THE DETECTION SYSTEM IN THZ IMAGING SETUP. THE GAUSSIAN THZ FIELD (I) PASSES THROUGH THE TRANSPARENT PHASE PLATE WITH A RANDOM DISTRIBUTION, CHANGING ITS SPATIAL DISTRIBUTION. (B) INITIAL THZ PROFILES AND RESULTING THZ SPECKLE PATTERNS WERE OBTAINED FROM THE RADIATION INTENSITY RECORDED ON AN IMAGING SETUP FOR THE CASE IN WHICH THZ RADIATION PROPAGATES THROUGH THE PHASE PLATES LOCATED AT A DISTANCE OF 5 CM FROM THE ZNTE CRYSTAL. (C) SCHEME OF ACQUISITION OF SPECKLE PATTERNS FOR MONOCHROMATIC THZ RADIATION. TWO SAMPLES OF GAUSSIAN RANDOM ROUGH SURFACE. FIGURES WERE ADAPTED FROM [112] AND RE-USED UNDER THE CREATIVE COMMONS ATTRIBUTION 4.0 (CC-BY ARTICLES). 34
FIGURE 2.1 (A) FLOWCHART OF THE THZ GHOST IMAGING. SETUP OF A THZ GHOST IMAGING. (B) IDEAL SETUP OF THE THZ GHOST IMAGING. FIGURES WERE ADAPTED FROM [119] AND RE-USED UNDER THE CREATIVE COMMONS ATTRIBUTION 4.0 (CC-BY ARTICLES). 37
FIGURE 2.2 CONCEPTUAL SETUP FOR THE TNGI AND AN EXAMPLE OF A TERAHERTZ FULL-WAVE SPATIOTEMPORAL IMAGE OF A METALLIC SAMPLE. NOTICE THE FIELD EVOLUTION (COLOUR CHANGE AT THE TIME $t1, t2, t3$) UNDERNEATH THE METALLIC MASK AS THE STRUCTURE RESONANCE PRODUCES A SECONDARY EMISSION. IN THE RECONSTRUCTION VIDEO, IT CAN BE OBSERVED THAT AT DIFFERENT SCANNING TIMES, THE OBJECT DOES NOT APPEAR JUST AS A BLOCKING MASK, BUT IT FEATURES COMPLEX RESONANCES FROM THE EDGES OF THE OBJECT. ADDITIONALLY, A FUNDAMENTAL FACT IS THAT THE TIME-RESOLVED MEASUREMENT OF THE SCATTERED FIELD ALSO ALLOWS THE RECONSTRUCTION OF THE HYPERSPECTRAL IMAGE OF THE SAMPLE. AND BECAUSE OF THE NEAR-FIELD CONDITION, WE WERE ABLE TO RESOLVE FEATURES WITHIN A 50 μM SCALE EVEN IN THE PRESENCE OF A RELATIVELY THICK GENERATION CRYSTAL. 40
FIGURE 3.1 ILLUSTRATIVE FIGURE OF A THZ SPATIOTEMPORAL SUPERFOCUSING. 70
FIGURE 4.1 CONCEPTUAL FIGURE OF A THZ PULSE PROPAGATING THROUGHOUT A RANDOM MEDIA. 99
FIGURE 4.2 SPATIOTEMPORAL FOCUSING OF A TERAHERTZ PULSE. (A, D) CONCEPTUAL FIGURE OF SPATIOTEMPORAL FOCUSING RESULTS: THE THZ PLANE WAVE IS PROJECTED ON A DISORDERED MEDIUM, TRANSMITTING UNOPTIMISED LIGHT SCATTERING. (B) THE WAVEFRONT OF THE INCIDENT THZ PULSE IS SHAPED SO THAT SCATTERING ACTS AS A SPATIOTEMPORAL LENS CREATING A FOCUS AT THE OUTPUT OF THE SAMPLE. THE PINHOLE IS

in contact with the scattering medium (i.e., ideally $h \sim 0$). (b) Optimised pulse (blue) and unoptimised field - with SLM off - (in red). (c) The second central moment and peak field value optimisation. (e) The set of TDS ranked relative to the cost function A in Table 4.1. (f) Spectrums of the reference, the optimised and the unoptimised pulses. 103
Figure 4.3 Optimised pulse with inverted phase. (a) Illustrative figure. (b) Temporal profile of the output THz pulse with inverted phase relative to the reference (scanned without scattering medium). (c) Peak fields are ranked relative to cost function B in Table 4.1. 104
Figure 4.4 Field temporal shift. (a) Illustrative figure. (b) Four THz pulses, time-shifted at around $1\,ps$, respectively pattern $\{1, 30, 80,\ 100\}$. (c) The first central moment value optimisation. (d) The TDS ranked relative to the cost function. The measurements of the temporal shift are taken with the cost function C from Table 4.1. 105
Figure 4.5 Schematic of the apparatus. 106
Figure A.1 The illustrative figure of the all-optical two-colour terahertz emission. 128
Figure B.1 Illustrative figure of the excitation scheme for Optical Rectification (OR) of ultrashort pulses in a $\chi(2)$nonlinear medium. 138
Figure B.2 The experimental setup for an electro-optic sampling of a THz (green) pulse. The input optical (red) pulse is linearly polarised before the $ZnTe$, after which is a quarter wave plate, Wollaston prism (all included in a purple box for simplicity) and a pair of balanced photodiodes. 139
Figure C.1 Genetic algorithm flowchart. 141

List of Abbreviations

EOS	Electro-Optic Sampling
GI	Ghost Imaging
OR	Optical Rectification
PD	Photo-Dember
SLM	Spatial Light Modulator
SNR	Signal-to-Noise Ratio
SF	Superfocusing
SOR	Surface Optical Rectification
TNGI	Time-Resolved Nonlinear Ghost Imaging
TDS	Time Domain Spectroscopy
THz	Terahertz

Chapter 1: Introduction

In modern physics, a complex system is a dynamical system composed of several units or subsystems that typically interact with each other. These systems are typically studied through a holistic investigation of the behaviour of the subsystems and their reciprocal interactions - eventually nonlinear - and not through the reductionism analysis of the individual components [1]. It is crucial to notice that a fundamental property of complex systems is the presence of 'emergent' behaviours where the traits of a system are not apparent from its isolated components; however, as the result of the interactions and relationships they form when placed together in the system. In other words, in a complex system, 'the whole is greater than the sum of the single parts'. The relevance of complex systems was discovered in various areas of research, and the commonalities among these fields have become the topic of its independent area of research; for instance, the earth's global climate, the human brain, social and economic organizations, ecosystems, and ultimately the structure of the universe. The first research institute focused on complex systems, the Santa Fe Institute, was founded in 1984 [2]. Early participants included Physics Nobel laureates Murray Gell-Mann and Philip Anderson. Today, there are many institutes around the world and research centres focusing on complex systems. Notably, in 2021, the Nobel Prize in Physics was awarded to Syukuro Manabe, Klaus Hasselmann, and Giorgio Parisi for their work on understanding complex systems. Their work has not only helped make more accurate computer models for studying the problem of global warming [3], but it has also unveiled the profound richness found at the intersection between physics and the science of complexity.

Interestingly, in optics, the exciting field commonly known as 'Complex photonics' is a novel branch of photonics that studies the phenomena emerging from light propagation in complex optical systems), ranging from random lasing [4] to Anderson localization [5]. It is worth mentioning, however, that in the disordered photonics community, the term complexity is generally used as synonymous with complex multibody systems (i.e., scattering media). Generally, scattering is a fundamental light-matter interaction in optics. When an electromagnetic wave encounters an object, it may be scattered in a variety of ways, i.e. the object contributes to a change in the spatial momenta-spectrum of the wave. Different scattering regimes can be identified by the ratio between the typical average size of the scattering element and the wavelength. Rayleigh and Mie scattering, for example, correspond to scenarios where particles are much smaller than the wavelength or comparable to the wavelength. In the presence of multiple objects, the number of scattering events experienced by a wave component before reaching an observer, determines the typical 'Single' or

'Multiple' scattering regimes. Upon propagation in a scattering media, an observer generally experiences a combination of ballistic waves (an unscattered portion of the impinging wave), single- and multiple-scattering waves.

Scattering was commonly perceived as a detrimental effect in standard optical applications; however, it is essential to mention that light-matter interaction problem can be expressed in terms of a scattering matrix – or impulse response – and this would allow treating the scattering system as a deterministic, linear 'black-box'. The input-output relation of the system can then be modelled as a matrix multiplication (in frequency) or convolution (in time). Once the problem is set in this framework, field control can be pursued by retrieving the experimental equivalent of such an operator based on the setup detection capabilities (e.g., intensity, field). And indeed, even though counterintuitively, it has been proven that disordered media can be leveraged to synthesise optical devices with outstanding imaging performances [6]. A typical example is scattering-assisted focusing, where a complex medium behaves as a sub-diffraction focusing device [7]. Such harnessing can be pursued by retrieving the scattering input-output transfer matrix, as it allows to handle scattering medium as a completely deterministic optical filter [8]. However, at optical frequencies, the electric field is not generally a measurable quantity, and the extraction of the transmission matrix from intensity measurement is pursued with indirect spectral-interferometric approaches [9]. An alternative route would be using principles of light field synthesis within a scattering system, where a broadband spectrum is divided into individual spectral channels; an external modulator item would then harness the relative phases and field amplitudes of the spectral channels and finally combine them to generate the synthesised waveform at the output of the scatterer. Nonetheless, a full-waveform synthesis must rely upon absolute phase knowledge or ways to assess the field dynamics in time instead of intensity-based measurements, and if the source pulse's absolute phase profile is unknown, its effect on the output scattered field is also unknown.

On the other hand, in domains where the field dynamics of scattering waves are directly measurable (e.g., microwaves, terahertz), it is possible to target a new scattered waveform by accessing the accessible 'modes' of the scattered waves and simply assuming that their linear combinations are all predictable output waveforms. Field-sensitive detection is well-mature in the art of Terahertz (THz) photonics, where time-domain spectroscopy is able to access the time-resolved electric field of single-cycle THz pulses. Indeed, by leveraging the state-of-the-art THz time-domain spectroscopy, the core of my PhD thesis is the development of novel field manipulation methodology in complex systems; this work could suggest solutions for future applications in complex and inexpensive pulse shapers.

In the following paragraph, I will introduce the fundamental literature on the spatiotemporal control of electromagnetic radiation in random systems.

1.1 Spatiotemporal Control of Light through Scattering Media at Optical Frequencies

1.1.1 Light Propagation in Random Systems

Collecting morphological information about the microscopic and macroscopic world is routinely achieved via detecting (visible) light, and, depending on the situation, refractive-index inhomogeneities cause light to be scattered and diffused in many materials [10–12]. A fundamental qualifying parameter that is a combined property between the scattering system and light propagation is the mean free path l (for instance, the proportionality with the scattering cross section depends on the size of the scatterers and the relative wavelength in use), which represents the average distance between two successive scattering events. When light propagates within a scattering sample, it is possible to observe the radiation fading as it propagates deeper into the medium, a phenomenon known as attenuation. In a non-absorbing system, the radiation is converted into a diffused component with a spatial spectrum progressively broadened upon propagation.

Scattering represents a considerable obstacle for imaging and light focusing in fields such as biomedical imaging, where most samples are highly complex [13]. In other scenarios, scattering management and compensation play a key role in laser therapy [14], art preservation [15], and photonic crystal fabrication [16]. Early studies in holography [17] highlighted that light scattering does not necessarily lead to an irretrievable loss of information [18]. Indeed, due to multiple scattering, the field is transformed into a particular interference pattern, also known as 'speckles' [19]. The significant knowledge achieved in early mesoscopic transport theory for electron dynamics [8,20] has been of tremendous inspiration for many proposals for extracting imaging information from laser speckles [18,21] and therefore giving birth to a novel (at the time) focusing and imaging methodologies in which the nature of the scattering, rather than being detrimental, aids the process of imaging/light focusing. Undoubtedly, many innovative imaging techniques have been proposed over the years. Among the most important and elegant methodologies, coherent optical tomography [22] is a technique based on purging the scattered light by selecting the signal based on its propagation time, with the idea to isolate the non-scattered light components. However, when considering depths larger than $5l$, the unscattered (ballistic) fraction is attenuated to levels that make those methods not viable. In the last two decades, there has been substantial work in diffuse optical imaging to locate objects inside multiple-scattering media [26], and adopted for deep optical tomography [13]. Generally, these techniques suffer from relatively coarse spatial resolution, which can be improved by combining ultrasound and optical methods [23]. Also, many robust methods, ranging from adaptive optics [24,25] to stellar speckle interferometry [26], are currently used in astrophysics experiments to overcome atmospheric distortion.

Often the description of light propagation in complex media is described as the diffusion of particles (photons) that perform a random-walk-like propagation. More generally, the propagation of light waves is expressed by the wave equation $\nabla^2\Psi(\vec{r},\mathrm{t}) = \frac{\mathrm{n}^2(\vec{r})}{c^2}\frac{\partial^2\Psi(\vec{r},t)}{\partial t^2}$. In this equation, the term $\Psi(\vec{r},\mathrm{t})$ represents the electric field of light. The propagation of the speed of light is expressed by $\frac{c}{n(\vec{r})}$, where c is the speed of light in a vacuum and $n(\vec{r})$ is the index of refraction of the medium. In general terms, scattering is a consequence of local variations of $n(\vec{r})$ in the medium, which can occur, for instance, due to the presence of randomly dispersed dielectric particles. If we consider a scattering medium as an optical input-output system with input surface area A, a common estimation is that the maximum number of independent incident modes able to radiate (channels) lies within the scale $N_s = \frac{2\pi A}{\lambda^2}$ [9] for the light of wavelength λ. Visible light can account for $\sim 10^6$ transversal modes per square millimetre. By a simple combinatory view, those modes are a decomposition basis for the transmission matrix [8,20].
The time that a photon spends travelling inside a medium is defined by the Thouless time τ_D [27–29] and in an open medium (energy enters and leaves the medium at the edges), the solutions of the wave equation are quasi-modes with a frequency width of the order of $\delta\omega = \frac{1}{\tau D}$ [12,30]. When two distinct propagating monochromatic field components have a frequency spacing smaller than $\delta\omega$, scattering will produce a strongly spatially correlated transmitted field; on the contrary, when the frequency difference is larger than $\delta\omega$ the two scattered fields will be spatially uncorrelated. This means that the fields experience different uncorrelated transformation matrices. More generally, considering a broadband field with a bandwidth of $\Delta\omega \gg \delta\omega$, we would expect N incident spatiotemporal degrees of freedom as $N = N_s \cdot N_f = N_s \frac{\Delta\omega}{\delta\omega}$, with N_s the number of spatial modes and N_f the number of independent frequency decompositions [31]. The working hypothesis in scattering functionalisation is that in a diffusive regime, a significant fraction of these incident modes is transmitted with reasonable efficiency. Therefore, they can be exploited to achieve control over the transmitted and internal fields. This situation is not dissimilar to settings in which control is achieved in waveguides or photonic crystals, although in those examples, the number of accessible modes tends to be lower [32]. The basic scattering description is then quite similar across different domains, including acoustic, fluids, microwaves, and optics. However, the way scattering waves are harnessed significantly differs because of the different available technologies and methodologies. In addition, typical scales and scattering densities also tend to be different.

1.1.2 A Random System as a Lens

Historically, a seminal experiment that proved the focusing of waves in opaque media was realised by exploiting ultrasonic waves in water volumes containing an array of steel rods [33,34]. In essence, an array of transducers - specifically, ultrasonic time-reversal mirror (TRM) [35] - was used to focus through the water–steel scattering medium onto distant points. While measuring the transverse size of the focus obtained through water without steel rods, researchers found that the optimised focal point generated through the scattering media was surprisingly smaller compared to the diffraction limit of the TRM used in the experiment. This experiment can be considered the first demonstration of the ultrasonic superfocusing (SF) technique. The subtle implication of this demonstration is that field localisation does not necessarily depend on the angular aperture of the focusing device but instead on the angular aperture of the scattering system, which can be extremely large, up to 4π steradians. Similar results were first observed in acoustics using time reversal [33] and later in microwaves through time reversal and phase-conjugation experiments [36,37].

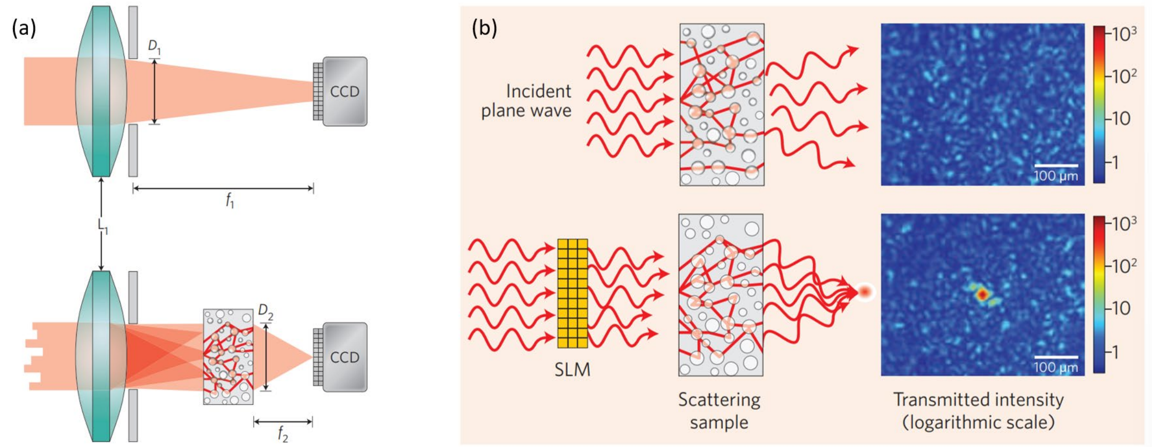

Figure 1.1 (a) Illustrative figure that shows wavefront shaping through a disordered medium is able to create a smaller focus compared to the limited numerical aperture of the lens thanks to the higher numerical aperture of the medium, $\lambda f_2 / D_2$. (b) Schematic of a refocusing experiment. When the input phase profile is optimized, the intensity at the target point is enhanced more than 10^3 times. Figures adapted with permission from [9].

In optics, Vellekoop and co-workers [58] showed that a thin layer of white paint (precisely, rutile particles) could be used to tightly focus a laser beam (see Fig. 1.1). The layer of paint was placed between a spatial light modulator (SLM) and a CCD camera. Different incident spatial light patterns give rise to different speckle patterns behind the sample. After shaping the input illumination through an iterative algorithm [7,39], they could achieve a tightly confined focus at the target point and even inside the scatterer [40].

This approach requires a standard detector at the target location, and the optimization scheme (for instance, a genetic algorithm) is similar to the phased array methods in adaptive optics [24]. The experimental intensity enhancement reported, defined as the ratio between the optimised intensity and the average intensity before optimisation, was up to $\eta = 1{,}080$ [38]. Similarly, in phase-conjugation experiments, it has also been observed that scattering in biological tissue can be exploited to increase image resolution [41].

A way to understand the statistical properties of wave propagation in scattering media can be by employing mesoscopic transport theory, and exhaustive work on this matter can be found in the review of Beenakker [20]. The concepts of open and closed scattering channels are critical in this framework, representing the different types of propagating modes inside the scattering system. A fully open channel transmits diffused light with almost no back reflection, whereas closed channels have a generally small transmission. Dorokhov and co-workers [42,43] have indeed shown that a small number of open channels drive the transmission of waves through a scattering sample-although this would depend on the nature of the scattering medium. The first direct observation of open transmission optical channels was by a wavefront-shaping experiment [44], and researchers were able to control and optimize a significant fraction of all incident modes to form a focus on the output. Remarkably, in the microwave regime, researchers have further proven the propagation of radiation in open channels with transmission close to unity [45].

1.1.3 Time and Frequency Control

An interesting question is whether scattering can be utilized to achieve control of the temporal waveform properties. Ideally, the accessible scattering channels in a scattering medium would provide great flexibility for wavefront-shaping experiments. What is understood is that we would expect a set of open channels corresponding to a particular frequency; however, by detuning the source, we would expect a different set of open channels and potentially lose the overall optimisation. Indeed, as shown in Ref. [46], wavefront shaping only worked for a narrow frequency range, and the effect of the optimisation is lost after the laser has been detuned beyond the speckle correlation frequency $\delta\omega$. Indeed, for every frequency, one would expect a different set of open/close channels, and therefore, in a non-monochromatic scenario, we could introduce temporal reshaping. The manuscript in Ref. [31] shows that this would allow access to even more degrees of freedom compared to the monochromatic case. Indeed, the incident light will excite all the modes - within its bandwidth - in the scattering system. Therefore, for instance, an optical pulse source is formed by many frequency components, each corresponding to a unique speckle pattern (see Fig. 1.2).

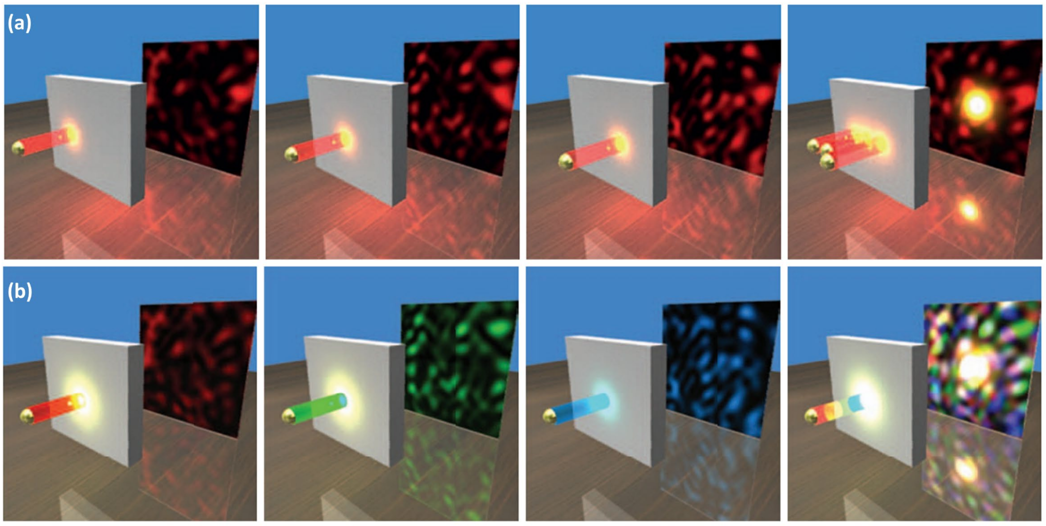

Figure 1.2 (a) The figure shows a monochromatic beam of light impinging at different positions on a scattering medium, and at the output, the uncorrelated transmitted field patterns (aka speckles) are observed. However, a particularly shaped wavefront can give rise to a bright transmitted focus at the output of the sample. (b) The figure shows that tuning the laser frequency by more than the correlation frequency δω of the medium provides an uncorrelated speckle pattern. By sending all the frequencies, we can create a focus in space and time by adjusting the phases and amplitudes. The speckle correlations are lost when moving the beam in space or tuned in frequency. Figures adapted with permission from [9].

Consequently, when an ultrashort pulse impinges on a scattering system, it is possible to observe both spatial and temporal distortions. Critical work on this problem has been extensively studied in the paper by Katz and co-workers [47], showing that correction of both spatial and temporal distortions can be achieved by manipulating the spatial degrees of freedom of the incident wavefront solely by a standard SLM.

They demonstrated the spatiotemporal focusing and compression of chirped ultrashort pulses through scattering media by optimising a nonlinear signal at the output of the scattering media. Specifically, they could refocus 100 fs pulses in both space and time through thick brain and bone samples. This work opened new possibilities for optical manipulation and nonlinear imaging in scattering media (see Fig. 1.3).

In parallel, there have been several theoretical proposals for time-reversal symmetry at optical frequencies, fundamentally corresponding to the physical property where events can occur in a forward or backward direction through time, with no fundamental distinction due to the direction. First to mention are Yariv [48] and Miller [49]; they proposed the use of four-wave mixing to compensate for the dispersion of an optical pulse spread in time. Yanik and Fan also numerically demonstrated the possibility of time-reversing optical pulses by dynamically modulating the refractive index of a dielectric photonic crystal [50]. Longhi expanded this work in the Bloch oscillations [51] framework. Sivan and Pendry proposed a model using the dynamic modulation of a zero-gap periodic system to time-reversed a broadband light pulse [52], and finally, Pendry found the link between time-reversal and negative refraction [53], later experimentally verified by Katko and co-workers [54].

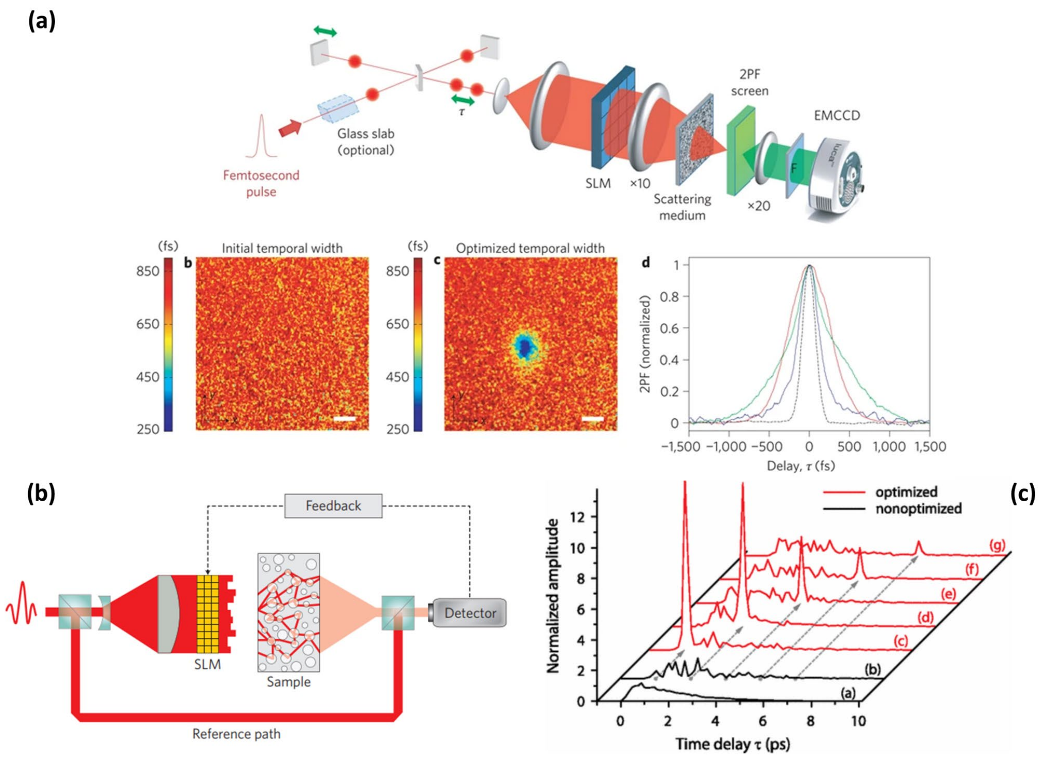

Figure 1.3 (a) Illustrative figure showing the focusing and compression of ultrashort pulses through scattering media. Figure adapted with permission from [47]. (b) Typical schematic of a setup for refocusing through an iterative feedback methodology. Figure adapted with permission from [9]. (c) Experimental demonstration of spatial and temporal control of light through opaque media. The control is achieved by spatial manipulation of the incident wavefront. Figure adapted with permission from [55].

However, as mentioned before, at optical frequencies, a full-waveform control of the fields is not a trivial task; this is where the state of the art of THz allows a possible route to access the field dynamics. In the following paragraphs, I will overview the fundamentals of the art of THz photonics. I will start with a brief introduction and share some properties of this electromagnetic band. Following, I will explain its crucial application in the field of complex photonics.

1.2 Brief overview of Terahertz Radiation

Photonics relies on the wide availability of laser sources to investigate physical processes. After more than half a century, there has been considerable development in advanced laser devices emitting light from the Mid-IR to the UV frequency regions. On the lower end of the electromagnetic spectrum, electronic oscillators and antenna devices are able to produce bright electromagnetic radiation from the long-wave (kHz) to the microwave (GHz) bands. The Terahertz band lies between these two regimes (see Fig. 1.4) and has been known as the THz "gap" for many years due to a lack of efficient sources and detectors [56] until the introduction of powerful ultrafast (femtosecond) laser sources - nowadays, reasonably available in the market - has brought a completely different solution via the exploitation of several nonlinear optical processes. Some highly promising application scenarios have fueled the pursuit of bright THz sources and efficient detectors.

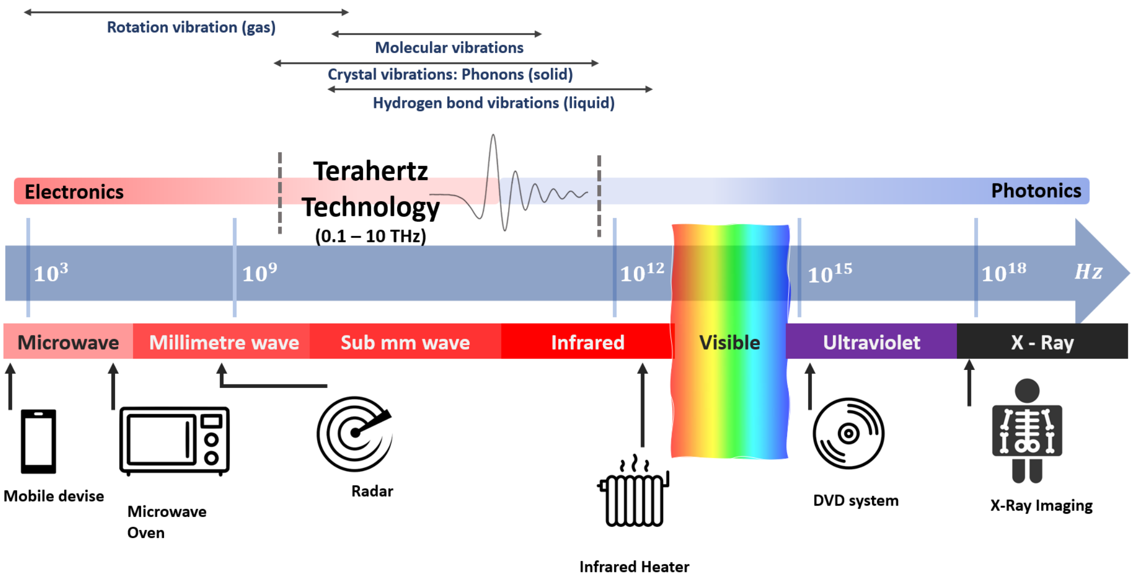

Figure 1.4 The electromagnetic spectrum with applications associated with each band. Notice that the terahertz band that ranges from $0.1 - 10\,THz$ *is located in between electronics and photonics.*

Many materials' rotational and vibrational resonances fall within the THz region, including many forms of biological matter [57]. Furthermore, modern designs of Time-Domain THz spectroscopy (TDS) are able to measure the temporal dynamics of the scattered THz field, hence enabling the retrieval of the complete complex refractive index and absorption of the sample under investigation [58]. Last but not least, imaging applications at THz frequencies have many potential applications. For instance, for security purposes, as many common plastics and fabrics are transparent to THz waves, therefore, able to identify potential metallic and non-metallic hidden items [59]. And in medical applications, the highly absorbing nature of water in the THz range results in high contrast when skin tumours are imaged [60].

1.2.1 Terahertz Time-Domain Spectroscopy

In this paragraph, I will illustrate how broadband THz radiation can be generated and detected. Since the emergence of terahertz spectroscopy, there has been a constant endeavour to search for novel materials with efficient emission of broadband terahertz radiation. There have been notable developments in utilizing electro-optic (EO) crystals, such as Zinc Telluride, over the years. In this case, the electro-optic terahertz transceiver transmits pulsed electromagnetic radiation via optical rectification (OR) and receives the return signal using electro-optic sampling (EOS).

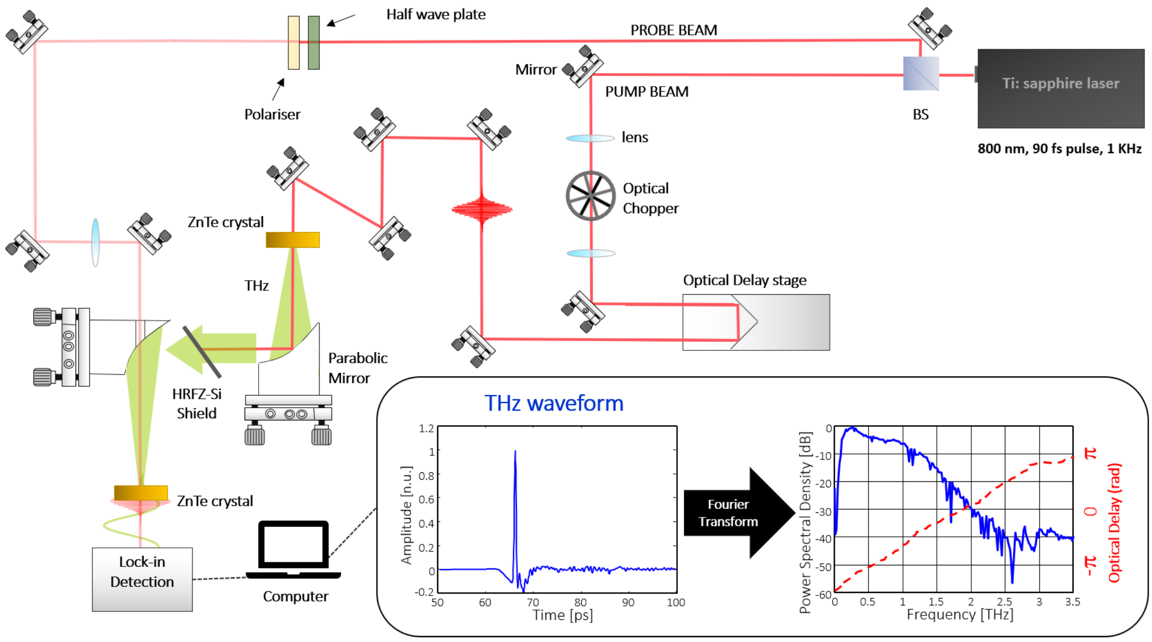

Figure 1.5 The experimental setup for a typical THz-TDS exploiting OR and EOS from ZnTe <110> crystals for generation and detection, respectively. BS: Beam Splitter.

In the appendices, you will find a detailed explanation of the mechanism of both OR and EOS. The synchronisation between the OR and EOS is the fundamental element of standard THz Time-Domain Spectroscopy (TDS). In THz-TDS, the same ultrashort pulse is exploited for generation and detection as in a pump-probe setup. Note that the optical pulse is much shorter in wavelength than the THz transient, and therefore it enables the reconstruction of the THz temporal waveform inside the EO crystal (i.e., Nyquist theorem). The optical pulse will probe a temporal moment of the THz field depending on their mutual temporal overlap (time-overlap). As a result, by delaying the optical probe with respect to the THz waveform, the value of the THz electric field is temporally encoded into the optical pulse polarisation that can then be detected. The remarkable nature of THz-TDS is then to measure both the temporal envelope and phase simultaneously $E_{THz}(t) = \sqrt{I(t)}e^{-i\phi t}\, e^{i\Omega t}$, which is quite complex to achieve generally in photonics. Also, measuring the ‘time-delay’ means that we know the phase at every frequency, which removes a classical ambiguity in coherent optical measurements. By applying the Fourier transform to this time trace, we also retrieve the full spectral amplitude and phase $E_{THz}(\omega - \Omega) = \sqrt{I(\omega - \Omega)}e^{-i\phi(\omega-\Omega)}$. Differently to standard spectroscopy (where you have an intensity-based measurement), THz-TDS has access to the spectral phase as well as amplitude and therefore making it possible to derive the complete complex refractive index and the extinction coefficient, $\tilde{n} = n + i\alpha$, as detailed next (full derivation in Ref. [61]).

Practically, a reference spectrum (with no sample) and a signal spectrum of the sample of thickness d are measured, and the resulting absorption coefficient is given by

$$\alpha(\omega) = \frac{1}{d}\ln\left(\frac{E_{ref}(\omega)}{E_{sig}(\omega)}\right), \tag{1.1}$$

and refractive index

$$n(\omega) = 1 + \frac{c}{d \cdot \omega}\left(\phi_{sig}(\omega) - \phi_{ref}(\omega)\right), \tag{1.2}$$

with c the speed of light in a vacuum, $E_{ref,sig}(\omega)$ the reference and signal THz spectra and $\phi_{ref,sig}(\omega)$ the reference and signal spectral phases, respectively. It is possible to appreciate the fundamental relevance of this method, stressing that the refractive index is usually not a direct and handy measurement in optical frequencies, and its knowledge usually requires relative measurements of the phase mapped onto intensity variations.

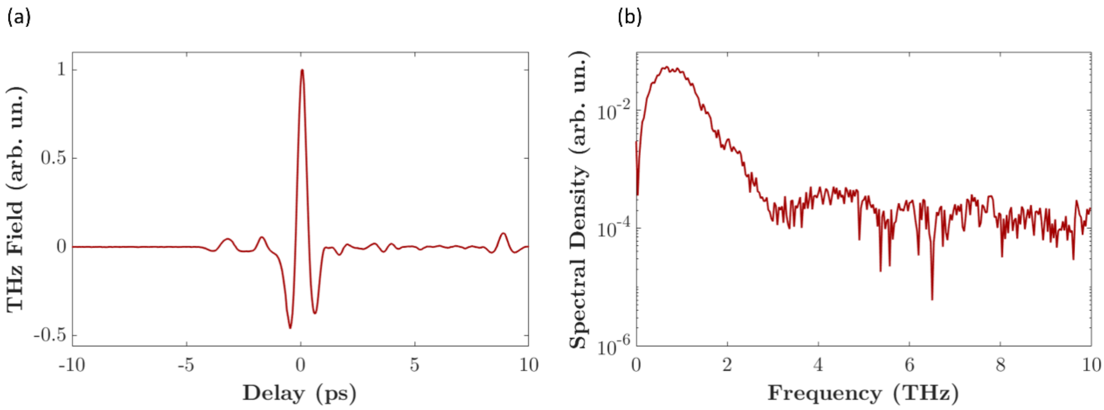

Figure 1.6 (a) Example of the experimental THz electric field from a <110> ZnTe and (b) its spectrum as measured with the THz TDS shown in Fig. 1.5.

The standard setup for THz-TDS spectroscopy is shown in Fig. 1.5. Whereas an example of a measured THz temporal waveform is shown in Fig. 1.6a, where the single-cycle THz pulse is followed by a 'coherent ringing' due to the resonant excitation frequencies of water molecules in the air (however, one conventional way to avoid the presence of water vapour in the terahertz beam path is to purge the setup with dry nitrogen (N_2)). The Fourier transform of the electric field is shown in Fig. 1.6b. It provides the spectral components of the temporal pulse, extending from $0.1 \rightarrow 2.7\,THz$ with several sharp water absorption lines—and oxygen contribution—characteristic of rotational and vibrational excitation modes in the laboratory atmosphere [62].

We could say that THz-TDS is still today in a relatively early state, and as with any evolving technology, there are many challenges to be addressed before its widespread use. For instance, the relatively long time required to acquire the entire THz waveform is already being tackled by including single-shot embodiments that can encode or directly map the THz electric field onto an optical spectrum [63,64]. Also, it is desirable to extend the usable THz bandwidth beyond that provided by the most common THz emitters, such as $ZnTe$. A potential solution to this involves reducing the interaction length for broader phase matching, and discussed in Appendix A, see Ref. [65].

In the following subchapter, I will discuss how the study of complex photonics has been extended to THz frequencies and discuss relevant literature. I will start this section by discussing the first experiments from Pearce and co-workers [66] of ultrafast THz pulses in random media; I will then extend the subject of scattering, illustrating some recent results on THz imaging in complex media.

1.3 Broadband Terahertz Propagation in Random Media

In recent years, scientists have focused on using scale models to elucidate the physics of THz-wave propagation in complex systems [67]. At THz frequencies, one could have the advantage of studying a simplified and well-controlled model at a millimetre scale. Thanks to the invariance of Maxwell's equations to length, one can scale these results to either larger or smaller length scales and thus gain a more general insight into the underlying physics [68]. Probably the first documented study is from Cheville and Grischkowsky, who recognised the potential of THz-TDS for scale model experimentation to simulate broadband radar [69] and another critical study used THz waves to study radar cross-sections of aircraft models [70]. T.D.Dorney and co-workers [71] studied related techniques for scaled studies of acoustic pulse propagation in geophysical cases. The same group further applied scaling methods in the opposite direction, suggesting a new way of probing optical pulse propagation in complex media. These studies were beneficial for applications of THz light propagation in strongly scattering media, like biological samples. For instance, the relevance of such research can be found in spectroscopic measurements of biochemical systems (e.g., DNA, proteins, etc.) [72–74] and THz imaging of biological samples, such as teeth, skin, and tissue samples [75–78]. Indeed, the problem of controlling light propagating in biological media has great potential for promoting optical methods as novel imaging diagnostics. However, because of the random nature of these samples, finding a complete solution to the problem is very challenging. Generally, inside a random medium, the propagated wave consists of an in-phase, unscattered wave and an out-of-phase scattered wave (photons scattered one or multiple times). By studying the complex propagation of light within turbid media, both coherent [79,80] and incoherent [81,82] radiation have been used to form images of various medium properties.

One of the first demonstrations of the utility of THz scale models was the study of the ballistic transport of THz pulses through dense distributions of spherical dielectric scatterers by Pearce and Mittleman [83] (see Fig. 1.7).

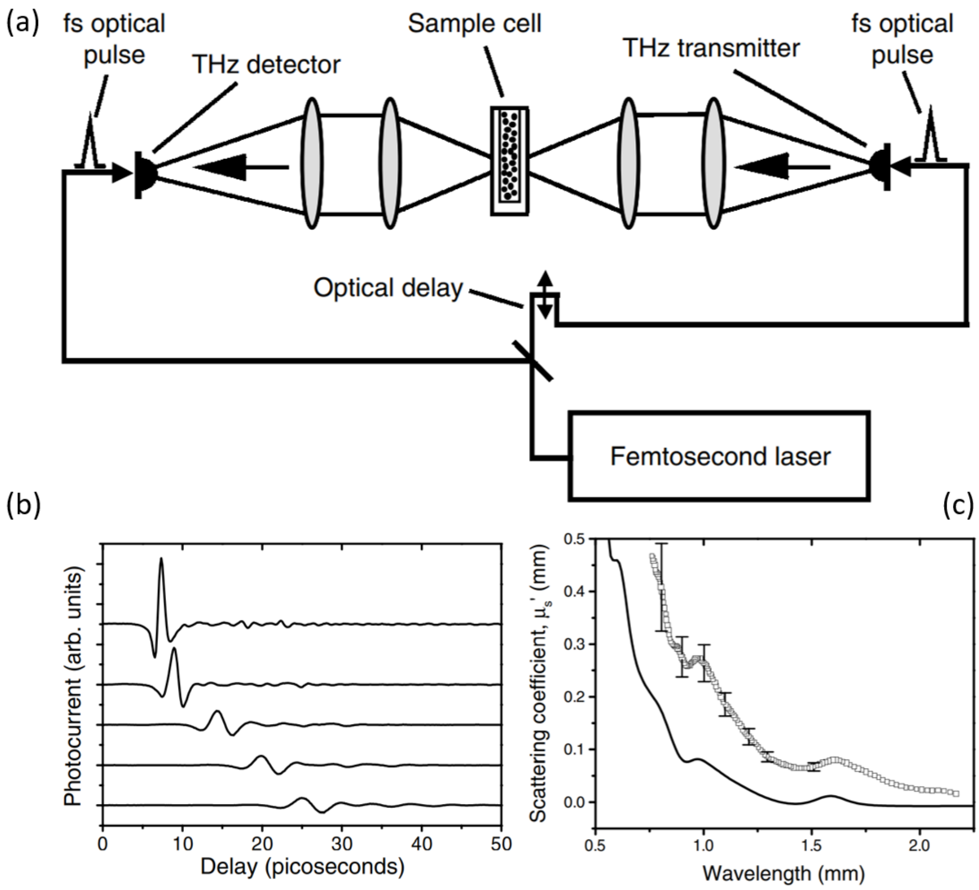

Figure 1.7 (a) Illustrative figure of the setup of the transmission experiment. (b) The first pulse is the reference, transmitted through an empty cell. The four waveforms are described and delayed in time due to the increasing path length (1.59, 7.94, 14.29, 20.64) mm. (c) The scattering coefficient as a function of wavelength, extracted from the time-domain waveforms. Notice that the solid curve represents a prediction of the quasi-crystalline approximation. Figure adapted with permission from [67].

Notice that at optical frequencies, it is straightforward to obtain the imaginary part of the effective propagation constant, linked to attenuation and absorption, but not as much to extract the real part [84]. However, it is a different case when using the art of terahertz spectroscopy because it directly grants access to the real and imaginary parts. In addition, THz-TDS is, by nature, a broadband technique making it possible to perform measurements that span the entire scattering range from Rayleigh scattering ($ka \ll 1$, where k is the free-space wave vector and a is the scatterer diameter) through Mie scattering ($ka \geq 1$) [85]. In addition, the ability to measure the real part of the refractive index grants access to additional parameters, such as the group velocity, in close analogy with previous studies in the microwave regime [86]. Lastly, operating in the THz domain also provides practical advantages in the fabrication of the scattering samples. The different scale of THz radiation is more robust against the thermal and displacement of the scatterers composing the scattering medium as the scattering centres are usually more significant in size than those used in optics. At optical frequencies, the experiments are more sensitive to thermal drifts (from minutes in the case of solid-state to milliseconds for biological samples) or displacement of the scatterers due to the typical optical wavelength being much smaller.

In the following paragraph, I will illustrate the basis of electromagnetic scattering. Specifically, I will discuss single and multiple scattering, illustrating the differences between the two regimes and physical models.

1.3.1 Light Propagation in Random Media

We call single scattering when radiation is only scattered by one localized scattering site, whereas when the radiation scatters multiple times, we define this as multiple scattering (see Fig. 1.8).

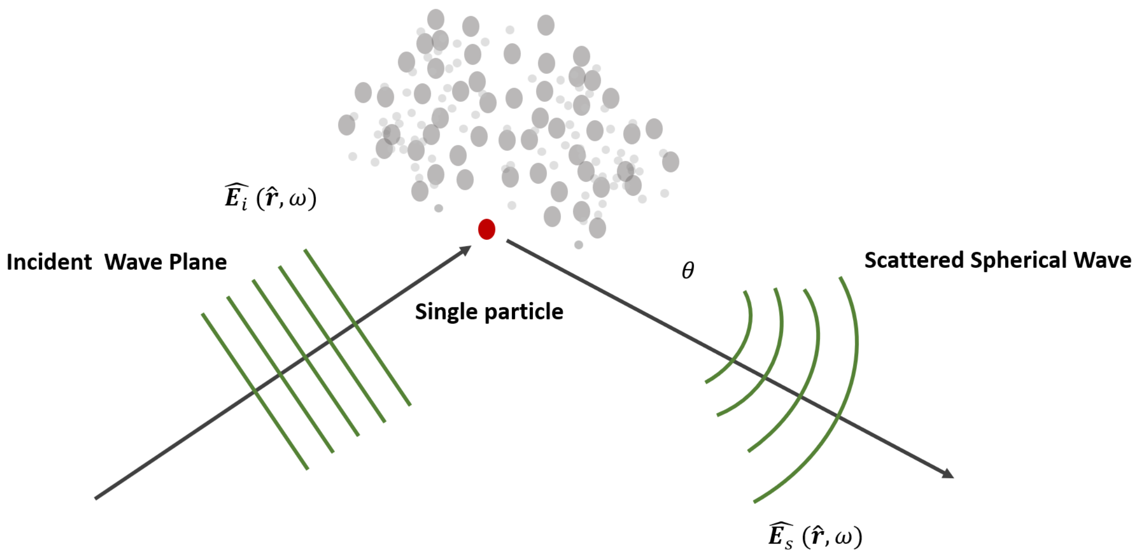

Figure 1.8 An Incident plane wave $\vec{E}_{inc}$ scattered by a single object producing a spherical wave $\vec{E}_s$.

And the crucial difference between the two kinds of scattering is that single scattering can be treated as a random phenomenon, and multiple scattering, counterintuitively, can be described as a deterministic phenomenon as the combined results of a considerable number of scattering events tend to average out.

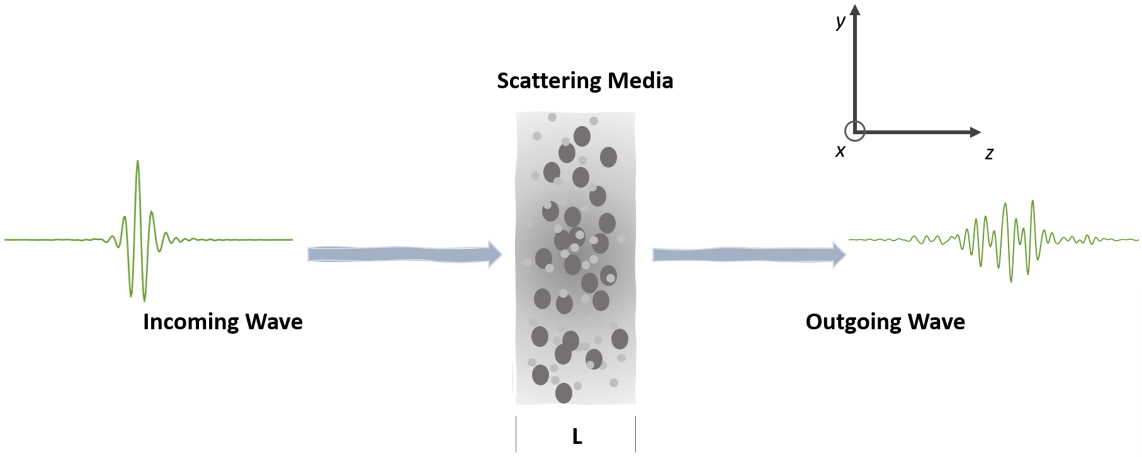

Figure 1.9 *Infinite sample of thickness L with randomly distributed scattering particles embedded in a homogeneous medium.*

Thus it can be modelled with diffusion theory (for instance, light passing through thick fog). Indeed the terms multiple scattering and diffusion are interchangeable in many contexts; for instance, optical elements designed to produce multiple scattering are known as diffusers. However, not all multiple scattering is deterministic and sometimes has random outcomes, particularly with coherent radiation.

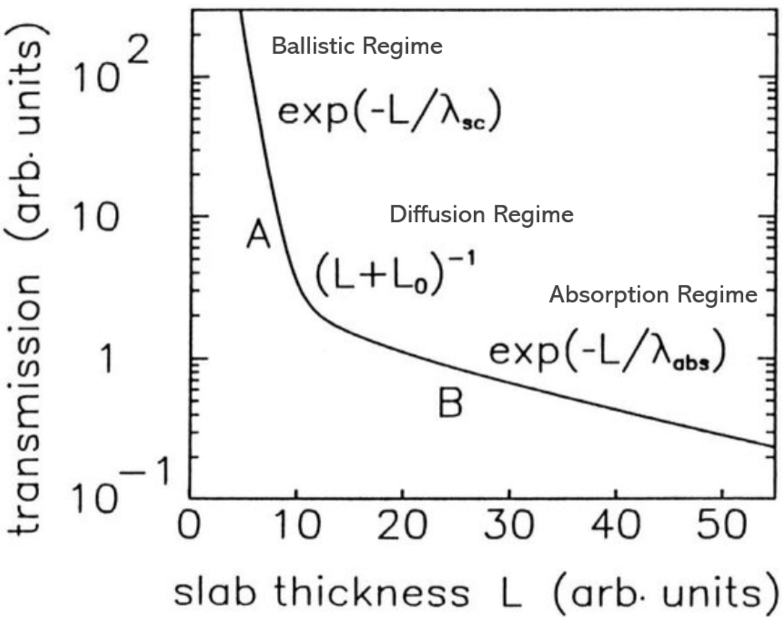

Figure 1.10 *The three main scattering regimes. We note an exponential decay of the transmission coefficient, whereas the diffusion regime decays as* 1 /*L*. *Figure adapted from [87].*

Speckles, for instance, are random fluctuations in the multiply scattered intensity of coherent radiation. Unlike single-particle models, where several theories prove exact and approximate solutions, the problem becomes more complicated to study in the presence of many scattering particle systems.

Multiple scattering phenomena led to explore a variety of novel physics frameworks [10,88–90], such as photon localization [5] and diffusion [91,92].

In Fig. 1.9, we show an incoming wave propagating through randomly distributed dielectric particles embedded in a homogeneous binding with different refractive indices.

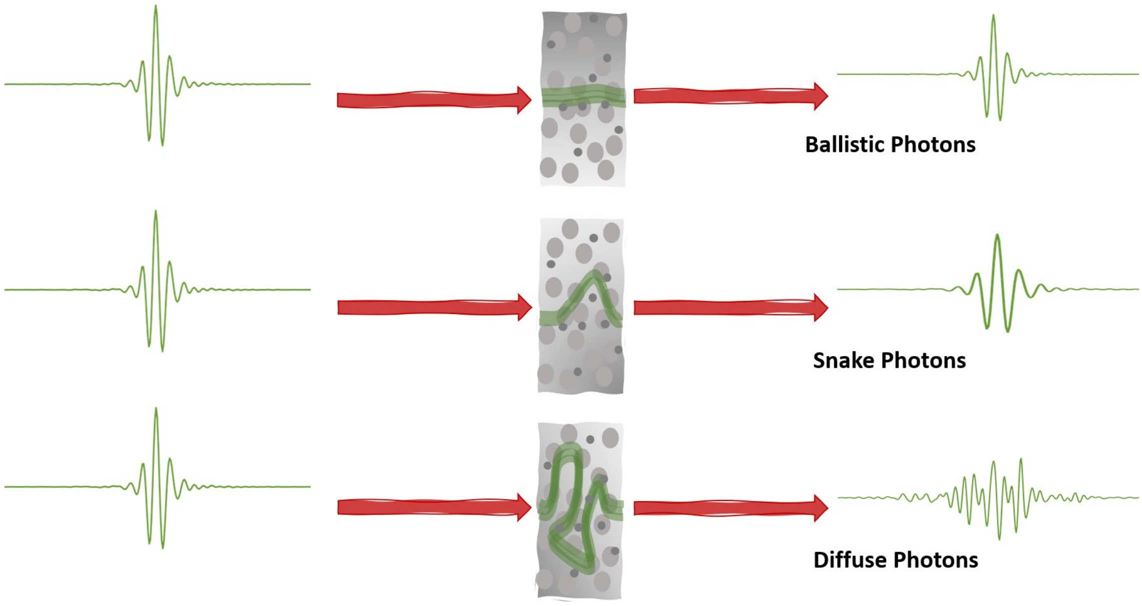

Figure 1.11 Three scattering mechanisms form set spherical scattering particles: ballistic, snake, and diffuse photons.

We consider dimension $x-y$ infinite, and $z=L$; the thickness of the sample L influences the way light propagates inside the medium. Indeed, from this parameter, we are led to define three main regimes: ballistic, diffusion, and absorption regime [87].

Figure 1.10 shows the heuristic plot of the three main regimes: the transmission coefficient as a function of the thickness slab. The ballistic regime decays exponentially, and the decay rate represents the scattering mean free path λ_{sc} (average distance between two scattering events). In the diffusion regime, we notice a milder decay proportional to $(L+L_0)^{-1}$, whereas the absorption regime dominates over long path thickness.

When considering spherical scatterers, the ballistic and diffusive regimes differ in many properties; apart from the transmission characteristics, the two regimes differ in polarisation maintenance. Indeed, ballistic waves maintain their polarisation contrary to diffused photons, where photons encounter many scattering events. In between the two regimes from Fig. 1.11, we see the snake photons [93], a condition where photons encounter more than one scattering event. In this regime, light still maintains some 'memory'; for instance, its polarisation is partially preserved.

1.3.2 Ultrafast Terahertz Imaging in Complex Media

In the optical domain, recent imaging techniques have made it possible to investigate objects placed beneath a scattering medium [94,95]. Both the spatial [7] and temporal [47] control of light propagation through an inhomogeneous sample (by means of wavefront-shaping [9]) have made possible super-resolution imaging in a variety of applications, such as fluorescence microscopy [96]. Computational techniques based on the speckle-pattern correlation analysis have further dramatically simplified the experimental geometries required for single-shot monochromatic or narrowband imaging through complex media [97]. Furthermore, computational methodologies such as diffusing tomography [81], temporal-field correlation analysis [98,99], and speckle tomography through correlation functions of the light's patterns interference [100] have enabled the study of heterogeneity in dynamic turbid media. To date, these studies have been limited to monochromatic and narrowband sources. Hence, the necessity of broadband spectroscopic capabilities for complex material characterization has been many scientists' focus.

In the THz domain, the temporal correlations of diffused THz pulses have been used to characterize single scattering events in complex media [83,101]. Due to the spectral artefacts caused by multiple scattering events, only a few works to this day use broadband THz imaging to characterise scattering samples fully. A recent work by Khani and co-workers [102] used THz time-domain spectroscopy (THz-TDS) spectra to resolve the resonant frequencies of different materials in a heterogeneous sample buried beneath a turbid scattering medium.

They extracted a spectral image of the diffused THz extinction using an oblique detection angle combined with a computational imaging approach (see Fig. 1.12). THz-TDS techniques have been used to detect and study the ballistic and quasi-ballistic portions of the transmitted THz waves [57]. So far, scientists have either neglected the diffused transmitted THz radiation [103,104] or collected the whole scattered field - both ballistic and diffused components - by averaging with the ballistic forward-scattering field [105] (for instance, the effect of volume scattering in pellets [103,104,106–110]).

However, the number of works focusing on purely diffusive waves has been scarce, primarily because of the drastically reduced signal-to-noise ratio (SNR) characterising highly-scattering media [105,111].

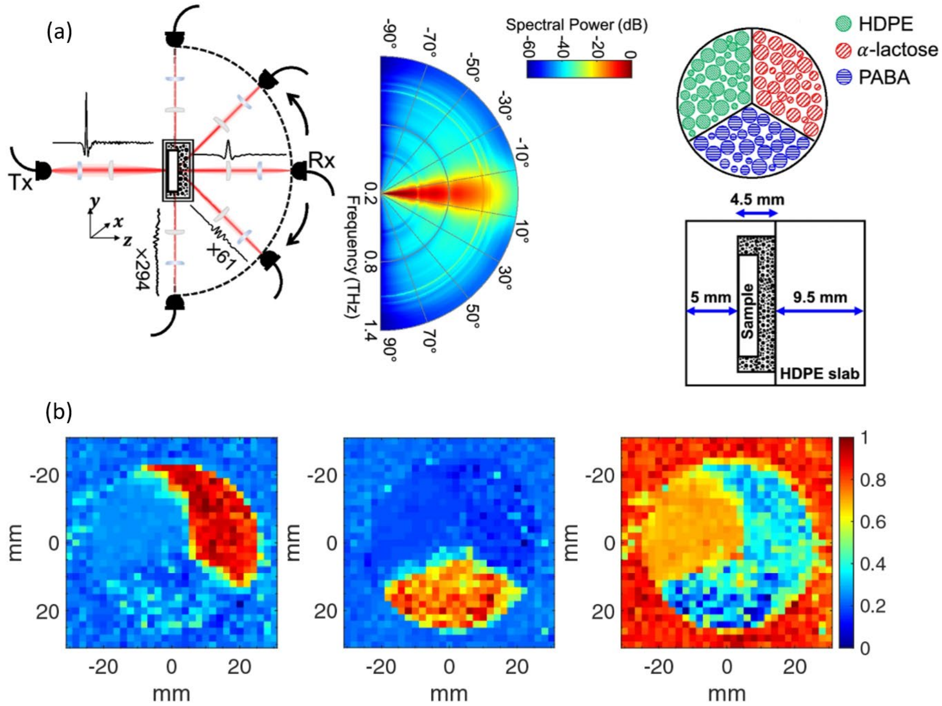

Figure 1.12 (a) The schematic of the imaging setup for measuring the diffused THz field. The measurement shows the angular distribution of the scattered THz spectral power. The sample is made of three different materials: HDPE, α-lactose, and PABA. (b) The chemical THz maps. Figures were adapted from [102] and re-used under the Creative Commons Attribution 4.0 (CC-by articles).

1.3.3 Ultrafast Terahertz Radiation and their Applications for Ghost Imaging

Interestingly, speckle illuminations can be promising for various applications. Leibov and co-workers [112] have recently provided a numerical and experimental study of the formation of speckle patterns using broadband ultrafast THz pulses. Features such as size and sharpness on the diffuser parameters are demonstrated to have a strong dependence on the statistical parameters of speckles: for instance, the deviation of the phase surface inhomogeneity and the correlation length. Indeed, the speckle size increases as the surface correlation length increases. Utilizing random speckle patterns has been part of the idea behind the numerical method for the implementation of novel ghost imaging techniques, and in Ref. [112], scientists work on the experimental formation of speckle patterns using ultrafast THz pulses, see Fig. 1.13.

Quite surprisingly, in agreement with the statistical characteristics, the experimentally obtained speckle patterns corresponded to the numerical results. This represents the experimental verification that, in principle, it is possible to form speckle patterns using broadband THz radiation and demonstrates the possibility of using these speckles in the imaging system based on the nonlinear ghost imaging method [113].

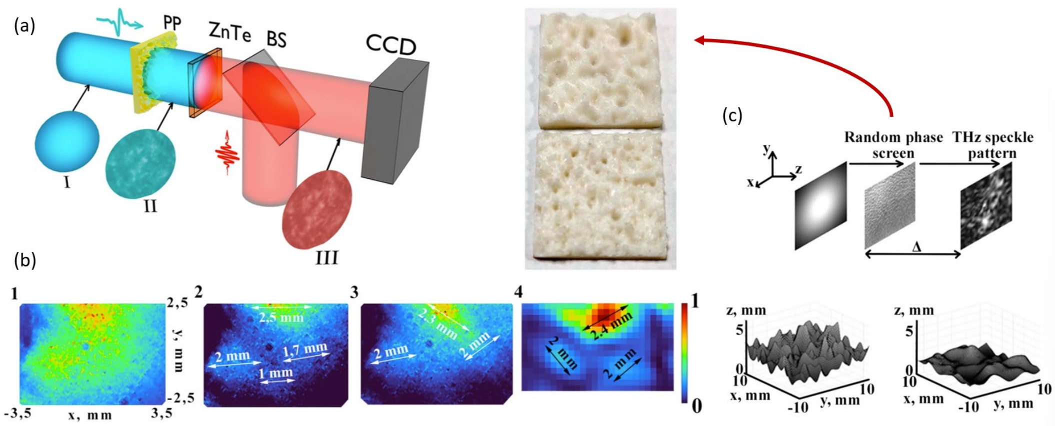

*Figure 1.13 **(a)** Schematic diagram of the detection system in THz imaging setup. The Gaussian THz field (I) passes through the transparent phase plate with a random distribution, changing its spatial distribution. **(b)** Initial THz profiles and resulting THz speckle patterns were obtained from the radiation intensity recorded on an imaging setup for the case in which THz radiation propagates through the phase plates located at a distance of 5 cm from the ZnTe crystal. **(c)** Scheme of acquisition of speckle patterns for monochromatic THz radiation. Two samples of Gaussian random rough surface. Figures were adapted from [112] and re-used under the Creative Commons Attribution 4.0 (CC-by articles).*

It is essential to highlight that utilizing broadband THz would potentially allow for the full spectral features of the image (hyperspectral imaging).

1.4 The Structure of the Thesis

This thesis presents a theoretical and experimental framework to demonstrate spatiotemporal superfocusing (SF) and field modulation of ultrafast THz waves in scattering media. Leveraging the Nonlinear Ghost Imaging methodology [113–115], I show that THz state-of-the-art time-domain technology provides access to the full-wave control of electromagnetic radiation transmitted through a scattering medium.

The thesis is structured as follows. Following the introduction to Complex Photonics discussed in this first part of the thesis, in chapter 2, I will showcase the Nonlinear Ghost Imaging work; chapter 3 illustrates the theoretical work related to the scattering assisted at THz frequencies; and in chapter 4, I will showcase the experimental demonstration. In chapter 5, I will draw a conclusion on my work and some potential future applications and studies still to investigate related to my subject. Finally, in chapter 6, I will also separately show my publications, talks, conferences, and awards.

As mentioned in the abstract, the thesis is compliant with the 'paper-style' format, and the main results are presented as a collection of published articles. Last but not least, I will insert some parallel projects that I have been working on during my PhD course; I will collocate them inside the appendix, along with some elucidations on nonlinear optics. I will focus on the fundamental nonlinear mechanism that scientists use today for generating and detecting ultrafast THz pulses, for instance, the basis of optical rectification and electro-optic sampling. The order of the chapters (not necessarily listed chronologically) mirrors the logical escalation of the research conducted in the doctoral course.

Chapter 2: Terahertz Time-Resolved Nonlinear Ghost Imaging

In this chapter, I will discuss the work on Time-Resolved Nonlinear Ghost Imaging (TNGI). The underlying physical background has been developed in Ref. [114], and the implemented methodology can perform super-resolution hyperspectral THz images. Also, at terahertz frequencies, time-domain reconstruction of the fields is possible by employing Time-Domain Spectroscopy (TDS) [116–118], therefore, enabling an analysis of temporal properties of samples (and, consequently, spectral information), in contrast to the intensity-only measurements commonly performed at optical frequencies.

A super-resolution imaging methodology would require the generation of THz patterns whose minimum feature size is equal to the required physical pixel size and is comparable to or less than the wavelength associated with THz radiation being generated: this regime is called the "sub-wavelength regime", and diffraction dramatically affects patterns quality after just a few hundreds of microns of propagation; to avoid this, the THz patterns need to be sampled just after interaction with the sample, implementing in fact, a "near-field" technique. The generation of THz patterns is achieved by the nonlinear conversion of optical patterns by means of optical rectification: this process is convenient because it allows the THz field to be modulated by the use of a standard optical spatial light modulator (SLM). In this methodology, the SLM allows pushing the THz patterns to the optical resolution (and, consequently, to sub-wavelength resolution at THz frequencies).

Typically in a ghost imaging (GI) setup, a light beam is split into two branches; one is sent to a multi-pixel detector, such as a camera CCD, the other is sent to the object, and a single-pixel detector collects its scattered light, usually referred to as "bucket" detector. A digital system acquires intensity data over time from both of the sensors and performs a correlation: it is surprising to find out that this correlation is an estimate of the object's image, and it is more accurate as more data is acquired and correlated. The term "ghost" is given because the CCD camera is not taking pictures of the object itself but is just acquiring the intensity profile of the light, which will impinge on the object. The ability to manipulate light with an SLM allows the implementation of a "computational" approach. The SLM is used to superimpose a spatial pattern over the incident coherent beam, which propagates until scattered by the unknown object and then gets collected from the bucket detector. Object reconstruction is possible even if the patterns are random as long as they are known and stored for the final reconstruction of the image. Analytically this is done with the same relations developed in a non-computational GI context. The only difference is that random-generated patterns here are known and imposed by an SLM, while in the non-computational case, they are derived from some scattering medium (diffuser) and have to be acquired by the CCD camera sensor because they are initially unknown. In both cases, a known set of patterns is used to reconstruct the image; one can move from a random set of patterns to a deterministic set, constituting a base at a given resolution for the image. Following this, we will discuss the fundamental theoretical background of TNGI.

First, a transmissivity $T(x, y, t)$ function is defined to model both the spatial and the temporal information of the sample:

$$E^{+}(x, y, t) = T(x, y, t) * E^{-}(x, y, t),$$

referring to E^{+} and E^{-} as the electric fields immediately after and before the sample surfaces, respectively. A crucial step is to provide the correct analytical form for the incident electric field, which in the hypotheses of spatiotemporal coupling absence in the patterns can be expressed as:

$$E^{-}(x, y, t) = P(x, y) \cdot f(t).$$

This hypothesis is strong, and this condition is verified in the actual system built in this work because of the nonlinear process involved in generating the required THz patterns.

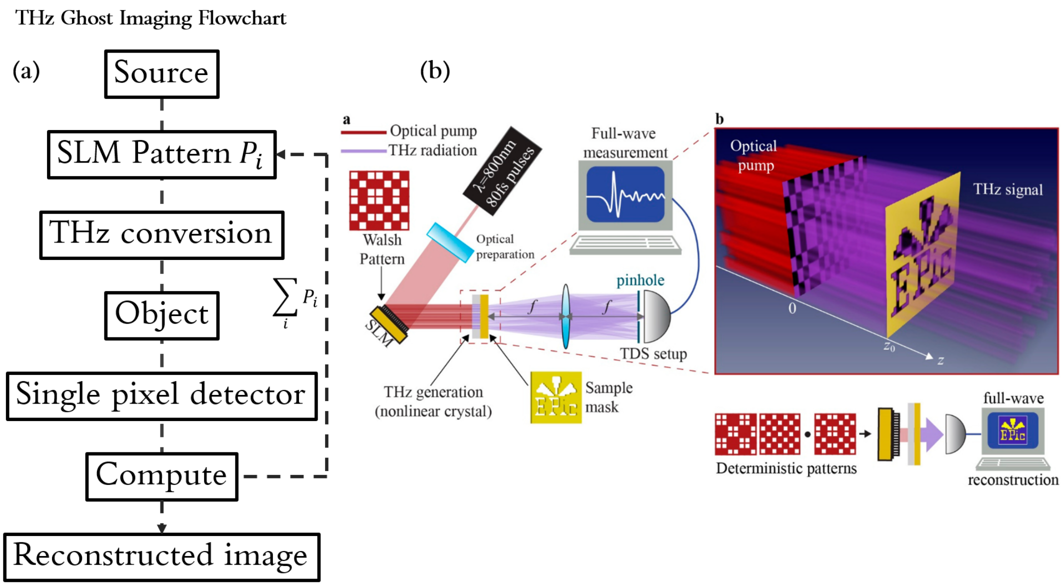

Figure 2.1 (a) Flowchart of the THz Ghost Imaging. Setup of a THz Ghost Imaging. (b) Ideal setup of the THz Ghost Imaging. The figure was adapted from [114] and re-used under the Creative Commons Attribution 4.0 (CC-by articles).

Other ways to shape the THz spatial profile require, for instance, metallic masks and, in general, apertures, which violate this condition as soon as deeply subwavelength features are required to be present on that mask, and the THz patterns would undergo strong diffraction. Therefore, the nonlinear process, such as optical rectification discussed in the previous sections, is so desirable: a direct proportionality relation between optical intensity and THz field assures precise control over THz pattern shapes while eliminating any THz diffraction process that avoids spatiotemporal coupling. The task of shaping THz patterns now becomes the task of shaping optical patterns impinging on a THz generation crystal, which can be accomplished very easily with several techniques (see the flowchart and setup of the THz Ghost Imaging in Fig. 2.1). Notice that the diffraction limit is not violated and is still valid. Indeed, in the generation process, no diffraction phenomenon occurs because of nonlinear near-field conversion, and the problem is shifted to the optical pattern generation, whose feature size is way smaller but still diffraction-limited. All of the previous considerations also explain the presence of the "nonlinear" adjective in the name of this technique. The transmissivity of the sample is given by

$$T(x, y, t) = < C_n(t) P_n(x, y) >_n < C_n(t) >_n < P_n(x, y) >_n , \qquad (2.0)$$

where $< \cdots >_n$ is an average over a set of n patterns, and C_n is the temporal dependent weight associated with the n-th pattern defined as

$$C_n = \int_{xy} dx\, dy\, E^+(x, y, t)$$

which is the spatial average over the entire sample plane of the THz field time-dependent signal associated with the n-th pattern right at the exit surface of the sample. The last statement requires direct measurement of field (amplitude and phase), in contrast to the classic GI theory, which requires intensity-only measurements, and this descends directly from the need to retrieve the temporal behaviour of the sample as well.

Fortunately, this is not a concern since THz field signals can be acquired with a TDS system. The definition of the term C_n is very easy to be implemented, exploiting the capability of a lens to produce the spatial Fourier transform at a focal plane of the field present on the other focal plane. The spectrum is helpful because it contains the average spatial information at the point determined by the condition $k_x = k_y = 0$, which is the focus itself. Indeed, equation (2.0) determines a sequence of actions to retrieve the transmissivity. Firstly, the n-th optical pattern is prepared through the configuration of the SLM to have a nonlinear generation of $E^-(x, y, t)$ with spatial shape given by $P_n(x, y)$. Moreover, a complete TDS acquisition is performed to calculate $C_n(t)$; finally, the estimation of $T(x,y,t)$ updated with new data, and the process repeats with a new pattern until the completion of the set.

In practice, it is more efficient to cycle all the patterns while making a fixed-time acquisition for each pattern of the set and then to move on to the next point in time (and it should have more SNR due to experimental errors of the delay stage), repeating until the required number of points in time is reached: this is mainly to reduce the number of translation steps required to be done by the translational stage; if each TDS scan needs P points to be completed and N is the number of patterns, with the first approach the translational stage moves NP times, while with the last one only P times, which in turn determines a significant reduction of the time required and of the stage wear.

Note that this discussion holds until the effects of generation crystal thickness can be negligible: assuming THz generation as a process happening at the input surface of the crystal, while THz propagates to reach the exit of the crystal, it changes its original shape. If z= 0 is the surface where nonlinear optical to THz conversion happens and $z = z_0 - \epsilon$ is the surface where the sample lies and where the actual previously defined E_n^- field is projected, follows:

$$E_n^- = E_n^{THz}(x,y,z = z_0 - \epsilon, t) = G(x,y,z,t) * E_n^{THz}(x,y,z = 0,t),$$

where $G(x,y,z,t)$ is the dyadic Green's function tensor. This step could be avoided by reducing the generation crystal thickness to, for instance, $100\ \mu m$. Also, notice that already around $90\ \mu m$, the incident pattern is severely distorted [114], and this suggests that it could not be exploited to perform imaging without back-propagation. In the case of thin (two-dimensional) samples, fixed-time scans could be performed to reduce the acquisition time at the cost of losing temporal dispersion information about the sample. For instance, if the sample is constituted of metallic letters deposited on a Kapton film, this is not a concern because no different materials are involved: indeed, the THz field is expected to pass where letters are absent, to be blocked where it meets the letters because of the metal. If the sample is more complicated than that, features related to different materials are detected at different times because of the different THz refractive index, and this approach is not applicable, as stated in [114]. These kinds of images will be referred to as "fixed-time images"; however, when a sufficient number of temporal points is acquired, they will be referred to as "full-wave images" instead.

Regarding the set of patterns used in this work, the Hadamard-Walsh patterns form a two-dimensional mathematical base for a digital image at a given resolution $N \times N$, which, in this case, is also the order of the patterns. Hadamard patterns can acquire spatial information about an object image since they form an orthogonal set.

Reconstruction of the image can be carried out losslessly once the image has been fully sampled. Another advantage is measurement reduction.

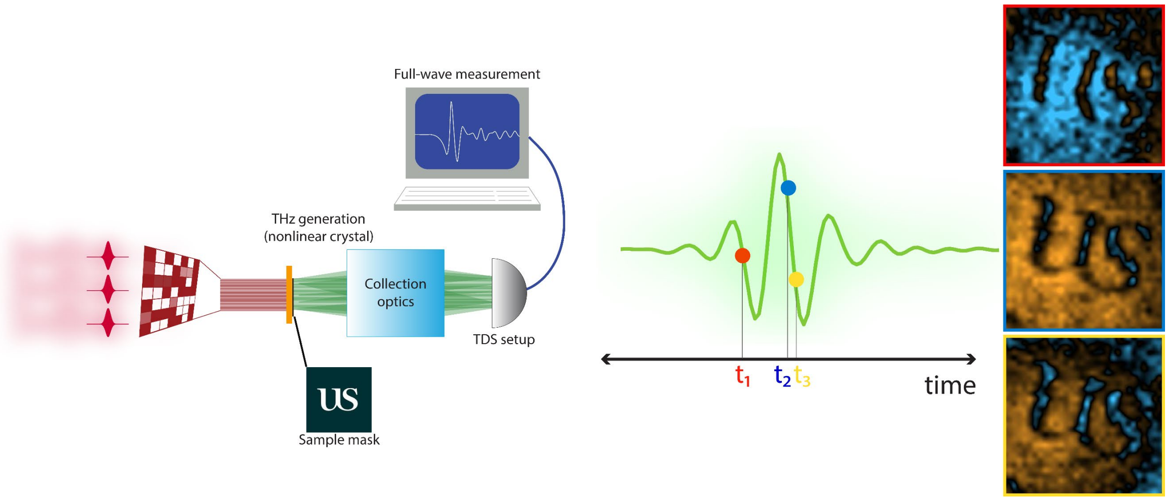

Figure 2.2 Conceptual setup for the TNGI and an example of a terahertz full-wave spatiotemporal image of a metallic sample. Notice the field evolution (colour change at the time t_1, t_2, t_3) underneath the metallic mask as the structure resonance produces a secondary emission. In the reconstruction video, it can be observed that at different scanning times, the object does not appear just as a blocking mask, but it features complex resonances from the edges of the object. Additionally, a fundamental fact is that the time-resolved measurement of the scattered field also allows the reconstruction of the hyperspectral image of the sample. And because of the near-field condition, we were able to resolve features within a 50 μm scale even in the presence of a relatively thick generation crystal.

With under-sampled data, an image can be reconstructed from a sparse representation in either Hadamard or Fourier domain. As a result, the long acquisition time problem in ghost imaging is solved. Each vector of this base is a $2D$ matrix containing $+1, -1, 0$ elements. However, since an intensity modulation is going to be implemented, the -1 element cannot be reproduced. Therefore, a modified set is then prepared, in which each pattern is split into two patterns with the following relations:
These patterns now have only $+1$, 0 elements, and they are compatible with an intensity modulation process, but they have been doubled in number, and the total number of patterns is now $2N^2$. Notice that this number is also the number of lock-in measurements required for each image to be taken with this system in fixed-time mode.

$$H_n(x,y) \rightarrow \begin{cases} H_n^+(x,y) = \dfrac{H_n(x,y)+1}{2}; \\ H_n^-(x,y) = 1 - H_n^+(x,y). \end{cases}$$

Figure 2.2 shows a full-wave image reconstruction of the US sample. Notice that $32 \times 32 \times 2$ images are acquired at 20 different instants of time (TDS). Also, observe that not every part of the logo is visible at any time. In addition, the same information enables the plot of the figures in spectral amplitude. Since the temporal reconstruction produces a set of THz time-domain signals at the exit of each pixel, the amplitude spectrum can be easily calculated out of it.

Note that a back-propagation would also enable the use of thicker generation crystals, increasing the generated THz radiation and, consequently, the SNR; indeed, a higher SNR would allow using lower lock-in time constants, reducing the scan time. Currently, the time required for these images to be completed is in the range of hours, preventing this technique from being used to scan samples in motion.
Another property of full-wave imaging is to characterise samples with a known spectral response in the THz region; then, some heterogeneous samples could be imaged to demonstrate the usefulness of spectral imaging as a tool to investigate the composition of a sample when it is constituted of unknown materials [113].

About the paper: Route to Intelligent Imaging Reconstruction via Terahertz Ghost Imaging

The Nonlinear Ghost Imaging methodology is based on detecting the transmitted THz pulse with a Fourier detection scheme (ideally, by detecting only the $k = 0$ point). However, experimentally, the probe spot size condition is substantially smaller than the THz focal point, and a deep analysis of how the image reconstruction is affected by its dimension is shown. In this invited review paper published in the MDPI Micromachines journal, I contributed to the text's writing and reviewing prior to submission.

Impact

The article was published on the 20th of May 2020 and targeted the MDPI Micromachine journal, with a 5-year impact factor of 2.943. The journal's scope spans all optics and photonics, which is obviously fitting with the article's claims. The article currently has 11 citations, and the potential impact is highly significant within the THz imaging community. The Altmetric Attention is 6.
Link

About the paper: Hyperspectral Terahertz Microscopy via Nonlinear Ghost Imaging

The previously pursued projects on spatiotemporal control in scattering media have been based on a novel near-field THz imaging methodology that I contributed to developing during my PhD, the Nonlinear Ghost Imaging. Generally, ghost-imaging systems use a single bucket detector (which is much more convenient in the THz region thanks to TDS) and a spatial light modulator (SLM) to spatially illuminate patterns with a series of orthogonal matrices (for instance, Hadamard basis) in order to retrieve the image. Fundamentally, the idea is that, depending on the spatial frequencies of the pattern, the single-pixel detector signal varies with each illumination, and by correlating the patterns with the detected field and summing them, the image is formed. The motivation for using such a scheme in the THz range is because, in principle, by patterning the optical beam prior to THz generation, the actual observed resolution is limited by the spatial light modulator pixel size instead of the much larger THz wavelength. Indeed, the article is an experimental demonstration of hyperspectral THz nonlinear ghost imaging, where the diffraction in the THz fields is overcome by detecting the entire time-resolved waveform and backpropagating the image.

Last but not least, overcoming the space-time coupling via inverse propagation dramatically improved the hyperspectral image. My role in this work was to design and implement the experimental setup by using a spatial light modulator (SLM). The setup worked and measured the first spatiotemporal images of a metal mask (the mask was a combination of metal and a Kapton with imprinted the University of Sussex logo 'US'). Also, I contributed to the text's writing prior to submission.

Impact

The article was published in Optica on the 19th of February, 2020. The article targeted the Optical Society of America journal Optica, which has a 5-year impact factor of 14.526. The journal's scope spans all optics and photonics, obviously fitting with the article's claims. The article currently has 76 citations, and the potential impact is highly significant within the THz imaging community. The Altmetric Attention is 131.
Link

2.1 Route to Intelligent Imaging Reconstruction via Terahertz Ghost Imaging

micromachines

MDPI

Article

Route to Intelligent Imaging Reconstruction via Terahertz Nonlinear Ghost Imaging

Juan S. Totero Gongora, Luana Olivieri, Luke Peters, Jacob Tunesi, Vittorio Cecconi, Antonio Cutrona, Robyn Tucker, Vivek Kumar, Alessia Pasquazi and Marco Peccianti *

Emergent Photonics (EP*ic*) Laboratory, Department of Physics and Astronomy, University of Sussex, Brighton BN1 9QH, UK; jt420@sussex.ac.uk (J.S.T.G.); l.olivieri@sussex.ac.uk (L.O.); l.peters@sussex.ac.uk (L.P.); jt298@sussex.ac.uk (J.T.); v.cecconi@sussex.ac.uk (V.C.); ac878@sussex.ac.uk (A.C.); rt232@sussex.ac.uk (R.T.); vk230@sussex.ac.uk (V.K.); a.pasquazi@sussex.ac.uk (A.P.)

* Correspondence: m.peccianti@sussex.ac.uk; Tel.: +44-(0)1273-873171

Received: 21 January 2020; Accepted: 17 May 2020; Published: 20 May 2020

Abstract: Terahertz (THz) imaging is a rapidly emerging field, thanks to many potential applications in diagnostics, manufacturing, medicine and material characterisation. However, the relatively coarse resolution stemming from the large wavelength limits the deployment of THz imaging in micro- and nano-technologies, keeping its potential benefits out-of-reach in many practical scenarios and devices. In this context, single-pixel techniques are a promising alternative to imaging arrays, in particular when targeting subwavelength resolutions. In this work, we discuss the key advantages and practical challenges in the implementation of time-resolved nonlinear ghost imaging (TIMING), an imaging technique combining nonlinear THz generation with time-resolved time-domain spectroscopy detection. We numerically demonstrate the high-resolution reconstruction of semi-transparent samples, and we show how the Walsh–Hadamard reconstruction scheme can be optimised to significantly reduce the reconstruction time. We also discuss how, in sharp contrast with traditional intensity-based ghost imaging, the field detection at the heart of TIMING enables high-fidelity image reconstruction via low numerical-aperture detection. Even more striking—and to the best of our knowledge, an issue never tackled before—the general concept of "resolution" of the imaging system as the "smallest feature discernible" appears to be not well suited to describing the fidelity limits of nonlinear ghost-imaging systems. Our results suggest that the drop in reconstruction accuracy stemming from non-ideal detection conditions is complex and not driven by the attenuation of high-frequency spatial components (i.e., blurring) as in standard imaging. On the technological side, we further show how achieving efficient optical-to-terahertz conversion in extremely short propagation lengths is crucial regarding imaging performance, and we propose low-bandgap semiconductors as a practical framework to obtain THz emission from quasi-2D structures, i.e., structure in which the interaction occurs on a deeply subwavelength scale. Our results establish a comprehensive theoretical and experimental framework for the development of a new generation of terahertz hyperspectral imaging devices.

Keywords: terahertz; nonlinear optical conversion; complex optical systems; adaptive imaging; single-pixel imaging; surface nonlinear photonics

1. Introduction

In recent years, there has been increasing interest in the development of imaging techniques that are capable of reconstructing the full-wave properties (amplitude and phase) of arbitrary electromagnetic field distributions [1–3]. While standard optical technologies, such as cameras and photodiodes, are usually sensitive to the field intensity, a large part of the sample information is encoded in the optical phase of the scattered field [4]. Interestingly, the direct detection of the field evolution is achievable at terahertz (THz) frequencies thanks to the availability of the time-domain spectroscopy (TDS) technique. TDS detection provides a time-resolved measurement of the electric field (e.g., via electro-optical sampling [5]), allowing researchers to retrieve the complex-valued dielectric function of a sample. Such a capability, coupled with the existence of specific and distinctive spectral fingerprints in the terahertz frequency range, are critical enabling tools for advanced applications, such as explosive detection, biological imaging, artwork conservation and medical diagnosis [6–10]. However, despite the vast body of potential applications, the development of TDS devices that are capable of high-resolution imaging is still regarded as an open challenge. A typical TDS implementation relies on complex and expensive optical components that cannot be easily integrated into high-density sensor arrays [11].

To date, THz imaging mostly relies on thermal cameras, essentially the equivalent of optical cameras, which employ arrays of micro-bolometers to measure the time-averaged intensity of the THz signal. As such, they cannot be employed for time-resolved THz detection and they are insensitive to the optical phase and temporal delay of the transmitted THz field. In an attempt to develop arrays of TDS detectors, researchers have proposed two-dimensional full-wave imaging devices that are composed of arrays of photoconductive antennas or Shack–Hartmann sensors [12,13]. However, these devices require complex and expensive technological platforms and their practicality is still a matter of debate. Furthermore, they fundamentally sample the image information in an array of single and well-separated small points. Hence, obtaining a high resolution can still require mechanical action on the sample.

A promising alternative to TDS imaging arrays is single-pixel imaging, or ghost imaging (GI). In these approaches, the sensor array is replaced by a single bucket detector, which collects the field scattered by the sample in response to a specific sequence of incident patterns. By correlating each acquired signal with its corresponding incident field distribution, it is possible to reconstruct the sample image [14–17]. However, despite its simplicity, the implementation of GI at terahertz frequencies is affected by the limited availability of wavefront-shaping devices (e.g., spatial light modulators) that are capable of impressing arbitrary patterns on an incident THz pulse. Following the initial experimental demonstrations with metallic masks and metamaterial devices [18,19], several research groups' researchers have proposed indirect patterning techniques for the generation of high-resolution THz patterns. One of the most successful approaches relies on the generation of transient photocarrier masks on semiconductor substrates [20–23]. In these experiments, a standard optical Spatial Light Modulator (SLM) impresses a spatial pattern on an ultrafast optical beam. Upon impinging on a semiconductor substrate, the latter generates a distribution of carriers matching the desired pattern profile, which acts as a transient metallic mask and can be used to pattern an external THz beam. While this technique has been successfully employed to achieve THz imaging with a deeply subwavelength resolution, it is also affected by a few limitations. In particular, recent works have shown that the maximum resolution achievable with these techniques is strongly dependent on the semiconductor substrate thickness: in Stantchev and coworkers [20,21], for example, researchers have demonstrated that deeply subwavelength resolutions are achievable only when considering patterning substrates with a thickness below 10 µm.

In a series of recent works, we have proposed a new imaging technique, time-resolved nonlinear ghost imaging (TIMING), which overcomes several of these limitations [24–26]. TIMING relies on the integration of nonlinear THz pattern generation with TDS single-pixel field detection. In this work, we discuss the main features of our approach and present our latest results on the theoretical framework underlying our image reconstruction process. Via analysis of the compression properties of the incident pattern distribution, we show how a TIMING implementation based on an optimised Walsh–Hadamard encoding scheme can significantly reduce the number of incident patterns required to obtain a high-fidelity image of the sample. Finally, we discuss how the development of ultra-thin THz emitters can provide a significant improvement to the imaging performance of TIMING.

2. Time-Resolved Nonlinear Ghost Imaging: A Conceptual Overview

A conceptual schematic of our imaging setup is shown in Figure 1a. A spatial pattern is impressed on the optical beam through a binary spatial light simulator, e.g., a digital micromirror device (DMD), obtaining the optical intensity distribution $I_n^{opt}(x,y,\omega)$. The THz patterns $E_n^0(x,y,t)$ are generated using a nonlinear conversion of $I_n^{opt}(x,y,\omega)$ in a nonlinear quadratic crystal (ZnTe) of thickness z_0. The THz pattern propagates across the crystal and interacts with the object, yielding a transmitted field, which is collected by a TDS detection setup. Different from the standard formulations in optics, which relies on the optical intensity, our object reconstruction scheme relies on the time-resolved detection of the electric field scattered by the object. More specifically, the electric field distribution is defined immediately before and after the object as $E^-(x,y,t \;=\; E(x,y,z_0-\epsilon,t)$ and $E^+(x,y,t) \;=\; E(x,y,z_0+\epsilon,t)$, respectively, where z_0 is the object plane and $\epsilon > 0$ is an arbitrarily small distance (Figure 1a, inset). Without loss of generality, the transmission properties of the object are represented by defining the transmission function $T(x,y,t)$, which is defined on both the spatial and temporal components to account for the spectral response of the sample. To simplify our analysis, in the following, we considered two-dimensional objects, i.e., we restricted ourselves to transmission functions of the form $T(x,y,t)$. Under this position, the transmitted field is straightforwardly defined as:

$$E^+(x,y,t) \;=\; \int \mathrm{d}t' T(x,y,t-t')E^-(x,y,t). \tag{1}$$

The objective of a single-pixel imaging methodology is to reconstruct the transmitted field distribution $E^+(x,y,t)$ through a sequence of measurements to retrieve the transmission function of the object. In our approach, this corresponds to measuring the TDS trace of the spatially-averaged transmitted field from the object in response to a sequence of predefined patterns (a procedure known as computational ghost imaging) [27]. The nth pattern is denoted by $E_n^-(x,y,t) \;=\; P_n(x,y)f(t)$, where $P_n(x,y)$ is the deterministic spatial distribution of the pattern and $f(t)$ is the temporal profile of the THz pulse. The reconstruction process is defined as follows:

$$T(x,y,t) \;=\; C_n(t)P_n\,(x,y)_n - C_n(t)_n P_n(x,y)_n\,, \tag{2}$$

where $\langle\cdots\rangle_n$ represents an average over the distribution patterns and the expansion coefficients $C_n(t)$ are defined as follows:

$$C_n(t) \;=\; \int \mathrm{d}x\mathrm{d}y\, E_n^+(x,y,t) \;=\; \int \mathrm{d}x\mathrm{d}y\mathrm{d}t' T(x,y,t-t')E_n^-(x,y,t). \tag{3}$$

A numerical implementation of the image reconstruction process is shown in Figure 1b,c, where we employed TIMING to reconstruct the transmitted field from a semi-transparent sample (a leaf). In Figure 1b, we report the spatial average of the reconstructed field, exhibiting the characteristic temporal profile of the incident THz pulse. Since our image reconstruction operates simultaneously in time and space, it allows for not only retrieving the spatial distribution of the object but also its temporal/spectral features. The specific result of a TIMING scan is a spatiotemporal image of the transmitted field, as shown in Figure 1c.

An interesting question is whether the distance between the distribution of THz sources and the sample has any effect on the image reconstruction capability of our setup. This point is pivotal when time-resolved imaging is desired, as propagation always induces space–time coupling. This condition represents a typical challenge in mask-based ghost imaging when time-domain detection is sought. The propagation within the patterning crystal is known to lead to significant reconstruction issues when considering deeply subwavelength patterns [20–22]. These issues are related to the intrinsic space–time coupling that takes place within the crystal [28]. In essence, once the patterns are impressed on the THz wave at the surface of the crystal (at $z \;=\; 0$), they undergo diffraction. As a result, the electric field distribution $E_n^-(x,y,t)$ probing the sample is not the initial distribution $E_n^0(x,y,t)$, but rather a space-time propagated version of it. The latter is mathematically expressed as:

$$E_n^-(x,y,t) = E_n(x,y,z_0-\epsilon,t) = \int \mathrm{d}x\mathrm{d}y\mathrm{d}t' G(x-x',y-y',z_0-\epsilon,t-t')E_n^0(x,y,t), \tag{4}$$

where $G(x,y,z_0-\epsilon,t)$ is the dyadic Green's function propagating the field from $z = 0$ to $z = z_0-\epsilon$. Since space–time coupling is essentially a linear process, it can be inverted by applying a Weiner filter to the reconstructed image to mitigate the effects of diffraction. In the angular spectrum coordinates (k_x,k_y,z,ω), the Weiner filter is defined as:

$$W(k_x,k_y,z,\omega) = \frac{G^\dagger(k_x,k_y,z,\omega)}{\left|G(k_x,k_y,z,\omega)\right| + \alpha NSR(k_x,k_y,\omega)}, \tag{5}$$

where $NSR(k_x,k_y,\omega)$ is the spectral noise-to-signal distribution, α is a noise-filtering fitting parameter and † stands for Hermitian conjugation [24]. As expressed by Equation (5), the Weiner filter is the equivalent of an inverse Green's function operator that is modified to take into account the presence of noise in the experimental measurements. The effect of the NSR term in the denominator, which is controlled by the parameter α, is to suppress the regions of the spectrum that are dominated by noise and could render the inversion operation an intrinsically ill-posed problem [29].

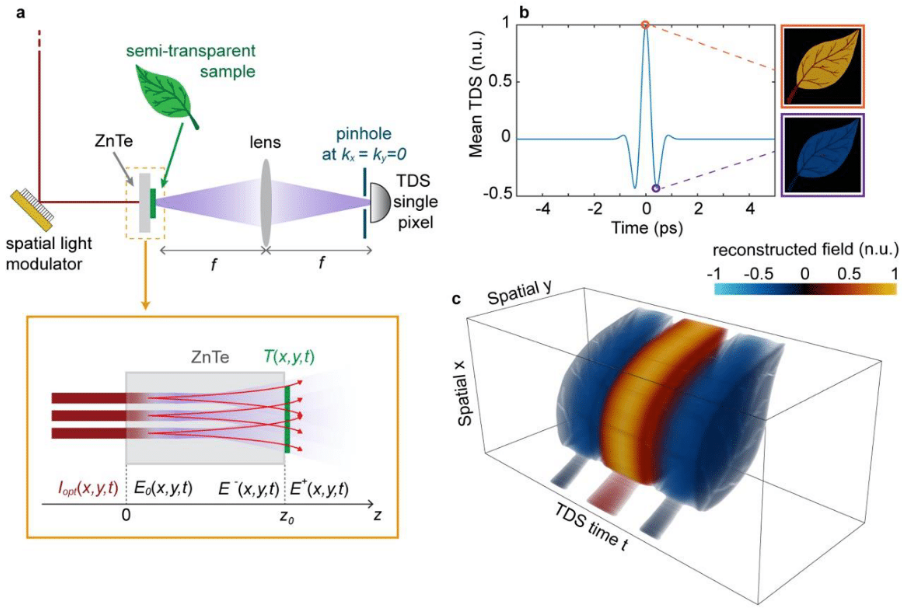

Figure 1. Conceptual description of time-resolved nonlinear ghost imaging (TIMING). (**a**) Schematic of the experimental setup. (**b**,**c**) Simulation of the TIMING reconstruction of a semi-transparent sample, including the average field transmission (panel b) and the full spatiotemporal image of the sample (panel c). The simulated object size was 10.24 cm × 10.24 cm, sampled with a spatial resolution of 512 × 512 pixels (Δx = 200 µm) and a temporal resolution of Δt = 19.5 fs. The nonlinear crystal thickness was z_0 = 10 µm. n.u.: normalised units, TDS: Time-domain spectroscopy.

From a physical point of view, Equations (4) and (5) can be read as follows: when performing a time-domain reconstruction of the image, the spatial distribution of $E_n^+(x,y,t)$ is acquired at a given time. However, this is not the scattered field from the object in response to the incident pattern E_n^0 at that time; there is no time in which the scattered field $E_n^0(x,y,t)$ is univocally represented in the sampling pattern E_n^-. The reason is simply that the method is slicing a fixed-time contribution of a piece of information that is warped in the space-time. This warping is introduced by the distance between sources and the object plane; therefore, it is different for any plane of the object being imaged.

Said differently, using fixed-time images to reconstruct planar features produces a fundamentally incorrect picture of the evolving scattered field, with different degrees of "distortion" introduced by the amount of propagation. It is worth noting that, although related, this is not the same concept as that of resolution degradation of incoherent near-field systems. In fact, Equation (4) shows that any space-time information retained by the field can be accessed only by accounting for near-field propagation. TIMING reconstructs the image of a scattered field from an object with fidelity by applying the backpropagation kernel from Equation (5). Another interesting aspect is whether the thickness of the nonlinear crystal accounts for an overall separation between terahertz sources and the object, affecting the achievable resolution. The difference here is that the propagation is inherently nonlinear and although the generated terahertz signal diffracts linearly, for any desired resolution, there is always a given generating crystal section that is sufficiently close to the object to illuminate it within the required near-field condition. We have recently theoretically and experimentally demonstrated that the diffraction limit does not directly apply in the nonlinear GI via the generation crystal thickness since the nonlinear conversion from optical to THz patterns is a process distributed across the crystal [25]. We argue that this general approach is particularly useful when considering samples stored in cuvettes or sample holders.

3. Compressed and Adaptive Sensing Applications

In this section, we discuss the image reconstruction performance of TIMING as a result of our particular choice of input pattern distribution. To reconstruct the sample, TIMING relies on the Walsh–Hadamard (WH) image decomposition, which constitutes the binary counterpart of standard Fourier-based image analysis [30]. In our approach, the choice of the incident pattern distribution was driven by three considerations: (i) the compatibility with the available wavefront-shaping technology impressing patterns on the optical beam, (ii) the average signal-to-noise ratio (SNR) of the signal associated with each incident pattern and (iii) the energy compaction (compressibility) properties of the image expansion base. The WH patterns can be implemented straightforwardly through a digital micromirror device (DMD) and they are known to maximise the SNR of the acquired signals in experiments [31,32]. The latter is a significant advantage when compared to standard TDS imagers, which rely on a raster-scan reconstruction approach, where either the source or receiver (or both) are sequentially moved across the sample, leading to a combination of single-pixel detection and illumination [10]. While this approach is intuitive and straightforward to implement, a single-pixel illumination usually implies a degradation of the SNR of the expansion coefficients for a fixed intensity per pixel. Furthermore, raster-scan imaging is a local reconstruction algorithm that is not suitable for compressed sensing; in mathematical terms, the raster scan corresponds to expanding the sample image in the canonical Cartesian base $E_{n,m}(x,y) = \delta(x-x_n, y-y_n)$. Trivially speaking, to reconstruct the entire image with this approach, each pixel composing it needs to be scanned.

In contrast, the WH encoding scheme is a very popular example of energy compacting (compressive) decomposition, as in the case of Fourier-based or wavelet-based image analysis [33,34]. In these approaches, the image is represented as an orthogonal basis of extended spatial functions. For example, in the case of Fourier image analysis, the sampling patterns are the basis of the two-dimensional Fourier Transform [29,35]. The choice of an expansion basis composed of extended patterns has two main advantages. First, extended patterns are generally characterised by transmitted fields with higher SNRs because distributed sources generally carry more power. In fact, for a given power limit per pixel, the Walsh–Hadamard decomposition allows for a total energy per pattern that is about N/2 higher than single-pixel illumination. Second, and more importantly, there is no one-to-one correspondence between individual image pixels and distinct measurements (as in the case of the raster scan). In fact, the incident patterns not only probe different parts of the sample in parallel but can also provide useful insights into its spatial structure, even before completing the entire set of illuminating patterns.

In practical terms, a WH pattern of size $N \times N$ is obtained by considering the tensor product between the columns (or, invariantly, rows) of the corresponding $N \times N$ Walsh–Hadamard matrix (see Figure 2a). The columns (or rows) are mutually orthogonal and form a complete tensor basis for any two-dimensional matrix. Interestingly, the columns of the Hadamard matrix can be re-arranged in different configurations, leading to matrices with different orderings [36–38]. In Figure 2, we compare two configurations: the Walsh (or sequency) order and the Hadamard (or natural) order. The Walsh ordering is particularly useful in image reconstruction as it mirrors the standard order of the discrete Fourier basis, i.e., the columns are sorted in terms of increasing spatial frequencies. This means that by using the Walsh matrix, it is possible to acquire complete lower-resolution images before completing the illumination set, which can be useful for applying decisional approaches and reducing the set dimension [39,40].

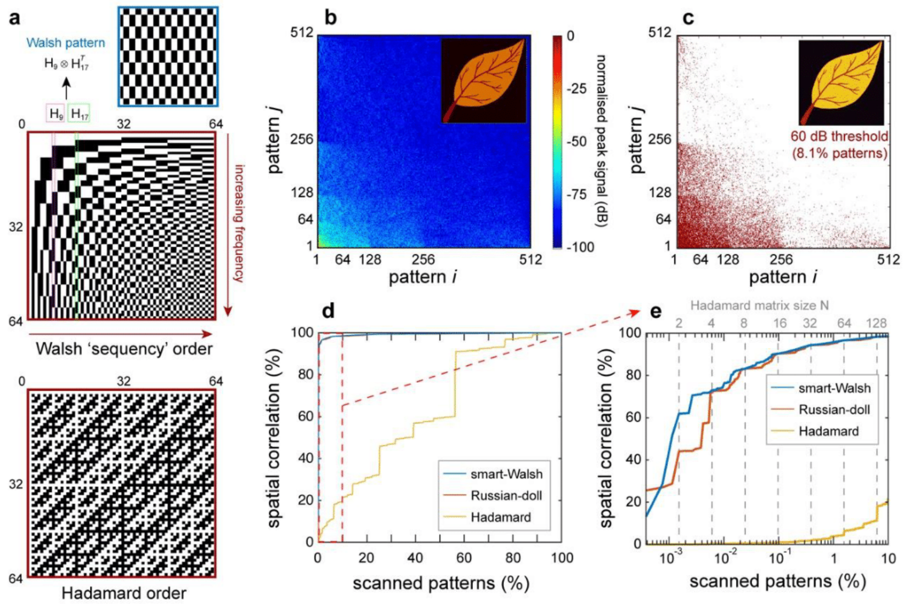

Figure 2. Walsh–Hadamard image reconstruction. (**a**) Generation of incident patterns from the Walsh–Hadamard matrix. Each pattern is defined as the tensor product between two columns of the generating matrix. The patterns can be generated from different configurations of a Hadamard matrix: we show the Walsh, or "sequency", order (top, used in TIMING) and the standard Hadamard, or "natural", order (bottom). (**b**,**c**) Reconstructed Walsh spectrum of the peak-field object transmission. Interestingly, only a fraction of the patterns (8.1%) were associated with a spectral amplitude exceeding the −60 dB threshold (with 0 dB being the energy correlation of the fittest pattern—panel c). Nevertheless, these patterns were sufficient to provide a high-fidelity reconstruction of the image (insets). (**d**,**e**) Pearson correlation coefficients between reconstructed and original images as a function of the number of patterns employed in the reconstruction. The results refer to the entire scan (panel d) and the initial 10% of patterns (panel e).

To illustrate how the image information is distributed across the basis of incident patterns, it is useful to analyse the peak-field Walsh spectrum of the reconstructed image, which is shown in Figure 2b. The WH spectrum is obtained by plotting the $C_n\left(t = t_{peak}\right)$ coefficients as a function of their generating pattern indexes. As can be evinced from Figure 2b, the WH decomposition re-organises the image information into a hierarchical structure, which mirrors the spectral content of the image. Interestingly, this property is at the core of the compression properties of the WH encoding scheme, as can be exploited to significantly reduce the number of measurements required to reconstruct the image. We illustrate this result in Figure 2c, where we identify the coefficients with an amplitude exceeding a −60 dB threshold with a red marker. As shown in Figure 2c, these significant coefficients were mostly localised in correspondence with the smaller spatial frequencies of the image, and for this image, they represented 8.1% of the total number of patterns. Remarkably, this limited number of patterns was sufficient to accurately reconstruct the image (as shown in Figure 2c, inset).

For a given Walsh–Hadamard matrix, it is also critical to consider the specific order employed when selecting the sequence of columns forming the distribution of incident patterns. In our approach, we implemented an optimised ordering of the WH patterns (denoted as "smart-Walsh"), which sorts the incident patterns in terms of increasing spatial frequency (see Supplementary Video 1). In Figure 2d,e, we illustrate the fidelity of the TIMING reconstruction across the ensemble of incident patterns for different sorting schemes. The fidelity between reconstructed and original images is estimated through the Pearson correlation coefficient, which measures the spatial correlation between the two datasets and is defined as:

$$\rho(A,B) = \frac{\sum_{mn}\left(A_{mn}-\overline{A}\right)\left(B_{mn}-\overline{B}\right)}{\sqrt{\sum_{mn}\left(A_{mn}-\overline{A}\right)^2 \cdot \sum_{mn}\left(B_{mn}-\overline{B}\right)^2}}, \tag{6}$$

where $\overline{A}$ and $\overline{B}$ are the spatial averages of A and B, respectively. In our analysis, we considered the performance of our "smart-Walsh" sorting (blue line) with the natural Hadamard sorting (yellow line) and the recently proposed "Russian-doll" sorting (orange line) [38]. As shown in Figure 2d, both the smart-Walsh and the Russian-doll sorting were capable of high-fidelity reconstructions of the sample image, even just by using a fraction of patterns, especially when compared to the standard Hadamard case. Further insights on the image reconstruction performance can be obtained by analysing the image reconstruction across the first 10% of patterns (Figure 2e). Remarkably, both our approach and the Russian-doll sorting outperformed the standard Hadamard sorting, yielding a high-fidelity image (spatial correlation exceeding 90%) by considering only 0.1% of the total number of patterns. Interestingly, while the performance of our "smart-Walsh" approach matched the Russian-doll sorting as soon as each Hadamard order was completed (dashed grey lines), we observed that it outperformed it across incomplete scans.

4. Performance of Field-Based Ghost-Imaging Detection in the Fourier Plane

The possibility of performing field-sensitive detection provides TIMING with a significant advantage when compared with traditional GI. However, the typical GI correlation between detection parameters and image fidelity is broken by the nonlinear ghost imaging transformation, i.e., the need for establishing a correlation between coherent-field detection and the optical intensity patterns. More precisely, the implementation of a field average in the image extraction radically changes the way the image quality depends on the experimental parameters. Standard GI reconstruction relies on detecting the integrated scattered field to estimate the spatial correlation between the incident patterns and the sample, where:

$$C_n = \int \mathrm{d}x\mathrm{d}y\, I_n^+(x,y) = \int \mathrm{d}x\mathrm{d}y\mathrm{d}t' \left|T(x,y,t-t')E_n^-(x,y,t)\right|^2. \tag{7}$$

This corresponds to the direct acquisition of the total scattered field with a standard bucket detector, which integrates the transmitted intensity distribution. Fundamentally, it is an estimator of the total scattered power, and as such, it is directly affected by the numerical aperture of the detector and by the distance between the detector and the sample. As discussed in the literature on optical

GI, both these factors directly fix the amount of information that is available when reconstructing the image and directly affect its fidelity [15].

TIMING inherits the direct detection of the scattered THz field distribution from time-domain spectroscopy systems. By operating directly on the electric field, it allows for measuring the average THz scattered field (in a fully coherent sense) by performing a point-like detection in the Fourier plane. As defined by Equation (3), the coefficients C_n can be obtained by measuring the $\left(k_x, k_y\right) = 0$ spectral components of the THz transmitted field:

$$C_n(t) = \int \mathrm{d}x\mathrm{d}y\, E_n^+(x, y, t) = \mathcal{F}\left[E_n^+(x, y, t)\right] |_{k_x = 0,\, k_y = 0}. \tag{8}$$

This implementation implies that the experimental measurement of the correlations C_n is not limited at all by the numerical aperture of the bucket detector. This type of measurement can be obtained by placing the object in the focal point of an arbitrary lens and by acquiring the signal in the central point of the opposite focal plane (Figure 1a). The electric field in the focal plane reads as follows:

$$E_{focal}(x,' y') \propto \mathcal{F}\left[E_n^+(x, y, t)\right]\left(k_x = \frac{x'}{\lambda f}, k_y = \frac{y'}{\lambda f}\right), \tag{9}$$

where x' and y' are the physical coordinates in the Fourier plane [41].

However, in terms of implementation, the detector samples a finite small area of the Fourier plane with an area-sampling function $PH\left(k_x, k_y\right)$, obtaining the estimation $C_n{}'(t)$:

$$C_n^{'(t)} = \int PH\left(k_x, k_y\right) * \mathcal{F}\left[E_n^+(x, y, t)\right] dk_x dk_y, \tag{10}$$

where $PH\left(k_x, k_y\right)$ is physically represented by the profile of the probe beam in the electro-optical sampling (e.g., a Gaussian function), or by the shape of any aperture implemented in front of the nonlinear detection to fix its interaction area with the THz field.

The accuracy of the measurements is then directly related to how "point-like" our detection can be made. Although one could be tempted to foresee a general benefit of the high signal-to-noise ratio (SNR) resulting from large detection apertures as in the standard GI, this is also a source of artefacts, fundamentally establishing a trade-off between SNR and fidelity.

Figure 3 illustrates the effects of the size d of the sampling function $PH\left(x' = k_x\lambda f, y' = k_y\lambda f\right)$ on the image reconstruction fidelity (Figure 3e). Interestingly, the reduction of fidelity observed for increasing the sampling diameter is different from the typical limitations in standard imaging. In our case, a too-large area sampling function in the Fourier plane did not lead to a reduction in the discernible details but rather in the disappearance of entire parts of the image (see Figure 3e, insets).

Similarly, in Figure 4, we illustrate the effect of a misalignment of the sampling function PH centre with respect to the centre of the Fourier plane. Trivially, the spatial correlation between the reconstructed and original images peaks at the centre of the Fourier plane and swiftly decayed in the case of off-axis detection (Figure 4a). In these conditions, the reconstructed image showed the appearance of spurious spatial frequencies, corresponding to the $\left(k_x,\, k_y\right)$ sampling position (Figure 4b,d). Interestingly, however, the overall morphology and details of the image were still present in the images, and no noticeable blurring occurred.

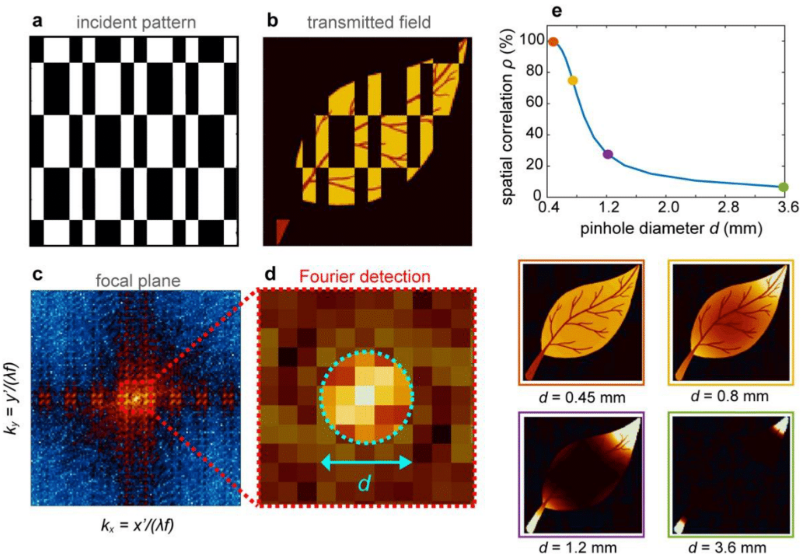

Figure 3. Influence of the pinhole size on the Fourier detection of TIMING reconstruction coefficients. (**a**–**d**) The spatial average of the transmitted field (**b**) associated with each incident pattern (**a**) could be measured by performing a point-like detection in the centre of the Fourier plane (**c**,**d**). In realistic implementations, the centre of the Fourier plane is sampled using a sampling function *PH* of finite diameter d. (**e**) Spatial correlation between the reconstructed and original image as a function of the sampling function diameter. A departure from the point-like approximation led to a significant corruption of the reconstructed image (insets). Interestingly, the typical image degradation did not necessarily involve the total disappearance of highly resolved details.

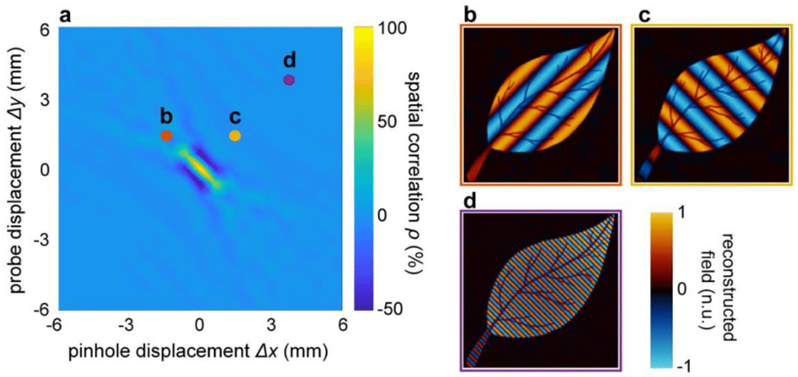

Figure 4. Influence of the pinhole displacement on the Fourier detection of TIMING reconstruction coefficients. (**a**) Spatial correlation between the reconstructed and original image as a function of the sampling function position in the focal plane. The displacement $(\Delta x, \Delta y)$ was measured with respect to the lens axis and the sampling function diameter was set to $d = 0.36$ mm, corresponding to a spatial correlation of 100% at the centre of the Fourier plane (cf. Figure 3e). (**b**–**d**) Examples of image reconstruction with off-axis detection, illustrating the appearance of spurious spatial frequencies. Interestingly, the object morphology was still noticeable, even at a relatively large distance from the optical axis.

5. A Route towards Thinner THz Emitters: Surface Emission from Quasi-2D Semiconductor Structures

Deep near-field regimes are in general a requirement to obtain deep-subwavelength image resolutions. Here, we review this current technological solution that is under development in TIMING towards this goal.

In terms of nonlinear ghost imaging, the high resolution fundamentally results from the ability to achieve significant optical-to-terahertz conversions, keeping the sample in the proximity of the distribution of terahertz sources. This translates into the need for generating terahertz from quite thin devices (although we argued how TIMING exhibits significantly more relaxed constraints compared to previous literature [25]).

Although the technology is continuously evolving, the best-performing and most practical off-the-shelf sources are within the class of electro-optical switches. The terahertz emission is generated by a transient current that is sustained by an external electric source and is triggered by a change of conductivity induced by an ultrafast optical absorption [5]. This specific approach benefits from a virtually high optical-to-terahertz conversion efficiency since the actual source of radiation is a current sustained by the electric source. However, this technology is difficult to translate to TIMING since the integration into a single device of a dense distribution of independent electrical switches emitting terahertz signals is extremely challenging.

In terms of direct optical-to-terahertz conversion, improving the efficiency of nonlinear converters is undoubtedly a central research area with a vast spectrum of proposed solutions ranging from novel materials to the design of sophisticated propagation geometries, which allows for very long interaction lengths. However, very few alternatives are currently available for emitters with a thickness below the micrometre scale. One general issue is that the efficiency of bulk nonlinear interactions tend to be vanishingly low at this scale, whereas the ruling mechanisms of the nonlinear interactions are dominated by peculiar physical mechanisms that exist only in quasi-2D frameworks. Some very promising, recently explored solutions comprise exploiting spin-mediated current transients (spintronic emitters) in nano-hetero-metallic structures [42]. On the other hand, a significant fraction of the work in this research area focuses on achieving a very large interfacial nonlinear response or inducing carrier-mediated nonlinear dynamics at a surface.

In general, these effects are fundamentally driven by breaking the lattice symmetry, which is produced by the material discontinuity at the interface. The requirement of tightly reduced interaction lengths makes low-bandgap semiconductors, such as Indium Arsenide (InAs) and Indium Antimonide (InSb), very popular experimental frameworks. What motivated the interest in these systems is the surprisingly high conversion efficiency per interaction length [43–45]. In a traditional NIR ultrafast excitation setting, the mean absorption length for photons is very small, typically within the scale of l_d = 140 nm at a wavelength λ = 800 nm. At low fluences (below 100 nJ/cm^2), InAs is probably considered the benchmark surface emitter. In this case, the generation is driven by the very large difference in mobility between holes and electrons via the photo-Dember effect (Figure 5c,d): when a high density of photogenerated pairs is induced in the proximity of the surface, electrons quickly diffuse away from the surface, leaving uncompensated carriers of the opposite sign. Such a charge unbalance creates a fast stretching dipole, or equivalently, a local current transient that is the source of the terahertz emission [46].

At very high pumping energies (above 10 μJ/cm^2), this phenomenon becomes critically saturated due to the electromagnetic screening role of dense carrier densities. Conversely, the optical surface rectification (SOR) dominates the emission [43]. The optical surface rectification is a quadratic phenomenon induced by the contribution of a local static field at the surface, which is induced by surface states within the bulk cubic nonlinear response (Figure 5a,b). The DC field effectively plays the role of a field contribution in a four-wave mixing process in a mechanism commonly referred to as a field-induced quadratic response [45,47] and is described using:

$$E_{THz} \propto \chi^{(3)} E_{surf} E_{\omega}^{*} E_{\omega}, \tag{11}$$

where $\chi^{(3)}$ is the third-order susceptibility of InAs, E_{surf} is the intrinsic surface potential field, E_{ω} is the incident optical field and $*$ stands for the complex conjugate. Quite interestingly, because the phenomenon is driven by a surface potential, it is also a measurable way to probe the dynamics of the carrier at the surface, and it has been proposed as the optical analogy of a Kelvin probe [48].

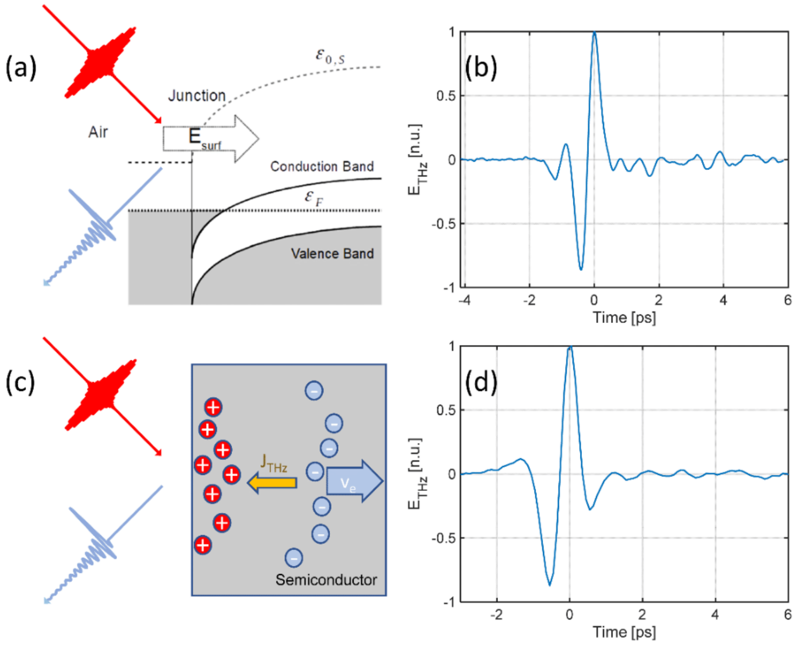

Figure 5. Surface emission driving mechanisms. (**a**) Surface optical rectification—a surface field at the air–semiconductor barrier combines with the optical field in a four-wave mixing process (cubic), generating a terahertz mixing product (see Equation (7)). (**b**) Measurement of the terahertz emission using surface optical rectification with an optical pulsed excitation fluence of 7 mJ/cm^2 (1 kHz repetition rate) and a pulse with a wavelength of 800 nm and a duration of 90 fs. (**c**) Simplified sketch of the photo-Dember process in InAs. The absorption of an ultrashort pulse generates a high density of photogenerated hole–electron pairs within the optical penetration depth (140 nm). The fast diffusion of the electrons induces a transient current J_{THz}, which is the source of the terahertz emission. (**d**) Measurement of the terahertz emission by photo-Dember mechanism with an optical pulsed excitation fluence of 0.28 µJ/cm^2 (80 MHz repetition rate) and pulse with a wavelength of 800 nm and a duration of 140 fs.

6. Discussions and Conclusions

In this work, we have provided an overview of the advantages and implementation challenges of a time-resolved nonlinear ghost-imaging approach to THz single-pixel imaging. By combining nonlinear THz generation and single-pixel TDS detection, we demonstrated the high-resolution reconstruction of a semi-transparent sample with a subwavelength resolution (512 × 512 pixels). By providing a detailed analysis of the Walsh–Hadamard reconstruction scheme, we have shown how a specific choice of patterns and the order of acquisition can play a beneficial role in speeding-up the reconstruction of the peak-field transmission from the sample. Remarkably, we have shown that less than 10% of the incident samples were required to achieve a high-fidelity reconstruction of the sample image in a general sequential reconstruction. Our approach, which is based on a lexicographical sorting of the incident patterns in terms of their spatial frequency (an approach we denoted as a "smart-Walsh" reconstruction), is general and image-independent and can be applied to reduce the overall reconstruction time for unknown samples. Interestingly, such a result could be further improved by considering that even a smaller percentage of incident patterns are required to reconstruct the sample: in our case, only 8% of the patterns were associated with an expansion coefficient exceeding 60dB. In practical terms, this would correspond to a 92% shorter acquisition time, corresponding to a 12.5× speed up of the image reconstruction process when compared to a full scan based on the Hadamard encoding scheme. These numbers suggest that the reconstruction process could be significantly sped up through the application of adaptive-basis-scan algorithms and deep-learning-enhanced imaging, which identify and predict the best set of scanning patterns in real time [40,49–51].

Interestingly, our results suggest that the nonlinear GI methodology is not limited by the numerical aperture of the optical system in a "conventional" sense. Said differently, it operates under the assumption of a very low numerical aperture to obtain a faithful spectral representation of the image. However, our results highlight that the image reconstruction is quite sensitive to the size and alignment of the pinhole function selecting the $\left(k_x, k_y\right) = 0$ components of the scattered field. Most importantly, in sharp contrast with previous literature on the topic, the reconstruction accuracy cannot simply be represented as a matter of effective "resolution". The drop in reconstruction fidelity, in fact, is not driven by the attenuation of high-frequency spatial components (i.e., blurring) as in standard imaging, but it can lead to the appearance of artefacts and spurious spatial frequencies. To the best of our knowledge, the reconstruction limits of single-pixel time-domain imaging have never been formalised elsewhere.

Finally, although thin emitters are a general requirement for this approach, TIMING exhibits relaxed constraints between the nonlinear interaction length and the image resolution. Yet, solutions for sub-micron-thick large-area terahertz generation are practically possible, enabling resolutions within the same scale or better. A promising platform to achieve this goal is narrow-bandgap semiconductor devices based on InAs or InSb platforms. These materials not only provide extremely high optical-to-terahertz conversion efficiency per unit length but they are also suitable for large-scale fabrication and deployment in real-world devices thanks to their established deployment in the electronic domain.

We believe that TIMING is a significant step forward in the development of terahertz micro-diagnostics based on hyperspectral imaging devices. Our approach also addresses fundamental criticalities in the imaging reconstruction process, which generally affect any high-resolution imaging domain where high temporal resolution is sought. As such, TIMING establishes a comprehensive theoretical and technological platform that paves the way for new generations of terahertz imaging devices satisfying the requirements for high-resolution and spectral sensitivity in real-world applications.

Supplementary Materials: The following are available online at http://www.mdpi.com/2072-666X/11/5/521/s1.

Author Contributions: Conceptualisation, J.S.T.G., A.P. and M.P.; Methodology, J.S.T.G., L.O., A.P. and M.P.; Investigation, J.S.T.G., J.T., L.P., V.C., A.C., L.O., R.T. and V.K.; Supervision, J.S.T.G., A.P. and M.P.; Writing—original draft, J.S.T.G.; Writing—review & editing, J.S.T.G. and M.P. Project administration, M.P.; Funding acquisition, M.P. All authors have read and agreed to the published version of the manuscript.

Funding: This project has received funding from the European Research Council (ERC) under the European Union's Horizon 2020 research and innovation programme (grant agreement no. 725046). J.T. acknowledges the support of the Engineering and Physical Sciences Research Council (EPSRC) through the studentship EP/N509784/1. J.S.T.G, L.P., V.C., V.K. and R.T. acknowledge the support of the European Union's "Horizon 2020" research and innovation program, grant agreement no. 725046, ERC-CoG project TIMING. J.S.T.G. acknowledges funding from the Helena Normanton Fellowship of the University of Sussex, UK. A.C. acknowledges the support from the University of Palermo, Italy through the mobility fellowship "Corso di Perfezionamento all'estero 2018".

Conflicts of Interest: The authors declare no conflict of interest.

References

1. Tikan, A.; Bielawski, S.; Szwaj, C.; Randoux, S.; Suret, P. Single-shot measurement of phase and amplitude by using a heterodyne time-lens system and ultrafast digital time-holography. *Nat. Photonics* **2018**, *12*, 228. [CrossRef]
2. Shechtman, Y.; Eldar, Y.C.; Cohen, O.; Chapman, H.N.; Miao, J.; Segev, M. Phase Retrieval with Application to Optical Imaging: A contemporary overview. *IEEE Signal Process. Mag.* **2015**, *32*, 87–109. [CrossRef]
3. Rivenson, Y.; Zhang, Y.; Günaydın, H.; Teng, D.; Ozcan, A. Phase recovery and holographic image reconstruction using deep learning in neural networks. *Light Sci. Appl.* **2018**, *7*, 17141. [CrossRef] [PubMed]
4. Hack, E.; Zolliker, P. Terahertz holography for imaging amplitude and phase objects. *Opt. Express* **2014**, *22*, 16079–16086. [CrossRef]
5. Song, H.-J.; Nagatsuma, T. *Handbook of Terahertz Technologies: Devices and Applications*; CRC Press: New York, NY, USA, 2015.
6. Kampfrath, T.; Tanaka, K.; Nelson, K.A. Resonant and nonresonant control over matter and light by intense terahertz transients. *Nat. Photonics* **2013**, *7*, 680–690. [CrossRef]
7. Frühling, U.; Wieland, M.; Gensch, M.; Gebert, T.; Schütte, B.; Krikunova, M.; Kalms, R.; Budzyn, F.; Grimm, O.; Rossbach, J.; et al. Single-shot terahertz-field-driven X-ray streak camera. *Nat. Photonics* **2009**, *3*, 523–528. [CrossRef]
8. Yu, L.; Hao, L.; Meiqiong, T.; Jiaoqi, H.; Wei, L.; Jinying, D.; Xueping, C.; Weiling, F.; Yang, Z. The medical application of terahertz technology in non-invasive detection of cells and tissues: Opportunities and challenges. *RSC Adv.* **2019**, *9*, 9354–9363. [CrossRef]
9. Yang, X.; Zhao, X.; Yang, K.; Liu, Y.; Liu, Y.; Fu, W.; Luo, Y. Biomedical Applications of Terahertz Spectroscopy and Imaging. *Trends Biotechnol.* **2016**, *34*, 810–824. [CrossRef]
10. Mittleman, D.M. Twenty years of terahertz imaging [Invited]. *Opt. ExpressOe* **2018**, *26*, 9417–9431. [CrossRef]
11. Sengupta, K.; Nagatsuma, T.; Mittleman, D.M. Terahertz integrated electronic and hybrid electronic–photonic systems. *Nat. Electron.* **2018**, *1*, 622–635. [CrossRef]
12. Lee, A.W.; Hu, Q. Real-time, continuous-wave terahertz imaging by use of a microbolometer focal-plane array. *Opt. Lett.* **2005**, *30*, 2563–2565. [CrossRef] [PubMed]
13. Abraham, E.; Cahyadi, H.; Brossard, M.; Degert, J.; Freysz, E.; Yasui, T. Development of a wavefront sensor for terahertz pulses. *Opt. Express* **2016**, *24*, 5203. [CrossRef] [PubMed]
14. Moreau, P.-A.; Toninelli, E.; Gregory, T.; Padgett, M.J. Ghost Imaging Using Optical Correlations. *Laser Photonics Rev.* **2018**, *12*, 1700143. [CrossRef]
15. Padgett, M.J.; Boyd, R.W. An introduction to ghost imaging: Quantum and classical. *Phsical Eng. Sci.* **2017**, *375*, 20160233. [CrossRef] [PubMed]
16. Shapiro, J.H.; Boyd, R.W. The physics of ghost imaging. *Quantum Inf Process* **2012**, *11*, 949–993. [CrossRef]
17. Erkmen, B.I.; Shapiro, J.H. Ghost imaging: From quantum to classical to computational. *Adv. Opt. Photon. Aop* **2010**, *2*, 405–450. [CrossRef]
18. Chan, W.L.; Charan, K.; Takhar, D.; Kelly, K.F.; Baraniuk, R.G.; Mittleman, D.M. A single-pixel terahertz imaging system based on compressed sensing. *Appl. Phys. Lett.* **2008**, *93*, 121105. [CrossRef]
19. Watts, C.M.; Shrekenhamer, D.; Montoya, J.; Lipworth, G.; Hunt, J.; Sleasman, T.; Krishna, S.; Smith, D.R.; Padilla, W.J. Terahertz compressive imaging with metamaterial spatial light modulators. *Nat. Photonics* **2014**, *8*, 605–609. [CrossRef]
20. Stantchev, R.I.; Sun, B.; Hornett, S.M.; Hobson, P.A.; Gibson, G.M.; Padgett, M.J.; Hendry, E. Noninvasive, near-field terahertz imaging of hidden objects using a single-pixel detector. *Sci. Adv.* **2016**, *2*, e1600190. [CrossRef]
21. Stantchev, R.I.; Phillips, D.B.; Hobson, P.; Hornett, S.M.; Padgett, M.J.; Hendry, E. Compressed sensing with near-field THz radiation. *Optica* **2017**, *4*, 989. [CrossRef]
22. Zhao, J.; Yiwen, E.; Williams, K.; Zhang, X.-C.; Boyd, R.W. Spatial sampling of terahertz fields with sub-wavelength accuracy via probe-beam encoding. *Light Sci. Appl.* **2019**, *8*, 55. [CrossRef] [PubMed]

23. Chen, S.-C.; Du, L.-H.; Meng, K.; Li, J.; Zhai, Z.-H.; Shi, Q.-W.; Li, Z.-R.; Zhu, L.-G. Terahertz wave near-field compressive imaging with a spatial resolution of over λ/100. *Opt. Lett.* **2019**, *44*, 21. [CrossRef] [PubMed]
24. Olivieri, L.; Totero Gongora, J.S.; Pasquazi, A.; Peccianti, M. Time-Resolved Nonlinear Ghost Imaging. *ACS Photonics* **2018**, *5*, 3379–3388. [CrossRef]
25. Olivieri, L.; Gongora, J.S.T.; Peters, L.; Cecconi, V.; Cutrona, A.; Tunesi, J.; Tucker, R.; Pasquazi, A.; Peccianti, M. Hyperspectral terahertz microscopy via nonlinear ghost imaging. *Optica* **2019**, *7*, 186. [CrossRef]
26. Olivieri, L.; Totero Gongora, J.S.; Pasquazi, A.; Peccianti, M. Time-resolved nonlinear ghost imaging: Route to hyperspectral single-pixel reconstruction of complex samples at THz frequencies. In *Society of Photo-Optical Instrumentation Engineers (SPIE) Conference Series, Proceedings of the Nonlinear Frequency Generation and Conversion: Materials and Devices XVIII, San Francisco, CA, USA, 5–9 Feberuary 2019*; Schunemann, P.G., Schepler, K.L., Eds.; SPIE: San Francisco, CA, USA, 2019; p. 44.
27. Shapiro, J.H. Computational ghost imaging. *Phys. Rev. A At. Mol. Opt. Phys.* **2008**, *78*, 061802. [CrossRef]
28. Peccianti, M.; Clerici, M.; Pasquazi, A.; Caspani, L.; Ho, S.P.; Buccheri, F.; Ali, J.; Busacca, A.; Ozaki, T.; Morandotti, R. Exact Reconstruction of THz Sub-λSource Features in Knife-Edge Measurements. *IEEE J. Sel. Top. Quantum Electron.* **2013**, *19*, 8401211. [CrossRef]
29. Khare, K. *Fourier Optics and Computational Imaging*; Wiley, John Wiley & Sons Ltd.: Chichester, West Sussex, 2016; ISBN 978-1-118-90034-5.
30. Harwit, M. *Hadamard Transform Optics*; Elsevier: New York, NY, USA, 2012; ISBN 978-0-323-15864-0.
31. Davis, D.S. Multiplexed imaging by means of optically generated Kronecker products: 1. The basic concept. *Appl. Opt.* **1995**, *34*, 1170–1176. [CrossRef]
32. Streeter, L.; Burling-Claridge, G.R.; Cree, M.J.; Künnemeyer, R. Optical full Hadamard matrix multiplexing and noise effects. *Appl. Opt.* **2009**, *48*, 2078–2085. [CrossRef]
33. Eldar, Y.C.; Kutyniok, G. *Compressed Sensing: Theory and Applications*; Cambridge University Press: Cambridge, UK, 2012; ISBN 978-1-107-00558-7.
34. Dongfeng, S.; Jian, H.; Wenwen, M.; Kaixin, Y.; Baoqing, S.; Yingjian, W.; Kee, Y.; Chenbo, X.; Dong, L.; Wenyue, Z. Radon single-pixel imaging with projective sampling. *Opt. ExpressOe* **2019**, *27*, 14594–14609. [CrossRef]
35. Wenwen, M.; Wenwen, M.; Dongfeng, S.; Dongfeng, S.; Jian, H.; Jian, H.; Kee, Y.; Kee, Y.; Kee, Y.; Yingjian, W.; et al. Sparse Fourier single-pixel imaging. *Opt. ExpressOe* **2019**, *27*, 31490–31503. [CrossRef]
36. Hedayat, A.; Wallis, W.D. Hadamard Matrices and Their Applications. *Ann. Stat.* **1978**, *6*, 1184–1238. [CrossRef]
37. Wang, L.; Zhao, S. Fast reconstructed and high-quality ghost imaging with fast Walsh–Hadamard transform. *Photonics Res.* **2016**, *4*, 240. [CrossRef]
38. Sun, M.-J.; Meng, L.-T.; Edgar, M.P.; Padgett, M.J.; Radwell, N. A Russian Dolls ordering of the Hadamard basis for compressive single-pixel imaging. *Sci. Rep.* **2017**, *7*. [CrossRef] [PubMed]
39. Rousset, F.; Ducros, N.; Farina, A.; Valentini, G.; D'Andrea, C.; Peyrin, F. Adaptive Basis Scan by Wavelet Prediction for Single-Pixel Imaging. *IEEE Trans. Comput. Imaging* **2017**, *3*, 36–46. [CrossRef]
40. Kravets, V.; Kondrashov, P.; Stern, A. Compressive ultraspectral imaging using multiscale structured illumination. *Appl. Opt. AO* **2019**, *58*, F32–F39. [CrossRef] [PubMed]
41. Born, M.; Wolf, E. *Principles of Optics: Electromagnetic Theory of Propagation, Interference and Diffraction of Light*, 7th expanded; Cambridge University Press: Cambridge, NY, USA, 1999; ISBN 978-0-521-64222-4.
42. Seifert, T.; Jaiswal, S.; Martens, U.; Hannegan, J.; Braun, L.; Maldonado, P.; Freimuth, F.; Kronenberg, A.; Henrizi, J.; Radu, I.; et al. Efficient metallic spintronic emitters of ultrabroadband terahertz radiation. *Nat. Photonics* **2016**, *10*, 483–488. [CrossRef]
43. Reid, M.; Fedosejevs, R. Terahertz emission from (100) InAs surfaces at high excitation fluences. *Appl. Phys. Lett.* **2005**, *86*, 011906. [CrossRef]
44. Reid, M.; Cravetchi, I.V.; Fedosejevs, R. Terahertz radiation and second-harmonic generation from InAs: Bulk versus surface electric-field-induced contributions. *Phys. Rev. B* **2005**, *72*, 035201. [CrossRef]
45. Peters, L.; Tunesi, J.; Pasquazi, A.; Peccianti, M. High-energy terahertz surface optical rectification. *Nano Energy* **2018**, *46*, 128–132. [CrossRef]
46. Apostolopoulos, V.; Barnes, M.E. THz emitters based on the photo-Dember effect. *J. Phys. D Appl. Phys.* **2014**, *47*, 374002. [CrossRef]

47. Cazzanelli, M.; Schilling, J. Second order optical nonlinearity in silicon by symmetry breaking. *Appl. Phys. Rev.* **2016**, *3*, 011104. [CrossRef]
48. Peters, L.; Tunesi, J.; Pasquazi, A.; Peccianti, M. Optical Pump Rectification Emission: Route to Terahertz Free-Standing Surface Potential Diagnostics. *Sci. Rep.* **2017**, *7*. [CrossRef] [PubMed]
49. Dai, H.; Gu, G.; He, W.; Liao, F.; Zhuang, J.; Liu, X.; Chen, Q. Adaptive compressed sampling based on extended wavelet trees. *Appl. Opt.* **2014**, *53*, 6619. [CrossRef] [PubMed]
50. Dai, H.; Gu, G.; He, W.; Ye, L.; Mao, T.; Chen, Q. Adaptive compressed photon counting 3D imaging based on wavelet trees and depth map sparse representation. *Opt. Express* **2016**, *24*, 26080. [CrossRef]
51. Barbastathis, G.; Ozcan, A.; Situ, G. On the use of deep learning for computational imaging. *Opt. Opt.* **2019**, *6*, 921–943. [CrossRef]

2.2 Hyperspectral Terahertz Microscopy via Nonlinear Ghost Imaging

186 Vol. 7, No. 2 / February 2020 / Optica Research Article

optica

Hyperspectral terahertz microscopy via nonlinear ghost imaging

Luana Olivieri,[1] Juan S. Totero Gongora,[1] Luke Peters,[1] Vittorio Cecconi,[1] Antonio Cutrona,[1,2] Jacob Tunesi,[1] Robyn Tucker,[1] Alessia Pasquazi,[1] and Marco Peccianti[1,*]

[1] Emergent Photonics (EPic) Laboratory, Department of Physics and Astronomy, University of Sussex, Brighton, UK
[2] Department of Engineering, University of Palermo, Palermo, Italy
*Corresponding author: m.peccianti@sussex.ac.uk

Received 25 October 2019; revised 9 January 2020; accepted 9 January 2020 (Doc. ID 381035); published 19 February 2020

Ghost imaging, based on single-pixel detection and multiple pattern illumination, is a crucial investigative tool in difficult-to-access wavelength regions. In the terahertz domain, where high-resolution imagers are mostly unavailable, ghost imaging is an optimal approach to embed the temporal dimension, creating a "hyperspectral" imager. In this framework, high resolution is mostly out of reach. Hence, it is particularly critical to developing practical approaches for microscopy. Here we experimentally demonstrate time-resolved nonlinear ghost imaging, a technique based on near-field, optical-to-terahertz nonlinear conversion and detection of illumination patterns. We show how space–time coupling affects near-field time-domain imaging, and we develop a complete methodology that overcomes fundamental systematic reconstruction issues. Our theoretical-experimental platform enables high-fidelity subwavelength imaging and carries relaxed constraints on the nonlinear generation crystal thickness. Our work establishes a rigorous framework to reconstruct hyperspectral images of complex samples inaccessible through standard fixed-time methods.

https://doi.org/10.1364/OPTICA.381035

1. INTRODUCTION

The reconstruction of complex field distributions in space and time is a challenge in many domains, with a significant transversal impact in fields beyond optics, such as microwave beam steering, ultrasound imaging, and biology [1–9]. On another front, hyperspectral imaging has a pivotal assessment role in many disciplines, as it allows one to determine the 2D morphology of an absorption spectrum [10–12]. Hyperspectral imaging assumes a broader probing significance in time-resolved systems; in particular, the delay of each frequency component can be profitably used to access the 3D morphology of the spectral phase response of a target, i.e., its spatially resolved complex dielectric function. Modern photonic approaches have produced essential breakthroughs in medicine, biology, and material science imaging [12–16]. In this context, the ability to reconstruct the time-domain waveforms provides direct access to the field [17]; although these approaches are well established in microwave and ultrasound imaging [2,5–7], they are sensibly less diffused in photonics. Terahertz (THz), in this regard, has emerged as one of the most relevant photonics frameworks in which the time evolution of a field amplitude is experimentally accessible. Indeed, THz time-domain spectroscopy (TDS) has played a pivotal role in establishing THz as an independent research field [18–21].

Single-pixel imaging approaches find their origin in domains where single-point detectors outperform detector-arrays in terms of specifications or availability [22,23]; for this reason, they have attracted interest also in the THz community [24–26]. In photonics, these methods have unlocked the powerful ability to add multiple dimensions and novel functionalities to simple spatial probing, enabling several breakthroughs in classical and quantum imaging [25,27–32]. In its most modern connotation, ghost imaging (GI) is a form of computational imaging that employs the sequential illumination of an object with a set of predetermined patterns [23,33–37].

In terms of accessing newly emerging wave domains, such as THz, GI offers the option of closing relevant technological gaps while raising new challenges, such as the limited availability of THz spatial light modulators (SLMs) and the coarse diffraction limit [25].

The combination of single-pixel imaging and TDS provides the exciting possibility of exploiting novel space–time computational imaging approaches [31,32], and the TDS-GI has been recently proposed as viable for THz imaging [38–42]. The THz field can be densely sampled in space, giving access to subwavelength microscopy when an object is exposed to the near field of a THz source, detector, or mask. Besides its potential practical impact in THz microscopy, GI microscopy provides an accessible fundamental framework for investigating time-resolved imaging in the presence

2334-2536/20/020186-06 Journal © 2020 Optical Society of America

of strong spatiotemporal coupling, a dominant condition in the near-field domain.

In this paper, we experimentally implement an imaging protocol based on the time-resolved nonlinear ghost imaging (TNGI), which we have recently theoretically proposed as a single-pixel imaging method where a set of nonlinear wavelength transformations are inserted in both the illumination and detection chains [43]. We generate the THz patterns used for the GI reconstruction by nonlinear conversion of spatially modulated optical pulses in a quadratic medium. Leveraging the time-dependent field detection, as opposed to the intensity detection usually implemented in the optics GI-equivalent, we implement the detection in the Fourier plane, effectively acquiring the average value of the scattered field. With this approach, the system resolution is effectively independent of the numerical aperture of the detection system, in sharp contrast with standard single-pixel approaches working in optics. We test our time-dependent THz microscope on benchmark images, showing the capability of our system to extract the spectrally resolved morphology, such as the water content in a leaf.

Most importantly, we demonstrate near-field, coherent hyperspectral imaging in a regime where spatiotemporal coupling is strongly evident. We experimentally show that, in this regime, the image information is inherently inaccessible when the reconstruction is performed at fixed-time slices of the transmitted field, as the traditional isotime imaging approaches become affected by errors and artifacts. We show experimentally that in the near field, the full spatiotemporal signal is required to preserve space–time imaging, and we provide a methodology, which we refer to as "space–time refocusing" for high-fidelity reconstruction. Interestingly, we also show experimentally that the thickness of the generation crystal does not preclude significantly higher resolutions (as in some of the proposed THz-GI approaches).

2. METHODS: THE TNGI

We formulated the TNGI as a single-pixel imaging approach based on the time-resolved detection of the electromagnetic field scattered by a sample, as opposed to the standard formulation of GI that relies on the time-averaged field intensity [43]. Without loss of generality, the TNGI describes the optical and morphological features of a sample through a spatiotemporal transfer function $T_{\text{sample}}(x, y, t)$ that is reconstructed through a sequence of measurements as follows:

$$T_{\text{sample}}(x, y, t) = \langle C_n(t) I_n(x, y)\rangle_n - \langle C_n(t)\rangle_n \langle I_n(x, y)\rangle_n, \quad (1)$$

where $I_n(x, y)$ is the intensity distribution of the nth incident optical pattern, and $\langle \cdots \rangle_n$ is the average over the distribution of patterns. In Eq. (1), the expansion coefficients $C_n(t)$ are defined as

$$C_n(t) = \int E_n^+(x, y, t)\mathrm{d}x\mathrm{d}y, \quad (2)$$

and correspond to the spatial average of the complex electric field $E_n^+(x, y, t)$ transmitted by the sample and acquired by TDS detection (see Supplement 1 Section S3). Note that Eq. (1) is closely related to the linear formulation of standard GI, where the incident and scattered intensities are linearly related. Such a similarity is a direct consequence of the optical-to-THz conversion taking place in quadratic media, where the generated THz field is expressed as

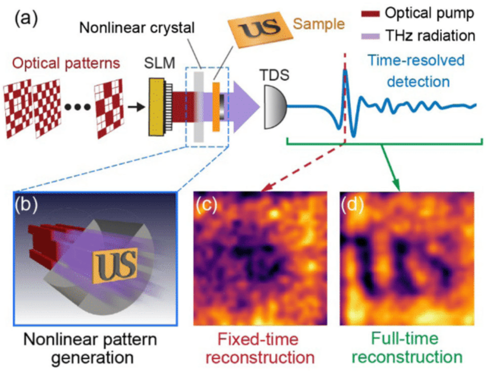

Fig. 1. Conceptual description of the TNGI approach. (a) Key experimental components and methodology; (b) volumetric representation of the nonlinear generation of THz patterns; (c) fixed-time reconstruction with a field of view 2 mm × 2 mm and 32 × 32 spatial sampling; (d) backpropagated hyperspectral image, averaged between 1 and 2 THz.

$$E_{\text{THz}}(x, y) \propto \chi^{(2)} I_n(x, y), \quad (3)$$

where $\chi^{(2)}$ is the second-order nonlinear susceptibility of the nonlinear medium. The capability of directly controlling the THz field by acting on the incident optical intensity is an essential feature of our approach, as in casting Eq. (1) we do not require any assumption stemming from the binary nature of the illumination (as required, e.g., in mask-based GI [39–42]). It is also worth noting that, differently from the standard GI formulation, the coefficients in Eqs. (1) and (2) are built up by coherent measurements of the electric field, and they do not represent the scattered intensity.

The principal elements of our experimental implementation of the TNGI are shown in Fig. 1. We impressed a series of intensity patterns on an ultrafast optical beam ($\lambda = 800$ nm, repetition rate 1 kHz, pulse duration 75 fs) using a commercial wavefront-shaping device. In our experiments, we employed both a binary amplitude digital micromirror device (DMD) and a phase-only liquid crystal on silicon (LCoS) SLM. We converted the optical pattern to a THz field distribution $E_{\text{THz}}(x, y, t)$ through nonlinear optical rectification in a quadratic crystal (ZnTe) of thickness z_0. The generated THz pattern sampled different targets (in our experiments different metallic masks and dielectrics) placed in proximity to the crystal surface, and the average transmitted field was measured through electro-optic (EO) detection. In our THz implementation, the $C_n(t)$ coincide with the electric field detected via TDS at the center of the Fourier plane (i.e., at $k_x = k_y = 0$) [44]. As an image-reconstruction protocol, we exploited a Walsh–Hadamard encoding scheme (with "Russian doll" ordering [45]) based on binary amplitude patterns, which is known to maximize the SNR of single-pixel imaging schemes [39]. A detailed schematic and further details on the optical setups are included in the supplementary information (SI).

The use of nonlinear conversion to generate THz patterns provides a series of features when developing a single-pixel TDS imaging scheme. First, the ability to control the THz field distribution by shaping the optical field, as expressed by Eq. (3), allows us to generate patterns with subwavelength resolution when compared to the THz wavelength (300 μm, at 1 THz). The resolution of the optical pattern $I_n(x, y)$ is ultimately bound by the optical diffraction limit and the numerical aperture of the optical setup. Second, the SNR of the detected THz signal increases linearly with the incident optical intensity. Finally, there is perfect temporal coherence and spatial correspondence between the pump pulse and the distribution of THz sources. Temporal and spatial coherence is a direct consequence of the nonlinear conversion process and has significant consequences for our abililty to image samples in challenging experimental conditions. An open issue in THz-GI concerns the impact of the distance between the THz pattern source and the sample, as required when assessing the transmission from a sample placed on a holding substrate. As discussed in Refs. [39,43], the near-field propagation of subwavelength patterns exhibits spatiotemporal coupling, altering the spatial and temporal features of the pattern [46]. Under these conditions, the sampling function impinging on the object is not the original, predetermined pattern, but its space–time "propagated" version. Such discrepancy introduces a systematic and uneliminable error in determining the scattered waveform from the object using a

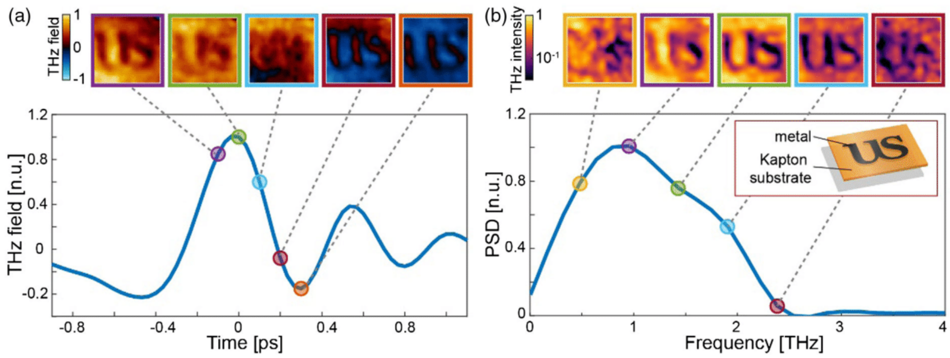

Fig. 2. Spatiotemporal image of a metallic sample. (a) Temporal response of the metallic sample with fixed-time image reconstructions. It is worth noting that field evolution (color change) can be appreciated underneath the metallic mask as the structure resonance produces a secondary emission. (b) Spectral response with hyperspectral images. The field of view was 2 mm × 2 mm with a 16 × 16 spatial sampling.

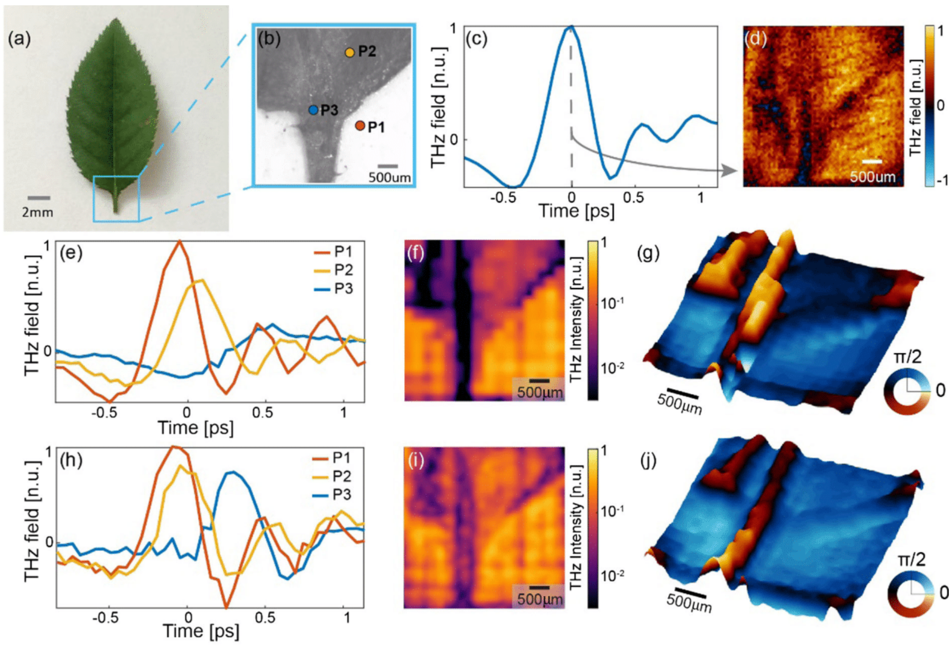

Fig. 3. Hyperspectral image of a leaf. (a) Optical image of the leaf; (b) microscope image; (c) temporal response of the field transmitted by the leaf; (d) fixed-time reconstruction (128 pixels × 128 pixels); (e) local temporal response of the fresh leaf in the points indicated in (b); (f) hyperspectral image of a fresh leaf at 1.5 THz (16 pixels × 16 pixels); (g) phase image of the fresh leaf, obtained without phase unwrapping of the experimental data; (h)–(j) same as the previous panel for a dried leaf (32 pixel × 32 pixel images). All the images correspond to a field of view of 4 mm × 4 mm.

time-sliced (or isotime) imaging. While the effect of spatiotemporal coupling could be reduced when the sample distance from the sources is much smaller than the resolution targeted (i.e., by employing a thin patterning substrate), the error introduced by diffraction (and by the interaction with samples with complex transmission properties) is always present. Such an error is not quantifiable in the case of single time-slice acquisition, and it cannot be represented by standard definitions of SNR employed in image analysis. The combination of optical coherence and direct field detection allows us to reverse the effects of spatiotemporal coupling, to obtain the correct time-domain reconstruction of a sample within one wavelength of distance, and to perform coherent hyperspectral imaging through TNGI.

3. EXPERIMENTAL RESULTS: HYPERSPECTRAL IMAGING

As a first case study, in Fig. 2 we present the 2 mm × 2 mm spatiotemporal image of a metallic structure deposited on a 50 µm Kapton substrate. The image was retrieved by shaping the optical illumination with a binary DMD and by placing the metallic structure in the proximity of a $z_0 = 1$ mm thick ZnTe generation crystal. We achieved analogous results using an LCoS modulator, as shown in Supplement 1 Fig. 2. By retrieving the spatiotemporal image of the sample [Fig. 2(a)], we can capture the full effects of the interaction between the THz field and its subwavelength metallic features. As can be observed at $t = 0.2$ ps, in fact, the object does not appear just as a blocking mask, but it features complex resonances from the edges of the object. The time-resolved measurement of the scattered field also allows us to reconstruct the hyperspectral image of the sample [Fig. 2(b)]. Interestingly, in our experiments, we were able to resolve features within the 50–100 µm scale even in the presence of a relatively thick generation crystal (as opposed to the typical thickness requirements in other approaches [39–42]). This is a direct consequence of the nonlinear conversion of optical patterns taking place across the entire volume of the generating crystal and not only at its surface. In this condition, the field-spatial spectra of each generating layer in the ZnTe do not mix incoherently and, differently from the linear case, allow single-pixel reconstruction of subwavelength features (see Supplement 1 Section S2 for a detailed discussion).

The access to the coherent temporal field response allowed us to reconstruct full spatiotemporal images of semitransparent samples. As a relevant example (and to credit a similar image in Ref. [20], widely considered one of the first milestones in THz imaging), we show in Fig. 3 an image of a leaf at different stages of desiccation. As can be evinced from Figs. 3(c) and 3(d), the isotime image of a semitransparent sample is significantly harder to interpret than a standard metallic mask, as the different parts of the sample induce different temporal delays and phase shifts. Nevertheless, we were able to retrieve the TDS time trace in different points of the sample [Figs. 3(e) and 3(h)] and retrieve its hyperspectral image both in terms of amplitude [Figs. 3(f) and 3(i)] and spectral phase [Figs. 3(g) and 3(j)], allowing us to reconstruct its morphology and spectral fingerprint. As relevant examples, we present data for a fresh leaf [Figs. 3(e)–3(g)] and a dried leaf [Figs. 3(h)–3(j)]. By comparing the transmission from the two samples, it is possible to assess the changes in water content, as in Ref. [20].

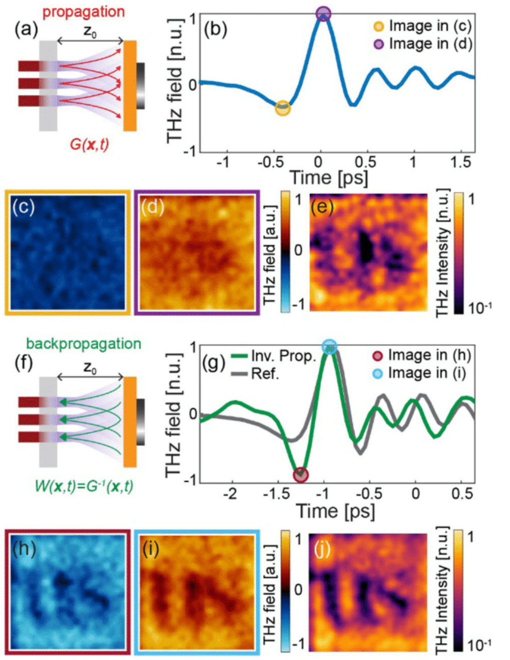

Fig. 4. Time-resolved image reconstruction: inverse propagation approach. (a) Conceptual illustration of the propagating imaging scheme: the sample is placed at $z_0 = 300$ µm from the crystal. (b) Temporal response of the sample; (c)–(d) fixed-time reconstructed images at the points indicated in (b); (e) hyperspectral image averaged between 1 and 2 THz; (f) conceptual illustration of the backpropagation scheme; (g) temporal response of the backpropagated image (green) and the temporal response without the sample (gray); (h)–(i) fixed-time reconstruction of the backpropagated image at the points indicated in (g); (j) backpropagated hyperspectral image, averaged between 1 and 2 THz. In all panels, the field of view was 2 mm × 2 mm with a 32 × 32 spatial sampling.

4. IMAGING THROUGH INVERSE PROPAGATION

The experimental results presented in Fig. 4 explore a relevant consequence of the space–time coupling in near-field TNGI. In this case, we collected the image of a metallic sample, analogous to the one in Fig. 2, but introducing a nonnegligible distance between the sample and the emitter, which includes the Kapton substrate, in a typical time-of-flight imaging case.

In these conditions, the sample morphology cannot be appreciated in any of the isotime images regardless of their temporal position [Figs. 4(c), 4(d) show some examples], or in the hyperspectral image [Fig. 4(e)], which shows a quite distorted image even if in some pixels a high contrast is reached. As theoretically demonstrated in Ref. [43], such a limitation is a direct consequence of spatiotemporal coupling, which leads to a substantial modification of the incident sampling patterns as they propagate [Fig. 4(a)]. At this stage, it should be observed that our TNGI protocol relies on the collection of the average field as performed by sampling the origin of an optical Fourier plane (i.e., $k_x = k_y = 0$). As a result, it only requires an optical system capable of collecting a very narrow spatial spectrum, and the numerical aperture of the imaging system plays a minimal role in defining the image resolution. On the contrary, the SNR of the THz detection plays a fundamental role in resolving the vanishing near-field scattered contributions (at high spatial frequencies) for increasing values of the distance between the sample and the emitter.

With the sensitivity available, we could then backpropagate the pattern sampling function in order to "space–time refocus" the image [Fig. 4(f)] and reverse the effect of spatiotemporal coupling (see Supplement 1 Section S3 for a theoretical discussion on the inverse propagation reconstruction) [43]. This procedure allows us to retrieve the correct time-resolved image of the scattered field in the proximity of the sample, restoring the morphological and spectral features of its hyperspectral image [Figs. 4(i)–4(j)]. We argue that the inverse propagation reconstruction is a strict requirement to reconstruct the sample properties at different depths, i.e., in near-field time-of-flight imaging.

5. CONCLUSIONS

In conclusion, we performed the first experimental example of the TNGI approach exploiting a nonlinear quadratic conversion. We devised a general reconstruction method based on the linear dependence between impinging optical patterns and the detected THz time-domain field average. The approach enables hyperspectral imaging as performed in the state-of-the-art by TDS imagers. It features near-field imaging and shows relaxed constraints in terms of thickness of the nonlinear converter (our proof-of-concept exploits off-the-shelf nonlinear substrates). As predicted in Ref. [43], we demonstrated that popular isotime approaches are not suitable for near-field spatiotemporal microscopy, and this is a central issue when an object comprises elements at different optical depths. We proved experimentally that, thanks to the spatial and temporal coherence, it is possible to devise an inverse propagation operator capable of "refocusing" the image in space–time and, therefore, correctly reconstructing the hyperspectral image of the sample. We believe this work can have a substantial impact in the field of near-field imaging, especially in light of the emergence of thinner and more efficient THz emitters (e.g., spintronic substrates, surface emitters, or novel materials with exceptionally high nonlinear coefficients such as DSTMS crystals) [47–50].

Funding. European Research Council under the European Union's Horizon 2020 Research and Innovation Programme (725046); UK Engineering and Physical Sciences Research Council (EP/N509784/1, EP/S001018/1); University of Sussex (UK) ("Helena Normanton" Fellowship); University of Palermo (Italy) (mobility fellowship "Corso di Perfezionamento all'estero 2018").

Acknowledgment. This project has received funding from the European Research Council (ERC) under the European Union's Horizon 2020 research and innovation programme (grant agreement No 725046). J.S.T.G, L.P., V.C., and R.T. acknowledge the support of the European Union's "Horizon 2020" research and innovation program, grant agreement No 725046, ERC-CoG project TIMING. J.T. acknowledges the support of the EPSRC through the studentship EP/N509784/1. J.S.T.G. acknowledges funding from the Helena Normanton Fellowship of the University of Sussex, UK. A.C. acknowledges the support from the University of Palermo, Italy through the mobility fellowship "Corso di Perfezionamento all'estero 2018".

Disclosures. The authors declare no conflicts of interest.

See Supplement 1 for supporting content. The datasets for all figures are freely accessible at [51].

REFERENCES

1. D. Huang, E. A. Swanson, C. P. Lin, J. S. Schuman, W. G. Stinson, W. Chang, M. R. Hee, T. Flotte, K. Gregory, C. A. Puliafito, and A. Et, "Optical coherence tomography," Science **254**, 1178–1181 (1991).
2. L. Borcea, G. Papanicolaou, C. Tsogka, and J. Berryman, "Imaging and time reversal in random media," Inverse Probl. **18**, 1247–1279 (2002).
3. G. Lerosey, J. de Rosny, A. Tourin, and M. Fink, "Focusing beyond the diffraction limit with far-field time reversal," Science **315**, 1120–1122 (2007).
4. J. Bertolotti, E. G. van Putten, C. Blum, A. Lagendijk, W. L. Vos, and A. P. Mosk, "Non-invasive imaging through opaque scattering layers," Nature **491**, 232–234 (2012).
5. C. Errico, J. Pierre, S. Pezet, Y. Desailly, Z. Lenkei, O. Couture, and M. Tanter, "Ultrafast ultrasound localization microscopy for deep super-resolution vascular imaging," Nature **527**, 499–502 (2015).
6. I. N. Papadopoulos, J.-S. Jouhanneau, J. F. A. Poulet, and B. Judkewitz, "Scattering compensation by focus scanning holographic aberration probing (F-SHARP)," Nat. Photonics **11**, 116–123 (2017).
7. A. V. Diebold, M. F. Imani, T. Sleasman, and D. R. Smith, "Phaseless coherent and incoherent microwave ghost imaging with dynamic metasurface apertures," Optica **5**, 1529–1541 (2018).
8. Y. Rivenson, Y. Zhang, H. Günaydın, D. Teng, and A. Ozcan, "Phase recovery and holographic image reconstruction using deep learning in neural networks," Light Sci. Appl. **7**, 17141 (2018).
9. L. Li, H. Ruan, C. Liu, Y. Li, Y. Shuang, A. Alù, C.-W. Qiu, and T. J. Cui, "Machine-learning reprogrammable metasurface imager," Nat. Commun. **10**, 1082 (2019).
10. A. A. Gowen, "Hyperspectral imaging: an emerging process analytical tool for food quality and safety control," Trends Food Sci. Technol. **18**, 590–598 (2007).
11. D. Bannon, "Cubes and slices," Nat. Photonics **3**, 627–629 (2009).
12. G. Lu and B. Fei, "Medical hyperspectral imaging: a review," J. Biomed. Opt. **19**, 010901 (2014).
13. W. Jahr, B. Schmid, C. Schmied, F. O. Fahrbach, and J. Huisken, "Hyperspectral light sheet microscopy," Nat. Commun. **6**, 7990 (2015).
14. I. Amenabar, S. Poly, M. Goikoetxea, W. Nuansing, P. Lasch, and R. Hillenbrand, "Hyperspectral infrared nanoimaging of organic samples based on Fourier transform infrared nanospectroscopy," Nat. Commun. **8**, 14402 (2017).
15. X. Hadoux, F. Hui, J. K. H. Lim, C. L. Masters, A. Pébay, S. Chevalier, J. Ha, S. Loi, C. J. Fowler, C. Rowe, V. L. Villemagne, E. N. Taylor, C. Fluke, J.-P. Soucy, F. Lesage, J.-P. Sylvestre, P. Rosa-Neto, S. Mathotaarachchi, S. Gauthier, Z. S. Nasreddine, J. D. Arbour, M.-A. Rhéaume, S. Beaulieu, M. Dirani, C. T. O. Nguyen, B. V. Bui, R. Williamson, J. G. Crowston, and P. van Wijngaarden, "Non-invasive in vivo hyperspectral imaging of the retina for potential biomarker use in Alzheimer's disease," Nat. Commun. **10**, 4227 (2019).
16. F. Yesilkoy, E. R. Arvelo, Y. Jahani, M. Liu, A. Tittl, V. Cevher, Y. Kivshar, and H. Altug, "Ultrasensitive hyperspectral imaging and biodetection enabled by dielectric metasurfaces," Nat. Photonics **13**, 390–396 (2019).
17. X. Yin, B. W.-H. Ng, and D. Abbott, *Terahertz Imaging for Biomedical Applications: Pattern Recognition and Tomographic Reconstruction* (Springer, 2012).
18. D. H. Auston and M. C. Nuss, "Electrooptical generation and detection of femtosecond electrical transients," IEEE J. Quantum Electron. **24**, 184–197 (1988).
19. Ch. Fattinger and D. Grischkowsky, "Terahertz beams," Appl. Phys. Lett. **54**, 490–492 (1989).
20. B. B. Hu and M. C. Nuss, "Imaging with terahertz waves," Opt. Lett. **20**, 1716–1718 (1995).
21. N. Horiuchi, "Terahertz technology: endless applications," Nat. Photonics **4**, 140 (2010).

22. J. H. Shapiro, "Computational ghost imaging," Phys. Rev. A **78**, 061802R (2008).
23. Y. Bromberg, O. Katz, and Y. Silberberg, "Ghost imaging with a single detector," Phys. Rev. A **79**, 053840 (2009).
24. W. L. Chan, K. Charan, D. Takhar, K. F. Kelly, R. G. Baraniuk, and D. M. Mittleman, "A single-pixel terahertz imaging system based on compressed sensing," Appl. Phys. Lett. **93**, 121105 (2008).
25. C. M. Watts, D. Shrekenhamer, J. Montoya, G. Lipworth, J. Hunt, T. Sleasman, S. Krishna, D. R. Smith, and W. J. Padilla, "Terahertz compressive imaging with metamaterial spatial light modulators," Nat. Photonics **8**, 605–609 (2014).
26. T. Yuan, J. Z. Xu, and X.-C. Zhang, "Development of terahertz wave microscopes," Infrared Phys. Technol. **45**, 417–425 (2004).
27. M. Unternährer, B. Bessire, L. Gasparini, M. Perenzoni, and A. Stefanov, "Super-resolution quantum imaging at the Heisenberg limit," Optica **5**, 1150–1154 (2018).
28. A. P. Spencer, B. Spokoyny, S. Ray, F. Sarvari, and E. Harel, "Mapping multidimensional electronic structure and ultrafast dynamics with single-element detection and compressive sensing," Nat. Commun. **7**, 10434 (2016).
29. D. B. Phillips, M.-J. Sun, J. M. Taylor, M. P. Edgar, S. M. Barnett, G. M. Gibson, and M. J. Padgett, "Adaptive foveated single-pixel imaging with dynamic supersampling," Sci. Adv. **3**, e1601782 (2017).
30. B. Sun, M. P. Edgar, R. Bowman, L. E. Vittert, S. Welsh, A. Bowman, and M. J. Padgett, "3D computational imaging with single-pixel detectors," Science **340**, 844–847 (2013).
31. C. Amiot, P. Ryczkowski, A. T. Friberg, J. M. Dudley, and G. Genty, "Supercontinuum spectral-domain ghost imaging," Opt. Lett. **43**, 5025–5028 (2018).
32. H. Wu, P. Ryczkowski, A. T. Friberg, J. M. Dudley, and G. Genty, "Temporal ghost imaging using wavelength conversion and two-color detection," Optica **6**, 902–906 (2019).
33. R. S. Bennink, S. J. Bentley, and R. W. Boyd, "Two-photon" coincidence imaging with a classical source," Phys. Rev. Lett. **89**, 113601 (2002).
34. Y. Altmann, S. McLaughlin, M. J. Padgett, V. K. Goyal, A. O. Hero, and D. Faccio, "Quantum-inspired computational imaging," Science **361**, eaat2298 (2018).
35. H. Defienne, M. Reichert, J. W. Fleischer, and D. Faccio, "Quantum image distillation," Sci. Adv. **5**, eaax0307 (2019).
36. P. Caramazza, O. Moran, R. Murray-Smith, and D. Faccio, "Transmission of natural scene images through a multimode fibre," Nat. Commun. **10**, 1–6 (2019).
37. A. Lyons, F. Tonolini, A. Boccolini, A. Repetti, R. Henderson, Y. Wiaux, and D. Faccio, "Computational time-of-flight diffuse optical tomography," Nat. Photonics **13**, 575–579 (2019).
38. R. I. Stantchev, B. Sun, S. M. Hornett, P. A. Hobson, G. M. Gibson, M. J. Padgett, and E. Hendry, "Noninvasive, near-field terahertz imaging of hidden objects using a single-pixel detector," Sci. Adv. **2**, e1600190 (2016).
39. R. I. Stantchev, D. B. Phillips, P. Hobson, S. M. Hornett, M. J. Padgett, and E. Hendry, "Compressed sensing with near-field THz radiation," Optica **4**, 989–992 (2017).
40. R. I. Stantchev, J. C. Mansfield, R. S. Edginton, P. Hobson, F. Palombo, and E. Hendry, "Subwavelength hyperspectral THz studies of articular cartilage," Sci. Rep. **8**, 6924 (2018).
41. S.-C. Chen, L.-H. Du, K. Meng, J. Li, Z.-H. Zhai, Q.-W. Shi, Z.-R. Li, and L.-G. Zhu, "Terahertz wave near-field compressive imaging with a spatial resolution of over $\lambda/100$," Opt. Lett. **44**, 21–24 (2019).
42. J. Zhao, E. Yiwen, K. Williams, X.-C. Zhang, and R. W. Boyd, "Spatial sampling of terahertz fields with sub-wavelength accuracy via probe-beam encoding," Light Sci. Appl. **8**, 55 (2019).
43. L. Olivieri, J. S. Totero Gongora, A. Pasquazi, and M. Peccianti, "Time-resolved nonlinear ghost imaging," ACS Photon. **5**, 3379–3388 (2018).
44. H. Guerboukha, K. Nallappan, and M. Skorobogatiy, "Exploiting k-space/frequency duality toward real-time terahertz imaging," Optica **5**, 109–116 (2018).
45. M.-J. Sun, L.-T. Meng, M. P. Edgar, M. J. Padgett, and N. Radwell, "A Russian Dolls ordering of the Hadamard basis for compressive single-pixel imaging," Sci. Rep. **7**, 3464 (2017).
46. M. Peccianti, M. Clerici, A. Pasquazi, L. Caspani, S. P. Ho, F. Buccheri, J. Ali, A. Busacca, T. Ozaki, and R. Morandotti, "Exact reconstruction of THz sub-lambda source features in knife-edge measurements," IEEE J. Sel. Top. Quantum Electron. **19**, 8401211 (2013).
47. L. Peters, J. Tunesi, A. Pasquazi, and M. Peccianti, "High-energy terahertz surface optical rectification," Nano Energy **46**, 128–132 (2018).
48. T. Seifert, S. Jaiswal, U. Martens, J. Hannegan, L. Braun, P. Maldonado, F. Freimuth, A. Kronenberg, J. Henrizi, I. Radu, E. Beaurepaire, Y. Mokrousov, P. M. Oppeneer, M. Jourdan, G. Jakob, D. Turchinovich, L. M. Hayden, M. Wolf, M. Münzenberg, M. Kläui, and T. Kampfrath, "Efficient metallic spintronic emitters of ultrabroadband terahertz radiation," Nat. Photonics **10**, 483–488 (2016).
49. C. Vicario, B. Monoszlai, and C. P. Hauri, "GV/m single-cycle terahertz fields from a laser-driven large-size partitioned organic crystal," Phys. Rev. Lett. **112**, 213901 (2014).
50. C. Vicario, A. V. Ovchinnikov, S. I. Ashitkov, M. B. Agranat, V. E. Fortov, and C. P. Hauri, "Generation of 0.9-mJ THz pulses in DSTMS pumped by a Cr:Mg2SiO4 laser," Opt. Lett. **39**, 6632–6635 (2014).
51. https://doi.org/10.6084/m9.figshare.c.4829289

optica

Hyperspectral terahertz microscopy via nonlinear ghost imaging: supplementary material

L. OLIVIERI[1], J. S. TOTERO GONGORA[1], L. PETERS[1], V. CECCONI[1], A. CUTRONA[1,2], J. TUNESI[1], R. TUCKER[1], A. PASQUAZI[1] AND M. PECCIANTI[1,*]

[1] Emergent Photonics (Epic) Laboratory, Department of Physics and Astronomy, University of Sussex, Brighton, UK

[2] Department of Engineering, University of Palermo, Palermo, Italy

*Corresponding author: m.peccianti@sussex.ac.uk

Published 19 February 2020

This document provides supplementary information to "Hyperspectral terahertz microscopy via nonlinear ghost imaging," https://doi.org/10.1364/OPTICA.381035. Section 1 describes the experimental setup. Section 2 describes the theoretical analysis of THz pattern formation in the presence of a distributed volume source. Section 3 describes the theoretical foundations of inverse-propagation reconstruction.

S1. EXPERIMENTAL SETUP

S1.1 Experimental configuration

Supp. Fig. 1. Shows the experimental configuration using the DMD (Texas instrument DLP4500NIR) the main optical pump line is split into two independent paths by a beam sampler, the THz generation pump and the probe line. The THz generation pump impinges on an optical grating with 300mm^{-1} line spacing (here α=26.3° and β= 71.3°). The optical grating is required to compensate for the tilt group front introduced by the periodic mirror distribution in the DMD. The Hadamard patterns generated by the DMD are imaged by the lens L2 onto the ZnTe crystal. The ZnTe crystal generates the THz pulse, which propagates through the object under inspection before being detected via a second ZnTe crystal (further details on the detection are included in a subsequent section) and a polarization discriminator, forming a standard electro-optical sampler.

Supp. Fig. 2. outlines the experimental SLM (LCOS-SLM X13138) setup. The key difference when compared with the DMD setup (Supp. Fig. 1) is related to the method employed to generate optical patterns from a phase-only SLM (here φ= 10°). In our experiments,

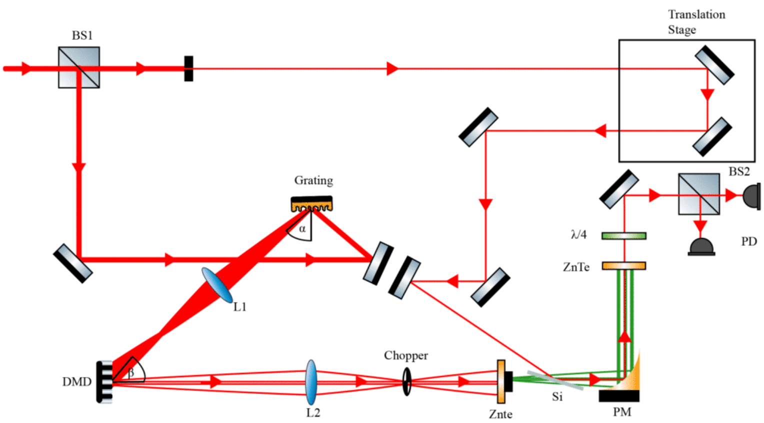

Supplementary. Figure 1. Schematic of the experimental setup used for generating THz patterns using an amplitude DMD spatial-light-modulator.

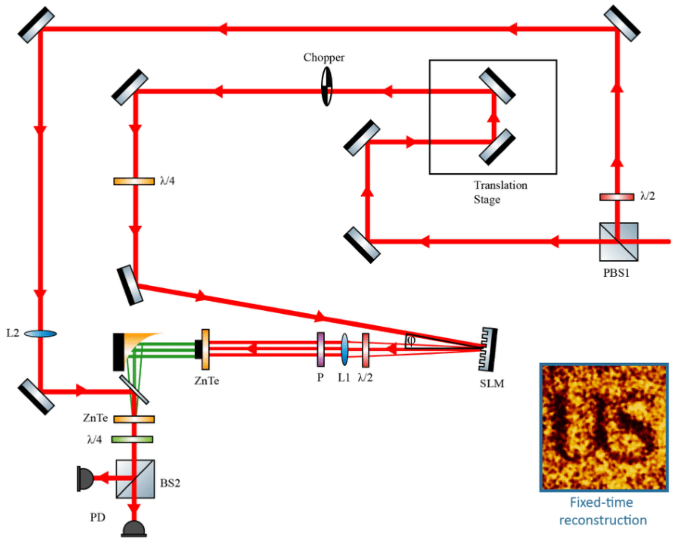

Supplementary Figure 2. Schematic showing the experimental setup used for shaping the beam with a phase-only Hamamatsu LCOS spatial-light-modulator. Inset showing the fixed-time reconstruction taken at the field peak (128x128 pixels).

we employed common-path interferometry to create the Hadamard patterns [1], via the half-wave-plate $\lambda/2$ and the polariser P.

In both cases, the experimental setup is supplied by a regeneratively amplified Titanium Sapphire ultrafast source (Coherent Libra-HE), which generates an ultrashort pulse train. The pulse properties are 1 kHz repetition rate, 4mJ pulse energy, 70fs pulse duration, center wavelength at 800nm and diameter (intensity at 1/e2) 9mm (assessed via knife-edge technique). The probe and THz pulses are mutually delayed using a motorized translation stage.

S1.2 THz generation and Fourier detection

The THz patterns are generated by propagating the generation pump through a <110> ZnTe crystal, of thickness 1mm. Note that in the SLM we used a thickness of 0.1mm for comparison. ZnTe substrates generate THz radiation through the second-order nonlinear mechanism known as optical rectification, in which an ultrashort pulse induces a quasi-DC nonlinear polarization as it propagates through a second-order nonlinear medium. This leads to the emission of a broadband single-cycle THz pulse [2]. The ZnTe crystals had been oriented to maximize emission along the p-polarization direction [3].

Upon interaction with the object, the THz pulses are detected via a second 1mm <110> ZnTe crystal. The detection occurs via electro-optic detection via THz-driven Pockels effect [4]. The polarization discriminator setup consists of a λ/4 waveplate, a Wollaston prism and a pair of balanced photodiodes [5]. A combination of optical chopper and lock-in amplifier is used to maximize the SNR of the detection. The detection crystals have been rotated to detect p-polarized THz for an s-polarized probe [6]. To implement a Fourier detection scheme, the field amplitude of the patterned THz field is detected coherently in k-space after Fourier transformation through a parabolic mirror, with the probe beam sampling the Fourier plane along the optical axis [7]. In our experiments, we considered a temporal resolution of 50fs and total acquisition times between 3ps and 5ps, corresponding to a spectral resolution of 0.33 and 0.2 THz, respectively.

S2. NONLINEAR GHOST-IMAGING WITH DISTRIBUTED VOLUME SOURCES

An interesting feature of the proposed TNGI methodology is the possibility of achieving subwavelength resolutions even in the presence of relatively thick generation crystals. In our experiments, in particular, we were able to retrieve sample features within the 50-100µm scale by employing a 1mm thick ZnTe substrate. Such a possibility is enabled by the coherence of the nonlinear process mediating the conversion from incident optical patterns to THz field distribution (as described by Eq. (3) in the manuscript). The nonlinear optical conversion, in fact, takes place across the entire volume of the generating crystal, with a THz generation source defined as:

$$\boldsymbol{J}_{NL}(x,y,z,t) = \alpha I_{opt}(x,y)\cdot f\left(t-|z|\frac{n}{c}\right)\boldsymbol{p} \qquad \text{(S1)}$$

where $I_{opt}(x,y)$ is the optical intensity distribution, $\boldsymbol{p}$ is the field polarisation direction, α is a normalization constant, n is the refractive index of the crystal and

$$f(t) = \partial_t\left|E_{opt}(t)\right|^2 \qquad \text{(S2)}$$

is the time evolution of the nonlinear polarization current. The temporal delay $t_0 = zn/c$ in Eq. (S1) has an important physical meaning, as it imposes temporal synchronization of the emission from different layers of the crystal.

To illustrate this point, we report in Figure S3 two different simulations for the TNGI reconstruction of a two-dimensional

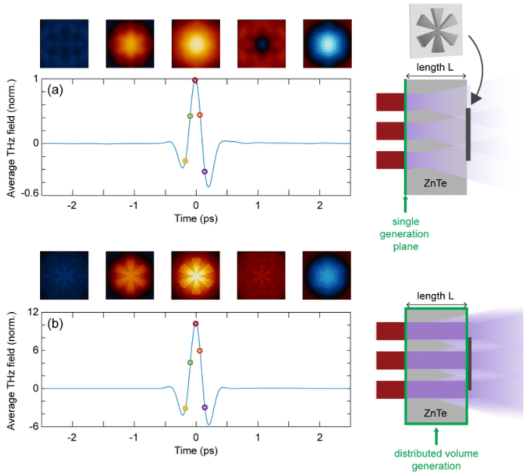

Supplementary Figure 3. Simulation of TNGI in the case of (a) surface and (b) volume generation.

metallic sample (a 960x960μm cartwheel) in the case of a localized surface source (Supp. Fig. 3a) and with the distributed volume source (Supp. Fig. 3b). In our simulations, we computed the THz field generated by the source currents $\boldsymbol{J}_{NL}(x,y,z,t)$ using the dyadic Green's Function method [8]. The numerical reconstruction of the object was performed by considering Walsh-Hadamard patterns of order 32, where each pixel of the Hadamard patterns has a size of $\Delta x = 30\mu m$, roughly corresponding to $\lambda/10$ at 1 THz. In our simulations, we considered a thickness of $L = 295\mu m$.
As can be evinced from the figure, in the case of a nonlinear source localized on the surface of the crystal (Supp Fig. 3a), the presence of spatiotemporal coupling leads to a reconstructed image which is a "propagated" version of the sample transmission (see main text and [9] for a full description of the effects of spatiotemporal coupling). In the presence of a distributed source, conversely, the TNGI is capable of reconstructing the sample morphology with a remarkable degree of fidelity.

S3. THEORY OF SPATIOTEMPORAL IMAGE RECONSTRUCTION USING AN INVERSE-PROPAGATION OPERATOR

In Fig. 4 of the main text we have shown how the experimental reconstruction of an object placed at a distance from the THz emitter can be "back-propagated" to overcome the effect of spatiotemporal coupling. In the following section, we will provide an essential summary of the back-propagation process while referring the reader to [5] for a detailed theoretical derivation.
When an object is placed at a distance z_0 from the THz emitter, each generated THz pattern will undergo propagation before reaching the sample (Supp. Fig. 4). As discussed in the main text, the propagation of the pattern can lead to a significant change in the spatial and temporal properties of the pattern. In the particular case of a subwavelength source, the spatial and temporal spectra of the source become coupled by the propagation. Mathematically, this corresponds to a THz field in the proximity of the sample expressed as [9]:

$$E_n^-(\boldsymbol{x},t) = \int dt' dx' \overleftrightarrow{G}(\boldsymbol{x}-\boldsymbol{x}', t-t')\, J_n(x',t') \\ = \overleftrightarrow{G}(\boldsymbol{x},t) * J_n(\boldsymbol{x},t) \qquad (S3)$$

where $\overleftrightarrow{\boldsymbol{G}}$ is the dyadic Green's function (defined in terms of the magnetic vector potential $\boldsymbol{A}$) and $\boldsymbol{J_n}$ is the nonlinear polarization current acting as a source of the THz field and associated with the n-th pattern. After interaction with the object, the electric field in Eq (2) of the main text is therefore expressed as:

$$E_n^+(\boldsymbol{x},t) = \int dt'\, T(\boldsymbol{x},t-t') E_n^-(\boldsymbol{x},t') \qquad (S4)$$

and the expansion coefficients read:

$$C_n(t) = \int d\boldsymbol{x}\, \mathrm{p}_{TDS} \cdot \left[T(\boldsymbol{x},t) * \left[\overleftrightarrow{\boldsymbol{G}}(\boldsymbol{x},t) * \boldsymbol{J}_n(\boldsymbol{x},t)\right]\right] \qquad (S5)$$

where $\mathbf{p}_{TDS}$ denotes the selected polarisation direction of the TDS detection.
As discussed in [9], the use of the expansion coefficients from Eq. (S5) in Eq. (1) of the main text leads to a reconstructed transfer function T^{exp} of the form:

$$\boldsymbol{T}^{exp}(\boldsymbol{x},t) = [\,\overleftrightarrow{\mathbf{G}}(\boldsymbol{x},t) * T(\boldsymbol{x},t)] \qquad (S6)$$

i.e., a space-time propagated transmission function of the sample. The fundamental idea underlying the inverse propagation operator is to define an inverse function $\overleftrightarrow{\mathbf{W}}(\boldsymbol{x},\boldsymbol{t})$ which inverts Eq. (S6) to retrieve the non-propagated transmission function of the sample by $T(\boldsymbol{x},t) = \overleftrightarrow{\mathbf{W}}(\boldsymbol{x},t) * \boldsymbol{T}^{exp}(\boldsymbol{x},t)$. Following standard approaches, we define our inverse-propagation operator in the Fourier domain as follows:

$$\overleftrightarrow{W}(k,\omega) = \frac{\overleftrightarrow{G}(k,\omega)^*}{\left|\overleftrightarrow{G}(k,\omega)\right|^2 + \alpha NSR(k,\omega)} \qquad (S7)$$

where $\boldsymbol{G}(\boldsymbol{k},\omega)$ is the dyadic Green's function in the Fourier domain, NSR =1/SNR is the average spectral noise-to-signal ratio, and α is a fitting parameter.
In the results presented in Fig. 4 of the main text, we set $\alpha = 0$ as we are smoothing the THz fields acquired through the TDS

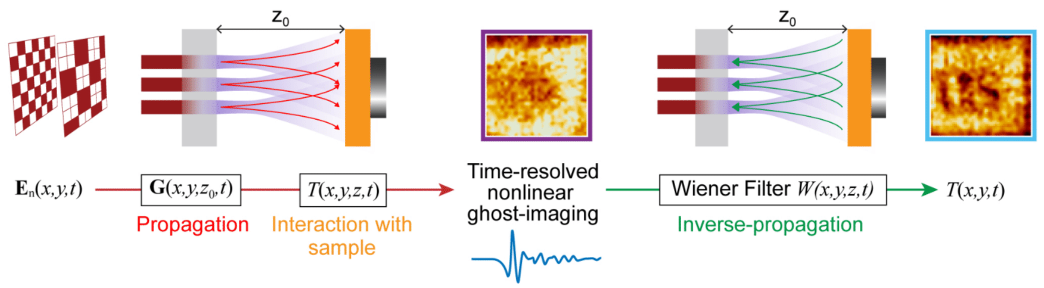

Supplementary Figure 4. Conceptual overview of time-resolved image reconstruction based on the inverse-propagation operator from Eq. (S7).

measurements. A similar result can be obtained considering NSR the difference in the Fourier domain between the 3 dimensional image with and without smoothing while setting $\boldsymbol{\alpha} > \mathbf{1}$. The backpropagation is performed using zero-padding in both spatial and temporal dimensions. A super-gaussian absorber is used to prevent reflections from the boundaries.

REFERENCES

1. J. Zhao, Y. E, K. Williams, X.-C. Zhang, and R. W. Boyd, "Spatial sampling of terahertz fields with sub-wavelength accuracy via probe-beam encoding," Light Sci. Appl. 8, 55 (2019).
2. M. Bass, P. A. Franken, J. F. Ward, and G. Weinreich. “Optical rectification”. Phys. Rev. Lett., 9:446, 1962.
3. F. Blanchard, L. Razzari, H. C. Bandulet, G. Sharma, R. Morandotti, J. C. Kieffer, T. Ozaki, M. Reid, H. F. Tiedje, H. K. Haugen, and F. a Hegmann, "Generation of 1.5 microJ single-cycle terahertz pulses by optical rectification from a large aperture ZnTe crystal.," Opt. Express 15, 13212–20 (2007).
4. Gallot and D. Grischkowsky, "Electro-optic detection of terahertz radiation," J. Opt. Soc. Am. B. 16, 1204–1204 (1999).
5. Q. Wu and X.-C. Zhang, "Free-space electro-optics sampling of mid-infrared pulses," Appl. Phys. Lett. 71, 1285–1286 (1997).
6. P. C. M. Planken, H.-K. Nienhuys, H. J. Bakker, and T. Wenckebach, "Measurement and calculation of the orientation dependence of terahertz pulse detection in ZnTe," J. Opt. Soc. Am. B. 18, 313–313 (2001).
7. H. Guerboukha, K. Nallappan and M. Skorobogatiy, "Exploiting k-space/frequency duality toward real-time terahertz imaging," Optica, 5 109-116, (2018).
8. M. Peccianti et al., “Exact Reconstruction of THz Sub-λSource Features in Knife-Edge Measurements”, IEEE Journal of Selected Topics in Quantum Electronics, 19 (1), 8401211–8401211 (2013).
9. L. Olivieri, J.S. Totero Gongora, A. Pasquazi, and M. Peccianti, “Time-Resolved Nonlinear Ghost Imaging”. ACS Photonics 5, 3379–3388 (2018).

Chapter 3: Terahertz Spatiotemporal Superfocusing - Theoretical Framework

This chapter will show the numerical investigation of broadband spatiotemporal control of THz pulses in random systems. The idea is to develop an experimental-driven approach combining THz waves' state-of-the-art nonlinear wavefront shaping with a deterministic technique suitable for the typical measurement conditions of THz Time-Domain Spectroscopy (TDS). As highlighted in the introduction, the ability of TDS to coherently detect the scattered field's full-wave properties (amplitude and phase) allows for optimising the spatiotemporal properties of the transmitted field, a possibility usually out of reach at optical and infrared frequencies.

The combination of THz technology with concepts and methodologies from complex photonics opens up the intriguing (and unexplored) possibilities of performing time-resolved, full-wave scattering matrix retrieval experiments. Such a remarkable result would have a profound impact, especially for THz imaging, since time-resolved characterisation techniques are currently highly desired due to the broad spectra of potential applications, including deep-tissue biological imaging and time-reversal control of optical waves [119,120].

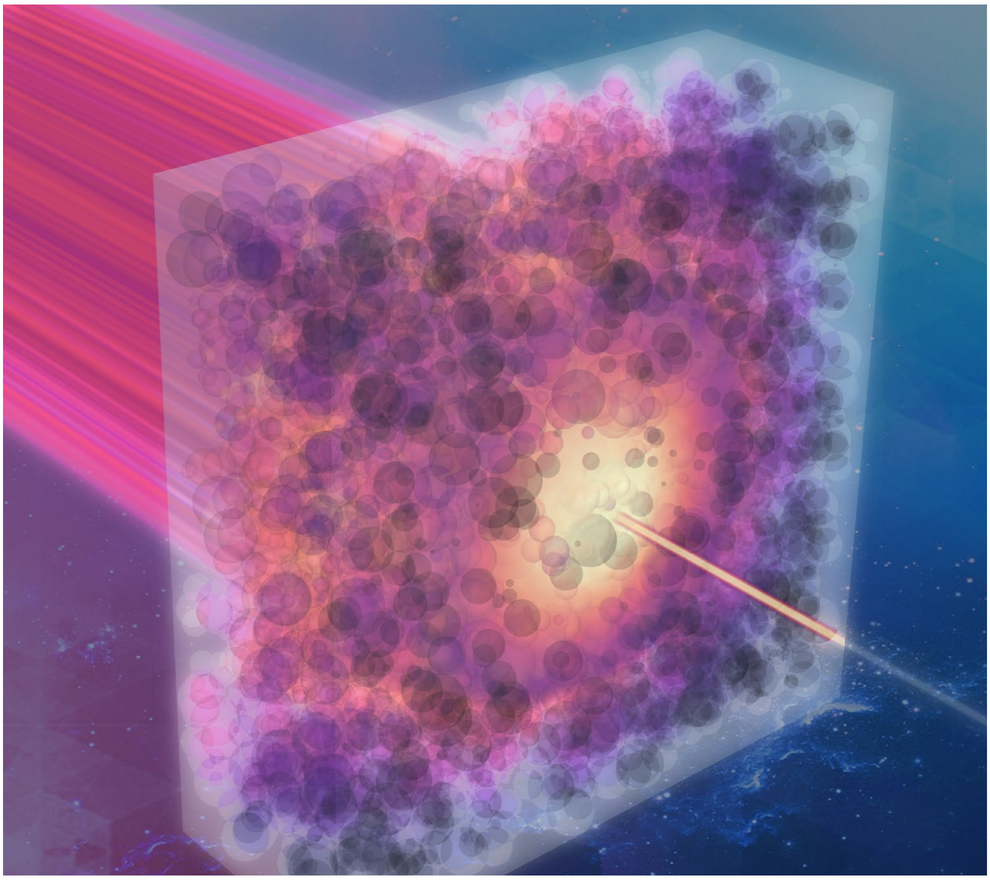

Figure 3.1 Illustrative figure of a THz spatiotemporal superfocusing.

Indeed, THz wavefront shaping has several advantages, such as broadband excitation and coherent, field-sensitive detection, over its optical counterpart to measure field-sensitive transmission properties of scattering media.

In conclusion, this chapter will demonstrate a numerical approach to the coherent spatiotemporal control of THz waves propagating through a random system. Similarly to the Nonlinear Ghost Imaging presented in the previous chapter, the methodology combines the nonlinear conversion of optical patterns to THz structured fields with field-sensitive THz field detection, as enabled by state-of-the-art TDS technology. I will show how the full-wave detection of the scattered THz field enables retrieving the field-sensitive transfer function of the medium directly in a deterministic fashion.

About the paper: Nonlinear Field-Control of Terahertz Waves in Random Media for Spatiotemporal Focusing

In this work, I theoretically investigate a field-sensitive wavefront shaping methodology to control the spatiotemporal properties of terahertz pulses transmitted through a random medium. These results differ from traditional spatiotemporal focusing at optical frequencies, as THz-TDS detection enables a direct, coherent measure of the properties of the transmitted electric field. Such a remarkable result would profoundly impact THz imaging, as time-resolved characterisation techniques are highly desired due to the broad spectrum of potential applications, including deep-tissue biological imaging and time-reversal control of optical waves [119,120]. I considered different wavefront control applications in relevant case studies, including spatiotemporal focusing, phase inversion, temporal shifting control, and re-compression of a chirped THz pulse. Also, I show the ability to manipulate the carrier-envelope-phase (CEP) of a single-cycle incident pulse. My role in this work was to design and framework the theoretical model and perform the simulations. Also, I contributed to the text's writing prior to submission. Finally, in the appendix, I shared the MATLAB code for the pulse retrieval case.

Impact

The article was published in Open Research Europe (ORE) on the 8th of March, 2022. ORE is a new publishing platform for open-access publication. The service enables open peer review for research stemming from Horizon 2020 and Horizon Europe funding. The Altmetric Attention is 7.

Link

About the paper: Deterministic Terahertz Wave Control in Scattering Media

This theoretical work demonstrates a deterministic approach toward the coherent spatiotemporal control of THz waves propagating through a scattering medium. The methodology combines the nonlinear conversion of optical patterns to THz structured fields with field-sensitive THz field detection, as enabled by state-of-the-art TDS technology. Notably, the full-wave detection of the scattered THz field allows retrieving the field-sensitive transfer function of the medium directly in a deterministic fashion, as described through a coherent transfer matrix modelling. The complex time-domain elements of the coherent transfer matrix are sampled by projecting a sequence of orthogonal Walsh-Hadamard patterns. The TDS allows for a sufficient description of the coherent transfer matrix to enable spatiotemporal control through a direct inversion approach. The project demonstrates the formation of the retrieval complex field distribution and phase-only image concealed by the scatterer as relevant examples. Such control could impact THz imaging, where wave-shaping is generally a challenge. My role in this work was to help design the theoretical framework, and I contributed to the text's writing prior to submission.

Impact

The article was published on 19th July 2022 in ACS Photonics, which has an impact factor of 7.529 (2022), and the journal scope spans all of optics and photonics, fitting with the article's claims.

Link

3.1 Nonlinear Field-Control of Terahertz Waves in Random Media for Spatiotemporal Focusing

Open Research Europe

Open Research Europe 2022, 2:32 Last updated: 12 JAN 2023

Check for updates

RESEARCH ARTICLE

REVISED Nonlinear field-control of terahertz waves in random media for spatiotemporal focusing [version 2; peer review: 2 approved]

Vittorio Cecconi[1], Vivek Kumar[1], Alessia Pasquazi[1,2], Juan Sebastian Totero Gongora[1,2], Marco Peccianti[1,2]

[1]Emergent Photonics (EPic) Lab, Department of Physics and Astronomy, University of Sussex, Brighton, BN19QH, UK
[2]Emergent Photonics Research Centre and Dept. of Physics, Loughborough University, Loughborough, LE11 3TU, UK

v2 **First published:** 08 Mar 2022, **2**:32
https://doi.org/10.12688/openreseurope.14508.1

Latest published: 01 Aug 2022, **2**:32
https://doi.org/10.12688/openreseurope.14508.2

Abstract

Controlling the transmission of broadband optical pulses in scattering media is a critical open challenge in photonics. To date, wavefront shaping techniques at optical frequencies have been successfully applied to control the spatial properties of multiple-scattered light. However, a fundamental restriction in achieving an equivalent degree of control over the temporal properties of a broadband pulse is the limited availability of experimental techniques to detect the coherent properties (i.e., the spectral amplitude and absolute phase) of the transmitted field. Terahertz experimental frameworks, on the contrary, enable measuring the field dynamics of broadband pulses at ultrafast (sub-cycle) time scales directly. In this work, we provide a theoretical/numerical demonstration that, within this context, complex scattering can be used to achieve spatio-temporal control of instantaneous fields and manipulate the temporal properties of single-cycle pulses by solely acting on spatial degrees of freedom of the illuminating field. As direct application scenarios, we demonstrate spatio-temporal focusing, chirp compensation, and control of the carrier-envelope-phase (CEP) of a CP-stable, transform-limited THz pulse.

Keywords

Scattering, terahertz, time-domain spectroscopy, random medium, spatiotemporal focusing, superfocusing, genetic algorithm

This article is included in the Advances in Optics collection.

Open Peer Review

Approval Status ✔ ✔

	1	2
version 2 (revision) 01 Aug 2022	✔ view	✔ view
version 1 08 Mar 2022		

1. **Romain Peretti**, IEMN - CNRS, Villeneuve d'Ascq, France

2. **Silvia Gentilini**, Institute for Complex Systems, National Research Council (ISC-CNR), Rome, Italy

Any reports and responses or comments on the article can be found at the end of the article.

This article is included in the Advances in Optics collection.

Corresponding author: Marco Peccianti (m.peccianti@lboro.ac.uk)

Author roles: Cecconi V: Investigation, Methodology, Software, Validation, Writing – Original Draft Preparation, Writing – Review & Editing; **Kumar V**: Investigation, Writing – Review & Editing; **Pasquazi A**: Conceptualization, Methodology, Supervision, Writing – Review & Editing; **Totero Gongora JS**: Conceptualization, Formal Analysis, Methodology, Software, Supervision, Validation, Writing – Review & Editing; **Peccianti M**: Conceptualization, Funding Acquisition, Methodology, Project Administration, Supervision, Validation, Writing – Review & Editing

Competing interests: No competing interests were disclosed.

Grant information: This project has received funding from the European Research Council (ERC) under the European Union's Horizon 2020 research and innovation programme (grant agreement No 725046). JSTG acknowledges support from The Leverhulme Trust (Leverhulme Early Career Fellowship ECF-2020-537).
The funders had no role in study design, data collection and analysis, decision to publish, or preparation of the manuscript.

How to cite this article: Cecconi V, Kumar V, Pasquazi A *et al.* **Nonlinear field-control of terahertz waves in random media for spatiotemporal focusing [version 2; peer review: awaiting peer review]** Open Research Europe 2022, **2**:32 https://doi.org/10.12688/openreseurope.14508.2

First published: 08 Mar 2022, **2**:32 https://doi.org/10.12688/openreseurope.14508.1

REVISED **Amendments from Version 1**

1) We addressed some typos related to the ability to control the Carrier-Envelope-Phase (CEP) of the THz pulse, previously referred to as Carrier-Envelope-Offset (CEO).

2) Inclusion of a new affiliation for the authors Alessia Pasquazi, Juan Sebastian Totero Gongora, and Marco Peccianti.

3) Change of the email address of the corresponding author.

Any further responses from the reviewers can be found at the end of the article

Plain language summary

Multiple scattering of light is a common phenomenon in everyday life. The opaqueness of fog, milk, and clouds are excellent examples of how light is scrambled when travelling through materials composed of thousands of particles scattering light in all directions. While scattering is generally perceived as unwanted, researchers have shown that complex but inexpensive substances like white paint or frosted glass can be adapted to behave as expensive optical devices, such as high-resolution lenses or optical computing devices. This surprising result is achieved by using particular projectors on the incident light to impress specific patterns yielding a desired shape at the output. While manipulating the spatial profile of light is now well-understood, controlling how scattering affects ultra-short light pulses remains exceptionally challenging, primarily due to the difficulty in measuring the effects of scattering at the ultrafast timescales of the pulse (quadrillionths of a second).

In this theoretical work, we propose a new way to tackle this challenge by leveraging the unique properties of terahertz light waves. Terahertz light lies between microwaves and infrared in the electromagnetic spectrum and is highly sought in research and industry. It can easily reveal the material composition of an object and penetrate common materials like paper and plastic as X-rays do, but without being harmful. More importantly, we can experimentally detect the individual oscillations in a terahertz pulse and extract an unprecedented understanding of how scattering affects it.

We show that this added knowledge gives us the ability to finely manipulate the properties of the pulse, compensate the pulse-broadening effects of scattering, and "engineer" specific pulse shapes, a highly-sought ability in photonics. In the long term, this ability could be applied to reveal the internal composition of complex samples, such as biological tissue, or extract images of samples placed behind (or within) scattering materials.

Introduction

Multiple scattering is generally perceived as detrimental in photonics, as it is commonly associated with unpredictability and loss of information. For instance, in microscopy or astronomy, scattering is widely known to severely affect the resolution and fidelity of an imaging system[1,2]. As a result, a large body of research has historically focused on compensating or straight-out eliminating scattering effects[3–5]. In a stark paradigm shift, researchers have recently demonstrated that disordered media can become essential ingredients in developing photonic devices with sophisticated optical performances[6–9]. These include, among others, scattering-assisted super-resolution imaging lenses, wavefront-shaping components, or optical neuro-computing devices[10–18]. At their heart, these demonstrations rely on wavefront shaping techniques, i.e., on the identification of an optimal incident field distribution, or pattern, yielding a desired intensity distribution at the output of a scattering medium[19,20]. While the ability to control monochromatic beams' spatial properties has matured recently, manipulating the temporal and spectral properties of the scattered field remains challenging, particularly when considering broadband ultrafast illumination[21–25]. Multiple scattering is an inherently dispersive phenomenon that naturally leads to the broadening of optical pulses[26,27]. Recent works have shown that the intrinsic coupling between spatial and temporal dimensions in scattering media can be leveraged to manipulate the temporal properties of pulses by controlling the spatial features of the illumination[28,29]. As a result, spatial wavefront shaping can be applied to achieve spatiotemporal focusing, corresponding to a simultaneous focusing in space and pulse re-compression in time, either through iterative approaches or by measuring the frequency-dependent transmission matrix of the sample[21,30–32]. These approaches have shown how to control the envelope of the transmitted waveform successfully (e.g., to adjust the centre of the transmitted pulse[32–35]), but they remain unsuitable for manipulating the carrier-wave properties (e.g., the carrier-envelope offset of the transmitted pulse). Further advances in this area are fundamentally hindered by the inability to directly measure the full-wave properties of the scattered field, most notably the absolute spectral phase[23,35]. An interesting question is whether a direct measurement of the electric field oscillations could enable controlling the coherent features of the transmitted pulse and devising advanced forms of waveform synthesis and spectral shaping currently out-of-reach at optical frequencies. In this context, field-sensitive detection is well-established in terahertz (THz) photonics, where time-domain spectroscopy (TDS) grants access to the time-resolved detection of the electric field of single-cycle THz pulses[36]. Leveraging this ability, THz-TDS has been applied to study the broadband properties of scattering samples, with a particular emphasis on the role of multiple scattering in biomedical applications[26,27,37–40] and the effects of resonant excitation of the scatterers composing the medium[41–45]. However, the implementation of a complete, field-based wavefront control methodology to manipulate broadband pulses is essentially unexplored in the THz frequency band. In this work, we provide a first theoretical exploration of the potential advantages offered by time-resolved, field-sensitive detection in manipulating broadband THz pulses using scattering media. We combine the nonlinear generation of THz patterns from structured optical beams with an evolutionary optimisation feedback-loop targeting the coherent, full-field properties of the transmitted field, showcasing the ability to achieve spatiotemporal focus and control the absolute phase of the transmitted pulse. Quite interestingly, access to the absolute spectral phase of the pulse enables the definition of effective spectral shaping strategies, such as the ability to compress an incident chirped-pulse or control the carrier-envelop-phase (CEP) of an incident pulse, a significantly challenging task at optical frequencies.

Physical framework and methodology

Problem definition: full-wave control of THz pulses in complex media

We model the linear transmission properties of the scattering medium through a dispersive transmission operator $TM(x, y, \omega)$[33,46]. For the sake of simplicity, we focus on a scalar description of the scatterer, but our approach can be easily extended to a full-vector formulation[47].

In the presence of an input field distribution $E^-(x, y, \omega)$, the field transmitted through the scatterer $E^+(x, y, \omega)$ is expressed through a (spatial) convolution relation:

$$E^{+}(x,y,\omega)=\int dx'dy'\, TM\,(x-x',y-y',\omega)\,E^{-}(x',y',\omega). \quad (1)$$

Following Ref. 48, we discretize the output and input planes in M and N two-dimensional, square pixels, respectively. In such a formulation, the spectral components of the fields are re-defined as column arrays, and Equation (1) is rewritten in terms of a frequency-dependent transfer matrix $T_{mn}(\omega)$ as follows:

$$E_m^{+}(\omega)=\sum_{n=k}^{N} TM_{mn}(\omega)\cdot E_n^{-}(\omega), \quad (2)$$

where E_m^+ E_n^- represents the field in the m-th (n-th) pixel of the output (input) field distributions. Following standard approaches, we express the transmission matrix as a complex-valued, random Gaussian matrix:

$$TM_{mn}(\omega)=\exp[i\phi_{mn}(\omega)]/N, \quad (3)$$

where $\phi_{mn}(\omega)$ is a random phase distribution uncorrelated in space and gaussian-correlated along the frequency axis. The degree of spectral correlation, generally expressed in terms of the spectral correlation bandwidth Δv_c, is commonly employed to characterise the spectral response of a scattering medium, and it is generally defined as the inverse of the Thouless time[24]. In practice, a frequency-correlated transfer matrix can be modelled numerically by applying a Gaussian spectral filter of width Δv_c to a white-noise random matrix[49,50].

In general terms, a wavefront control approach aims to identify the optimal incident field distribution $E^{-}_{optimal}(x,y,t)$ yielding the desired output field $E^{+}_{target}(x,y,t)$ at the output facet of the scatterer[51]. However, when operating at THz frequencies, the ability to control the incident electric field distribution is hindered by the limited availability of spatial light modulator (SLM) devices. To overcome this limitation, we employ the nonlinear conversion of structured optical beams, an approach we have recently developed within the framework of time-resolved nonlinear ghost imaging (NGI)[52–54]. With this approach, any optical pattern generated through a standard SLM device can act as a direct source of broadband THz patterns. By considering a nonlinear quadratic process (e.g., in a $\chi^{(2)}$ crystal such as ZnTe), the relation between incident optical intensity and generated THz field is linear, i.e., $E_{THz}(x, y, t) \propto I_{pumb}(x, y, t)$, enabling the precise control over the THz field profile by simply shaping the incident optical pulse. A key advantage is that the spatial resolution of the THz patterns can be pushed way below the standard THz wavelength scale, as it is only bound by the diffraction limit of the optical beam. Besides, the nonlinear conversion ensures that the spatial pattern is well-defined across the whole THz band, enabling the generation and control of single-cycle, THz structured beams. We can assume that the incident THz patterns are expressed as:

$$E^{-}(x,y,\omega)\ \alpha\ A_0 P(x,y) f_{THz}(\omega),\infty \quad (4)$$

where A_0 is an amplitude, $P(x, y)$ is the (all positive) spatial profile, and $f_{THz}(\omega)$ is the spectrum of the THz pulse, which is assumed to be the same for all input points. Figure 1 outlines a possible implementation of our wavefront-control methodology[52–54]. The spatial pattern, impressed by an optical SLM on the pump field, is transferred to the THz pulse through nonlinear conversion in a quadratic crystal. The patterned THz field impinges on the scatterer, that is placed in close proximity (i.e., in the near-field or direct contact) of the generating crystal. Upon propagation, an electro-optical sampler collects the transmitted field in the typical fashion of standard TDS detection[55]. As our objective is to manipulate the full-field properties of the transmitted THz pulse in a specific pixel of the output plane, we introduce a spatial pinhole at the output facet of the scatterer, corresponding to the desired focal spot (x_0, y_0). To optimise the wavefront of the transmitted pulse, the collected THz field from a predetermined ensemble of patterns is analysed and ranked through an evolutionary optimisation algorithm (e.g., a genetic algorithm (GA)) that provides the feedback required to iteratively optimise the transmitted field. This configuration enables establishing an optimisation feedback loop relying on the temporal field properties instead of average intensity, as is generally the case when operating at optical frequencies. In our configuration, the combination of near-field coupling and generation of THz patterns from structured optical fields provides a significant advantage in terms of available degrees of freedom. The THz field can be densely sampled in space, with patterns reaching sub-wavelength spatial resolution in the near-field region. This is a drastic difference from typical optical embodiments, where the spatial sampling is limited by the numerical aperture of the illumination[56]. On the contrary, in our case, the sampling can exceed the density of the modes accessible from the scatterer input facet, and the spatial density of the transfer matrix can be as high as required to represent the scattering medium accurately[48].

Numerical implementation and optimisation strategy

To demonstrate this concept, we numerically simulated the configuration in Figure 1 using MATLAB 2021b. The plotting and simulation codes are fully compatible with Octave open-source software[57]. The simulation codes require the "statistics" Octave package, freely available through the Octave Forge repository. The plotting codes require the "signal" Octave package, freely available through the Octave Forge repository. As a THz input field, we considered a transform-limited THz pulse with a duration of 1 ps, a typical product of a bandwidth-limited optical rectification process in a nonlinear crystal. The incident pulse spectrum is centred at 1 THz ($\Delta\nu \cdot \tau_p \simeq 0.44$, where τ_p is the full width half maximum (FWHM) pulse duration and $\Delta\nu$ the bandwidth of the power spectral distribution). In terms of spatial features, we considered grayscale spatial patterns composed of 33 × 33 square pixels of side $\Delta x = 100\ \mu m$. The scattered field spectral correlation bandwidth is $\Delta\nu_c = 250\ GHz$, a value that is compatible with experimental literature and which places us in a non-monochromatic case[38–40,58]. The optimisation is performed via a standard GA targeting different fitness functions, and corresponding to the genetic algorithm described in Ref. 59. Leveraging the ability to resolve in time the transmitted electric field, we define the fitness functions maximised by the GA in terms of the statistical moments of the electric field waveform, defined as follows:

$$
\begin{aligned}
E_0 &= \int dt\,|E(t)|,\\
\mu[E(t)] &= \int dt\, t\frac{|E(t)|}{E_0},\\
\sigma[E(t)] &= \sqrt{\int dt\,(t-\mu)^2\frac{|E(t)|}{E_0}},\\
S[E(t)] &= \frac{1}{\sigma^3}\int dt\,(t-\mu)^3\frac{|E(t)|}{E_0},
\end{aligned}
\tag{5}
$$

where μ, σ, and S are the first, second (standard deviation) and third moments (skewness) of the probability

distribution defined by $|E(t)|$. Practically speaking, these quantities correspond to the centre, duration, and symmetry of the pulse waveform. We stress that all those quantities do not relate to the pulse envelope or to locally averaged intensity profiles, as in the common optical practice. Table 1 summarises the different types of fitness functions employed in our analysis.

Results

Spatiotemporal focusing and temporal shift of recompressed pulses.

As an initial test case, we targeted the ability to simultaneously focus the transmitted field in space and time (spatiotemporal focusing). Our simulation results are shown in Figure 2. As an input field, we considered a single-cycle, transform-limited THz pulse (Figure 2a). As illustrated in Figure 2b and c, the corresponding transmitted wavefront for a non-optimised pattern is generally spread in time (Figure 2b) and scattered in space (Figure 2c). To obtain a spatiotemporal focus, we applied our GA algorithm to maximise the cost function A, where max $E_0(t) \equiv$ max $E(x_0, y_0, t)$ is the peak electric-field value in the desired focal spot (x_0, y_0). Such a fitness function simultaneously maximises the transmitted field's peak value and minimises the pulse profile's standard deviation in time.

A typical optimised pulse is shown in Figure 2e and f. showcasing our ability to simultaneously focus and recompress the transmitted pulse in the desired focal spot. The ability to restore the spectral properties of the pulse is particularly evident by comparing the spectrum of the optimised pulsed (Figure 2d, solid green line) with the incident one (Figure 2e, blue dashed line). Quantitatively, the optimised spectrum has an FWHM band of 0.52 THz (input 0.8 THz). Quite interestingly, our approach is sensitive to the coherent field properties of the pulse, as illustrated in Figure 2g and h, where we demonstrate the ability

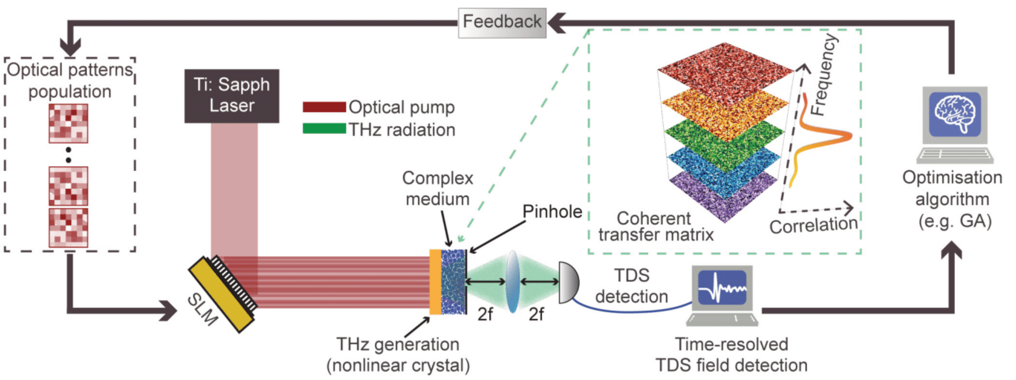

Figure 1. Nonlinear wavefront control of THz complex media and conceptual overview of the iterative algorithm. Illustrative imaging setup, including a nonlinear crystal (yellow) emitting structured THz waves (green) generated from optical patterns (red) through a standard spatial light modulator (SLM). The transmitted THz field is collected via time-domain spectroscopy (TDS). The generation crystal is placed close to the scattering medium. The black arrows describe the schematic loop of the iterative identification of an optimal pattern producing a pulse with the desired spatiotemporal properties via a genetic algorithm (GA) approach. In the green-dashed box, we show a conceptual picture of the hyperspectral transfer matrix and its frequency correlation.

Table 1. The set of cost functions used in the genetic algorithm. In all these expressions, the electric field is measured in the desired focal point, i.e. $E_0(t) \equiv E(x_0, y_0, t)$. The statistical moments of the electric field μ, σ, and S are defined in Equation (5). For the fitness function C, the variables α, β, γ, and ξ are weights controlling the relative importance of each component of the multi-objective fitness function. For the fitness function D, *c.c.* stands for complex conjugate.

Fitness function	Definition	Type of Optimisation
A	$\frac{\max(E_0(t))}{\sigma[E_0(t)]}$	Spatiotemporal focusing
B	$-\frac{min(E_0(t))}{\sigma[E_0(t)]}$	Spatiotemporal focusing and phase inversion
C	$\alpha \max(E_0(t)) - \beta\lvert\mu[E_0(t)] - t_0\rvert - \gamma\lvert\sigma[E_0(t)] - \sigma_0\rvert - \zeta\lvert S[E_0(t)] - S_0\rvert$	Achieving a desired time delay t_0, temporal deviation σ_0 and skeweness S_0
D	$\frac{\int d\omega\, E_0(\omega)\, E^*_{target}(\omega) + c.c.}{\sigma[E_0(t)]}$	Phase-sensitive spectral shaping, where the aim is to obtain a measured field $E_0(\omega)$ as close as possible to a target field $E_{target}(\omega)$

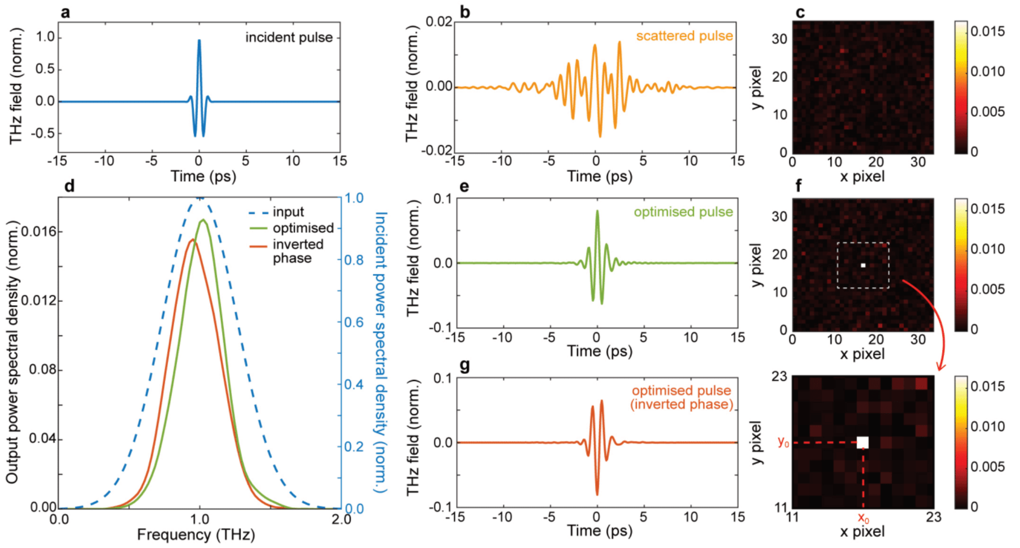

Figure 2. Spatiotemporal refocusing and pulse flip. a. Input temporal profile. **b.** Temporal profile of a scattered pulse at the output of the scattering medium; the pulse is normalised with respect to the incident pulse. **c.** Non-optimised spatial intensity distribution at 1 *THz*. **d.** Power spectral density (PSD) spectrum of the optimal terahertz pulse (green line), optimised flipped pulse (orange line) and incident pulse (blue dashed line, right y-axis). **e.** Temporal profile of an optimised pulse. **f.** Optimised spatial intensity distribution at 1 *THz*. **g.** Temporal profile of an optimised pulse with an inverted (flipped) phase. Numerical parameters: spectral correlation $\Delta\nu_c = 250$ *GHz*, number of generations 10000, size of population per generation 100.

to flip, or invert, the optical phase of the THz pulse by employing the fitness function B from Table 1. The corresponding spectral profile is shown in Figure 2d (orange line).

Figure 3 illustrates the ability to simultaneously optimise several temporal properties of the transmitted wavefront in a single GA optimisation cycle. For this scenario, we employed the multi-objective optimisation fitness function C in Table 1, which maximises the peak field in time while simultaneously searching for incident patterns yielding an output wavefront with the desired centre t_0, duration σ_0 and skewness S_0. Specifically, we performed a series of simulations with a target duration t_0 and skewness S_0 coinciding with the transform-limited incident pulse, while we varied the target time-shift within the interval $t_0 \in [-5ps, 5ps]$. The factors $\{\alpha, \beta, \gamma, \zeta\}$ multiplying each term are the cost function's weights. As illustrated in Figure 3a, the pulse can be simultaneously recompressed and controllably time-shifted in a similar fashion to the case studied in Ref. 25.

However, the ability to control the pulse centre comes at the price of a reduced ability to achieve a good degree of spatio-temporal focusing, as can be evinced by assessing the properties of the optimised wavefronts (Figure 3b–e). While in our simulations, we achieved a broad degree of control of the centre of the pulse μ (Figure 3b), we observed an overall decrease in the peak field (Figure 3b) and an increase in the pulse duration (Figure 3d). This behaviour is in good qualitative agreement with the experimental results of Ref. 25. However, in the framework of THz-TDS, these results suggest that one could ideally scan the THz pulse profile within a range of a few ps without mechanical time-delay devices (i.e., translation stages), commonly used in ultrafast optical setups.

Field-sensitive spectral shaping: chirp and CEO control

A key advantage of our methodology is the possibility of detecting the coherent properties of the transmitted THz pulse. These correspond, in particular, to the spectral amplitude and absolute phase, which are generally not directly measurable quantities in experiments at optical frequencies.

The ability to coherently resolve the complex-valued spectrum of the transmitted waveforms is particularly suited to perform phase-sensitive spectral shaping of the incident pulse. For this type of task, we employ the cost function D in Table 1, where $E_{target}(\omega)$ is the desired spectral profile, $E_{out}(\omega)$ is the output spectrum, and $\sigma(E(t))$ denotes the standard deviation of the pulse in the desired focal point.

This particular choice of fitness function selects patterns yielding output waveforms with a short duration and a high degree of spectral correlation with the desired waveform. As a first example, in Figure 4, we illustrate the possibility of 'recompressing' at the output of the scatterer an incident pulse characterised by a linear chirp. The field profile of the incident pulse is shown in Figure 4a, while the spectral amplitude (blue line) and absolute phase (orange dots) are shown in Figure 4c, respectively. In this scenario, we choose the transform-limited version of the incident pulse as the target waveform in Figure 4a. As can be readily evinced from the optimised pulse profile shown in Figure 4b, in our simulations, we were able to restore the symmetry of the optimised wavefront, albeit for a slightly longer pulse. The ability to flatten the spectral phase is clearly shown in Figure 3d, where we report the spectral amplitude and absolute phase of the optimised pulse. Interestingly, our approach to pulse shaping can be directly applied to achieve extremely fine control of the absolute phase of the output waveform. As a final example, we assessed the possibility of finely tuning the carrier-envelope-phase (CEP) of the optimised waveform. Our results are shown in Figure. 5. In all four cases, we considered an input field corresponding to a transform-limited THz pulse (identical to the case in Figure 2a). As output wavefront targets, we considered waveforms with different CEP values (Figure 5a–c). The corresponding optimised output fields, illustrated in Figure 5d–f, demonstrate the ability to finely tune the CEP of the output waveform, showcasing a remarkable ability to manipulate the coherent properties of the incident pulse.

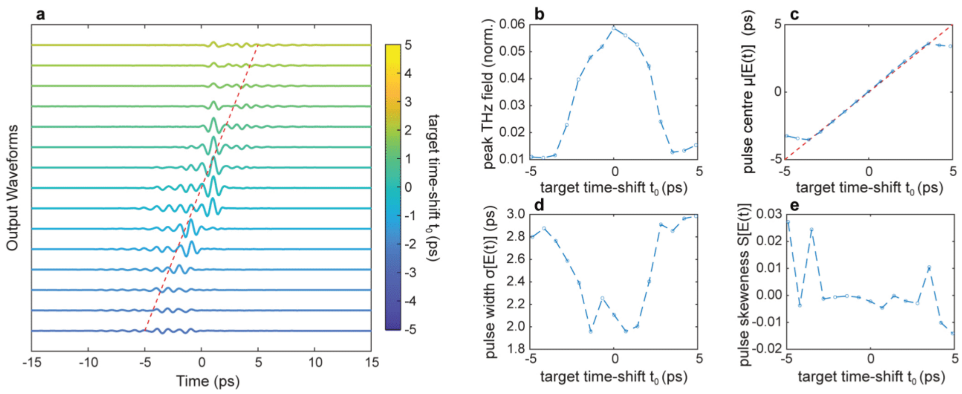

Figure 3. Time shift control of a THz pulse. a. Temporal profiles of the output THz pulses optimised for different values of time delay t_0. **b**. THz peak field as a function of the time delay t_0. **c** First central moment μ, corresponding to the pulse centre, as a function of the time delay t_0. The red dashed line represents the desired time-delay $\mu = t_0$. **d**. The second central moment σ, corresponding to the pulse width, as a function of the time delay t_0. **e** Third central moment S, corresponding to the pulse symmetry, as a function of the time delay t_0. Numerical parameters: spectral correlation $\Delta\nu_c$ = 250 *GHz*, number of generations 20000, size of population per generation 50, and weight factors $\{\alpha, \beta, \gamma, \zeta\} \equiv \{10^2, 5 \cdot 10^{12}, 10^{12}, 1\}$.

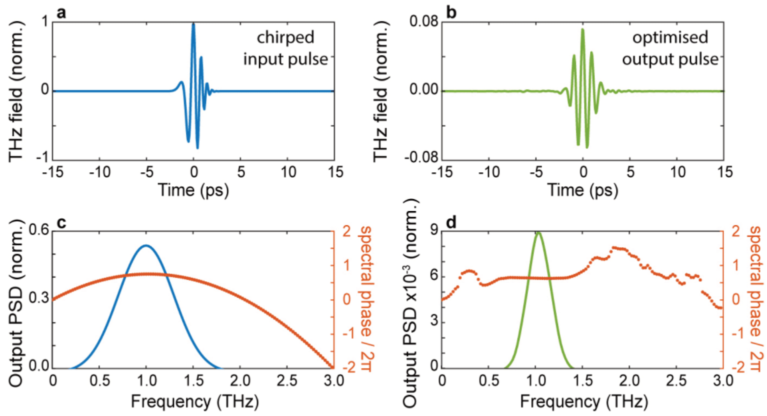

Figure 4. Chirped-pulse compression. a. The input temporal trace of an initially chirped pulse. **b**. Temporal trace of the optimised pulse. **c**. Power spectral density of the input pulse (blue line) and spectral phase (orange dots). **d**. Power spectral density of the optimised pulse (blue line) and spectral phase (orange dots). The algorithm tries to fit the output spectral phase as close as possible to the phase of a transform-limited pulse. Numerical parameters: spectral correlation Δv_c = 250 *GHz*, number of generations 10000, size of population per generation 300.

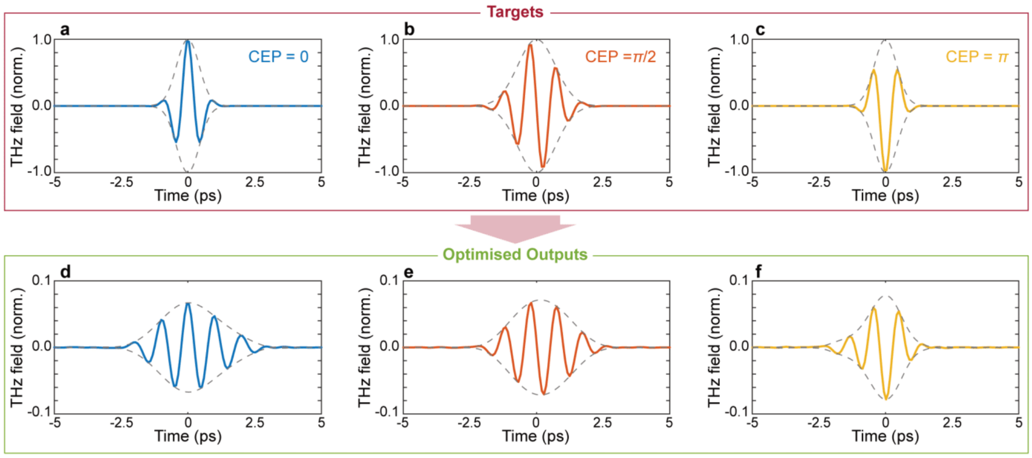

Figure 5. Carrier envelope phase (CEP) modulation. Temporal profiles of target and optimised pulses for CEP ϕ = 0. (**a**, **d**), $\phi = \frac{\pi}{2}$ (**b**, **e**), and $\phi = \pi$ (**c**, **f**). For all cases, the input field is the transform limited pulse shown in Figure 2a. Numerical parameters: spectral correlation Δv_c = 250 *GHz*, number of generations 50000, size of population per generation 50.

Discussion and conclusions

In this work, we theoretically investigate a field-sensitive wavefront shaping methodology to control the spatiotemporal properties of terahertz pulses transmitted through a scattering medium. Our approach combines the field detection capabilities of TDS techniques with the generation of terahertz structured beams through nonlinear conversion of optical beams. Our simulations show how the full access to the coherent properties of the transmitted terahertz field enables defining phase-sensitive evolutionary optimisation strategies to manipulate the carrier-wave properties of THz pulses as they travel through complex media. As in relevant case studies, we considered different wavefront control applications, including spatiotemporal focusing, phase inversion, temporal shifting control, and re-compression of a chirped THz pulse. Quite remarkably, we demonstrated the ability to manipulate the CEP of a single-cycle, CP-stable incident pulse. Controlling the CEO of ultrafast pulses is a highly challenging task in photonics that usually requires the ability to independently control the group and phase velocity of CP-stable pulse or implementing advanced detection techniques such as *f-2f* interferometry[60–62]. Our results differ from traditional spatiotemporal focusing at optical and infrared frequencies as THz-TDS detection provides a direct, coherent measure of the properties of the transmitted electric field. Such a remarkable result would have a profound impact, especially for THz imaging, since time-resolved characterisation techniques are currently highly desired due to the broad spectrum of potential applications, including deep-tissue biological imaging and time-reversal control of optical waves[63,64]. Although we did not provide specific modelling for near-field interactions in this work, the access to the near field modes is less challenging at terahertz frequencies. Hence, it is to be noted that if the THz source is located in near-field conditions with the sample and spatially controlled with NGI-methodology, the accessible modes within the scattering medium can potentially focus light under the diffraction limit, a potential route to subwavelength imaging resolution. Moreover, TDS-based wavefront control techniques could provide a practical approach to manipulating broadband terahertz pulses' spatiotemporal properties and design entirely new classes of wavefront and spectral shaping applications. It is also important to highlight that due to the scale of the wavelengths, working at THz frequencies offers a considerable advantage to have a precise and determinist approach in sample realisation (e.g., 3D printing)[65,66]. Additionally, the size of each scattering particle would be bigger (i.e., hundreds of micrometre[45]) compared to what is usually used in optical frequencies (e.g., nanometre-scale[67]), therefore rendering samples intrinsically more robust to thermal and mechanical effects. Finally, the combination of THz technology with concepts and methodologies from complex photonics opens up the intriguing (and unexplored) possibility of performing time-resolved, full-wave scattering matrix retrieval experiments.

Data availability

Underlying data

Figshare: Figure data for "Nonlinear field-control of terahertz waves in random media for spatiotemporal focusing". http://doi.org/10.6084/m9.figshare.19096859[57].

This project contains the following underlying data, organised by folder:

- Figure 2/
  - mat/ (folder containing raw datasets (in .fig and .mat formats) for each panel in Figure 2)
- Figure 3/
  - mat/ (folder containing raw datasets (in .mat format) for each panel in Figure 3)
- Figure 4/
  - mat/ (folder containing raw datasets (in .fig and .mat formats) for each panel in Figure 4)
- Figure 5/
  - mat/ (folder containing raw datasets (in .fig and .mat formats) for each panel in Figure 5)

Extended data

Figshare: Figure data for "Nonlinear field-control of terahertz waves in random media for spatiotemporal focusing". http://doi.org/10.6084/m9.figshare.19096859[57].

This project contains the following extended data, organised by folder:

- Figure 2/
  - make_f2.m (MATLAB script that reads and processes the raw data and plots the figure)
  - make_f2_octave.m (Octave script that reads and processes the raw data and plots the figure)
- Figure 3/
  - make_f3.m (MATLAB script that reads and processes the raw data and plots the figure)
  - make_f3_octave.m (Octave script that reads and processes the raw data and plots the figure)
- Figure 4/
  - make_f4.m (MATLAB script that reads and processes the raw data and plots the figure)
  - make_f4_octave.m (Octave script that reads and processes the raw data and plots the figure)
- Figure 5/
  - make_f5.m (MATLAB script that reads and processes the raw data and plots the figure)
  - make_f5_octave.m (Octave script that reads and processes the raw data and plots the figure)
- simulation_codes_octave/
  - Main_costfunction_A.m (simulation code with cost function A from Table 1)
  - Main_costfunction_B.m (simulation code with cost function B from Table 1)
  - Main_costfunction_C.m (simulation code with cost function C from Table 1)
  - Main_costfunction_D.m (simulation code with cost function D from Table 1)
  - rsgeng1D.m (function to generate gaussian-correlated 1D data)
  - TM_f.m (function to generate a frequency-correlated transmission matrix)
  - fwhm.m (function to estimate the FWHM of a temporal pulse profile)
  - compute_moment.m (function to calculate the statistical moments of temporal pulse profiles)

- spectr.m (function to calculate the Fourier spectrum of a temporal field profile)
- erdc_fireice_h.m (utility function for customised colormap)
- fireice.m (utility function for customised colormap)

Ethics and consent
Ethical approval and consent were not required.

References

1. Badon A, Boccara AC, Lerosey G, *et al.*: **Multiple scattering limit in optical microscopy.** *Opt Express.* 2017; **25**(23): 28914–28934. Publisher Full Text
2. Kelsall D: **Optical "seeing" through the atmosphere by an interferometric technique*.** *JOSA.* 1973; **63**(11): 1472–1484. Publisher Full Text
3. Muller RA, Buffington A: **Real-time correction of atmospherically degraded telescope images through image sharpening.** *JOSA.* 1974; **64**(9): 1200–1210. Publisher Full Text
4. Liu Y, Chen L, Liu W, *et al.*: **Resolution-enhanced imaging through scattering media by high-order correlation.** *Appl Opt.* 2019; **58**(9): 2350–2357. PubMed Abstract | Publisher Full Text
5. Hampson KM, Turcotte R, Miller DT, *et al.*: **Adaptive optics for high-resolution imaging.** *Nat Rev Methods Primers.* 2021; **1**: 68. PubMed Abstract | Publisher Full Text | Free Full Text
6. Vellekoop IM, Lagendijk A, Mosk AP: **Exploiting disorder for perfect focusing.** *Nat Photon.* 2010; **4**: 320–322. Publisher Full Text
7. **Waves and Imaging through Complex Media.** 2001. Publisher Full Text
8. Goodman PJ: **Speckle Phenomena in Optics.** 2010.
9. Bertolotti J, van Putten EG, Blum C, *et al.*: **Non-invasive imaging through opaque scattering layers.** *Nature.* 2012; **491**(7423): 232–234. PubMed Abstract | Publisher Full Text
10. Popoff SM, Lerosey G, Carminati R, *et al.*: **Measuring the Transmission Matrix in Optics: An Approach to the Study and Control of Light Propagation in Disordered Media.** *Phys Rev Lett.* 2010; **104**(10): 100601. PubMed Abstract | Publisher Full Text
11. Tyson RK: **Principles of Adaptive Optics, Second Edition.** 1997.
12. Shemonski ND, South FA, Liu YZ, *et al.*: **Computational high-resolution optical imaging of the living human retina.** *Nat Photonics.* 2015; **9**: 440–443. PubMed Abstract | Publisher Full Text | Free Full Text
13. Rueckel M, Mack-Bucher JA, Denk W: **Adaptive wavefront correction in two-photon microscopy using coherence-gated wavefront sensing.** *Proc Natl Acad Sci.* 2006; **103**(46): 17137–17142. PubMed Abstract | Publisher Full Text | Free Full Text
14. Pierangeli D, Palmieri V, Marcucci G, *et al.*: **Living optical random neural network with three dimensional tumor spheroids for cancer morphodynamics.** *Commun Phys.* 2020; **3**: 160. Publisher Full Text
15. Fleming A, Conti C, Falco AD: **Perturbation of Transmission Matrices in Nonlinear Random Media.** *Ann Phys.* 2019; **531**(9): 1900091. Publisher Full Text
16. Pierangeli D, Marcucci G, Conti C: **Photonic extreme learning machine by free-space optical propagation.** *Photonics Res.* 2021; **9**(8): 1446–1454. Publisher Full Text
17. Dong J, Gigan S, Krzakala F, *et al.*: **Scaling Up Echo-State Networks With Multiple Light Scattering.** In: *IEEE Stat Signal Processing Workshop (SSP).* 2018; 448–452. Publisher Full Text
18. Dong J, Rafayelyan M, Krzakala F, *et al.*: **Optical Reservoir Computing Using Multiple Light Scattering for Chaotic Systems Prediction.** *IEEE J Sel Top Quantum Electron.* 2020; **26**(1): 1–12. Publisher Full Text
19. Yaqoob Z, Psaltis D, Feld MS, *et al.*: **Optical phase conjugation for turbidity suppression in biological samples.** *Nat Photonics.* 2008; **2**(2): 110–115. PubMed Abstract | Publisher Full Text | Free Full Text
20. Cui M, Yang C: **Implementation of a digital optical phase conjugation system and its application to study the robustness of turbidity suppression by phase conjugation.** *Opt Express.* 2010; **18**(4): 3444–3455. PubMed Abstract | Publisher Full Text | Free Full Text
21. Katz O, Small E, Bromberg Y, *et al.*: **Focusing and compression of ultrashort pulses through scattering media.** *Nat Photon.* 2011; **5**: 372–377. Publisher Full Text
22. van Beijnum F, van Putten EG, Lagendijk A, *et al.*: **Frequency bandwidth of light focused through turbid media.** *Opt Lett.* 2011; **36**(3): 373–375. PubMed Abstract | Publisher Full Text
23. Mounaix M, Defienne H, Gigan S: **Deterministic light focusing in space and time through multiple scattering media with a time-resolved transmission matrix approach.** *Phys Rev A.* 2016; **94**(4): 041802. Publisher Full Text
24. Lemoult F, Lerosey G, de Rosny J, *et al.*: **Manipulating Spatiotemporal Degrees of Freedom of Waves in Random Media.** *Phys Rev Lett.* 2009; **103**(17): 173902. PubMed Abstract | Publisher Full Text
25. Aulbach J, Gjonaj B, Johnson PM, *et al.*: **Control of Light Transmission through Opaque Scattering Media in Space and Time.** *Phys Rev Lett.* 2011; **106**(10): 103901. PubMed Abstract | Publisher Full Text
26. Webster MA, Gerke TD, Weiner AM, *et al.*: **Spectral and temporal speckle field measurements of a random medium.** *Opt Lett.* 2004; **29**(13): 1491–3. PubMed Abstract | Publisher Full Text
27. Tal E, Silberberg Y: **Transformation from an ultrashort pulse to a spatiotemporal speckle by a thin scattering surface.** *Opt Lett.* 2006; **31**(23): 3529–3531. PubMed Abstract | Publisher Full Text
28. Johnson PM, Imhof A, Bret BP, *et al.*: **Time-resolved pulse propagation in a strongly scattering material.** *Phys Rev E Stat Nonlin Soft Matter Phys.* 2003; **68**(1 Pt 2): 016604. PubMed Abstract | Publisher Full Text
29. Bruce NC, Schmidt FE, Dainty JC, *et al.*: **Investigation of the temporal spread of an ultrashort light pulse on transmission through a highly scattering medium.** *Appl Opt.* 1995; **34**(25): 5823–5828. PubMed Abstract | Publisher Full Text
30. Vellekoop IM, Mosk AP: **Focusing coherent light through opaque strongly scattering media.** *Opt Lett.* 2007; **32**(16): 2309–11. PubMed Abstract | Publisher Full Text
31. Wei X, Shen Y, Jing JC, *et al.*: **Real-time frequency-encoded spatiotemporal focusing through scattering media using a programmable 2D ultrafine optical frequency comb.** *Sci Adv.* 2020; **6**(8): eaay1192. PubMed Abstract | Publisher Full Text | Free Full Text
32. McCabe DJ, Tajalli A, Austin DR, *et al.*: **Spatio-temporal focusing of an ultrafast pulse through a multiply scattering medium.** *Nat Commun.* 2011; **2**: 447. PubMed Abstract | Publisher Full Text
33. Boniface A, Gusachenko I, Dholakia K, *et al.*: **Rapid broadband characterization of scattering medium using hyperspectral imaging.** *Optica.* 2019; **6**(3): 274–279. Publisher Full Text
34. French R, Gigan S, Muskens OL: **Speckle-based hyperspectral imaging combining multiple scattering and compressive sensing in nanowire mats.** *Opt Lett.* 2017; **42**(9): 1820–1823. PubMed Abstract | Publisher Full Text
35. Andreoli D, Volpe G, Popoff S, *et al.*: **Deterministic control of broadband light through a multiply scattering medium via the multispectral transmission matrix.** *Sci Rep.* 2015; **5**: 10347. PubMed Abstract | Publisher Full Text | Free Full Text
36. Withayachumnankul W, Naftaly M: **Fundamentals of Measurement in Terahertz Time-Domain Spectroscopy.** *J Infrared Millim Terahertz Waves.* 2014; **35**: 610–637. Publisher Full Text
37. Gentilini S, Missori M, Ghofraniha N, *et al.*: **Terahertz Radiation Transport in Photonic Glasses.** *Ann Phys.* 2020; **532**(8): 2000005. Publisher Full Text
38. Pearce J, Mittleman DM: **Scale model experimentation: using terahertz

pulses to study light scattering. *Phys Med Biol.* 2002; **47**(21): 3823–3830.
PubMed Abstract | **Publisher Full Text**

39. Pearce J, Mittleman DM: **Using terahertz pulses to study light scattering.** *Phys B Condens Matter.* 2003; **338**(1–4): 92–96.
Publisher Full Text

40. Pearce J, Mittleman DM: **Propagation of single-cycle terahertz pulses in random media.** *Opt Lett.* 2001; **26**(24): 2002–2004.
PubMed Abstract | **Publisher Full Text**

41. Oldfield C, Bowman T, El-Shcnawcc M: **Development of Tunable Breast Tissue Phantoms for Terahertz Imaging**. In *2018 IEEE International Symposium on Antennas and Propagation USNC/URSI National Radio Science Meeting*. 2018; 1397–1398.
Publisher Full Text

42. Walker GC, Berry E, Smye SW, *et al.*: **Materials for phantoms for terahertz pulsed imaging.** *Phys Med Biol.* 2004; **49**(21): N363–N369.
PubMed Abstract | **Publisher Full Text**

43. Vilagosh Z, Lajevardipour A, Wood A: **Modelling terahertz radiation absorption and reflection with computational phantoms of skin and associated appendages**. 2018.
Publisher Full Text

44. Walker GC, Berry E, Smye SW, *et al.*: **Modelling the propagation of terahertz radiation through a tissue simulating phantom.** *Phys Med Biol.* 2004; **49**(10): 1853–1864.
PubMed Abstract | **Publisher Full Text**

45. Chau KJ, Elezzabi AY: **Terahertz transmission through ensembles of subwavelength-size metallic particles.** *Phys Rev B.* 2005; **72**(7–15): 075110.
Publisher Full Text

46. Mounaix M, Andreoli D, Defienne H, *et al.*: **Spatiotemporal Coherent Control of Light through a Multiple Scattering Medium with the Multispectral Transmission Matrix.** *Phys Rev Lett.* 2016; **116**(25): 253901.
PubMed Abstract | **Publisher Full Text**

47. Sadel C: **Relations between transfer and scattering matrices in the presence of hyperbolic channels.** *J Math Phys.* 2011; **52**: 123511.
Publisher Full Text

48. Judkewitz B, Horstmeyer R, Vellekoop IM, *et al.*: **Translation correlations in anisotropically scattering media.** *Nat Phys.* 2015; **11**: 684–689.
Reference Source

49. Arienzo A, Argenti F, Alparone L, *et al.*: **Accurate Despeckling and Estimation of Polarimetric Features by Means of a Spatial Decorrelation of the Noise in Complex PolSAR Data.** *Remote Sens.* 2020; **12**(2): 331.
Publisher Full Text

50. Bergström D: **Surface Generation & Analysis - MySimLabs**. 2012.
Reference Source

51. Mosk AP, Lagendijk A, Lerosey G, *et al.*: **Controlling waves in space and time for imaging and focusing in complex media.** *Nat Photon.* 2012; **6**: 283–292.
Reference Source

52. Olivieri L, Totero Gongora JS, Pasquazi A, *et al.*: **Time-Resolved Nonlinear Ghost Imaging.** *ACS Photonics.* 2018; **5**(8): 3379–3388.
Publisher Full Text

53. Olivieri L, Totero Gongora JS, Peters L, *et al.*: **Hyperspectral terahertz microscopy via nonlinear ghost imaging.** *Optica.* 2020; **7**(2): 186–191.
Publisher Full Text

54. Totero Gongora JS, Olivieri L, Peters L, *et al.*: **Route to Intelligent Imaging Reconstruction via Terahertz Nonlinear Ghost Imaging.** *Micromachines (Basel).* 2020; **11**(5): 521.
PubMed Abstract | **Publisher Full Text** | **Free Full Text**

55. Gallot G, Grischkowsky D: **Electro-optic detection of terahertz radiation.** *JOSA B.* 1999; **16**(8): 1204–1212.
Publisher Full Text

56. Jin H, Hwang B, Lee S, *et al.*: **Limiting the incident NA for efficient wavefront shaping through thin anisotropic scattering media.** *Optica.* 2021; **8**(4): 428–437.
Publisher Full Text

57. Totero Gongora JS, Peccianti M, Cecconi V, *et al.*: **Figure data for "Nonlinear field-control of terahertz waves in random media for spatiotemporal focusing"**. *figshare*. Dataset. 2022.
http://www.doi.org/10.6084/m9.figshare.19096859

58. van Albada MP, van Tiggelen BA, Lagendijk A, *et al.*: **Speed of propagation of classical waves in strongly scattering media.** *Phys Rev Lett.* 1991; **66**(24): 3132–3135.
PubMed Abstract | **Publisher Full Text**

59. Vellekoop IM, Mosk AP: **Phase control algorithms for focusing light through turbid media.** *Opt Commun.* 2008; **281**(11): 3071–3080.
Publisher Full Text

60. Schilt S, Südmeyer T: **Carrier-Envelope Offset Stabilized Ultrafast Diode-Pumped Solid-State Lasers.** *Appl Sci.* 2015; **5**(4): 787–816.
Publisher Full Text

61. Imran T, Lee YS, Nam CH, *et al.*: **Stabilization and control of the carrier-envelope phase of high-power femtosecond laser pulses using the direct locking technique.** *Opt Express.* 2007; **15**(1): 104–112.
PubMed Abstract | **Publisher Full Text**

62. Okubo S, Onae A, Nakamura K, *et al.*: **Offset-free optical frequency comb self-referencing with an f-2f interferometer.** *Optica.* 2018; **5**(2): 188–192.
Publisher Full Text

63. Papadopoulos IN, Jouhanneau JS, Poulet JFA, *et al.*: **Scattering compensation by focus scanning holographic aberration probing (F-SHARP).** *Nat Photon.* 2017; **11**: 116–123.
Publisher Full Text

64. Frazier M, Taddese B, Xiao B, *et al.*: **Nonlinear time reversal of classical waves: Experiment and model.** *Phys Rev E Stat Nonlin Soft Matter Phys.* 2013; **88**(6): 062910.
PubMed Abstract | **Publisher Full Text**

65. Veli M, Mengu D, Yardimci NT, *et al.*: **Terahertz pulse shaping using diffractive surfaces.** *Nat Commun.* 2021; **12**(1): 37.
PubMed Abstract | **Publisher Full Text** | **Free Full Text**

66. Li J, Mengu D, Yardimci NT, *et al.*: **Spectrally encoded single-pixel machine vision using diffractive networks.** *Sci Adv.* 2021; **7**(13): eabd7690.
PubMed Abstract | **Publisher Full Text** | **Free Full Text**

67. Vellekoop IM, Aegerter CM: **Scattered light fluorescence microscopy: imaging through turbid layers.** *Opt Lett.* 2010; **35**(8): 1245–1247.
PubMed Abstract | **Publisher Full Text**

3.2 Deterministic Terahertz Wave Control in Scattering Media

ACS Photonics
pubs.acs.org/journal/apchd5
Article

Deterministic Terahertz Wave Control in Scattering Media

Vivek Kumar, Vittorio Cecconi, Luke Peters, Jacopo Bertolotti, Alessia Pasquazi, Juan Sebastian Totero Gongora, and Marco Peccianti*

Cite This: https://doi.org/10.1021/acsphotonics.2c00061 Read Online

ACCESS | Metrics & More | Article Recommendations | Supporting Information

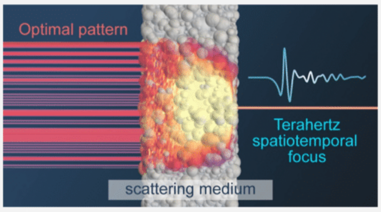

ABSTRACT: Scattering-assisted synthesis of broadband optical pulses is recognized to have a cross-disciplinary fundamental and application importance. Achieving full-waveform synthesis generally requires means for assessing the instantaneous electric field, i.e., the absolute electromagnetic phase. These are generally not accessible to established methodologies for scattering-assisted pulse envelope and phase shaping. The lack of field sensitivity also results in complex indirect approaches to evaluate the scattering space−time properties. The terahertz frequency domain potentially offers some distinctive new possibilities, thanks to the availability of methods to perform absolute measurements of the scattered electric field, as opposed to optical intensity-based diagnostics. An interesting conceptual question is whether this additional degree of freedom can lead to different types of methodologies toward wave shaping and direct field-waveform control. In this work, we theoretically investigate a deterministic scheme to achieve broadband, spatiotemporal waveform control of terahertz fields mediated by a scattering medium. Direct field access via time-domain spectroscopy enables a process in which the field and scattering matrix of the medium are assessed with minimal experimental efforts. Then, illumination conditions for an arbitrary targeted output field waveform are deterministically retrieved through numerical inversion. In addition, complete field knowledge enables reconstructing field distributions with complex phase profiles, as in the case of phase-only masks and optical vortices, a significantly challenging task for traditional implementations at optical frequencies based on intensity measurements aided with interferometric techniques.

KEYWORDS: *THz imaging, scattering media, THz wave control, spatiotemporal focusing, coherent transfer matrix*

■ INTRODUCTION

The propagation of waves in a scattering medium results in complex space−time interference patterns, i.e., in a complex time- and position-dependent response at the output.[1,2] These phenomena are ubiquitous features in the physics of random wave propagation and significantly impact applications in several domains ranging from electromagnetic to acoustic, mechanical, and matter waves.[2,3] For instance, in optical imaging, random propagation of light rapidly reduces the image fidelity in deep biological tissue characterization.[4] As such, the performance of state-of-the-art microscopes is traditionally affected by the ineliminable dynamical turbidity in the samples.[5,6]

Although light scattering is usually considered an impediment, it is not necessarily accompanied by an irreversible loss of information.[7] By leveraging this principle, researchers have recently developed a broad range of wavefront-shaping techniques to control complex light propagation through a scattering medium.[8,9] The basic principle is to spatially modulate the wave impinging onto the medium to harness the scattering-induced amplitude and phase distortions. Recently, various approaches toward optical wavefront compensation based on feedback,[10] guide stars,[11] and memory effect[12] have been demonstrated in different disciplines. These methodologies have enabled the manipulation of scattered waves for refocusing and imaging applications. Although approaches based on the iterative optimization of the scattered field rely on technically simple implementations, they fundamentally operate without direct knowledge of the scattering medium. As such, a specific optimization process provides little clues for a different one, and convergence is usually established solely by the inability to reduce an error function further. Deterministic approaches overcome this limitation. They rely on the knowledge provided by measuring the optical transfer matrix of the medium.[13,14] Deterministic methods first measure the scattered light field corresponding to different sets of amplitude[15,16] or phase[17,18] illumination patterns (preferably forming an orthogonal set). The measurements are then combined to achieve a single-step illumination retrieval for a desired optimized wavefront through numerical inversion.

Challenges of Field-Wave Synthesis Using Random Media. Within the process of exploiting random media for space−time wave synthesis, one can argue that the knowledge of the transmission matrix is insufficient. While the transmission matrix components can be retrieved via complex spectral interferometry approaches, a full spatiotemporal synthesis requires prior knowledge of the source. If the absolute phase

Received: January 11, 2022

profile of the source pulse is not known, its effect on the scattered field is also unknown.

Interestingly, when the detection can resolve the instantaneous field dynamics for a large set of spatially modulated fields, one can trivially target a new scattered waveform as a simple combination of the field scattered by different illuminations without directly referring to the scattering matrix. Indeed, powerful wave-synthesis approaches in optics do not generally rely upon absolute phase knowledge.[18] This rationale, for example, is one of the critical accelerating factors for optical frequency combs technology.[19] Conversely, persuasive, popular nonlinear pulse diagnostics (e.g., FROG or SPIDER) do not provide access to the instantaneous field.[20−22]

Full Time-Domain Field Approach. The ability to perform a complete time-domain detection brings a conceptual difference: by introducing a sparse-light modulation (as in the practice of random media functionalization) for each spatially orthogonal illumination p_i, one can detect the corresponding space−time waveform E_i^+ (x_o,t). These independently transmitted waveforms can, in principle, be used to decompose any desired space−time waveform E_T^+ (x_o, t) at the output as a linear superposition

$$E_T^+(x_o, t) = \sum_i c_i E_i^+(x_o, t) \tag{1}$$

where c_i are complex-valued expansion coefficients. Once one determines the set of c_i, experimentally achievable, this can provide access to the spectrum of available waveforms. While this approach does not require specific access to the source waveform, the latter is, however, trivially accessible via time-sensitive detection and would grant access to the scattering matrix.

In this context, terahertz time-domain spectroscopy (THz-TDS) is a mature and established technique capable of fully resolving the electric-field oscillations in a broadband pulse,[23] i.e., providing full knowledge of the complex spectral field.[24] The scientific question is whether THz-TDS can be exploited to develop a deterministic approach to waveform synthesis (closely related to time-reversal methods,[25−27] ultrasound, or radio-frequency approaches[28,29]). The idea is to extract sufficient information to obtain access to any scattering-allowed output field. The large relative THz bandwidth available in TDS embodiments (normally exceeding a decade) allows easily spanning a wide range of single and multiple scattering regimes for a given sample.[30,31] On the practical side, the relatively large wavelength of THz waves (spanning from roughly 30 μm to 3 mm) suggests that the typical subwavelength scales of scattering phenomena are significantly more accessible in experimental platforms when compared to optical embodiments.[32−34]

A general downside in implementing THz wavefront control methods is, however, the limited availability of wavefront-shaping devices.[35,36] In addition, the use of diffraction-limited systems at long wavelengths (which fixes the pattern resolution[37,38]) is undesirable because the experimental setting usually does not involve samples several orders of magnitude larger than the wavelength, trivial conditions in optics. This results in a relatively small number of modes that can be independently excited in a scattering structure with far-field illumination.[39] Very recently, the nonlinear conversion of structured optical beams has emerged as a promising approach toward deeply subwavelength spatial light modulation (SLM) of THz waves.[40,41] The combination of nonlinear THz pattern generation and time-resolved field detection, in particular, has enabled the development of hyperspectral THz imaging with deep subwavelength imaging resolution.[42] In essence, placing an object in the near-field of a nonlinear optical-to-THz converter makes it possible to produce terahertz illumination patterns with fine spatial features approaching the optical (i.e., the pump) diffraction limit.

In this work, we explore this framework in connection with scattering-assisted waveform synthesis, introducing the field equivalent of the traditional spatiotemporal focusing and image retrieval. We explore scenarios extremely challenging in optics, which include retrieval of field distributions with complex phase profiles, such as phase-only masks and optical vortices. In our approach, we expand the complex-valued, coherent transfer matrix of the scattering medium using an orthogonal Walsh−Hadamard decomposition of near-field THz illumination.[43] We leverage this knowledge to perform a direct single-step inversion using a constraint least-square optimization approach compatible with realistic experimental conditions.[44]

■ METHODS

Model Definition and Simulation Setup. We define the input/output field relation in terms of an impulse response T_x (x_o, x', t, t'),[45] as

$$E^+(x_o, t) = \iint T_x(x_o, x', t, t')E^-(x', t')\mathrm{d}x'\mathrm{d}t' \tag{2}$$

where E^- and E^+ denote the spatiotemporal electric-field distribution just before and after the scattering medium. To lighten the notation, we define x_o and x' as the one-dimensional representation of the input and output planes, respectively. In the frequency domain ω, eq 2 reads

$$\tilde{E}^+(x_o, \omega) = \int \tilde{T}_x(x_o, x', \omega)\tilde{E}^-(x', \omega)\mathrm{d}x' \tag{3}$$

where $\tilde{E}^+$ (x_o, ω) and $\tilde{E}^-$ (x', ω) are the time-Fourier transforms of the input and output fields.

Following standard approaches, we rewrite eq 3 in a discrete scalar transfer matrix formalism, where the response of the scattering medium for each incident frequency is described by an $M \times N$ field-based, random transmission matrix $T_{mn} \in \mathbb{C}^{M\times N}$.[46] We divide the output and input planes into M and N spatial independent segments (corresponding, e.g., to the physical pixels on the input wavefront-shaping and output imaging devices) and K spectral modes, a representation that is well-suited for experiments. In the discrete coordinates, the transfer matrix is an $N \times M \times K$ three-dimensional matrix defined as T_{mnk} = $T_{mn}(\omega_k)$. For a given kth frequency ω_k, the relationship between the THz fields E_m^+ (ω_k) and E_n^- (ω_k) at the nth input and mth output pixels reads

$$E_m^+(\omega_k) = \sum_n T_{mn}(\omega_k)E_n^-(\omega_k) \tag{4}$$

where we considered a coherent transfer matrix defined as

$$T_{mn}(\omega) = \frac{a_{mn}(\omega) + ib_{mn}(\omega)}{N} \tag{5}$$

with $a_{mn}(\omega)$ and $b_{mn}(\omega)$ random Gaussian variables with zero mean, and standard deviation $\sigma = 1/2$.[47] The $1/N$ normalization factor ensures that, on average, the power transmitted by the TM is roughly half of the incident power. To introduce a controllable spectral correlation in the new model, we applied a Gaussian filter of width $\Delta\omega_c$ to the real and imaginary part of the transfer matrix.[46,48−50] As illustrated in Figure S1, we verified that the

https://doi.org/10.1021/acsphotonics.2c00061
ACS Photonics XXXX, XXX, XXX−XXX

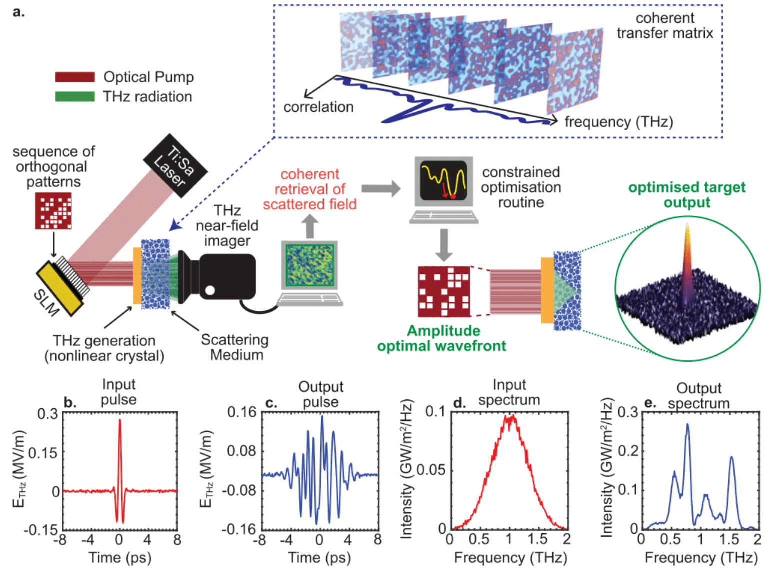

Figure 1. Schematic of experimental-driven methodology (a) Conceptual overview of methodology, including the nonlinear conversion of optical patterns to THz structural waves and the retrieval of transmission properties of the scattering medium defined in terms of a coherent transfer matrix. The full knowledge of the coherent transfer matrix retrieved using an orthogonal set of patterns can be used to achieve scattering-assisted focusing at the output of the scattering medium. (b) Input THz pulse electric-field profile. (c) Scattered THz pulse collected at a generic mth output pixel. (d) Intensity spectral density of the input THz field. (e) Intensity spectral density of the scattered THz pulse as collected at a generic mth pixel. In our simulations, we considered a 1 nJ THz pulse of duration 250 fs at the input with 40 dB SNR per pixel. The 6.4 × 6.4 mm^2 sample illumination area is spatially sampled at 200 μm resolution, corresponding to a number of pixels of 32 × 32.

introduction of a spectral correlation does not affect the statistical properties of the transfer matrix elements for each individual frequency. The spectral correlation is directly associated with the sample properties and inversely proportional to the Thouless time (corresponding to the average confinement time of the field in the medium).[49,50] In the presence of broadband illumination, the spectral correlation bandwidth $\Delta\omega_c$ is of critical importance, as it determines the total number of accessible spectral modes within the illumination bandwidth.[9,39,51] In our case, we convolve a white-noise distribution with a Gaussian filter with a standard deviation of $\Delta\nu_c = \Delta\omega_c/2\pi$ = 150 GHz along the frequency axis to impose a desired spectral correlation in the transfer matrix elements. Further details on our particular choice of parameters are included in Supporting Information Note 1.

Figure 1a provides a conceptual overview of the THz-TDS experimental configuration we referenced in our modeling. An optical spatial light modulator (SLM) impressed a desired spatial pattern on an ultrafast optical field (λ = 800 nm). The optical pattern is converted to a THz structured field via a nonlinear crystal, as discussed in ref 41. Without loss of generality, we assume a quadratic $\chi^{(2)}$ optical rectification process (e.g., ZnTe) that converts the optical intensity wavefront $I^{\text{optical}}(x')$ to a THz wavefront $E^{\text{THz}}(x, t)$ as follows

$$E^{\text{THz}}(x, t) \propto \chi^{(2)} I^{\text{optical}}(x', t) \tag{6}$$

where $\chi^{(2)}$ is the second-order susceptibility of the nonlinear crystal. With this position, the THz field impinging on the scattering medium is defined in the frequency domain as $\tilde{E}^{-}(x', \omega) = I^{\text{optical}}(x') f(\omega)$, where $f(\omega)$ is the spectrum of the THz pulse. Our scheme requires controlling the optical intensity distribution impinging on the nonlinear crystal. This could be easily achieved in experiments through an amplitude SLM (e.g., a Digital Micromirror Device or DMD)[41,52] or phase-only SLMs combined with interferometric techniques.[53] The THz pattern impinges upon the scattering medium and produces a complex, time-dependent interference pattern at the output. Finally, a TDS image of the scattered THz wave is collected through a parallel, near-field imaging scheme based on electrooptical sampling.[54] To assess the robustness of our numerical approach to experimental noise, we performed the theoretical analysis in this manuscript by assuming a 40 dB signal-to-noise ratio (SNR) per pixel at the detection. With this assumption, the THz pulse contains a white-noise term that is compatible with the experimental conditions. Such a relative low noise can be easily achieved in experiments based on electrooptic detection using balanced detectors of the THz field-induced birefringence in a nonlinear crystal.[55] In Figure 1b−e, we show an illustrative THz transmitted field as a function of the spatial and spectral coordinates as obtained for plane wave illumination and detected in a single pixel at the output. The temporal profile of the pulse is significantly broadened (Figure 1c), and the peak field is attenuated. When moving to the spectral domain (Figure 1e), the transmitted THz field is characterized by a random modulation of its spectrum as a consequence of interference and dispersion effects induced by multiple scattering.

In close analogy with the traditional experimental approaches, we simulated the reconstruction of the coherent transfer matrix by computing the TDS output images corresponding to a predefined set of illumination patterns. In our simulations, we

https://doi.org/10.1021/acsphotonics.2c00061
ACS Photonics XXXX, XXX, XXX−XXX

employed a Walsh−Hadamard decomposition scheme, i.e., we determined the full-wave responses corresponding to each column of an $N \times N$ Walsh−Hadamard matrix. We then extracted the frequency-dependent elements of the coherent transfer matrix through a linear inversion of the Walsh−Hadamard response (Figure 2). The detailed reconstruction method is described in Supporting Information Note 2.

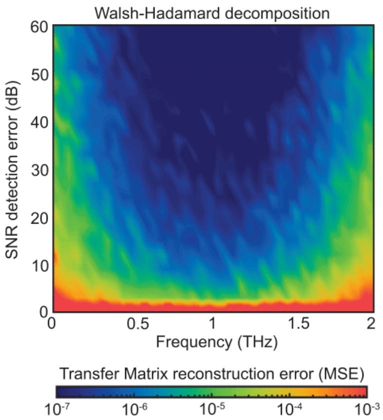

Figure 2. Transfer Matrix reconstruction. Mean squared error (MSE) of the coherent transfer matrix elements as reconstructed through a Walsh−Hadamard decomposition. The input and output planes are divided into 16 × 16 pixels, corresponding to a scattering matrix composed of 256 × 256 entries.

The identification of an optimized optical spatial pattern $I_{opt}(x')$ that produces a given field profile of interest $\tilde{Z}_{target}(x_o, \omega)$ carries a few significant challenges. First, as can be easily evinced from eq 6, in optical rectification, the THz field phase cannot be controlled through the incident optical phase, i.e., we can only control the THz amplitude distribution by varying the intensity distribution of the optical pump. Second, the spatial distribution of the optical intensity pattern is bound to be the same for all of the different frequencies carried by the THz pulse. Due to these two constraints, we cannot invert the coherent transfer matrix directly as the solution pattern is likely a frequency-dependent amplitude and phase distribution. On the contrary, we must identify a single, amplitude-only field distribution that best approximates the desired field distribution at the output. It is essential to stress that this is a post-measurement process, as opposed to the case of typical optimization techniques relying on feedback loops between illumination and measurement.

To this end, we cast our inversion problem in terms of a constraint least-square minimization of the following fitness function

$$f[I_{opt}(x')] = \frac{1}{2}\left\| \int \tilde{T}_x(x_o, x', \omega) I_{opt}(x') f(\omega) \mathrm{d}x' - \tilde{Z}_{target}(x_o, \omega) \right\|_2^2$$
$$\text{subject to } 0 \le I_{opt}(x') \le 1,\ I_{opt}(x') \in \mathbb{R} \tag{7}$$

where $\|\cdots\|_2$ is the Euclidean norm. In the discrete coordinate system, eq 7 reads

$$f[I_n] = \frac{1}{2}\sum_m \sum_k \left| \sum_n T_{mnk} I_n f_k - Z_{mk} \right|^2 \tag{8}$$

where $T_{mnk} = \tilde{T}_x(x_m, x'_n, \omega_k)$, $I_n = I_{opt}(x'_n)$, $f_k = f(\omega_k)$, and $Z_{mk} = \tilde{Z}_{target}(x_m, \omega_k)$, and where we replaced the Euclidean norm with the Frobenius norm. The constrained convex optimization problem defined in eqs 7 and 8 can be solved using various techniques. We use the Trust-Region-Reflective algorithm, a

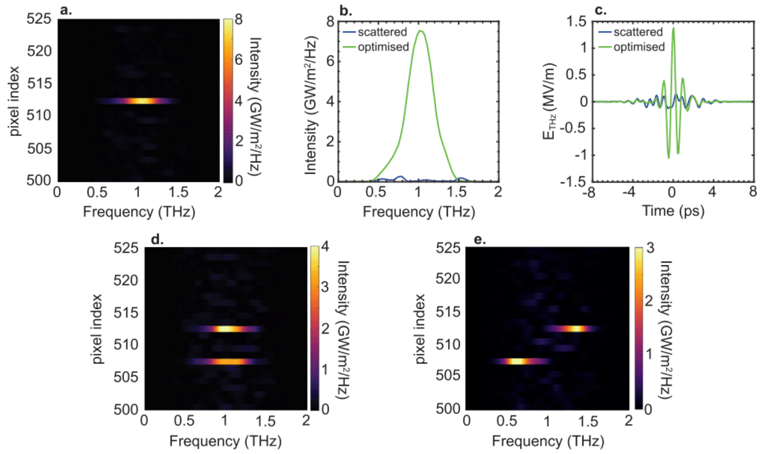

Figure 3. Spatiotemporal focusing of THz field: (a) optimized intensity spectral density distribution showing the focus spot in THz band. (b) Comparison between intensity spectral density profiles of the perturbed THz spectrum (blue) and optimized spectrum (green) at the mth pixel. (c) THz pulse profile of scattered field (blue) and optimized field (green) from *the* mth pixel of the output plane. (d) Intensity spectral density distribution of the output THz field showing two simultaneous focus spots at mth pixel and m'th pixel. (e) Intensity spectral density distribution of optimized THz field for two simultaneous focus spots at mth and m'th pixel with two different spectra centered around 0.7 and 1.3 THz. SNR per pixel: 40 dB. The 6.4 × 6.4 mm² sample illumination area is spatially sampled at 200 μm resolution, corresponding to a number of pixels of 32 × 32.

https://doi.org/10.1021/acsphotonics.2c00061
ACS Photonics XXXX, XXX, XXX−XXX

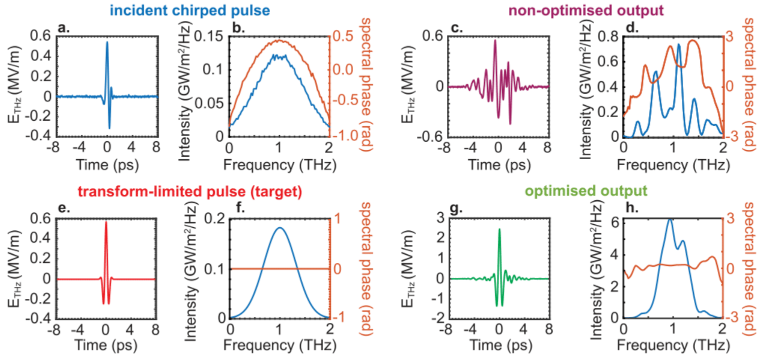

Figure 4. Deterministic coherent control without previous knowledge of the source. (a) Input field-temporal profile corresponding to a chirped pulse. The temporal profile includes the 40 dB noise applied at the detection. (b) Intensity spectral density (blue line) and spectral phase (orange line) for the field profile in panel (a). (c, d) Same as panels (a) and (b) but for a nonoptimized incident pattern. (e, f) Same as panels (a) and (b) for the optimized profile targeted by our optimization routine. (g, h) Same as panels a and b for the optimized output field. The 6.4 × 6.4 mm^2 sample illumination area is spatially sampled at 200 μm resolution, corresponding to a number of pixels of 32 × 32.

well-established method capable of rapidly solving relatively large-scale problems with low memory requirements.[56] The ability to optimize the full-field properties of the transmitted field is a distinctive feature of this approach; eqs 7 and 8 are, indeed, an absolute phase-sensitive optimization, corresponding to a field-driven best fit rather than an intensity-driven fit.

■ RESULTS AND DISCUSSION

Spatiotemporal Focusing of THz Waves through a Scattering Medium. Our first objective is to invert the coherent transfer matrix to obtain a spatiotemporal localized focus spot at the output of the scattering medium, a classical state-of-the-art scenario. Such a task has been explored in the optical and infrared domain both for monochromatic[15,52] and ultrafast pulses,[25,50,57−59] but never tackled for THz fields. In our approach, the realization of a spatiotemporal focus corresponds to imposing the following target field profile in eq 7

$$\tilde{Z}_{\text{target}}(x_o, \omega) = \delta(x_o - x_a)E_a f_a(\omega) \tag{9}$$

where x_a is the desired focus position, and E_a f_a (ω) is the spectrum of the incident THz pulse. Equation 9 targets an output field localized in one spatial point with the same spectral profile as the incident pulse. The results are shown in Figure 3a−c and effectively predict the formation of a sharp focus at the output. Quite remarkably, our amplitude-only optimized wavefront yields a spectral intensity enhancement η (defined as the ratio between the optimized and incident intensity spectral density at a specific frequency) of 78.43 (at 1 THz) at the focus spot (Figure 3b). The field peak (Figure 3c) is enhanced by a factor of 5.10, whereas the field-temporal standard deviation (the transient duration) is compressed by a factor of 4 with respect to the unoptimized case. It is worth stressing that, by observing Figure 3c, not just the pulse is recompressed. As expected from a full-field function reconstruction, the field dynamics are reconstructed locally, similar to Figure 1b. As illustrated in Figure S3, the performance of the optimal pattern is virtually identical to those obtained with standard iterative optimization techniques.[60,61]

Our approach is easily extendable to more challenging conditions, including the formation of separate spatial foci with different spectral profiles. To this end, we generalized eq 7 to the case of two foci by imposing

$$\tilde{Z}_{\text{target}}(x_o, \omega) = \delta(x_o - x_a)E_a f_a(\omega) + \delta(x_o - x_b)E_b f_b(\omega) \tag{10}$$

where x_a and x_b correspond to two different focus locations, and E_a $f_a(\omega)$ and E_b $f_b(\omega)$ denote two distinct spectral profiles, respectively. Our results are shown in Figure 3d,e. When considering identical spectral profiles at the output (Figure 3d, f_a $(\omega) = f_b$ (ω)), we achieved the THz intensity spectral densities of 4.087 GW/m^2/Hz (η = 43.10) and 3.17 GW/m^2/Hz (η = 33.43) at 1 THz and THz peak field enhancements of 3.64 and 3.73, respectively. When considering two different spectral profiles, centered at around 1.3 and 0.7 THz, respectively (Figure 3e), the two foci exhibit intensity spectral densities of 2.74 GW/m^2/Hz (η = 28.94) and 2.43 GW/m^2/Hz (η = 25.63), respectively. For the sake of clarity, we stress here that the two spectral profiles included in eq 10 are different from the incident pulse spectrum.

Deterministic Coherent Control without Previous Knowledge of the Source. The loss function defined in eq 7 targets the spatial distribution of the incident spatial distribution I_{opt} (x') (corresponding to the optical intensity distribution) producing a desired spatiotemporal electric-field distribution $\tilde{Z}_{\text{target}}$ (x_o, ω) at the output. However, one could easily perform waveform synthesis using the experimental measurements of the nonnormalized transfer matrix $\tilde{T}_{\text{exp}}$ (x_o, x', ω) that contains the (generally unknown) incident pulse information (see eq 1). In this approach, the optimization function simply reads as follows

$$\begin{aligned} &\text{f}[I_{\text{opt}}(x')] = \\ &\quad \frac{1}{2}\left\| \int \tilde{T}_{\text{exp}}(x_o, x', \omega) I_{\text{opt}}(x')\text{d}x' - \tilde{Z}_{\text{target}}(x_o, \omega) \right\|_2^2 \\ &\text{subject to } 0 \leq I_{\text{opt}}(x') \leq 1,\ I_{\text{opt}}(x') \in \mathbb{R} \end{aligned} \tag{11}$$

We stress that the optimization routine set by eqs 7 and 11 is field sensitive, and it simultaneously optimizes the amplitude and absolute phase of the transmitted field. This is a radically different scenario from the optical domain, where accessing the absolute phase with arbitrary precision is extremely challenging,

https://doi.org/10.1021/acsphotonics.2c00061
ACS Photonics XXXX, XXX, XXX−XXX

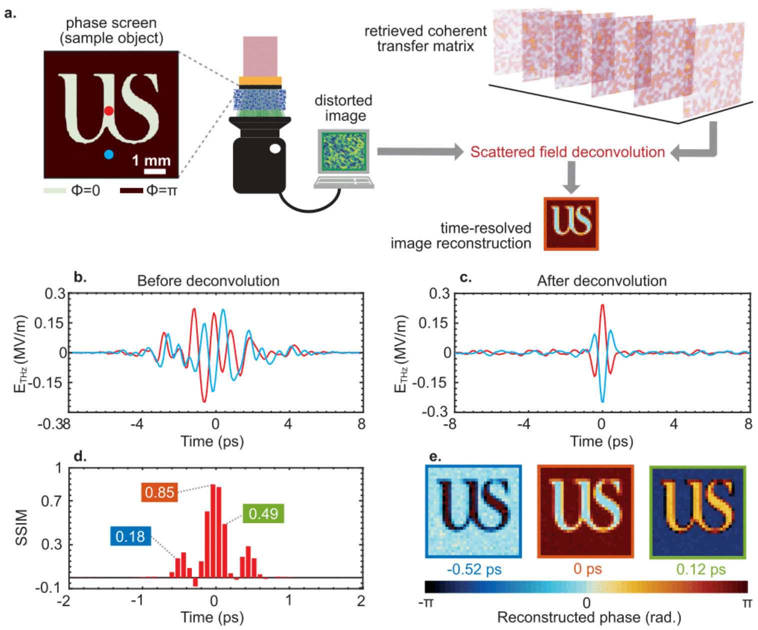

Figure 5. Time-resolved THz phase-sensitive imaging through the scattering medium. (a) Schematic of imaging methodology. Inset: time-resolved reconstruction of the image corresponds to the measurement at $t = 0$ ps in panel (e). (b) Temporal evolution of output speckles corresponding to two different pixels (red and cyan dots shown in panel (a)) before deconvolution. (c) Temporal evolution of reconstructed THz pulse (after deconvolution) for two different pixels (red and cyan dots shown in panel (a)). (d) Structural Similarity (SSIM) index in the time-resolved reconstruction of an image object. (e) Reconstructed phase images at $t = -0.52$, 0, and 0.12 ps. The 6.4×6.4 mm^2 sample illumination area is spatially sampled at 200 μm resolution, corresponding to a number of pixels of 32×32 (see Video S1). Logo used with permission from the University of Sussex.

and waveform synthesis can be attempted only if the absolute phase profile of the input is known beforehand (e.g., in the case of a transform-limited pulse).[50] To illustrate this point, in Figure 4, we report the recompression of a chirped THz pulse obtained without any knowledge of the incident field. As shown in Figure 4g,h, the fitness function from eq 11 is well-suited to convert the initially chirped pulse (Figure 4a,b) into a good approximated version of the transform-limited pulse chosen as a target (Figure 4e,f). Analogous to the case in Figure 3a−c, the electric field is measured in the desired focal spot on the output face of the scatterer.

Time-Resolved Retrieval of Image Object Obscured by a Scattering Medium. The reconstruction of the coherent transmission properties of the scatterer can be directly applied to reconstruct the image of an object concealed by the scattering medium.[62−64] A particular possibility enabled by our full-field methodology is the possibility of performing phase-sensitive reconstruction, i.e., the reconstruction of samples characterized by complex phase profiles.

A numerical implementation of the image reconstruction process is shown in Figure 5a, where we place a phase mask $U(x')$ between the generating crystal and the scattering medium. In the frequency domain, the corresponding transmitted field reads as follows

$$\tilde{M}(x_o, \omega) = \int \tilde{T}_x(x_o, x', \omega) \exp[iU(x')] \tilde{E}^-(x', \omega) \mathrm{d}x' \tag{12}$$

where $\tilde{M}(x_o, \omega)$ is the time-Fourier transform of space−time measurements. To retrieve the original image from the measurements, we perform a standard deconvolution of the retrieved coherent transfer matrix that yields the time-resolved image $E_{\text{retrieved}}$ as

$$E_{\text{retrieved}}(x, t) = F^{-1}\{[\tilde{T}_x(x_o, x', \omega)]^{-1} * \tilde{M}(x_o, \omega)\} \tag{13}$$

where $(*)$ denotes a spatial convolution, F^{-1} is the inverse time-Fourier transform, and $[...]^{(-1)}$ is the inversion operator. As is customary in deconvolution problems, the main task lies in finding the inverse of $\tilde{T}_x(x_o, x', \omega)$. We applied the Moore−Penrose pseudo-inversion method, implemented through a truncated singular-value decomposition.[65] As shown in Figure 5b, before applying the deconvolution routine, the THz pulses corresponding to the two distinct pixels are thoroughly perturbed, representing the multiplexing of waves due to multiple scattering. Figure 5c shows the waves corresponding to two separate pixels (red and cyan dots) after the deconvolution process. We calculated the Structural Similarity (SSIM) index[66] to quantify the quality of the reconstruction process, as shown in Figure 5d. SSIM values obtained at $t = -0.52$, 0, and 0.12 ps in our time reference are 0.18, 0.85, and 0.49, respectively, showing high fidelity in the time-resolved reconstruction of the image. The specific reconstruction results shown in Figure 5e are the fixed-time reconstructed phase images of the transmitted field at the same time values. Analogous results for an amplitude-only object (i.e., a metallic

https://doi.org/10.1021/acsphotonics.2c00061
ACS Photonics XXXX, XXX, XXX−XXX

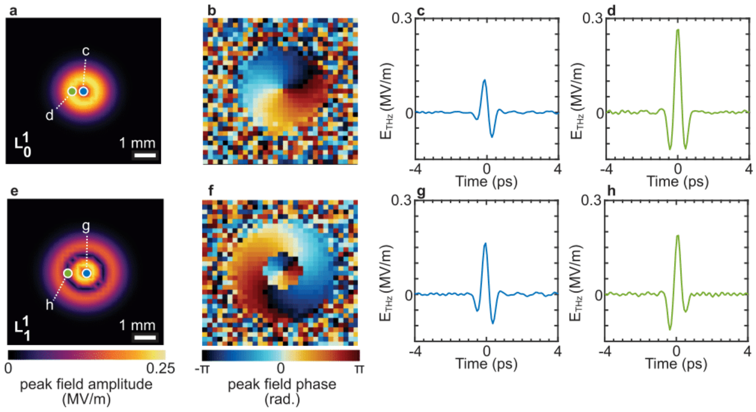

Figure 6. Complex propagation of THz vortex beam through the scattering medium. (a, b) Retrieved spatial field and phase distribution of L_0^1 vortex beam at $t = 0$ ps. (c, d) Temporal profile of the retrieved THz pulse corresponding to two different pixels for the L_0^1 vortex beam in panels (a) and (b). (e–h) Same as panels (a–d) for an L_1^1 vortex beam. The 6.4 × 6.4 mm^2 sample illumination area is spatially sampled at 200 μm resolution, corresponding to a number of pixels of 32 × 32 (see Video S2).

mask) are included in Figure S4. As a final example, we extended our image reconstruction approach for the case of THz vortex beam[67] and simulated the spatiotemporal field-phase profiles for the L_0^1 and L_1^1 beam profiles (see Figure S5). We deconvolved the spatial field-phase information of L_0^1 and L_1^1 THz vortex beams with the complex scrambled output obtained from propagation through the scattering medium. Figure 6 shows their retrieved spatial field-phase profiles at $t = 0$ ps (Figure 6a,b,e,f). In Figure 6c,d,g,h, we report the temporal profile of the retrieved THz field corresponding to the different pixels marked in Figure 6a,b,e,f.

■ CONCLUSIONS

In this work, we have theoretically demonstrated a deterministic approach toward the coherent spatiotemporal control of THz waves propagating through a scattering medium. Our methodology combines the nonlinear conversion of optical patterns to THz structured fields with field-sensitive THz field detection, as enabled by state-of-the-art TDS technology. We have shown how the full-wave detection of the scattered THz field enables retrieving the field-sensitive transfer function of the medium directly in a deterministic fashion, as described through a coherent transfer matrix modeling. We sample the complex time-domain elements of the coherent transfer matrix by projecting a sequence of orthogonal Walsh–Hadamard patterns. The TDS allows for a sufficient description of the coherent transfer matrix to enable spatiotemporal control through a direct inversion approach. We identified the spatial profiles that yield a desired output field distribution through a convex constraint optimization routine compatible with real-life experimental conditions. As relevant examples, we demonstrated the formation of single and multiple spatiotemporal foci and the retrieval of complex field distributions and phase-only images concealed by the scatterer. Our results suggest that it is still possible to investigate the scattering unaffected open path via a time-domain deterministic approach in an experimental-driven constrained scenario. Such control could have a profound impact, especially for THz imaging, where wave shaping is generally a challenge. In addition, we envision a role in time-resolved characterization techniques of complex media, including deep-tissue biological imaging.

■ ASSOCIATED CONTENT

Supporting Information

The Supporting Information is available free of charge at https://pubs.acs.org/doi/10.1021/acsphotonics.2c00061 The datasets for all figures are freely accessible at: http://doi.org/10.6084/m9.figshare.19447112.

Additional theoretical details, methods, and figures (PDF)

Video for the reconstruction of the phase object in Figure 5 (Video S1) (AVI)

Video for the reconstruction of the THz vortex beams in Figure 6 (Video S2) (MP4)

■ AUTHOR INFORMATION

Corresponding Author

Marco Peccianti – *Emergent Photonics Lab (EPic), Department of Physics and Astronomy, University of Sussex, Brighton BN1 9QH, U.K.*; Present Address: Emergent Photonics Research Centre and Dept. of Physics, Loughborough University, Loughborough, LE11 3TU, U.K. email: m.peccianti@lboro.ac.uk; Email: m.peccianti@sussex.ac.uk

Authors

Vivek Kumar – *Emergent Photonics Lab (EPic), Department of Physics and Astronomy, University of Sussex, Brighton BN1 9QH, U.K.*; orcid.org/0000-0002-5165-3541

Vittorio Cecconi – *Emergent Photonics Lab (EPic), Department of Physics and Astronomy, University of Sussex, Brighton BN1 9QH, U.K.*; orcid.org/0000-0002-4054-717X

Luke Peters – *Emergent Photonics Lab (EPic), Department of Physics and Astronomy, University of Sussex, Brighton BN1 9QH, U.K.*; Present Address: Emergent Photonics Research Centre and Dept. of Physics, Loughborough University, Loughborough, LE11 3TU, U.K

https://doi.org/10.1021/acsphotonics.2c00061
ACS Photonics XXXX, XXX, XXX–XXX

Jacopo Bertolotti − *Department of Physics and Astronomy, University of Exeter, Exeter, Devon EX4 4QL, U.K.*
Alessia Pasquazi − *Emergent Photonics Lab (EPic), Department of Physics and Astronomy, University of Sussex, Brighton BN1 9QH, U.K.;* Present Address: Emergent Photonics Research Centre and Dept. of Physics, Loughborough University, Loughborough, LE11 3TU, U.K
Juan Sebastian Totero Gongora − *Emergent Photonics Lab (EPic), Department of Physics and Astronomy, University of Sussex, Brighton BN1 9QH, U.K.;* Present Address: Emergent Photonics Research Centre and Dept. of Physics, Loughborough University, Loughborough, LE11 3TU, U.K; orcid.org/0000-0003-2300-4218

Complete contact information is available at: https://pubs.acs.org/10.1021/acsphotonics.2c00061

Author Contributions

All authors were engaged in the general discussion regarding the basic science of the paper. V.K. performed the calculations reported. All authors contributed to the general understanding of the results and drafting of the paper. J.S.T.G. and M.P supervised the general research activities.

Funding

This project received funding from the European Research Council (ERC) under the European Union's Horizon 2020 Research and Innovation Programme Grant No. 725046. The authors acknowledge financial support from the (UK) Engineering and Physical Sciences Research Council (EPSRC), Grant Nos. EP/S001018/1 and EP/T00097X/1 and the Leverhulme Trust (Early Career Fellowship ECF-2020-537).

Notes

The authors declare no competing financial interest.

■ ACKNOWLEDGMENTS

V.K., V.C., and L.P. acknowledge the support from the European Research Council (ERC) under the European Union's Horizon 2020 Research and Innovation Programme Grant No. 725046. J.S.T.G. acknowledges the support from the Leverhulme Trust (Early Career Fellowship ECF-2020-537).

■ ABBREVIATIONS

THz, terahertz; TDS, time-domain spectroscopy; FROG, frequency-resolved optical gating; SPIDER, spectral phase interferometry for direct electric-field reconstruction; SLM, spatial light modulator; ZnTe, zinc telluride; SNR, signal-to-noise ratio; SSIM, structural similarity index

■ REFERENCES

(1) *Laser Speckle and Related Phenomena*, Dainty, J. C., Ed.; Topics in Applied Physics; Springer-Verlag: Berlin, Heidelberg, 1975.
(2) Sheng, P. *Introduction to Wave Scattering, Localization and Mesoscopic Phenomena*, 2nd ed.; Springer Series in Materials Science; Springer-Verlag: Berlin, Heidelberg, 2006.
(3) Ishimaru, A. *Electromagnetic Wave Propagation, Radiation, and Scattering: From Fundamentals to Applications*, 2nd ed.; Wiley: Hoboken, New Jersey, 2017.
(4) Wax, A.; Backman, V. *Biomedical Applications of Light Scattering*; McGraw-Hill Education, 2010.
(5) Hofer, M.; Soeller, C.; Brasselet, S.; Bertolotti, J. Wide Field Fluorescence Epi-Microscopy behind a Scattering Medium Enabled by Speckle Correlations. *Opt. Express* **2018**, *26*, 9866−9881.
(6) Yoon, S.; Kim, M.; Jang, M.; Choi, Y.; Choi, W.; Kang, S.; Choi, W. Deep Optical Imaging within Complex Scattering Media. *Nat. Rev. Phys.* **2020**, *2*, 141−158.
(7) Booth, M. J. Adaptive Optics in Microscopy. *Philos. Trans. R. Soc., A* **2007**, *365*, 2829−2843.
(8) Hsu, C. W.; Liew, S. F.; Goetschy, A.; Cao, H.; Douglas Stone, A. Correlation-Enhanced Control of Wave Focusing in Disordered Media. *Nat. Phys.* **2017**, *13*, 497−502.
(9) Mosk, A. P.; Lagendijk, A.; Lerosey, G.; Fink, M. Controlling Waves in Space and Time for Imaging and Focusing in Complex Media. *Nat. Photonics* **2012**, *6*, 283−292.
(10) Vellekoop, I. M.; Mosk, A. P. Universal Optimal Transmission of Light Through Disordered Materials. *Phys. Rev. Lett.* **2008**, *101*, No. 120601.
(11) Horstmeyer, R.; Ruan, H.; Yang, C. Guidestar-Assisted Wavefront-Shaping Methods for Focusing Light into Biological Tissue. *Nat. Photonics* **2015**, *9*, 563−571.
(12) Judkewitz, B.; Horstmeyer, R.; Vellekoop, I. M.; Papadopoulos, I. N.; Yang, C. Translation Correlations in Anisotropically Scattering Media. *Nat. Phys.* **2015**, *11*, 684−689.
(13) Popoff, S. M.; Lerosey, G.; Carminati, R.; Fink, M.; Boccara, A. C.; Gigan, S. Measuring the Transmission Matrix in Optics: An Approach to the Study and Control of Light Propagation in Disordered Media. *Phys. Rev. Lett.* **2010**, *104*, No. 100601.
(14) Andreoli, D.; Volpe, G.; Popoff, S.; Katz, O.; Grésillon, S.; Gigan, S. Deterministic Control of Broadband Light through a Multiply Scattering Medium via the Multispectral Transmission Matrix. *Sci. Rep.* **2015**, *5*, No. 10347.
(15) Yu, H.; Lee, K.; Park, Y. Ultrahigh Enhancement of Light Focusing through Disordered Media Controlled by Mega-Pixel Modes. *Opt. Express* **2017**, *25*, 8036−8047.
(16) Tao, X.; Bodington, D.; Reinig, M.; Kubby, J. High-Speed Scanning Interferometric Focusing by Fast Measurement of Binary Transmission Matrix for Channel Demixing. *Opt. Express* **2015**, *23*, 14168−14187.
(17) Mariani, F.; Löffler, W.; Aas, M.; Ojambati, O. S.; Hong, P.; Vos, W. L.; van Exter, M. P. Scattering Media Characterization with Phase-Only Wavefront Modulation. *Opt. Express* **2018**, *26*, No. 2369.
(18) Mounaix, M.; Defienne, H.; Gigan, S. Deterministic Light Focusing in Space and Time through Multiple Scattering Media with a Time-Resolved Transmission Matrix Approach. *Phys. Rev. A* **2016**, *94*, No. 041802.
(19) Pasquazi, A.; Peccianti, M.; Razzari, L.; Moss, D. J.; Coen, S.; Erkintalo, M.; Chembo, Y. K.; Hansson, T.; Wabnitz, S.; Del'Haye, P.; Xue, X.; Weiner, A. M.; Morandotti, R. Micro-Combs: A Novel Generation of Optical Sources. *Phys. Rep.* **2018**, *729*, 1−81.
(20) Trebino, R.; DeLong, K. W. K. W.; Fittinghoff, D. N. D. N.; Sweetser, J. N.; Krumbügel, M. A.; Richman, B. B. A.; Kane, D. J. D. J.; Krumbügel, M. Measuring Ultrashort Laser Pulses in the Time-Frequency Domain Using Frequency-Resolved Optical Gating. *Rev. Sci. Instrum.* **1997**, *68*, 3277.
(21) Akturk, S.; Kimmel, M.; O'Shea, P.; Trebino, R. Measuring Pulse-Front Tilt in Ultrashort Pulses Using GRENOUILLE. *Opt. Express* **2003**, *11*, 491−501.
(22) Iaconis, C.; Walmsley, Ia. Spectral Phase Interferometry for Direct Electric-Field Reconstruction of Ultrashort Optical Pulses. *Opt. Lett.* **1998**, *23*, 792−794.
(23) Beard, M. C.; Turner, G. M.; Schmuttenmaer, C. A. Terahertz Spectroscopy. *J. Phys. Chem. B* **2002**, *106*, 7146−7159.
(24) Neu, J.; Schmuttenmaer, C. A. Tutorial: An Introduction to Terahertz Time Domain Spectroscopy (THz-TDS). *J. Appl. Phys.* **2018**, *124*, No. 231101.
(25) Mounaix, M.; Fontaine, N. K.; Neilson, D. T.; Ryf, R.; Chen, H.; Alvarado-Zacarias, J. C.; Carpenter, J. Time Reversed Optical Waves by Arbitrary Vector Spatiotemporal Field Generation. *Nat. Commun.* **2020**, *11*, No. 5813.
(26) Fink, M. Time-Reversal Acoustics. *J. Phys.: Conf. Ser.* **2008**, *118*, No. 012001.

(27) Lerosey, G.; de Rosny, J.; Tourin, A.; Derode, A.; Montaldo, G.; Fink, M. Time Reversal of Electromagnetic Waves. *Phys. Rev. Lett.* **2004**, *92*, No. 193904.
(28) Ulrich, T. J.; Johnson, P. A.; Sutin, A. Imaging Nonlinear Scatterers Applying the Time Reversal Mirror. *J. Acoust. Soc. Am.* **2006**, *119*, 1514−1518.
(29) Chen, Q.; Song, H.; Yu, J.; Kim, K. Current Development and Applications of Super-Resolution Ultrasound Imaging. *Sensors* **2021**, *21*, No. 2417.
(30) Pearce, J.; Mittleman, D. M. Propagation of Single-Cycle Terahertz Pulses in Random Media. *Opt. Lett.* **2001**, *26*, 2002−2004.
(31) Pearce, J.; Mittleman, D. M. Scale Model Experimentation: Using Terahertz Pulses to Study Light Scattering. *Phys. Med. Biol.* **2002**, *47*, 3823−3830.
(32) Gentilini, S.; Missori, M.; Ghofraniha, N.; Conti, C. Terahertz Radiation Transport in Photonic Glasses. *Ann. Phys.* **2020**, *532*, No. 2000005.
(33) Kaushik, M.; Ng, B. W.-H.; Fischer, B. M.; Abbott, D. Terahertz Scattering by Granular Composite Materials: An Effective Medium Theory. *Appl. Phys. Lett.* **2012**, *100*, No. 011107.
(34) Born, P.; Holldack, K. Analysis of Granular Packing Structure by Scattering of THz Radiation. *Rev. Sci. Instrum.* **2017**, *88*, No. 051802.
(35) Watts, C. M.; Shrekenhamer, D.; Montoya, J.; Lipworth, G.; Hunt, J.; Sleasman, T.; Krishna, S.; Smith, D. R.; Padilla, W. J. Terahertz Compressive Imaging with Metamaterial Spatial Light Modulators. *Nat. Photonics* **2014**, *8*, 605−609.
(36) Stantchev, R. I.; Sun, B.; Hornett, S. M.; Hobson, P. A.; Gibson, G. M.; Padgett, M. J.; Hendry, E. Noninvasive, near-Field Terahertz Imaging of Hidden Objects Using a Single-Pixel Detector. *Sci. Adv.* **2016**, *2*, No. e1600190.
(37) Shen, Y. C.; Gan, L.; Stringer, M.; Burnett, A.; Tych, K.; Shen, H.; Cunningham, J. E.; Parrott, E. P. J.; Zeitler, J. A.; Gladden, L. F.; Linfield, E. H.; Davies, A. G. Terahertz Pulsed Spectroscopic Imaging Using Optimized Binary Masks. *Appl. Phys. Lett.* **2009**, *95*, No. 231112.
(38) Chan, W. L.; Charan, K.; Takhar, D.; Kelly, K. F.; Baraniuk, R. G.; Mittleman, D. M. A Single-Pixel Terahertz Imaging System Based on Compressed Sensing. *Appl. Phys. Lett.* **2008**, *93*, No. 121105.
(39) Lemoult, F.; Lerosey, G.; de Rosny, J.; Fink, M. Manipulating Spatiotemporal Degrees of Freedom of Waves in Random Media. *Phys. Rev. Lett.* **2009**, *103*, No. 173902.
(40) Olivieri, L.; Totero Gongora, J. S.; Pasquazi, A.; Peccianti, M. Time-Resolved Nonlinear Ghost Imaging. *ACS Photonics* **2018**, *5*, 3379−3388.
(41) Olivieri, L.; Gongora, J. S. T.; Peters, L.; Cecconi, V.; Cutrona, A.; Tunesi, J.; Tucker, R.; Pasquazi, A.; Peccianti, M. Hyperspectral Terahertz Microscopy via Nonlinear Ghost Imaging. *Optica* **2020**, *7*, 186−191.
(42) Totero Gongora, J. S.; Olivieri, L.; Peters, L.; Tunesi, J.; Cecconi, V.; Cutrona, A.; Tucker, R.; Kumar, V.; Pasquazi, A.; Peccianti, M. Route to Intelligent Imaging Reconstruction via Terahertz Nonlinear Ghost Imaging. *Micromachines* **2020**, *11*, No. 521.
(43) Harwit, M.; Sloane, N. J. A. *Hadamard Transform Optics*; Academic Press: New York, 1979.
(44) Bertero, M.; Boccacci, M.; De Mol, C. *Introduction to Inverse Problems in Imaging*, 2nd ed.; CRC Press/Francis and Taylor: Boca Raton, 2021.
(45) van Beijnum, F.; Putten, E. G. van.; Lagendijk, A.; Mosk, A. P. Frequency Bandwidth of Light Focused through Turbid Media. *Opt. Lett.* **2011**, *36*, 373−375.
(46) Rotter, S.; Gigan, S. Light Fields in Complex Media: Mesoscopic Scattering Meets Wave Control. *Rev. Mod. Phys.* **2017**, *89*, No. 015005.
(47) Goodman, J. W. *Statistical Optics*; John Wiley & Sons, 2015.
(48) Garcia, N.; Stoll, E. Monte Carlo Calculation for Electromagnetic-Wave Scattering from Random Rough Surfaces. *Phys. Rev. Lett.* **1984**, *52*, 1798−1801.
(49) Berkovits, R.; Feng, S. Correlations in Coherent Multiple Scattering. *Phys. Rep.* **1994**, *238*, 135−172.
(50) Mounaix, M.; Andreoli, D.; Defienne, H.; Volpe, G.; Katz, O.; Grésillon, S.; Gigan, S. Spatiotemporal Coherent Control of Light through a Multiple Scattering Medium with the Multispectral Transmission Matrix. *Phys. Rev. Lett.* **2016**, *116*, No. 253901.
(51) Goodman, P. J. *Speckle Phenomena in Optics*; W. H. Freeman: Englewood, Colo, 2010.
(52) Conkey, D. B.; Caravaca-Aguirre, A. M.; Piestun, R. High-Speed Scattering Medium Characterization with Application to Focusing Light through Turbid Media. *Opt. Express* **2012**, *20*, 1733−1740.
(53) Zhao, J.; E, Y.; Williams, K.; Zhang, X.-C.; Boyd, R. W. Spatial Sampling of Terahertz Fields with Sub-Wavelength Accuracy via Probe-Beam Encoding. *Light: Sci. Appl.* **2019**, *8*, No. 55.
(54) Blanchard, F.; Doi, A.; Tanaka, T.; Tanaka, K. Real-Time, Subwavelength Terahertz Imaging. *Annu. Rev. Mater. Res.* **2013**, *43*, 237−259.
(55) Naftaly, M. Metrology Issues and Solutions in THz Time-Domain Spectroscopy: Noise, Errors, Calibration. *IEEE Sens. J.* **2013**, *13*, 8−17.
(56) Moré, J. J.; Sorensen, D. C. Computing a Trust Region Step. *SIAM J. Sci. Stat. Comput.* **1983**, *4*, 553−572.
(57) McCabe, D. J.; Tajalli, A.; Austin, D. R.; Bondareff, P.; Walmsley, I. A.; Gigan, S.; Chatel, B. Spatio-Temporal Focusing of an Ultrafast Pulse through a Multiply Scattering Medium. *Nat. Commun.* **2011**, *2*, No. 447.
(58) Katz, O.; Small, E.; Bromberg, Y.; Silberberg, Y. Focusing and Compression of Ultrashort Pulses through Scattering Media. *Nat. Photonics* **2011**, *5*, 372−377.
(59) Calba, C.; Méès, L.; Rozé, C.; Girasole, T. Ultrashort Pulse Propagation through a Strongly Scattering Medium: Simulation and Experiments. *J. Opt. Soc. Am. A* **2008**, *25*, 1541−1550.
(60) Bonyadi, M. R.; Michalewicz, Z. Particle Swarm Optimization for Single Objective Continuous Space Problems: A Review. *Evol. Comput.* **2017**, *25*, 1−54.
(61) Mitchell, M. *An Introduction to Genetic Algorithms: Complex Adaptive Systems*; A Bradford Book: Cambridge, MA, USA, 1996.
(62) Satat, G.; Heshmat, B.; Raviv, D.; Raskar, R. All Photons Imaging Through Volumetric Scattering. *Sci. Rep.* **2016**, *6*, No. 33946.
(63) Bertolotti, J.; van Putten, E. G.; Blum, C.; Lagendijk, A.; Vos, W. L.; Mosk, A. P. Non-Invasive Imaging through Opaque Scattering Layers. *Nature* **2012**, *491*, 232−234.
(64) Kim, K.; Somkuwar, A. S.; Park, Y.; Singh, R. K. Imaging through Scattering Media Using Digital Holography. *Opt. Commun.* **2019**, *439*, 218−223.
(65) Penrose, R. A Generalized Inverse for Matrices. *Math. Proc. Cambridge Philos. Soc.* **1955**, *51*, 406−413.
(66) Wang, Z.; Bovik, A. C.; Sheikh, H. R.; Simoncelli, E. P. Image Quality Assessment: From Error Visibility to Structural Similarity. *IEEE Trans. Image Process.* **2004**, *13*, 600−612.
(67) Lin, Q.; Zheng, S.; Song, Q.; Zeng, X.; Cai, Y.; Li, Y.; Chen, Z.; Zha, L.; Pan, X.; Xu, S. Generation of Terahertz Vortex Pulses without Any Need of Manipulation in the Terahertz Region. *Opt. Lett.* **2019**, *44*, 887−890.

https://doi.org/10.1021/acsphotonics.2c00061
ACS Photonics XXXX, XXX, XXX−XXX

Supplementary Information

Deterministic Terahertz wave control in scattering media

Vivek Kumar[1], Vittorio Cecconi[1], Luke Peters[1], Jacopo Bertolotti[2], Alessia Pasquazi[1], Juan Sebastian Totero Gongora, Marco Peccianti[1*]

[1] Emergent Photonics Lab (EP*ic*), Department of Physics and Astronomy, University of Sussex, Brighton, BN1 9QH, U.K.

[2] Department of Physics and Astronomy, University of Exeter, Exeter, Devon EX4 4QL, UK

The Supplementary Information comprises 5 pages and 5 figures.

Supplementary Note 1. Estimation of the spectral correlation bandwidth

We estimated our spectral correlation $\Delta\nu_c$ based on the experimental measurements included in Refs[2–4]. These are seminal works in the study of THz pulse propagation in random media and entail samples composed of closely packed, random collections of Teflon spheres in Teflon cuvettes. Teflon has significantly low absorption in the 0.1-2 THz frequency range of interest to our work, and the spheres have an average radius of ~0.8 mm. In their works, Pearce et al. have reported mean-free-paths of l_s~1-100 mm for samples thickness in the range 1-20 mm and characterized by strong forward scattering (g~1) [2–4]. These quantities correspond to spectral correlation widths in the range from 100 GHz to 500 GHz, as computed with the standard formula $\Delta\nu_c$=2.92$\pi D/L^2$ [5]. Our particular choice of $\Delta\nu_c$=150 GHz in the revised manuscript was dictated by numerical considerations in the generation of Gaussian-correlated random noise.

Supplementary Note 2. Reconstruction of the coherent transfer matrix

The reconstruction of the coherent transfer matrix can be generally performed by sampling the input-output relation with a series of orthogonal functions. The Walsh-Hadamard basis represents a canonical example known to provide a higher signal to noise (SNR) ratio compared to single-pixel, raster-scan illumination.[1] The general form of the coherent transfer matrix at particular frequency ω is given by:

$$\widetilde{\boldsymbol{T}}(\omega) = \begin{bmatrix} \tilde{T}_{11}(\omega) & \cdots & \tilde{T}_{1N}(\omega) \\ \vdots & \ddots & \vdots \\ \tilde{T}_{N1}(\omega) & \cdots & \tilde{T}_{NN}(\omega) \end{bmatrix} \tag{S1}$$

where $\tilde{T}_{ij}(\omega)$ is the complex-valued field propagator that connects j-th input mode and i-th output pixel and we assume that the transfer matrix is a $N \times N$ square matrix for simplicity. In the presence of broadband illumination, the incident field for a given pattern is expressed as:

$$\tilde{E}_n^-(\omega) = h_p^{\pm} f(\omega), \tag{S2}$$

where $f(\omega)$ is the THz pulse spectral profile. The spatial profiles $h_p^{\pm}$ are defined as follows:

$$h_p^{\pm} = \frac{1}{2} \pm \frac{1}{2} H_p, \tag{S3}$$

where H_P is the p-th column of the $N \times N$ Walsh-Hadamard matrix $\boldsymbol{H}$. With this approach, the corresponding output vectors for each binary pattern $\tilde{c}_p^+(\omega)$ and $\tilde{c}_p^-(\omega)$ can be acquired by performing the Fourier transform of the time-resolved measurements obtained from TDS. In an analogous fashion to differential ghost-imaging approaches, the coefficient corresponding to the p-th Walsh-Hadamard pattern is simply expressed as:

$$\tilde{c}_p(\omega) = \tilde{c}_p^+(\omega) - \tilde{c}_p^-(\omega) \tag{S4}$$

For each frequency, the differential signals are stacked into a measurement matrix $\widetilde{\boldsymbol{M}}(\omega) \in \mathbb{C}^{N\times N}$, and the transfer matrix elements can be obtained by a linear inversion of $\widetilde{\boldsymbol{M}}(\omega)$ for each frequency. In practical terms, the inversion can be obtained in two ways. The simplest approach is to take into account the orthogonality of the Walsh-Hadamard matrix as follows:

$$\widetilde{\boldsymbol{T}}_{reconstructed}(\omega_k) = \frac{1}{f(\omega_k)} \widetilde{\boldsymbol{M}}(\omega_k)\boldsymbol{H} \tag{S5}$$

Due to the presence of noise, however, the inversion is more precisely calculated in a least-square fashion as follows:

$$\widetilde{\boldsymbol{T}}_{reconstructed}(\omega_k) = \mathrm{argmin}_{\boldsymbol{T}\in\mathbb{C}^{N\times N}} \left\| \boldsymbol{T} - \frac{1}{f(\omega_k)} \widetilde{\boldsymbol{M}}(\omega_k)\boldsymbol{H} \right\|^2 \tag{S6}$$

In Figure 2 of the main text we quantitatively estimated the robustness of our approach against additive noise at the detection by computing the Mean Square Error (MSE) of our reconstruction for different values of the detection SNR. The MSE is defined as:

$$MSE(\omega_k) = \frac{1}{N} \left\| \widetilde{\boldsymbol{T}}_{reconstructed}(\omega_k) - \widetilde{\boldsymbol{T}}(\omega_k) \right\|_F^2 = \frac{1}{N} \sum_m \sum_n \left| \widetilde{\boldsymbol{T}}_{reconstructed,mn}(\omega_k) - \widetilde{\boldsymbol{T}}_{mn}(\omega_k) \right|^2 \tag{S7}$$

where $\|\ldots\|_{\mathrm{F}}$ is the Frobenius norm. We compared the MSE values for raster scan and Walsh-Hadamard decomposition (Fig 2 of the main text). As a direct comparison, in Figure S2 we report the same analysis for a single-pixel, raster scan measurement of the transfer matrix elements for different values of the detection SNR.

Supplementary Figures

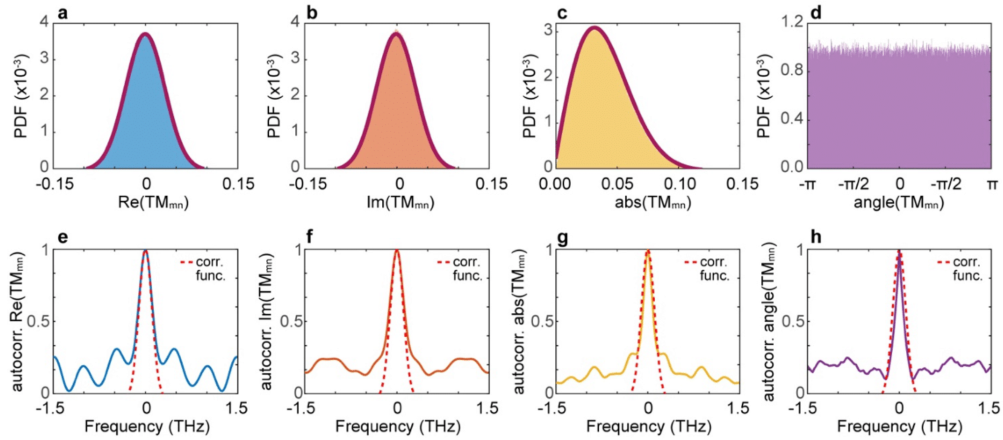

Figure S1: Histograms (Probability density function) and spectral autocorrelation functions for the real part (panels **a,e**), imaginary part (panels **b,f**), amplitude (panels **c,g**), and phase (panels **d,h**) of the transfer matrix elements. The histograms correspond to a single frequency, while the autocorrelation functions are computed for a single pixel. The red lines represent the expected statistical distributions for a circular random Gaussian distribution (Gaussian for the real and imaginary parts, Rayleigh for the amplitudes, and uniform for the phases). In panels **e-h**, the red dotted line is the Gaussian spectral correlation function with a standard deviation of 150 GHz applied to the transfer matrix elements.

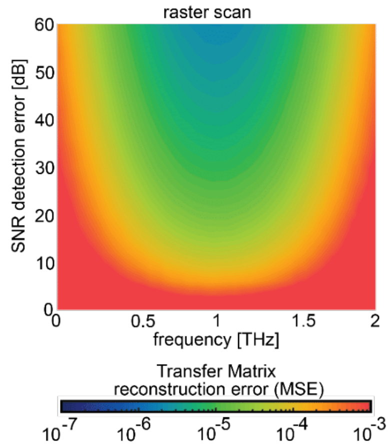

Figure S2: Mean Square Error in the retrieval of coherent transfer matrix using a raster scan reconstruction.

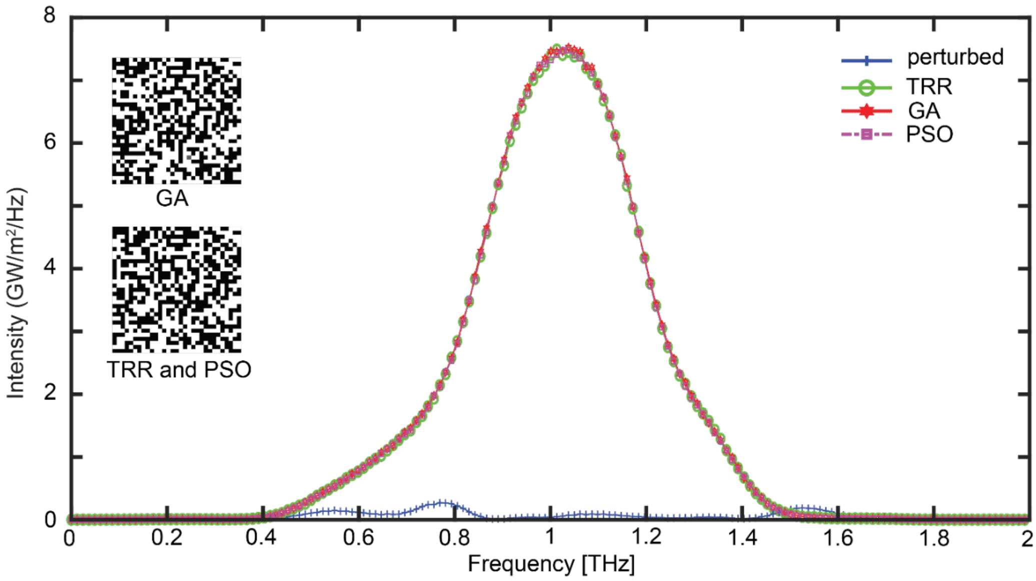

Figure S3. Performance analysis of spatiotemporal focusing of THz waves using Trust-Region-Reflective (TRR), Genetic algorithm (GA) and Particle Swarm Optimisation (PSO) for constraint inversion of the coherent transfer matrix. Optimized intensity spectral density at the focus spot obtained from TRR, GA and PSO (blue: scattered intensity, green circle: using TRR, red star: using GA and pink square: using PSO). Unlike to the GA, TRR and PSO are conversing to the same binary-based pattern solution as shown in the Inset: Optimized binary-based pattern (black: 0, white: 1).

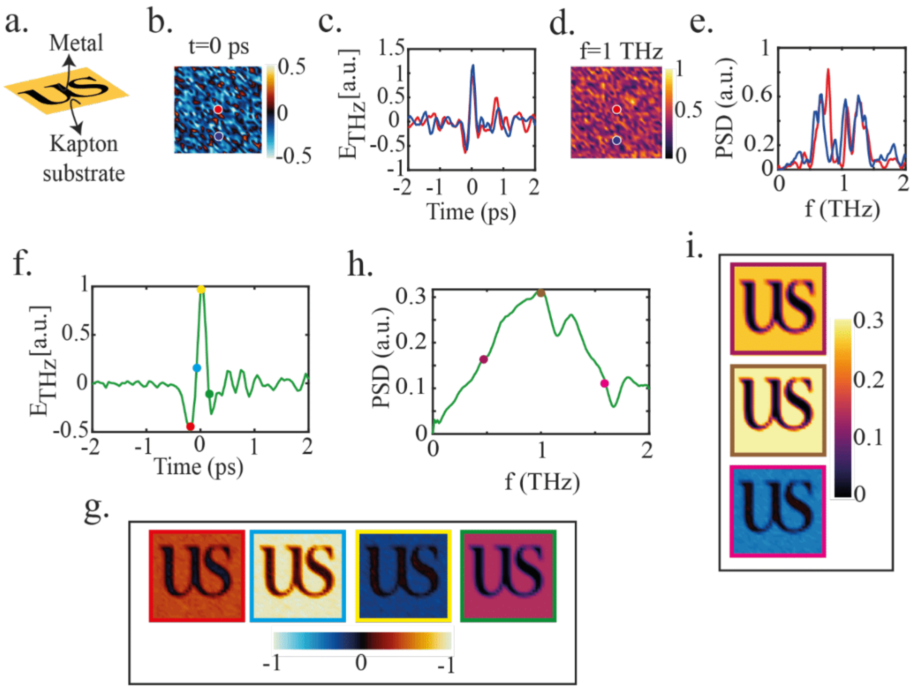

Figure S4: Hyperspectral THz imaging through the scattering medium. **a.** Schematic of metallic image object. **b.** Interference pattern formed at the output after propagation through the scattering medium. **c.** Temporal evolution of output speckle corresponding to two different pixels. **d.** Spectral intensity distribution of scrambled image object propagated through medium at 1 THz. **e.** Intensity profile of output speckle corresponding to two different pixels. **f.** Temporal evolution of reconstructed image object averaged over all the pixels. **g.** Fix time retrieval of images at -0.31 ps, -0.26 ps, 0 ps and 0.17 ps. **h**. The spatially averaged reconstruction of THz spectrum. **i.** Retrieved hyperspectral images at 0.55 THz, 1 THz and 1.55 THz. The 6.4×6.4 mm^2 sample illumination area is spatially sampled at 200 µm resolution. Logo used with permission from the University of Sussex.

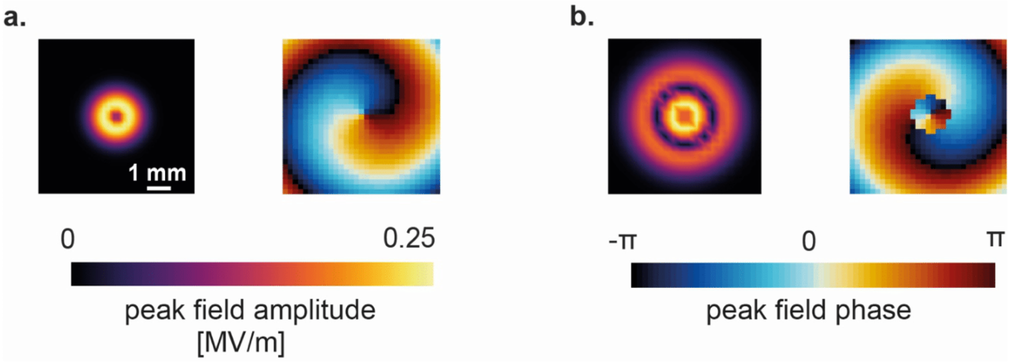

Figure S5: Simulated L_0^1 and L_1^1 THz vortex beams. a. Spatial field and phase distribution for radial index 0 and topological charge 1. **b.** Spatial field and phase profiles for radial index 1 and topological charge 1. THz vortex beams are plotted at the peak of the THz pulse after propagation of 0.5 mm in free space. The 6.4×6.4 mm^2 sample illumination area is spatially sampled at 200 µm resolution.

REFERENCES

(1) Streeter, L.; Burling-Claridge, G. R.; Cree, M. J.; Künnemeyer, R. Optical Full Hadamard Matrix Multiplexing and Noise Effects. *Applied optics* **2009**, *48* (11), 2078–2085.

(2) Pearce, J.; Mittleman, D. M. Propagation of Single-Cycle Terahertz Pulses in Random Media. *Opt. Lett., OL* **2001**, *26* (24), 2002–2004. https://doi.org/10.1364/OL.26.002002.

(3) Pearce, J.; Jian, Z.; Mittleman, D. M. Statistics of Multiply Scattered Broadband Terahertz Pulses. *Phys. Rev. Lett.* **2003**, *91* (4), 043903. https://doi.org/10.1103/PhysRevLett.91.043903.

(4) Pearce, J. Multiple Scattering of Broadband Terahertz Pulses. PhD Thesis, Rice University, 2005.

(5) Aulbach, J.; Gjonaj, B.; Johnson, P. M.; Mosk, A. P.; Lagendijk, A. Control of Light Transmission through Opaque Scattering Media in Space and Time. *Phys. Rev. Lett.* **2011**, *106* (10), 103901. https://doi.org/10.1103/PhysRevLett.106.103901.

Chapter 4: Experimental Spatiotemporal Superfocusing of Ultrafast Terahertz Pulses through Scattering Media

This chapter will present an experimental investigation of broadband, spatiotemporal focusing of ultrafast terahertz pulses in random media. The experiment combines state-of-the-art nonlinear wavefront shaping of terahertz waves with evolutionary optimisation techniques suitable for the typical measurement conditions of terahertz time-domain spectroscopy. The art coherently enables the detection of the full-wave properties of the scattered field, and it allows for the optimisation of the spatiotemporal properties of the transmitted field, a challenging task at optical and infrared frequencies. In this work, I will show that by tailoring the optical spatial intensity distribution, it is possible to achieve a spatiotemporal superfocusing at terahertz frequencies by accessing the internal modes of a random system.

4.1 Introduction

The physics of wave propagation in multiple scattering environments has been of interest in various domains ranging, for instance, from solid-state physics to optics or seismology, whether in quantum or classical regimes [121–125]. The study of statistical moments of the wave amplitude introduced many physical parameters such as the mean free path (i.e., the average distance over which a moving particle travels before substantially changing its direction or energy), the diffusion constant (i.e., physical constant that depends on the scatterer size and other properties of the diffusing substance), and the dimensionless conductance (alias, Thouless factor), which all are relevant concepts regardless of the type of wave considered.

Figure 4.1 Conceptual figure of a THz pulse propagating throughout a random media.

Empirical manifestations of multiple scattering in diffusive regimes, such as coherent backscattering, long-range correlation, and wave localisation, have also been observed for different kinds of waves [5,126–128]. In that respect, in the last two decades, scientists working in the field of photonics have taken inspiration from the previous theoretical concepts, bringing original possibilities to the study of multiple scattering. Indeed, when light propagates in an inhomogeneous medium, its wavefront is scattered and distorted due to multiple scattering. It is well acknowledged how multiple scattering can severely impact the transmitted field's features, hindering, for example, the ability to reconstruct images of an object. Indeed, the structural disorder is commonly perceived as detrimental in optics, as it is classically associated with unpredictability and decay of information. However, researchers have demonstrated that disordered media can be utilised in developing optical devices with outstanding imaging performances [94,96]. Indeed, the demonstration that an optimised spatial illumination pattern would reduce the distortion induced by the scattering medium opened a new class of spatial field manipulation methodologies [38]. Adaptive and computational imaging process based on iterative approaches has been successfully applied to the reconstruction of different field features after propagation in scattering media [129–131]. Indeed, in scattering conditions, light propagation produces complex speckle patterns that have a nontrivial connection to the incident wavefront. Many approaches have been proposed to determine the optimal pattern configuration either by feedback-driven optimisation [132–134], applying optical phase conjugation techniques [135,136], or probing the medium transmission matrix, which describes the transmission properties of random systems [137,138]. While the spatial focusing of monochromatic light has been extensively demonstrated, current research tackled the nontrivial problem of disorder-induced temporal broadening, an inherent challenge connected to the propagation of ultrashort broadband pulses [46,139,140]. When considering non-monochromatic waves, multiple scattering effects induce significant temporal distortions of the pulse shape and several forms of spectral aberrations [141,142]. Quite interestingly, recent results have suggested that the intrinsic spatiotemporal coupling induced by the scattering medium enables controlling the temporal properties of the scattered field by addressing only the spatial degrees of freedom at the input [143,144] (i.e., the incident wavefront profile). Despite these remarkable achievements, not many studies to date have reported a coherent, full-wave (field and phase) empirical characterisation and functionalisation of random media, as at optical frequencies accessing the time-domain full-field properties of the scattered field is remarkably challenging. In the art of optical frequencies, the combination of interferometric setups and tuneable monochromatic sources has been employed to infer the complex spectral properties of the transmitted field; however, these measurements are still incoherent [38]. Interestingly, optical frequency combs can be exploited to provide indirect access to temporal field properties [145].

In this chapter, I will show an experimental demonstration of the possibility of allowing complete space-time control at terahertz (THz) photonics, where time-resolved, field-sensitive detection is well-established [146], via the time-domain spectroscopy (TDS) approach. Based on the current theoretical framework discussed in Refs. [147,148], I will show the ability of THz-TDS to detect the broadband, full-field properties of a transmitted pulse, representing a different methodology to gain information about the scattering properties [67]. The application of THz-TDS to the modelling of random-material properties of scattered media is a relatively new field [85], although pioneering works explored the subject several years ago [149].

The possibility of implementing a field-based wavefront control methodology for scattering media is mainly unexplored.

4.2 Discussion

This work provides an experimental study of time-resolved, field-sensitive detection in spatiotemporal focusing of broadband THz pulses using scattering media. Specifically, I combined the nonlinear generation of THz patterns from structured optical beams with an evolutionary optimisation feedback loop to focus an ultrafast THz pulse spatially (i.e., throughout a pinhole at the output of the scattering medium) and temporally (i.e., compressing the pulse in time). The method relies on the Time-domain Nonlinear Ghost Imaging (TNGI) methodology [113,114,150] and is universally applicable to complex objects. With solely a spatial amplitude control, I prove control over the scattering field and manage to focus the radiation inside a sub-wavelength pinhole at the output of the scattering medium [67]. One way to model the transmission properties of the medium is to define a dispersive transmission operator $TM(x, y, \omega)$ [151] [147,152], and for the sake of simplicity, I limit a scalar description, but a more general approach could be extended to a full-vector formulation [153]. By defining the input field distribution $E^{-}(x, y, \omega)$, and the field transmitted through the scatterer $E^{+}(x, y, \omega)$, it is possible to express

$$E^{+}(x, y, \omega) = \int dx'dy'\, TM(x - x', y - y', \omega)\, E^{-}(x', y', \omega). \tag{4.1}$$

Thus, the optical wavefront control aims to identify the optimal incident field distribution $E^{-}_{optimal}(x, y, t)$ which produces the desired output field $E^{+}_{target}(x, y, t)$ after the scatterer [9]. When operating at THz frequencies, the ability to control the incident electric field distribution is hindered by the limited availability of spatial light modulators (SLM) devices at those frequencies. To overcome this limitation, it is possible to obtain the desired terahertz field distribution through the nonlinear conversion of structured optical beams, an approach I have developed in TNGI [113–115]. Hence, any optical pattern generated through a standard SLM device can act as a direct source of THz patterns. Indeed, by considering a nonlinear quadratic process generated by a 1 mm thick Zinc Telluride crystal, the relation between incident optical intensity and generated THz field is expressed as

$$E_{THz}(x,y) \propto \chi^{(2)} I_{pump}(x,y), \tag{4.2}$$

enabling precise control over the THz field profile by simply shaping the incident optical pulse. A key advantage of this methodology is that the spatial resolution of the THz patterns can go below the THz wavelength, as it is only bound by the diffraction limit of the optical beam. Besides, the nonlinear conversion ensures that the spatial pattern is well-defined across the whole THz band, enabling the generation and control of single-cycle, THz structured beams.

The objective is to manipulate the full-field properties of the transmitted THz pulse in a specific pixel of the output plane by placing a spatial pinhole at the output facet of the scatterer, corresponding to the desired focal spot (x_0, y_0). To optimise the wavefront of the transmitted pulse, the collected THz field from an ensemble of patterns is analysed and ranked through an optimisation algorithm (e.g., a Genetic Algorithm (GA)) that provides the feedback required to optimise the transmitted field iteratively. At the output of the scattering medium, I place a pinhole at a *2f-2f* imaging condition relative to the TDS detection. Therefore, the transmitted THz pulses are coherently sampled via a standard electro-optic sampling detection (i.e., detection crystal ZnTe). Notably, the configuration enables an optimisation feedback loop that considers the temporal field properties instead of average intensity, as is generally the case when operating at optical frequencies. Also, the near-field THz provides a significant advantage in terms of available degrees of freedom. The THz field can be densely sampled in space, with patterns of sub-wavelength spatial resolution.

Fitness function	*Definition*	*Optimisation*
A	$\dfrac{\max(E_0(t))}{\sigma[E_0(t)]}$	Spatiotemporal focusing
B	$-\ min(E_0(t))$	Phase inversion
C	$-\lvert\mu[E_0(t)] - t_0\rvert$	Time-shift

Table 4.1 The set of cost functions used in the GA. In all these expressions, the electric field is measured in the desired focal point, i.e. $E_0(t) \equiv E(x_0, y_0, t)$, *and* (x_0, y_0) *coincide with the spatial probe overlap,* $\mu[E_0(t)]$ *and* $\sigma(E_0(t))$ *is the first and second moments of the probability distribution defined by* $|E(t)|$.

This advantage makes the framework very different from typical optical embodiments, where the spatial sampling is limited by the numerical aperture of the illumination [154]. Moreover, the methodology iteratively seeks the optimal pattern by shaping the incident wavefronts by defining a target function used as a feedback cost function for the GA [147]. I performed the experiment using samples of float-zone (high resistivity) silicon flakes (around 150 µm diameter) embedded in paraffin wax. Silicon is almost transparent at THz frequencies, making the scattering media contribution less absorbing. The samples have an 8% Silicon mass fraction.

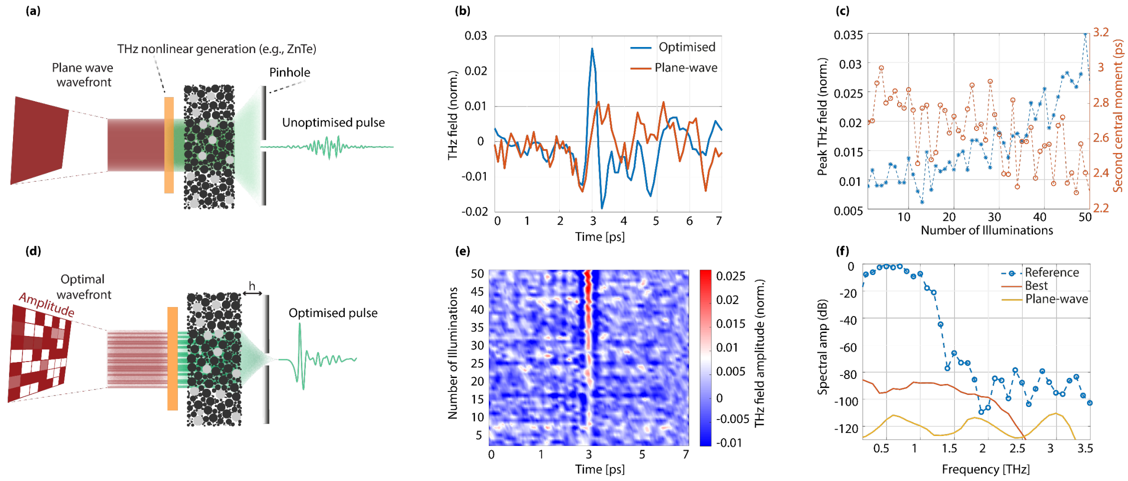

Figure 4.2 Spatiotemporal focusing of a terahertz pulse. (a, d) Conceptual figure of spatiotemporal focusing results: The THz plane wave is projected on a disordered medium, transmitting unoptimised light scattering. (b) The wavefront of the incident THz pulse is shaped so that scattering acts as a spatiotemporal lens creating a focus on the output of the sample. The pinhole is in contact with the scattering medium (i.e., ideally h ~ 0). (b) Optimised pulse (blue) and unoptimised field - with SLM off - (in red). (c) The second central moment and peak field value optimisation. (e) The set of TDS ranked relative to the cost function A in Table 4.1. (f) Spectrums of the reference, the optimised and the unoptimised pulses.

In Fig. 4.2(a, d), I show a conceptual figure of the experiment. In Fig. 4.2(b), I show the unoptimised and optimised pulses in red and blue, respectively (the unoptimised pulse corresponds to the measurement taken with the SLM off).

Fig. 4.2(c) shows the second central moment and peak field value optimisation, and in Fig. 4.2(e), I plot the set of TDS ranked relative to the cost function A in Table 4.1. In Fig. 4.2(f), the spectrums of the transmitted pulses are compared with the reference pulse (measurement taken with no scattering medium). I can notice that the optimised pulses have a significantly larger spectrum or pulse time compression. Because this approach is sensitive to the full-wave coherent field properties of the pulse, I demonstrate the ability to invert the optical phase of the THz pulse by employing the fitness function B from Table 4.1, as illustrated in Fig. 4.3. In this case, the algorithm seeks the best spatial pattern that minimises the THz peak field. In Fig. 4.3(a), I show a conceptual figure of the experiment. The corresponding temporal profile is shown in Fig. 4.3(b), and in Fig. 4.3(c), I show the peak fields ranked relative to cost function B in Table 4.1.

Furthermore, I illustrate the ability to optimise the temporal properties of the transmitted wavefront, specifically, the pulse's temporal delay.

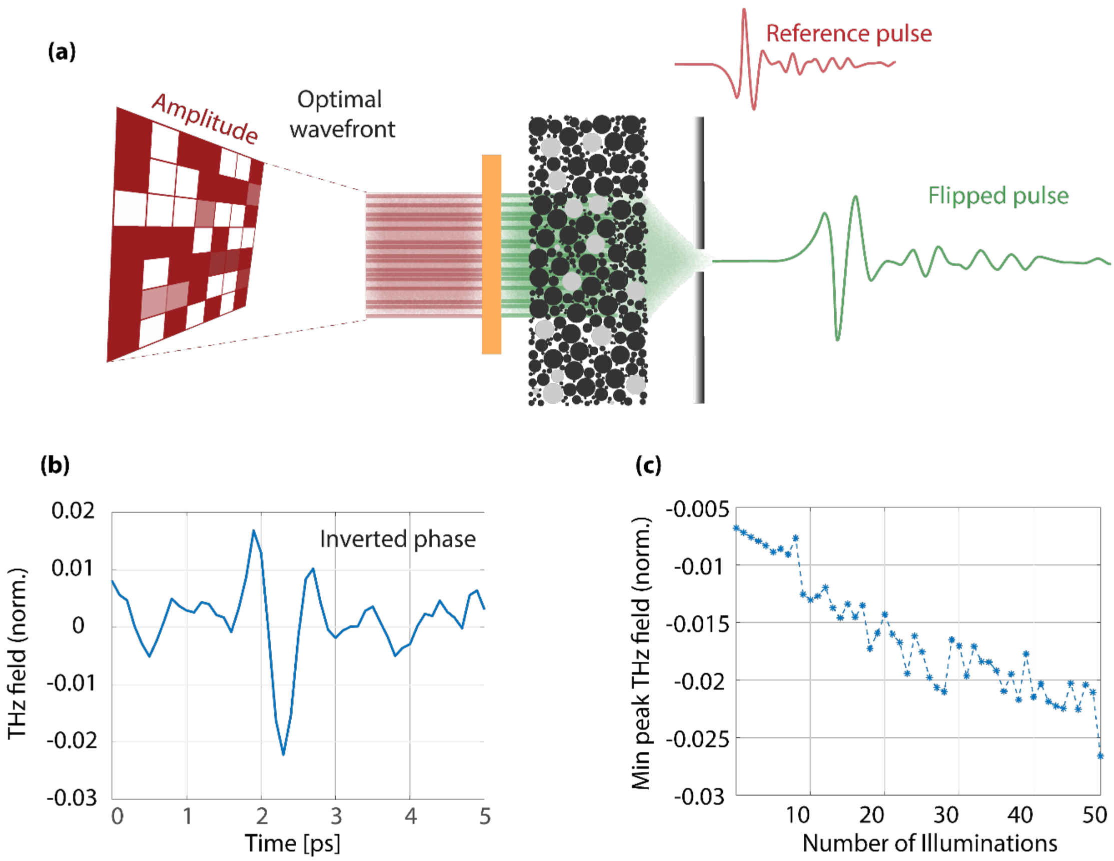

Figure 4.3 Optimised pulse with inverted phase. (a) Illustrative figure. (b) Temporal profile of the output THz pulse with inverted phase relative to the reference (scanned without scattering medium). (c) Peak fields are ranked relative to cost function B in Table 4.1.

For this scenario, I employed the optimisation fitness function C in Table 4.1, which seeks incident patterns yielding an output wavefront with the desired temporal mean t_0. In other words, I show that with a standard spatial light modulator, I can optically control the delay time of THz pulses. In Fig. 4.4(a), I show an illustrative picture of the experiment. In Fig. 4.4(b), I show four pulses time-shifted from pattern {1, 30, 80, 100}. In Fig. 4.4(c), I show the first central moment values. In Fig 4.4(d), I show the field map of the ranked pulses. It is achieved a time shift of roughly 1 ps.

Figure 4.2 shows the spatiotemporal focusing of a THz; in this case, by using the cost function A (Table 4.1), the algorithm looks for the best spatial pattern that simultaneously maximises the peak field passing throughout a subwavelength pinhole (200 μm aperture) and compresses the pulses in time.

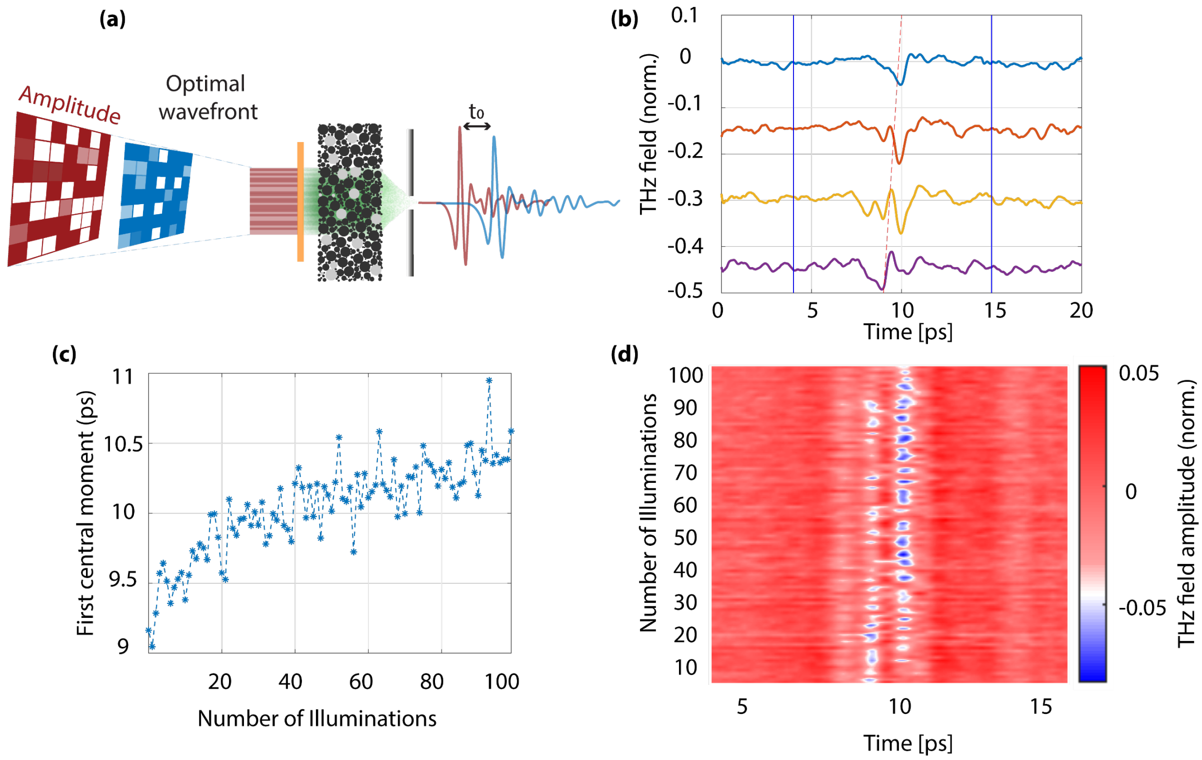

Figure 4.4 Field temporal shift. (a) Illustrative figure. (b) Four THz pulses, time-shifted at around 1 ps, respectively pattern {1, 30, 80, 100}. (c) The first central moment value optimisation. (d) The TDS ranked relative to the cost function. The measurements of the temporal shift are taken with the cost function C from Table 4.1.

4.3 Experimental Setup

A pulsed laser with a central wavelength of 800 nm (Coherent Libra, 1 kHz repetition rate) is reflected off an LCMOS-SLM (Hamamatsu X10468 Series). The SLM screen is imaged on the surface of a ZnTe crystal, and the THz-shaped pattern is created via optical rectification. The shaped THz wavefront is then projected on the scattering medium placed in contact with the nonlinear crystal to preserve the near-field condition. I place a pinhole at the output of the scattering medium. Therefore, the transmitted THz field is projected with a 2f-2f imaging condition and coherently detected with a standard electro-optic detection.

The scattering sample consists of high resistivity, float zone silicon flakes (n_{Si} = 1.46) embedded in paraffine (n_p = 1.52); n_{Si} and n_p are the refractive index of silicon and paraffin, respectively. The metal pinhole with a 200 μm aperture was a slice of aluminium foil, see Fig. 4.5.

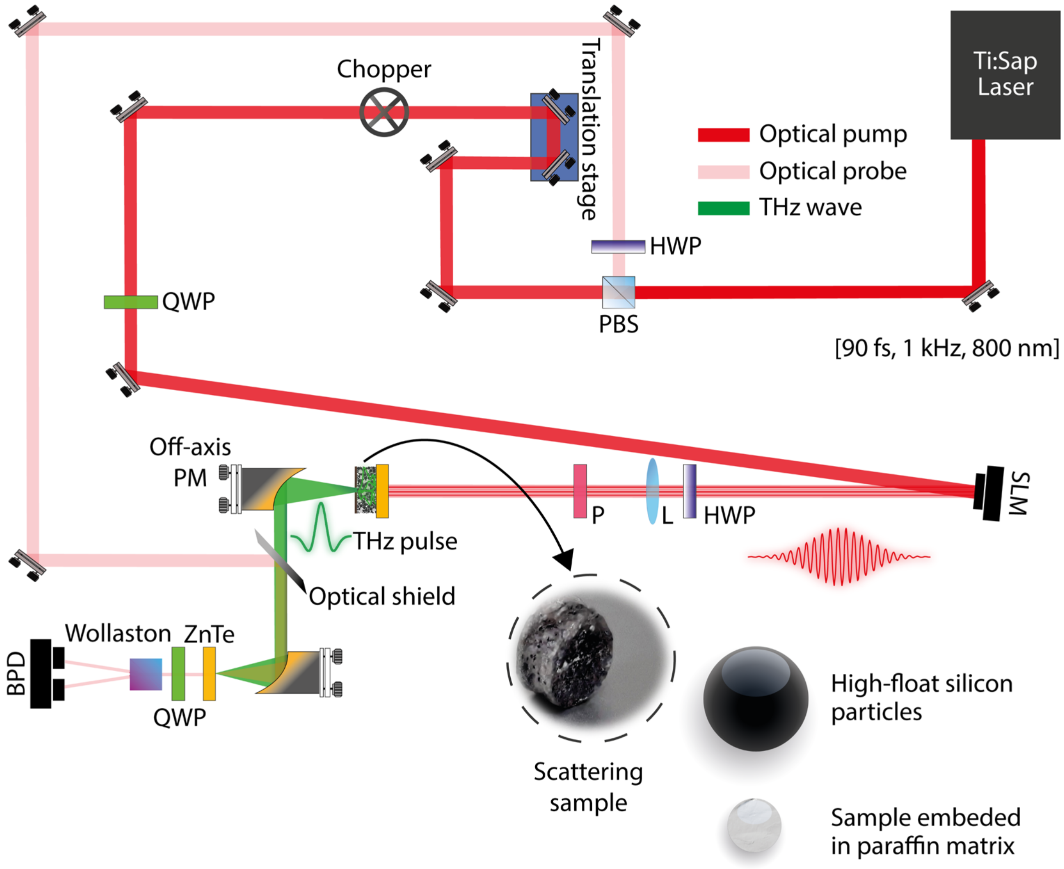

Figure 4.5 Schematic of the apparatus.

4.4 Conclusions

In summary, the results of this chapter show spatiotemporal control of diffuse ultrafast THz pulses in random media. As relevant examples, I show the spatiotemporal refocusing and compression of a broadband THz pulse by optimising the spatial and temporal features of the transmitted THz field. Also, I considered different wavefront control applications, including phase inversion and temporal shifting control. This work shows that wavefront control of the THz pulse's temporal and spatial properties can be achieved by acting only on the spatial degrees of freedom.

Chapter 5: Conclusions & Future Perspectives

This thesis defines and demonstrates a novel methodology for complete control over the spatial and temporal features of the THz patterns in random media. The approach relies on the generation of THz patterns by nonlinear conversion of a patterned optical beam and by the synergy of the 'Nonlinear Ghost Imaging' (TNGI) protocol that I contributed during my PhD. The methodology allows us to obtain a full-wave description of the light-matter interaction between THz illumination and the disordered sample. I believe this work can represent a substantial breakthrough in nearfield imaging and THz field modulation, especially in light of the emergence of more efficient THz modulators and emitters [112,155]. Veli et al., in particular, recently published a novel neural network methodology for THz field modulation [155], achieving a frequency range from 2 to 4 THz. Moreover, time-resolved field measurements can be employed to achieve remarkable performances in deep-tissue biological imaging and hyperspectral inspection, as defined in the TNGI publication. These applications rely on reconstructing the full-wave transmission properties of complex samples, such as turbid media or biological tissue, a task still challenging at optical frequencies.

Additionally, field-sensitive detection can open future projects, some of which are finalised, such as super-resolution THz imaging through scattering or turbid media. Another vision is to exploit scattering media at terahertz (THz) frequencies as encrypting combinatory structures for secure communication. Scattering-based encryption is a hot topic in general photonics [156–158]. The basic idea is to exploit a scattering medium as a space-time combinatory element in order to produce complex spatial-temporal dispersion behaviour. Indeed, the knowledge of the specific transmission response can be used to isolate the information between the intended and unwanted receivers.

In contrast, the inherent complexity of the scattering makes this combinatory element challenging to clone or guess. However, typical optical methodologies tend to be limited by intensity-only detection approaches. While the spatial distribution of the scattering is quite accessible, the temporal response is much more difficult to exploit. In this sense, the availability of the time-domain terahertz system and scattering exhibited by macroscopic structure at terahertz waves provides a platform with the opportunity to step beyond this scenario. In other words, the future project could be a terahertz encryption scheme by exploiting the full-wave properties of the scattering medium as the unique physical key. Such an optical scheme encrypts the information into the highly scattered wavefront of the light field and relies on the unique key to decrypt the data with an iterative algorithm. I expect this novel optical encryption strategy to benefit practical applications, such as terahertz-encrypted communication, authentication, and anti-counterfeiting. Indeed, this thesis represents a novel input to such a new subject. I aim to continue developing novel technologies for terahertz applications and hope this work will help the future generation of scientists unveil new fascinating, unexplored science.

Final Reflections

Finally, before I conclude, I will dedicate a few lines about my experience as a PhD student at the University of Sussex. Working in the Emergent Photonics Lab has been extremely exciting. I believe I have gained a solid understanding of many things during these years, from the different aspects of researching and writing scientific manuscripts to communication skills, and I thank my supervisors for allowing me to be part of their team. Also, I had an exceptional experience getting involved in outreach activities as president of the OPTICA student chapter; I am so honoured about all the work we have done together, and I will never forget those moments of joy and victory (for instance, winning the Wonderful World of Optics Competition Prize in 2021). I believe this has been an excellent experience and undoubtedly strengthened my transversal communication skills. Last but not least, a few words on the pandemic. Covid-19 did not make life any more manageable (I guess it was not a pleasant time for anybody on this planet). Nevertheless, even during these dark moments, I took the chance to get involved in volunteering activities. I volunteered as a Steward Volunteer to support the NHS with COVID-19 vaccines during the pandemic. For various reasons, I felt the need to give something back and help the community (at least in a small part) in these difficult times. Undoubtedly, this adventure provided an opportunity to develop new skills and meet many interesting people.

To conclude, I will never forget this experience and will keep a remembrance of Brighton in my heart. Moreover, I would recommend all students with some interest in this field to pursue a PhD course as I believe it will be a crucial step in their life.

Chapter 6: List of Publications, Conferences & Awards

Papers (Published)

[1] L. Olivieri, J. S. T. Gongora, L. Peters, V. Cecconi, A. Cutrona, J. Tunesi, R. Tucker, A. Pasquazi, and M. Peccianti, Hyperspectral Terahertz Microscopy via Nonlinear Ghost Imaging, Optica 7, 186 (2020).

[2] J. S. Totero Gongora, L. Peters, J. Tunesi, V. Cecconi, M. Clerici, A. Pasquazi, and M. Peccianti, All-Optical Two-Color Terahertz Emission from Quasi-2D Nonlinear Surfaces, Phys. Rev. Lett. 125, 263901 (2020).

[3] J. S. Totero Gongora, L. Olivieri, L. Peters, J. Tunesi, V. Cecconi, A. Cutrona, R. Tucker, V. Kumar, A. Pasquazi, and M. Peccianti, Route to Intelligent Imaging Reconstruction via Terahertz Nonlinear Ghost Imaging, Micromachines 11, 521 (2020).

[4] V. Cecconi, V. Kumar, A. Pasquazi, J. S. Totero Gongora, and M. Peccianti, Nonlinear Field-Control of Terahertz Waves in Random Media for Spatiotemporal Focusing, Open Res. Eur. **2**, 32 (2022).

[5] V. Kumar, V. Cecconi, L. Peters, J. Bertolotti, A. Pasquazi, J. S. T. Gongora, and M. Peccianti, Deterministic Terahertz Wave Control in Scattering Media, ACS Photonics (2022).

Papers (Work in Progress)

[1] V. Cecconi, V. Kumar, A. Pasquazi, J. S. Totero Gongora, and M. Peccianti, Experimental Spatiotemporal Superfocusing of Ultrafast THz Pulses through Scattering Media.

Patents

[1] Inventor of a patent (funded by the University of Sussex and in partnership with Advanced Material Design) on a novel terahertz ink. PCT - WO2022185040 - METHOD OF GENERATING TERAHERTZ EMISSION USING AN INK

Link: https://patentscope.wipo.int/search/en/detail.jsf?docId=WO2022185040

Conferences

[1] V. Cecconi, V. Kumar, A. Pasquazi, J. S. T. Gongora, and M. Peccianti, Time-Resolved, Nonlinear Control of Terahertz Waves in Random Media for Spatiotemporal Focusing, in 2021 Conference on Lasers and Electro-Optics Europe European Quantum Electronics Conference (CLEO/Europe-EQEC) (2021), p. CC-5.3.

[2] V. Cecconi, V. Kumar, A. Pasquazi, J. S. T. Gongora, and M. Peccianti, Full-Field Spatio-Temporal Shaping via Space-Time Coupling in Random Media, in OSA Advanced Photonics Congress 2021 (2021), Paper IF1A.2 (Optical Society of America, 2021), p. IF1A.2.

[3] V. Cecconi, V. Kumar, A. Pasquazi, J. S. T. Gongora, and M. Peccianti, Spatiotemporal control of ultrafast terahertz pulses in random media, in IONS IRELAND 2021 (2021).

[4] V. Cecconi, V. Kumar, J. S. T. Gongora, L. Peters, L. Olivieri, J. Bertolotti, A. Pasquazi, M. Peccianti, The Nonlinear Ghost Imaging Route to Harnessing Random Propagation, IEEE(SUM) Conference 2022 (Invited).

[5] V. Cecconi, V. Kumar, A. Pasquazi, J. S. T. Gongora, and M. Peccianti, Spatiotemporal Superfocusing of Ultrafast Terahertz Waves in Complex Media, in OPTICA Advanced Photonics Congress 2022 (Invited).

[6] V. Cecconi, V. Kumar, A. Pasquazi, J. S. T. Gongora, and M. Peccianti, Terahertz Field Spatiotemporal Superfocusing In Complex Media, IRMMW Conference 2022.

Peer-Reviews

I must thank my supervisor, Prof. Marco Peccianti, for allowing me the opportunity to start the experience of Peer-reviewing scientific papers. Indeed, reviewers are a critical part of the publication process. Journal editors rely on reviewers to help maintain their journals' high standards. In addition, reviewing journals can also be rewarding and provides insight into some of the most up-to-date research in the field.

During my PhD, I reviewed 30 articles for 12 scientific journals (Physical Review Letters, Physical Review A, Physical Review Applied, Optics Express, Photonics Research, Journal of the Optical Society of America A, Journal of the Optical Society of America B, Applied Optics, Optics Letters, MDPI Electronics, MDPI Applied Optics, Journal of Mechanical and Manufacturing Process). Link: Cecconi, Vittorio - Web of Science Core Collection

Awards and Grants

1. Best Poster - TERANET-NPL (2019)
2. Siegman International School on Lasers Grant (2020)
3. The Wonderful World of Optics Best Contribution – with the University of Sussex OPTICA Student Chapter Outreach Award – IONS IRELAND (2021)
4. Student Best Paper Award – CLEO/Europe-EQEC (2021)
5. Student Best Paper Award – Advanced Photonics Congress (2022)

Bibliography

[1] Y. Bar-Yam, *General Features of Complex Systems*, Knowl. Manag. 10 (n.d.).

[2] *History | Santa Fe Institute*, https://www.santafe.edu/about/history.

[3] *Nobel in Physics: Climate Science Breakthroughs Earn Prize*, BBC News (2021).

[4] N. M. Lawandy, R. M. Balachandran, A. S. L. Gomes, and E. Sauvain, *Laser Action in Strongly Scattering Media*, Nature **368**, 436 (1994).

[5] D. S. Wiersma, P. Bartolini, A. Lagendijk, and R. Righini, *Localization of Light in a Disordered Medium*, Nature **390**, 671 (1997).

[6] D. S. Wiersma, *Disordered Photonics*, Nat. Photonics **7**, 188 (2013).

[7] I. M. Vellekoop, A. Lagendijk, and A. P. Mosk, *Exploiting Disorder for Perfect Focusing*, Nat. Photonics **4**, 320 (2010).

[8] P. Sheng and B. van Tiggelen, *Introduction to Wave Scattering, Localization and Mesoscopic Phenomena. Second Edition*, Waves Random Complex Media **17**, 235 (2007).

[9] A. P. Mosk, A. Lagendijk, G. Lerosey, and M. Fink, *Controlling Waves in Space and Time for Imaging and Focusing in Complex Media*, Nat. Photonics **6**, 5 (2012).

[10] *Wave Propagation and Scattering in Random Media | IEEE EBooks | IEEE Xplore*, https://ieeexplore.ieee.org/book/5270963.

[11] V. Tuchin, *Tissue Optics Light Scattering Methods and Instruments for Medial Diagnosis*, SPIE **13**, (2000).

[12] P. Sebbah, editor , *Waves and Imaging through Complex Media* (Springer Netherlands, 2001).

[13] A. P. Gibson, J. C. Hebden, and S. R. Arridge, *Recent Advances in Diffuse Optical Imaging*, Phys. Med. Biol. **50**, R1 (2005).

[14] L. C. Kennedy, L. R. Bickford, N. A. Lewinski, A. J. Coughlin, Y. Hu, E. S. Day, J. L. West, and R. A. Drezek, *A New Era for Cancer Treatment: Gold-Nanoparticle-Mediated Thermal Therapies*, Small **7**, 169 (2011).

[15] M. Elias, N. Mas, and P. Cotte, *Review of Several Optical Non-Destructive Analyses of an Easel Painting. Complementarity and Crosschecking of the Results*, J. Cult. Herit. **12**, 335 (2011).

[16] A. F. Koenderink, A. Lagendijk, and W. L. Vos, *Optical Extinction Due to Intrinsic Structural Variations of Photonic Crystals*, Phys. Rev. B **72**, 153102 (2005).

[17] E. N. Leith and J. Upatnieks, *Holographic Imagery Through Diffusing Media*, JOSA **56**, 523 (1966).

[18] I. Freund, *Looking through Walls and around Corners*, Phys. Stat. Mech. Its Appl. **168**, 49 (1990).

[19] *Statistical Optics, 2nd Edition | Wiley*, https://www.wiley.com/en-us/Statistical+Optics%2C+2nd+Edition-p-9781119009450.

[20] C. W. J. Beenakker, *Random-Matrix Theory of Quantum Transport*, Rev. Mod. Phys. **69**, 731 (1997).

[21] L. C. Andrews, R. L. Phillips, and C. Y. Hopen, *Laser Beam Scintillation with Applications* (SPIE Press, 2001).

[22] D. Huang et al., *Optical Coherence Tomography*, Science **254**, 1178 (1991).

[23] V. Ntziachristos, *Fluorescence Molecular Imaging*, Annu. Rev. Biomed. Eng. **8**, 1 (2006).

[24] W. B. Bridges, P. T. Brunner, S. P. Lazzara, T. A. Nussmeier, T. R. O'Meara, J. A. Sanguinet, and W. P. Brown, *Coherent Optical Adaptive Techniques*, Appl. Opt. **13**, 291 (1974).

[25] J. W. Hardy, *Adaptive Optics for Astronomical Telescopes* (Oxford University Press, 1998).

[26] J. C. Dainty, editor , *Laser Speckle and Related Phenomena* (Springer-Verlag, Berlin Heidelberg, 1975).

[27] A. Lagendijk and B. A. van Tiggelen, *Resonant Multiple Scattering of Light*, Phys. Rep. **270**, 143 (1996).

[28] M. P. van Albada, B. A. van Tiggelen, A. Lagendijk, and A. Tip, *Speed of Propagation of Classical Waves in Strongly Scattering Media*, Phys. Rev. Lett. **66**, 3132 (1991).

[29] M. P. van Albada, J. F. de Boer, and A. Lagendijk, *Observation of Long-Range Intensity Correlation in the Transport of Coherent Light through a Random Medium*, Phys. Rev. Lett. **64**, 2787 (1990).

[30] J. Wang and A. Z. Genack, *Transport through Modes in Random Media*, Nature **471**, 7338 (2011).

[31] F. Lemoult, G. Lerosey, J. de Rosny, and M. Fink, *Manipulating Spatiotemporal Degrees of Freedom of Waves in Random Media*, Phys. Rev. Lett. **103**, 173902 (2009).

[32] M. Davy, Z. Shi, and A. Z. Genack, *Focusing through Random Media: Eigenchannel Participation Number and Intensity Correlation*, Phys. Rev. B **85**, 035105 (2012).

[33] A. Derode, P. Roux, and M. Fink, *Robust Acoustic Time Reversal with High-Order Multiple Scattering*, Phys. Rev. Lett. **75**, 4206 (1995).

[34] A. Derode, A. Tourin, and M. Fink, *Random Multiple Scattering of Ultrasound. II. Is Time Reversal a Self-Averaging Process?*, Phys. Rev. E **64**, 036606 (2001).

[35] D. Cassereau and M. Fink, *Focusing with Plane Time-reversal Mirrors: An Efficient Alternative to Closed Cavities*, J. Acoust. Soc. Am. **94**, 2373 (1993).

[36] B. E. Henty and D. D. Stancil, *Multipath-Enabled Super-Resolution for Rf and Microwave Communication Using Phase-Conjugate Arrays*, Phys. Rev. Lett. **93**, 243904 (2004).

[37] *Time Reversal of Wideband Microwaves: Applied Physics Letters: Vol 88, No 15*, https://aip.scitation.org/doi/full/10.1063/1.2194009.

[38] I. M. Vellekoop and A. P. Mosk, *Focusing Coherent Light through Opaque Strongly Scattering Media*, Opt. Lett. **32**, 2309 (2007).

[39] I. M. Vellekoop, *Controlling the Propagation of Light in Disordered Scattering Media*, ArXiv08071087 Phys. (2008).

[40] I. M. Vellekoop, E. G. van Putten, A. Lagendijk, and A. P. Mosk, *Demixing Light Paths inside Disordered Metamaterials*, Opt. Express **16**, 67 (2008).

[41] M. Cui, E. J. McDowell, and C. Yang, *Observation of Polarization-Gate Based Reconstruction Quality Improvement during the Process of Turbidity Suppression by Optical Phase Conjugation*, Appl. Phys. Lett. **95**, 123702 (2009).

[42] O. N. Dorokhov, *On the Coexistence of Localized and Extended Electronic States in the Metallic Phase*, in *30 Years of the Landau Institute ? Selected Papers*, Vol. Volume 11 (WORLD SCIENTIFIC, 1996), pp. 234–237.

[43] J. Pendry, *Light Finds a Way through the Maze*, Physics **1**, 20 (2008).

[44] I. M. Vellekoop and A. P. Mosk, *Universal Optimal Transmission of Light Through Disordered Materials*, Phys. Rev. Lett. **101**, 120601 (2008).

[45] Z. Shi and A. Z. Genack, *Transmission Eigenvalues and the Bare Conductance in the Crossover to Anderson Localization*, Phys. Rev. Lett. **108**, 043901 (2012).

[46] F. van Beijnum, E. G. van Putten, A. Lagendijk, and A. P. Mosk, *Frequency Bandwidth of Light Focused through Turbid Media*, Opt. Lett. **36**, 373 (2011).

[47] O. Katz, E. Small, Y. Bromberg, and Y. Silberberg, *Focusing and Compression of Ultrashort Pulses through Scattering Media*, Nat. Photonics **5**, 372 (2011).

[48] A. Yariv, *Four Wave Nonlinear Optical Mixing as Real Time Holography*, Opt. Commun. **25**, 23 (1978).

[49] D. A. B. Miller, *Time Reversal of Optical Pulses by Four-Wave Mixing*, Opt. Lett. **5**, 300 (1980).

[50] M. F. Yanik and S. Fan, *Time Reversal of Light with Linear Optics and Modulators*, Phys. Rev. Lett. **93**, 173903 (2004).

[51] S. Longhi, *Stopping and Time Reversal of Light in Dynamic Photonic Structures via Bloch Oscillations*, Phys. Rev. E **75**, 026606 (2007).

[52] Y. Sivan and J. B. Pendry, *Time Reversal in Dynamically Tuned Zero-Gap Periodic Systems*, Phys. Rev. Lett. **106**, 193902 (2011).

[53] J. B. Pendry, *Time Reversal and Negative Refraction*, Science **322**, 71 (2008).

[54] A. R. Katko, S. Gu, J. P. Barrett, B.-I. Popa, G. Shvets, and S. A. Cummer, *Phase Conjugation and Negative Refraction Using Nonlinear Active Metamaterials*, Phys. Rev. Lett. **105**, 123905 (2010).

[55] J. Aulbach, B. Gjonaj, P. M. Johnson, A. P. Mosk, and A. Lagendijk, *Control of Light Transmission through Opaque Scattering Media in Space and Time*, Phys. Rev. Lett. **106**, 103901 (2011).

[56] X.-C. Zhang and J. Xu, *Introduction to THz Wave Photonics* (Springer US, Boston, MA, 2010).

[57] P. u. Jepsen, D. g. Cooke, and M. Koch, *Terahertz Spectroscopy and Imaging – Modern Techniques and Applications*, Laser Photonics Rev. **5**, 124 (2011).

[58] D. Grischkowsky, S. Keiding, M. van Exter, and Ch. Fattinger, *Far-Infrared Time-Domain Spectroscopy with Terahertz Beams of Dielectrics and Semiconductors*, J. Opt. Soc. Am. B **7**, 2006 (1990).

[59] D. Zimdars, J. S. White, G. Stuk, A. Chernovsky, G. Fichter, and S. Williamson, *Large Area Terahertz Imaging and Non-Destructive Evaluation Applications*, Insight - Non-Destr. Test. Cond. Monit. **48**, 537 (2006).

[60] E. Pickwell and V. P. Wallace, *Biomedical Applications of Terahertz Technology*, J. Phys. Appl. Phys. **39**, R301 (2006).

[61] J. Neu and C. A. Schmuttenmaer, *Tutorial: An Introduction to Terahertz Time Domain Spectroscopy (THz-TDS)*, J. Appl. Phys. **124**, 231101 (2018).

[62] M. van Exter, C. Fattinger, and D. Grischkowsky, *Terahertz Time-Domain Spectroscopy of Water Vapor*, Opt. Lett. **14**, 1128 (1989).

[63] S. M. Teo, B. K. Ofori-Okai, C. A. Werley, and K. A. Nelson, *Invited Article: Single-Shot THz Detection Techniques Optimized for Multidimensional THz Spectroscopy*, Rev. Sci. Instrum. **86**, 051301 (2015).

[64] E. Roussel, C. Szwaj, C. Evain, B. Steffen, C. Gerth, B. Jalali, and S. Bielawski, *Phase Diversity Electro-Optic Sampling: A New Approach to Single-Shot Terahertz Waveform Recording*, Light Sci. Appl. **11**, 1 (2022).

[65] J. S. Totero Gongora, L. Peters, J. Tunesi, V. Cecconi, M. Clerici, A. Pasquazi, and M. Peccianti, *All-Optical Two-Color Terahertz Emission from Quasi-2D Nonlinear Surfaces*, Phys. Rev. Lett. **125**, 263901 (2020).

[66] J. Pearce, Z. Jian, and D. M. Mittleman, *Propagation of Terahertz Pulses in Random Media*, Philos. Trans. R. Soc. Lond. Ser. Math. Phys. Eng. Sci. **362**, 301 (2004).

[67] J. Pearce and D. M. Mittleman, *Scale Model Experimentation: Using Terahertz Pulses to Study Light Scattering*, Phys. Med. Biol. **47**, 3823 (2002).

[68] C. R. Schumacher, *Electrodynamic Similitude and Physical Scale Modeling of Nondispersive Targets*, J. Appl. Phys. **62**, 2616 (1987).

[69] R. A. Cheville and D. Grischkowsky, *Time Domain Terahertz Impulse Ranging Studies*, Appl. Phys. Lett. **67**, 1960 (1995).

[70] K. Iwaszczuk, H. Heiselberg, and P. U. Jepsen, *Terahertz Radar Cross Section Measurements*, Opt. Express **18**, 26399 (2010).

[71] T. D. Dorney, J. L. Johnson, J. V. Rudd, R. G. Baraniuk, W. W. Symes, and D. M. Mittleman, *Terahertz Reflection Imaging Using Kirchhoff Migration*, Opt. Lett. **26**, 1513 (2001).

[72] M. Walther, B. Fischer, M. Schall, H. Helm, and P. U. Jepsen, *Far-Infrared Vibrational Spectra of All-Trans, 9-Cis and 13-Cis Retinal Measured by THz Time-Domain Spectroscopy*, Chem. Phys. Lett. **332**, 389 (2000).

[73] A. G. Markelz, A. Roitberg, and E. J. Heilweil, *Pulsed Terahertz Spectroscopy of DNA, Bovine Serum Albumin and Collagen between 0.1 and 2.0 THz*, Chem. Phys. Lett. **320**, 42 (2000).

[74] D. L. Woolard et al., *Millimeter Wave-Induced Vibrational Modes in DNA as a Possible Alternative to Animal Tests to Probe for Carcinogenic Mutations*, J. Appl. Toxicol. **17**, 243 (1997).

[75] T. Löffler, T. Bauer, K. J. Siebert, H. G. Roskos, A. Fitzgerald, and S. Czasch, *Terahertz Dark-Field Imaging of Biomedical Tissue*, Opt. Express **9**, 616 (2001).

[76] P. Y. Han, G. C. Cho, and X.-C. Zhang, *Time-Domain Transillumination of Biological Tissues with Terahertz Pulses*, Opt. Lett. **25**, 242 (2000).

[77] D. D. Arnone, C. M. Ciesla, A. Corchia, S. Egusa, M. Pepper, J. M. Chamberlain, C. Bezant, E. H. Linfield, R. Clothier, and N. Khammo, *Applications of Terahertz (THz) Technology to Medical Imaging*, in *Terahertz Spectroscopy and Applications II*, Vol. 3828 (SPIE, 1999), pp. 209–219.

[78] D. M. Mittleman, M. Gupta, R. Neelamani, R. G. Baraniuk, J. V. Rudd, and M. Koch, *Recent Advances in Terahertz Imaging*, Appl. Phys. B **68**, 1085 (1999).

[79] D. A. Benaron and D. K. Stevenson, *Optical Time-of-Flight and Absorbance Imaging of Biologic Media*, Science **259**, 1463 (1993).

[80] L. Wang, P. P. Ho, and R. R. Alfano, *Time-Resolved Fourier Spectrum and Imaging in Highly Scattering Media*, Appl. Opt. **32**, 5043 (1993).

[81] M. A. O'Leary, D. A. Boas, B. Chance, and A. G. Yodh, *Experimental Images of Heterogeneous Turbid Media by Frequency-Domain Diffusing-Photon Tomography*, Opt. Lett. **20**, 426 (1995).

[82] L. Wang, P. P. Ho, C. Liu, G. Zhang, and R. R. Alfano, *Ballistic 2-D Imaging Through Scattering Walls Using an Ultrafast Optical Kerr Gate*, Science **253**, 769 (1991).

[83] J. Pearce and D. M. Mittleman, *Propagation of Single-Cycle Terahertz Pulses in Random Media*, Opt. Lett. **26**, 2002 (2001).

[84] A. L. Petoukhova, W. Steenbergen, and F. F. M. de Mul, *Path-Length Distribution and Path-Length-Resolved Doppler Measurements of Multiply Scattered Photons by Use of Low-Coherence Interferometry*, Opt. Lett. **26**, 1492 (2001).

[85] S. Gentilini, M. Missori, N. Ghofraniha, and C. Conti, *Terahertz Radiation Transport in Photonic Glasses*, Ann. Phys. **532**, 2000005 (2020).

[86] Y. Kuga, D. Rice, and R. D. West, *Propagation Constant and the Velocity of the Coherent Wave in a Dense Strongly Scattering Medium*, IEEE Trans. Antennas Propag. **44**, 326 (1996).

[87] M. van der Mark, Propagation of Light in Disordered Media: A Search for Anderson Localization, 1990.

[88] L. Tsang, J. A. Kong, and K.-H. Ding, *Scattering of Electromagnetic Waves: Theories and Applications* (John Wiley & Sons, 2004).

[89] L. Tsang, J. A. Kong, and R. T. Shin, *Theory of Microwave Remote Sensing* (Wiley, 1985).

[90] P. A. Robinson, *Wave Propagation in Disordered Media*, Philos. Mag. B **80**, 2087 (2000).

[91] X. Li, D. N. Pattanayak, T. Durduran, J. P. Culver, B. Chance, and A. G. Yodh, *Near-Field Diffraction Tomography with Diffuse Photon Density Waves*, Phys. Rev. E **61**, 4295 (2000).

[92] R. Graaff and J. J. T. Bosch, *Diffusion Coefficient in Photon Diffusion Theory*, Opt. Lett. **25**, 43 (2000).

[93] S. G. Demos and R. R. Alfano, *Temporal Gating in Highly Scattering Media by the Degree of Optical Polarization*, Opt. Lett. **21**, 161 (1996).

[94] J. Bertolotti, E. G. van Putten, C. Blum, A. Lagendijk, W. L. Vos, and A. P. Mosk, *Non-Invasive Imaging through Opaque Scattering Layers*, Nature **491**, 232 (2012).

[95] A. Lyons, F. Tonolini, A. Boccolini, A. Repetti, R. Henderson, Y. Wiaux, and D. Faccio, *Computational Time-of-Flight Diffuse Optical Tomography*, Nat. Photonics **13**, 575 (2019).

[96] I. M. Vellekoop and C. M. Aegerter, *Scattered Light Fluorescence Microscopy: Imaging through Turbid Layers*, Opt. Lett. **35**, 1245 (2010).

[97] O. Katz, P. Heidmann, M. Fink, and S. Gigan, *Non-Invasive Single-Shot Imaging through Scattering Layers and around Corners via Speckle Correlations*, Nat. Photonics **8**, 10 (2014).

[98] D. A. Boas and A. G. Yodh, *Spatially Varying Dynamical Properties of Turbid Media Probed with Diffusing Temporal Light Correlation*, J. Opt. Soc. Am. A **14**, 192 (1997).

[99] D. A. Boas, L. E. Campbell, and A. G. Yodh, *Scattering and Imaging with Diffusing Temporal Field Correlations*, Phys. Rev. Lett. **75**, 1855 (1995).

[100] R. Berkovits and S. Feng, *Theory of Speckle-Pattern Tomography in Multiple-Scattering Media*, Phys. Rev. Lett. **65**, 3120 (1990).

[101] Z. Jian, J. Pearce, and D. M. Mittleman, *Characterizing Individual Scattering Events by Measuring the Amplitude and Phase of the Electric Field Diffusing through a Random Medium*, Phys. Rev. Lett. **91**, 033903 (2003).

[102] M. E. Khani, O. B. Osman, and M. H. Arbab, *Diffuse Terahertz Spectroscopy in Turbid Media Using a Wavelet-Based Bimodality Spectral Analysis*, Sci. Rep. **11**, 1 (2021).

[103] M. Kaushik, B. W.-H. Ng, B. M. Fischer, and D. Abbott, *Terahertz Fingerprinting in Presence of Quasi-Ballistic Scattering*, Appl. Phys. Lett. **101**, 061108 (2012).

[104] L. M. Zurk, B. Orlowski, D. P. Winebrenner, E. I. Thorsos, M. R. Leahy-Hoppa, and L. M. Hayden, *Terahertz Scattering from Granular Material*, JOSA B **24**, 2238 (2007).

[105] O. B. Osman and M. H. Arbab, *Mitigating the Effects of Granular Scattering Using Cepstrum Analysis in Terahertz Time-Domain Spectral Imaging*, PLOS ONE **14**, e0216952 (2019).

[106] M. Kaushik, B. W.-H. Ng, B. M. Fischer, and D. Abbott, *Terahertz Scattering by Dense Media*, Appl. Phys. Lett. **100**, 241110 (2012).

[107] M. Kaushik, B. W.-H. Ng, B. M. Fischer, and D. Abbott, *Terahertz Scattering by Granular Composite Materials: An Effective Medium Theory*, Appl. Phys. Lett. **100**, 011107 (2012).

[108] M. Kaushik, B. W.-H. Ng, B. M. Fischer, and D. Abbott, *Reduction of Scattering Effects in THz-TDS Signals*, IEEE Photonics Technol. Lett. **24**, 155 (2012).

[109] Y. C. Shen, P. F. Taday, and M. Pepper, *Elimination of Scattering Effects in Spectral Measurement of Granulated Materials Using Terahertz Pulsed Spectroscopy*, Appl. Phys. Lett. **92**, 051103 (2008).

[110] M. Franz, B. M. Fischer, and M. Walther, *The Christiansen Effect in Terahertz Time-Domain Spectra of Coarse-Grained Powders*, Appl. Phys. Lett. **92**, 021107 (2008).

[111] H.-B. Liu, Y. Chen, G. J. Bastiaans, and X.-C. Zhang, *Detection and Identification of Explosive RDX by THz Diffuse Reflection Spectroscopy*, Opt. Express **14**, 415 (2006).

[112] L. Leibov, A. Ismagilov, V. Zalipaev, B. Nasedkin, Y. Grachev, N. Petrov, and A. Tcypkin, *Speckle Patterns Formed by Broadband Terahertz Radiation and Their Applications for Ghost Imaging*, Sci. Rep. **11**, 1 (2021).

[113] L. Olivieri, J. S. T. Gongora, L. Peters, V. Cecconi, A. Cutrona, J. Tunesi, R. Tucker, A. Pasquazi, and M. Peccianti, *Hyperspectral Terahertz Microscopy via Nonlinear Ghost Imaging*, Optica **7**, 186 (2020).

[114] L. Olivieri, J. S. Totero Gongora, A. Pasquazi, and M. Peccianti, *Time-Resolved Nonlinear Ghost Imaging*, ACS Photonics **5**, 3379 (2018).

[115] J. S. Totero Gongora, L. Olivieri, L. Peters, J. Tunesi, V. Cecconi, A. Cutrona, R. Tucker, V. Kumar, A. Pasquazi, and M. Peccianti, *Route to Intelligent Imaging Reconstruction via Terahertz Nonlinear Ghost Imaging*, Micromachines **11**, 5 (2020).

[116] Y.-S. Lee, *Principles of Terahertz Science and Technology*, 1st ed (Springer, New York, NY, 2008).

[117] A. Tomasino, A. Parisi, S. Stivala, P. Livreri, A. C. Cino, A. C. Busacca, M. Peccianti, and R. Morandotti, *Wideband THz Time Domain Spectroscopy Based on Optical Rectification and Electro-Optic Sampling*, Sci. Rep. **3**, (2013).

[118] L. A. S. Peters, *Surface Terahertz Phenomena*, 115 (n.d.).

[119] I. N. Papadopoulos, J.-S. Jouhanneau, J. F. A. Poulet, and B. Judkewitz, *Scattering Compensation by Focus Scanning Holographic Aberration Probing (F-SHARP)*, Nat. Photonics **11**, 116 (2017).

[120] M. Frazier, B. Taddese, B. Xiao, T. Antonsen, E. Ott, and S. M. Anlage, *Nonlinear Time Reversal of Classical Waves: Experiment and Model*, Phys. Rev. E **88**, 062910 (2013).

[121] P. Sheng, *Introduction to Wave Scattering, Localization and Mesoscopic Phenomena*, 2nd ed. (Springer-Verlag, Berlin Heidelberg, 2006).

[122] M. C. W. van Rossum and Th. M. Nieuwenhuizen, *Multiple Scattering of Classical Waves: Microscopy, Mesoscopy, and Diffusion*, Rev. Mod. Phys. **71**, 313 (1999).

[123] A. Z. Genack, J. H. Li, N. Garcia, and A. A. Lisyansky, *Photon Diffusion, Correlation and Localization*, in *Photonic Band Gaps and Localization*, edited by C. M. Soukoulis (Springer US, Boston, MA, 1993), pp. 23–55.

[124] P. A. Lee and T. V. Ramakrishnan, *Disordered Electronic Systems*, Rev. Mod. Phys. **57**, 287 (1985).

[125] A. Tourin, M. Fink, and A. Derode, *Multiple Scattering of Sound*, Waves Random Media **10**, R31 (2000).

[126] Y. Kuga and A. Ishimaru, *Retroreflectance from a Dense Distribution of Spherical Particles*, JOSA A **1**, 831 (1984).

[127] P.-E. Wolf and G. Maret, *Weak Localization and Coherent Backscattering of Photons in Disordered Media*, Phys. Rev. Lett. **55**, 2696 (1985).

[128] A. Tourin, A. Derode, P. Roux, B. A. van Tiggelen, and M. Fink, *Time-Dependent Coherent Backscattering of Acoustic Waves*, Phys. Rev. Lett. **79**, 3637 (1997).

[129] R. K. Tyson, *Principles of Adaptive Optics, Second Edition*, 2nd edition (Academic Press, Boston, 1997).

[130] N. D. Shemonski, F. A. South, Y.-Z. Liu, S. G. Adie, P. Scott Carney, and S. A. Boppart, *Computational High-Resolution Optical Imaging of the Living Human Retina*, Nat. Photonics **9**, 440 (2015).

[131] M. Rueckel, J. A. Mack-Bucher, and W. Denk, *Adaptive Wavefront Correction in Two-Photon Microscopy Using Coherence-Gated Wavefront Sensing*, Proc. Natl. Acad. Sci. **103**, 17137 (2006).

[132] D. B. Conkey, A. N. Brown, A. M. Caravaca-Aguirre, and R. Piestun, *Genetic Algorithm Optimization for Focusing through Turbid Media in Noisy Environments*, Opt. Express **20**, 4840 (2012).

[133] U. Mahlab, H. J. Caulfield, and J. Shamir, *Genetic Algorithm for Optical Pattern Recognition*, Opt. Lett. **16**, 648 (1991).

[134] Q. Feng, F. Yang, X. Xu, B. Zhang, Y. Ding, and Q. Liu, *Multi-Objective Optimization Genetic Algorithm for Multi-Point Light Focusing in Wavefront Shaping*, Opt. Express **27**, 36459 (2019).

[135] Z. Yaqoob, D. Psaltis, M. S. Feld, and C. Yang, *Optical Phase Conjugation for Turbidity Suppression in Biological Samples*, Nat. Photonics **2**, 110 (2008).

[136] M. Cui and C. Yang, *Implementation of a Digital Optical Phase Conjugation System and Its Application to Study the Robustness of Turbidity Suppression by Phase Conjugation*, Opt. Express **18**, 3444 (2010).

[137] S. M. Popoff, G. Lerosey, R. Carminati, M. Fink, A. C. Boccara, and S. Gigan, *Measuring the Transmission Matrix in Optics: An Approach to the Study and Control of Light Propagation in Disordered Media*, Phys. Rev. Lett. **104**, 100601 (2010).

[138] A. Drémeau, A. Liutkus, D. Martina, O. Katz, C. Schülke, F. Krzakala, S. Gigan, and L. Daudet, *Reference-Less Measurement of the Transmission*

Matrix of a Highly Scattering Material Using a DMD and Phase Retrieval Techniques, Opt. Express **23**, 11898 (2015).

[139] O. Katz, E. Small, Y. Bromberg, and Y. Silberberg, *Focusing and Compression of Ultrashort Pulses through Scattering Media*, Nat. Photonics **5**, 372 (2011).

[140] M. Mounaix, D. Andreoli, H. Defienne, G. Volpe, O. Katz, S. Grésillon, and S. Gigan, *Spatiotemporal Coherent Control of Light through a Multiple Scattering Medium with the Multispectral Transmission Matrix*, Phys. Rev. Lett. **116**, 253901 (2016).

[141] M. A. Webster, T. D. Gerke, A. M. Weiner, and K. J. Webb, *Spectral and Temporal Speckle Field Measurements of a Random Medium*, Opt. Lett. **29**, 1491 (2004).

[142] E. Tal and Y. Silberberg, *Transformation from an Ultrashort Pulse to a Spatiotemporal Speckle by a Thin Scattering Surface*, Opt. Lett. **31**, 3529 (2006).

[143] P. M. Johnson, A. Imhof, B. P. J. Bret, J. G. Rivas, and A. Lagendijk, *Time-Resolved Pulse Propagation in a Strongly Scattering Material*, Phys. Rev. E **68**, 016604 (2003).

[144] N. C. Bruce, F. E. Schmidt, J. C. Dainty, N. P. Barry, S. C. Hyde, and P. M. French, *Investigation of the Temporal Spread of an Ultrashort Light Pulse on Transmission through a Highly Scattering Medium*, Appl. Opt. **34**, 5823 (1995).

[145] X. Wei, Y. Shen, J. C. Jing, A. S. Hemphill, C. Yang, S. Xu, Z. Yang, and L. V. Wang, *Real-Time Frequency-Encoded Spatiotemporal Focusing through Scattering Media Using a Programmable 2D Ultrafine Optical Frequency Comb*, Sci. Adv. **6**, eaay1192 (2020).

[146] W. Withayachumnankul and M. Naftaly, *Fundamentals of Measurement in Terahertz Time-Domain Spectroscopy*, J. Infrared Millim. Terahertz Waves **35**, 610 (2014).

[147] V. Cecconi, V. Kumar, A. Pasquazi, J. S. Totero Gongora, and M. Peccianti, *Nonlinear Field-Control of Terahertz Waves in Random Media for Spatiotemporal Focusing*, Open Res. Eur. **2**, 32 (2022).

[148] V. Kumar, V. Cecconi, L. Peters, J. Bertolotti, A. Pasquazi, J. S. T. Gongora, and M. Peccianti, *Deterministic Terahertz Wave Control in Scattering Media*, ArXiv220316929 Phys. (2022).

[149] J. Pearce and D. M. Mittleman, *Using Terahertz Pulses to Study Light Scattering*, Phys. B Condens. Matter **338**, 92 (2003).

[150] J. S. Totero Gongora, L. Olivieri, L. Peters, J. Tunesi, V. Cecconi, A. Cutrona, R. Tucker, V. Kumar, A. Pasquazi, and M. Peccianti, *Route to Intelligent Imaging Reconstruction via Terahertz Nonlinear Ghost Imaging*, Micromachines **11**, 5 (2020).

[151] A. Boniface, I. Gusachenko, K. Dholakia, and S. Gigan, *Rapid Broadband Characterization of Scattering Medium Using Hyperspectral Imaging*, Optica **6**, 274 (2019).

[152] M. Mounaix, D. Andreoli, H. Defienne, G. Volpe, O. Katz, S. Grésillon, and S. Gigan, *Spatiotemporal Coherent Control of Light through a Multiple Scattering Medium with the Multispectral Transmission Matrix*, Phys. Rev. Lett. **116**, 253901 (2016).

[153] C. Sadel, *Relations between Transfer and Scattering Matrices in the Presence of Hyperbolic Channels*, J. Math. Phys. **52**, 123511 (2011).

[154] H. Jin, B. Hwang, S. Lee, and J.-H. Park, *Limiting the Incident NA for Efficient Wavefront Shaping through Thin Anisotropic Scattering Media*, Optica **8**, 428 (2021).

[155] M. Veli, D. Mengu, N. T. Yardimci, Y. Luo, J. Li, Y. Rivenson, M. Jarrahi, and A. Ozcan, *Terahertz Pulse Shaping Using Diffractive Surfaces*, Nat. Commun. **12**, 1 (2021).

[156] Y. Liu, P. Yu, Y. Li, Y. Li, and L. Gong, *Exploiting Light Field Imaging through Scattering Media for Optical Encryption*, OSA Contin. **3**, 2968 (2020).

[157] I. Muniraj and J. Sheridan, *Optical Encryption and Decryption*, Opt. Encryption Decryption **SL46**, 1 (2019).

[158] L. Zhou, Y. Xiao, and W. Chen, *Learning Complex Scattering Media for Optical Encryption*, Opt. Lett. **45**, 5279 (2020).

[159] J. Dai, N. Karpowicz, and X.-C. Zhang, *Coherent Polarization Control of Terahertz Waves Generated from Two-Color Laser-Induced Gas Plasma*, Phys. Rev. Lett. **103**, 023001 (2009).

[160] H. g. Roskos, M. d. Thomson, M. Kreß, and T. Löffler, *Broadband THz Emission from Gas Plasmas Induced by Femtosecond Optical Pulses: From Fundamentals to Applications*, Laser Photonics Rev. **1**, 349 (2007).

[161] D. J. Cook and R. M. Hochstrasser, *Intense Terahertz Pulses by Four-Wave Rectification in Air*, Opt. Lett. **25**, 1210 (2000).

[162] K. Y. Kim, A. J. Taylor, J. H. Glownia, and G. Rodriguez, *Coherent Control of Terahertz Supercontinuum Generation in Ultrafast Laser–Gas Interactions*, Nat. Photonics **2**, 10 (2008).

[163] A. V. Balakin, A. V. Borodin, I. A. Kotelnikov, and A. P. Shkurinov, *Terahertz Emission from a Femtosecond Laser Focus in a Two-Color Scheme*, JOSA B **27**, 16 (2010).

[164] L. E. Hargrove, R. L. Fork, and M. A. Pollack, *LOCKING OF He–Ne LASER MODES INDUCED BY SYNCHRONOUS INTRACAVITY MODULATION*, Appl. Phys. Lett. **5**, 4 (1964).

[165] G. Steinmeyer, D. H. Sutter, L. Gallmann, N. Matuschek, and U. Keller, *Frontiers in Ultrashort Pulse Generation: Pushing the Limits in Linear and Nonlinear Optics*, Science **286**, 1507 (1999).

[166] A. J. DeMaria, W. H. Glenn, M. J. Brienza, and M. E. Mack, *Picosecond Laser Pulses*, Proc. IEEE **57**, 2 (1969).

[167] R. W. Boyd, *Nonlinear Optics*, 2nd ed (Academic Press, San Diego, CA, 2003).

[168] T. K. Gustafson, J.-P. E. Taran, P. L. Kelley, and R. Y. Chiao, *Self-Modulation of Picosecond Pulses in Electro-Optic Crystals*, Opt. Commun. **2**, 17 (1970).

[169] G. Gallot, J. Zhang, R. W. McGowan, T.-I. Jeon, and D. Grischkowsky, *Measurements of the THz Absorption and Dispersion of ZnTe and Their Relevance to the Electro-Optic Detection of THz Radiation*, Appl. Phys. Lett. **74**, 3450 (1999).

[170] P. Y. Han and X.-C. Zhang, *Coherent, Broadband Midinfrared Terahertz Beam Sensors*, Appl. Phys. Lett. **73**, 3049 (1998).

[171] X. -C. Zhang, X. F. Ma, Y. Jin, T. -M. Lu, E. P. Boden, P. D. Phelps, K. R. Stewart, and C. P. Yakymyshyn, *Terahertz Optical Rectification from a Nonlinear Organic Crystal*, Appl. Phys. Lett. **61**, 3080 (1992).

[172] A. Schneider, M. Neis, M. Stillhart, B. Ruiz, R. U. A. Khan, and P. Günter, *Generation of Terahertz Pulses through Optical Rectification in Organic DAST Crystals: Theory and Experiment*, JOSA B **23**, 1822 (2006).

[173] D. H. Auston, K. P. Cheung, J. A. Valdmanis, and D. A. Kleinman, *Cherenkov Radiation from Femtosecond Optical Pulses in Electro-Optic Media*, Phys. Rev. Lett. **53**, 1555 (1984).

[174] J. A. Giordmaine, *Mixing of Light Beams in Crystals*, Phys. Rev. Lett. **8**, 19 (1962).

[175] T. Löffler, T. Hahn, M. Thomson, F. Jacob, and H. G. Roskos, *Large-Area Electro-Optic ZnTe Terahertz Emitters*, Opt. Express **13**, 5353 (2005).

[176] Q. Wu and X. C. Zhang, *Ultrafast Electro-Optic Field Sensors*, Appl. Phys. Lett. **68**, 1604 (1996).

[177] C. Winnewisser, P. U. Jepsen, M. Schall, V. Schyja, and H. Helm, *Electro-Optic Detection of THz Radiation in LiTaO3, LiNbO3 and ZnTe*, Appl. Phys. Lett. **70**, 3069 (1997).

[178] A. Yariv, *Quantum Electronics*, 3rd ed (Wiley, New York, 1989).

Appendix A: All-Optical Two-Colour Terahertz Emission from Quasi-2D Nonlinear Surfaces

A.1 About the paper: All-Optical Two-Colour Terahertz Emission from Quasi-2D Nonlinear Surfaces

Both the nonlinear ghost imaging and the study of nonlinear surfaces (addressed in this section) are linked to the main project of THz complex imaging. The idea stems directly from the ERC-CoG project TIMING (Time-Resolved Nonlinear Ghost Imaging), which focuses on THz imaging. And indeed, one of the main constraints in developing near-field THz imaging devices lies in minimising the thickness of the THz emitter. This chapter demonstrates the generation and control of THz radiation from the two-colour excitation of a semiconductor interface. Such a purely optical process is enabled by the tight confinement of the interacting fields in an extremely thin and large-area semiconductor surface composed of just a few atomic layers and compatible with existing electronic platforms. This work is a step ahead in placing terahertz sources in inaccessible places; this has excellent scientific appeal but is still very challenging in practice. Terahertz radiation can have a superlative role in material science, life science and security; nevertheless, it is still alien to most existing technology, and this piece of research is a milestone in our route to bringing terahertz functions closer to our everyday lives.

By taking inspiration from the generation of THz in the air using the highly nonlinear ionised plasma - a work done by Dai and co-workers [159] – this project aimed to investigate a novel physical mechanism for generating highly efficient THz-emitting nonlinear surfaces. Generally, an ultrafast pulse is combined with its second harmonic within a very tightly confined and highly intense region in the air. Initially, the description of this process was modelled as a third-order perturbative $\chi^{(3)}$ mixing with the incident fields to produce a rectified THz field [160,161], and the air provided as a medium that is naturally phase-matched. Furthermore, new studies have questioned the need for a more detailed interpretation of the THz conversion [162,163]. However, under the above bandgap excitation conditions at the semiconductor surfaces, the third-order susceptibility is significantly high and crucial, as shown by surface optical rectification (SOR). Therefore, instead of seeding the rectification with the surface field (which is now known to be heavily screened), we could seed the nonlinear product with the second harmonic of the pump field and consequently enhance the total emitted THz energy by surpassing the soft-saturation limits of SOR. Notice that the skin depth δd of the second harmonic in the experiment is dramatically shorter than that of the fundamental, ($\delta d_{400\,nm} = 16\,nm$ as opposed to $\delta d_{800\,nm} = 140\,nm$). Thus, the interaction region is highly subwavelength (compared to the generated THz) and is, in principle, free from any phase matching limitations of nonlinear bulk processes.

Also, in developing advanced integrated photonics platforms, nonlinear optics play a crucial role, for instance, when considering sub-wavelength structures. An attractive framework for fundamental investigation in light-matter interaction is the study of nonlinear surfaces, nanostructures and two-dimensional media, as they are inherently free from any longitudinal phase matching constraint; scientists have mainly studied this field in the optical and near-infrared spectral regions.

In this chapter, I will discuss the mechanism of generating ultrafast THz pulses from the nonlinear optical mixing enabled by surface third-order nonlinearity. Specifically, this work thoroughly investigates the coherent generation of THz radiation from narrow-bandgap semiconductor surfaces exploiting two colours, deeply above band-gap illumination. Notice that this process differs from the optical rectification field induced by symmetry breaking at the medium surface, and the THz generation is directly controllable by adjusting the relative phase between the interacting optical fields.

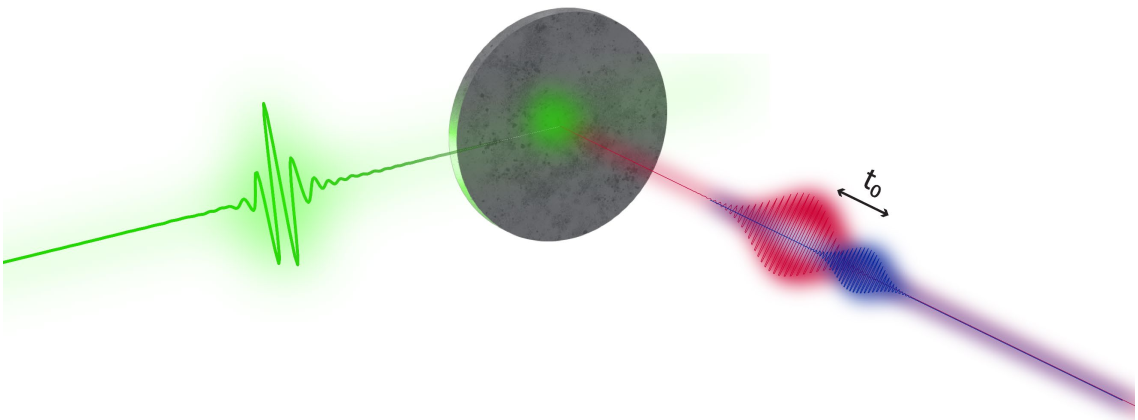

***Figure A.1** The illustrative figure of the all-optical two-colour terahertz emission.*

The process is denoted as All Optical Surface Optical Rectification (AO-SOR), and the relation describes it:

$$P_{THz} = \chi^{(3)}(\omega_{THz}, 2\omega, -\omega, -\omega) E_{2\omega}(t) \colon E_{\omega}^{*}(t) \colon E_{\omega}^{*}(t),$$

where $E_{\omega}(t)$ is the fundamental electric field of the optical pulse (e.g., $\lambda = 800\ nm$) and $E_{2\omega}(t)$ (e.g., $\lambda = 400\ nm$) is the second harmonic (SH). Firstly, to observe this emission, the fundamental field is projected through a type I phase matching in a β-BBO crystal cut and partially converted into its second harmonic. Moreover, by using a birefringent calcite plate, we imposed a controlled phase delay between the fundamental and second harmonic fields. Consequently, a beating between them was expected at the SH frequency; hence, it was possible to isolate the contributions from both SOR and AO-SOR, and thus, the enhanced bandwidth due to the thinner interaction region of AO-SOR was demonstrated. Also, the work demonstrates the high-energy behaviour of the emission. Indeed, the SOR component displays the same expected soft-saturating trend while the AO-SOR component increases quadratically with the square of the pump energy (i.e., $E_{2\omega} \propto E_{\omega}^{2}$). Last but not least, in this work, a quantitative estimation for the $\chi^{(3)}$ nonlinearity was made by considering the dependence on the AO-SOR component from the crystal orientation, which has a strong 4-fold symmetry when detecting the s-polarised THz field and illuminating with p-polarised optical fields; in other words

$$E_{s,THz} \propto E_{p,2\omega} E_{p,\omega}^{2} \left(\chi_{iiii}^{(3)} - 2\chi_{iijj}^{(3)} - \chi_{ijji}^{(3)}\right) \sin(4\phi),$$

where ϕ is the crystal orientation angle measured from the $< 100 >$ crystal axis. The estimation of the nonlinear susceptibility is $\chi^{(3)} \sim 9 \times 10^{-21}\ m^2/V^2$.

In this work, I contributed to taking the experimental measurements, and I contributed to the text's writing prior to submission.

A.1.1 Impact

The article was published on 21st December 2020 in the highly prestigious journal Physical Review Letters, which has a 5-year impact factor of 14.22 and a vast scope covering all areas of science. The Altmetric Attention is 80.

A.1.2 Link

A.2 Journal Article

PHYSICAL REVIEW LETTERS **125,** 263901 (2020)

All-Optical Two-Color Terahertz Emission from Quasi-2D Nonlinear Surfaces

J. S. Totero Gongora,[1,*] L. Peters,[1] J. Tunesi,[1] V. Cecconi,[1] M. Clerici,[2] A. Pasquazi,[1] and M. Peccianti[1,†]

[1]*Emergent Photonics Lab (EPic), Department of Physics and Astronomy, University of Sussex, Brighton, BN1 9QH, United Kingdom*

[2]*Ultrafast Nonlinear Optics Lab (UNO), James Watt School of Engineering, University of Glasgow, Glasgow, G12 8QQ, United Kingdom*

(Received 2 September 2020; revised 22 October 2020; accepted 18 November 2020; published 21 December 2020)

Two-color terahertz (THz) generation is a field-matter process combining an optical pulse and its second harmonic. Its application in condensed matter is challenged by the lack of phase matching among multiple interacting fields. Here, we demonstrate phase-matching-free two-color THz conversion in condensed matter by introducing a highly resonant absorptive system. The generation is driven by a third-order nonlinear interaction localized at the surface of a narrow-band-gap semiconductor, and depends directly on the relative phase between the two colors. We show how to isolate the third-order effect among other competitive THz-emitting surface mechanisms, exposing the general features of the two-color process.

DOI: 10.1103/PhysRevLett.125.263901

The nonlinear generation of broadband terahertz (THz) fields from ultrafast optical pulses is a subject of great interest for fundamental research and disruptive applications in imaging, spectroscopy, and the design of materials and devices [1–12]. Current research aims to identify new materials and generation mechanisms to boost the efficiency and versatility of nonlinear THz sources, as in the case of organic crystals [13,14], spintronic substrates [15], and tunable gas lasers [16]. Second-order optical rectification (OR) in $\chi^{(2)}$ bulk crystals, such as ZnTe or $LiNbO_3$ [17,18] has been at the core of bright THz source development for many years. The stringent requirement to maintain the longitudinal phase-matching condition across a wide optical bandwidth, however, strongly limits both the choice of laser sources and nonlinear materials. While phase matching can be achieved via sophisticated settings, it certainly poses growing challenges when synchronous propagation of multiple fields is required, as in the case of third-order phenomena. To overcome the limitations imposed by phase matching, a promising alternative is provided by new types of emitters capable of high-conversion efficiency over short propagation distances [13], as in the case of ultrathin spintronic substrates [15,19,20]. In this context, narrow-band-gap semiconductor surfaces have emerged as remarkably efficient surface THz sources, under ultrafast illumination (typically 100 fs class pulses). Indium arsenide (InAs), in particular, provides exceptionally high conversion efficiencies per unit length and stands as one of the standard benchmarks for surface nonlinear THz generation [21]. While at lower fluences ($< 100\ \mathrm{nJ/cm^2}$), InAs sources are mostly driven by carrier diffusion dynamics [22], in the high-pump regime ($> 10\ \mu\mathrm{J/cm^2}$) their emission is dominated by dc-biased surface optical rectification (DC-SOR) [23–25]. Similarly to second-harmonic generation from centrosymmetric surfaces [26], in DC-SOR the optical pump interacts with a symmetry-broken medium provided by the surface depletion field E_{surf} of the semiconductor, which leads to an effective quadratic response in the proximity of the surface [27]. Because of the neutralization of the surface field from excited photocarriers the emission from DC-SOR typically saturates at high pumping fluences [21,28]. This saturation, however, does not affect directly the third-order $\chi^{(3)}$ nonlinearity, which can be used to generate THz radiation by mixing an optical pulse with its second-harmonic through a process known as two-color optical rectification:

$$E_{\mathrm{THz}}(t) \propto \chi^{(3)}(\Omega, 2\omega, -\omega, -\omega) E_{2\omega}(t) E^{*}_{\omega}(t) E^{*}_{\omega}(t), \quad (1)$$

where $E_\omega(t)$ and $E_{2\omega}(t)$ are the electric fields of the optical and second-harmonic pulses, and * denotes the complex conjugate. The key signature of this interaction is the dependence of the THz amplitude from the mutual phase and frequencies of the interacting fields [29,30], a degree of control generally not attainable in $\chi^{(2)}$-based THz sources. Two-color generation has been extensively exploited in laser-induced gas plasmas, leading to the demonstration of THz sources with record-breaking bandwidths [31–38]. In these systems, the role of the four-wave-mixing is negligible, as demonstrated by Ref. [39], whereas the THz emission is rather the result of highly nonperturbative mechanisms. Two-color excitation also plays a key role in the injection and coherent control of ultrafast ballistic currents in bulk semiconductors [40–43]. In these experiments, the interference between two quantum pathways, single-photon absorption at 2ω and two-photon absorption at ω, leads to the ultrafast injection of directional currents acting as THz sources [41,44,45]. Quantum interference is mediated by a below-band-gap optical illumination seeding the two-photon absorption process ($\hbar\omega < E_g < 2\hbar\omega$, where E_g is the semiconductor band gap). However, in the presence of highly above-band-gap illumination in narrow-band-gap semiconductors, ($E_g < \hbar\omega$), the direct one-photon absorption is the dominant mechanism, effectively reducing the number of photons available for multiphoton nonlinear current injection processes. [45]. A central challenge in implementing Eq. (1) is in keeping synchronous interactions among all the interacting fields, a condition practically out of reach in bulk condensed matter.

In this Letter, we demonstrate, for the first time, two-color optical rectification at an air-InAs interface via a highly resonant above-band-gap excitation, a process we denote as all-optical surface optical rectification (AO-SOR) to distinguish it from the DC-SOR. The strong absorbing regime is responsible for the very high effective $\chi^{(3)}$ nonlinearity and results in a deeply subwavelength penetration depth that localizes the interaction within a quasi-2D surface (in the scale of 25 atomic layers). The dimensionally reduced interaction length allows the relaxation of typical phase-matching constraints found in bulks. It also affects the dynamics of competitive surface mechanisms, e.g., the photo-carrier-driven screening, on the emission. Figure 1 illustrates our experimental setup comprising a fundamental (FH) excitation beam ($\lambda = 800$ nm, 100 fs, 1 kHz, ≈ 1.0 mJ, red beam) copropagating with its second-harmonic (SH) signal ($\lambda = 400$ nm, ≈ 35.4 μJ, blue beam). The cross-polarized SH pulse at 400 nm was generated via type-I process (oo-e) in a 0.1 mm thick β-barium borate (BBO) crystal. A birefringent calcite plate (CP) [46] introduced a tunable phase delay $\tau_{\rm CP}(\phi)$ between the two cross-polarized fields. Specifically, the phase delay is due to the difference in optical path length between the ordinary wave at ω and the extraordinary wave at 2ω [47]. A second half-wave plate at 800 nm rotated the polarization of the fundamental field, resulting in the two pumps being copolarized. As a nonlinear surface, we exploited an undoped $\langle 100 \rangle$ InAs substrate. The pumps illuminated the surface at 45° with respect to its normal. The THz signal was collected along the specular reflection direction (green beam) through a standard time-domain spectroscopy (TDS) setup, implemented via a nonlinear $\langle 110 \rangle$ ZnTe crystal [48]. In this configuration, the generated THz field consists of three major contributions:

$$
\begin{aligned}
E_{\rm THz}(t) \propto\ & \chi^{(3)} E_\omega(t) E_\omega^*(t) E_{\rm surf} \\
& + \chi^{(3)} E_{2\omega}(t-\tau_{\rm CP}) E_{2\omega}^*(t-\tau_{\rm CP}) E_{\rm surf} \\
& + \chi^{(3)} E_{2\omega}(t-\tau_{\rm CP}) E_\omega^*(t) E_\omega^*(t) \cos(2\omega\tau_{\rm CP}). \quad (2)
\end{aligned}
$$

The first two terms account for separate DC-SOR contributions from the fundamental E_ω and second-harmonic $E_{2\omega}$

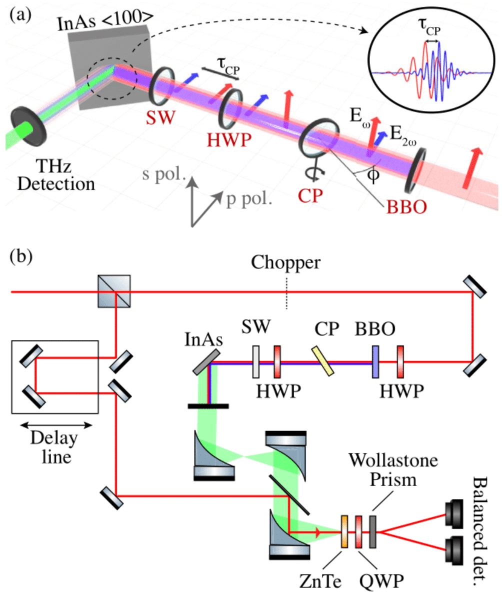

FIG. 1. Experimental setup. (a) The red, blue, and green beams denote the 800, 400 nm, and THz beam paths, respectively. The inset displays the role played by the phase delay. (b) A schematic of the whole setup. Half-wave plate (HWP), barium borate crystal (BBO), Calcite plate (CP), fused silica window (SW: UV), Quarter-wave plate (QWP), zinc telluride (ZnTe).

fields [Fig. 2(a)]. The third term, conversely, represents the AO-SOR mechanism under investigation, where fundamental and SH fields interact through the third-order $\chi^{(3)}$ process from Eq. (1) [Fig. 2(b)], where $\tau_{\rm CP}$ is the delay between E_ω

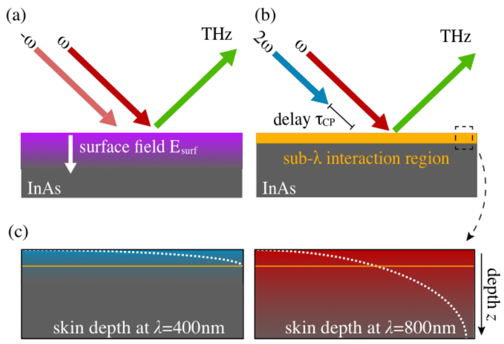

FIG. 2. THz emission from (a) DC-SOR and (b) AO-SOR. In (c), the interaction region (yellow line) is compared to the skin depth of the interacting fields, $\lambda = 400$ and $\lambda = 800$ nm, respectively.

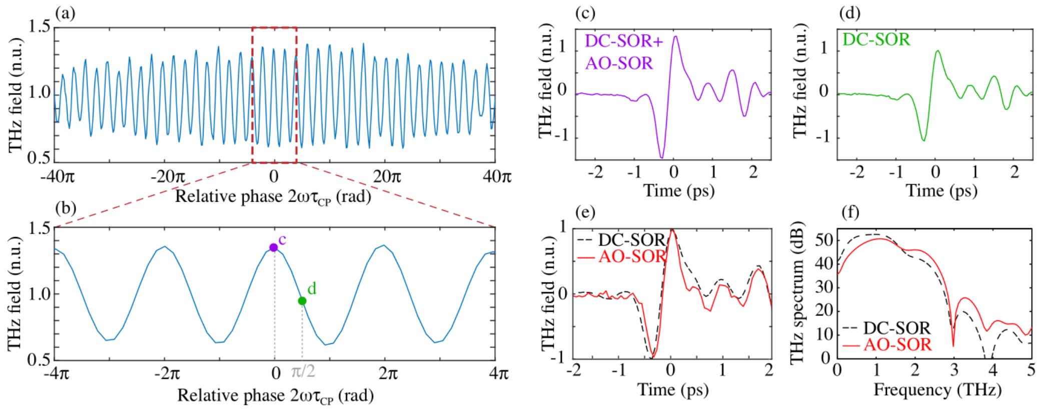

FIG. 3. (a),(b) Peak THz emitted field as a function of the phase delay τ_{CP}. In both plots, the THz field has been normalized to the DC-SOR contribution. (c),(d) Detected THz pulse for $\tau_{CP} = 0$ and $\tau_{CP} = \pi/4\omega$, respectively. In both cases, we considered p-polarized excitation and detection. (e),(f) Comparison of the pulse temporal and spectral amplitudes obtained by AO-SOR (red line) and DC-SOR (black dashed line), respectively. In these experiments, the incident pump energy was 1.2 mJ.

and $E_{2\omega}$. We neglected any term arising from carrier dynamics as they are highly saturated at the considered fluences [21,28]. Both DC-SOR and AO-SOR are localized within the subwavelength region defined by the short skin depth of the incident optical fields (approximately 140 nm at $\lambda_\omega = 800$ and 16 nm at $\lambda_{2\omega} = 400$ nm) [49]. In this condition, longitudinal phase matching does not play a significant role in the emission [Fig. 2(c)]. The delay τ_{CP} is controlled by rotating the calcite plate [47], and it affects only the amplitude of the all-optical process. By holding the TDS delay in the position of maximum field detected, a change of τ_{CP} produces a beating pattern of period $1/(2f) = \pi/\omega$ [Figs. 3(a)–3(b)], as predicted by Eq. (2). When $\tau_{CP} = 0$, all the sources components are in phase, resulting in a peak in the emission. Interestingly, in this case, the emitted THz field is enhanced by a factor of ≈40% (96% in power) [Fig. 3(c)] when considering an incident pump energy of 1.2 mJ. When $\tau_{CP} = \pi/4\omega$, conversely, the AO-SOR component is suppressed, and we can isolate the DC-SOR contribution [Fig. 3(d)]. By subtracting the two signals, we can thus determine the THz field generated solely by AO-SOR. As illustrated in Figs. 3(e), 3(f), the THz pulse generated by AO-SOR is shorter in time and broader in spectrum than that from DC-SOR. In the range 2–2.5 THz the AO-SOR power spectral density is 3.5–4 dB above the corresponding spectrum for the DC-SOR. It is worth noting that our current ZnTe-based detection limits the appreciable bandwidth creating a slope in the spectrum as the frequency approaches 3 THz. This limitation, however, could be removed by employing different nonlinear detection crystals operating at different wavelengths, such as GaP [50], or an air-ABCD detection scheme [51]. We obtained further insights into the AO-SOR emission mechanism by measuring the emitted THz field as a function of the incident optical power, as summarized in Fig. 4. To this end, we measured the peak THz field as a function of τ_{CP} and the incident pump energy [Fig. 4(a)]. As shown in Fig. 4(b), for each value of the pumping power we can employ the interference signal (green line) to isolate the DC-SOR contribution (mean value of the oscillation, dashed blue line) from the cosinelike AO-SOR contribution (amplitude of the interference oscillations, dashed orange line. For each pump energy, we extracted the individual contributions by fitting the experimental data (red circles). The analysis of these contributions is particularly useful to discriminate the saturation dynamics of the two competing mechanisms, as illustrated in Fig. 3(c). The DC-SOR contribution (blue dots) shows an initial linear trend at lower energies, followed by a soft saturation profile characteristic of the field-induced DC-SOR [21,28]. The AO-SOR, conversely, does not show any appreciable saturation effect at the high fluences of our experiment, as the mechanism is not affected by the screening of the semiconductor surface field. Note that direct THz photocarriers screening tends to be also negligible due to the extremely short skin depth of the second harmonic that defines the interaction region. This result is illustrated in Fig. 4(d): by extracting the AO-SOR field contribution, we observe how it increases quadratically with the square of the input optical energy [$P_{\rm pump}^2 \propto |E_\omega|^4$, Fig. 4(d)] as dictated by Eq. (1) in the presence of a second-harmonic field of the form $E_{2\omega} \propto E_\omega^2$. Quite interestingly, we were able to observe the onset of a subquartic trend for high pump energies. The main contributors to this effect are potentially the self-phase and cross-phase modulation in the BBO crystal, which can induce a change of the nonlinear product at the InAs surface by slightly detuning the fundamental and SH waves at high

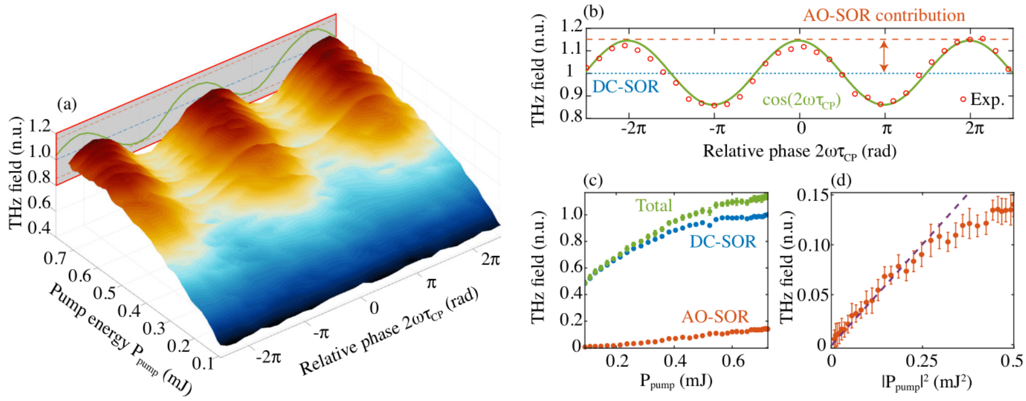

FIG. 4. (a),(b) THz peak emission as a function of the phase delay τ_{CP} and the pump energy P_{ω}. For each pump energy, we extracted the SOR contribution [panel (b), blue line], corresponding to the center value, and the AO-SOR contribution (orange line), corresponding to the beating amplitude. For each pump value, we extracted these values by fitting the experimental data (red circles). (c) Total emission and DC-SOR contribution as a function of the pump power, highlighting the soft saturation at high pump energies characteristic of the DC-SOR emission mechanism. (d) AO-SOR emission as a function of $|P_{\mathrm{pump}}|^2$. The dashed line highlights the fitted ideal quartic dependence.

pump rates. Further insights on the AO-SOR process can be obtained by observing the THz emission dependence from crystal rotation. To this end, we analytically calculated such a dependence by generalizing the full-vector approach described in Refs. [52–54]. We derived a set of nonlinear Fresnel reflection coefficients for the p and s polarization components by matching the incident fields with the nonlinear polarization field P_{NL} generating the THz field. Following the standard approach outlined in Ref. [55], we obtained the THz field generated in reflection by matching P_{NL} with a wave reflected at the air-InAs interface. Our calculations show that the crystal orientation affects each generation mechanism differently. A particularly relevant case involves the s-polarized THz field generated by a $\langle 100 \rangle$ InAs by p-polarized pumps. In this configuration, the standard DC-SOR is suppressed by the symmetry properties of the nonlinear tensor $\chi^{(3)}$ [23,28]. The two-color THz emission, on the contrary, reads as follows:

$$E_{p,s} = \frac{3}{4}\Omega L_{\mathrm{eff}} A_s f_c^2 f_{2c} t_p^2 t_{2p} \sin(4\phi)[\chi_{iiii} - 2\chi_{iijj} - \chi_{ijji}] E_{2\omega} E_{\omega}^2, \quad (3)$$

where ϕ is the crystal orientation angle measured from the 100 axis, and χ_{iiii}, χ_{iijj}, and χ_{ijji} are the three independent components of the tensor $\chi^{(3)}$. To ease a direct comparison with the DC-SOR case, all the other quantities in Eq. (3) are identical to those in Ref. [28]. Our experiments captured the fourfold symmetry predicted by Eq. (3), as illustrated in Fig. 5. These results confirm that the AO-SOR emission originates from the nonlinear susceptibility tensor of InAs. Interestingly, Eq. (3) allows us to also estimate the value of the nonlinear susceptibility $\chi^{(3)}$ for the AO-SOR process in InAs as $\chi^{(3)} \approx 9 \times 10^{-21}$ m^2/V^2.

In conclusion, we provide here the first experimental demonstration of phase-matching free, two-color THz generation in condensed matter. This process, which is not observed in bulk crystals, occurs in highly absorptive systems within a sub-wavelength interaction region dictated

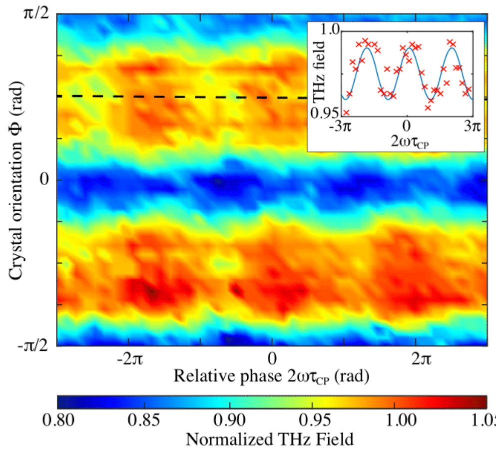

FIG. 5. AO-SOR THz emission as a function of the crystal orientation angle (φ) and the mutual delay τ_{CP}. As predicted by analytical theory, the emission is characterized by a fourfold symmetry which descends from the symmetry properties of the nonlinear susceptibility $\chi^{(3)}$ of InAs. (inset) Peak-field trace as a function of $2\omega\tau_{CP}$ for $\phi = \pi/4$ (dashed line).

by the skin depth of the SH field ($\sim$16 nm at $\lambda = 400$ nm). The reduced interaction length acts as a quasi-2D structure and ensures that the optical-to-THz conversion is unaffected by the longitudinal phase mismatch between the interacting waves. We predict that this approach could be ideal for the generation of THz waves with large frequency detuning between the two-color excitations, opening to the realization of non-zero-frequency-carrier THz parametric amplification. Our results also suggest that AO-SOR can significantly outperform DC-SOR for the same total input pump power. Indeed, in our experiments, a minor amount of SH contribution (about 3.5% in Fig. 3) produces a macroscopic enhancement of the optical to THz conversion from InAs. If we denote as α the total fractional power of the second-harmonic generated from the 800 nm pump, the THz fields increase as $E_{\mathrm{THz}} \propto (1-\alpha)\sqrt{\alpha}$. Such a function has a very steep gradient around $\alpha \approx 3.5\%$ and peaks at about $\alpha \approx 33\%$. Although this consideration does not account for the losses, it indicates that this process yields a much higher net efficiency when compared to standard benchmark surface emitters. We believe that our proof-of-concept results could seed new developments in the implementation of ultrathin THz emitters for, e.g., near field imaging applications and integrated nanophotonic devices, in which traditional nonlinear crystals cannot be scaled to the same size without reducing to unpractical levels the optical-THz conversion efficiency [11,12,56]. Besides, the lack of any observable physical saturation mechanisms typically related to photocarrier mediated screening of the surface field in DC-SOR, strongly suggests that the conversion limit of AO-SOR is set by mechanisms that become relevant only close to the damage threshold of the substrate.

The datasets for all figures are freely accessible at [57].

J. S. T. G. acknowledges funding from the University of Sussex (Helena Normanton Fellowship) and the Leverhulme Trust (Leverhulme Early Career Fellowship ECF-2020-537). M. C. acknowledges the support from the UK Research and Innovation (UKRI) and the UK Engineering and Physical Sciences Research Council (EPSRC) (Innovation Fellowship Programme, Grant No. EP/S001573/1). A. P. acknowledges the support from the UK Research and Innovation (UKRI) and the UK Engineering and Physical Sciences Research Council (EPSRC) (Innovation Fellowship Programme, Grant No. EP/S001018/1). This project received funding from the European Research Council (ERC) under the European Union's Horizon 2020 Research and Innovation Programme (Grant No. 725046 "TIMING" and Grant No. 851758 "TELSCOMBE").

*j.totero-gongora@sussex.ac.uk
†m.peccianti@sussex.ac.uk

[1] C. G. Wade, N. ibalic, N. R. de Melo, J. M. Kondo, C. S. Adams, and K. J. Weatherill, Nat. Photonics **11**, 40 (2017).
[2] U. Fruhling, M. Wieland, M. Gensch, T. Gebert, B. Schutte, M. Krikunova, R. Kalms, F. Budzyn, O. Grimm, J. Rossbach, E. Plnjes, and M. Drescher, Nat. Photonics **3**, 523 (2009).
[3] T. Kampfrath, K. Tanaka, and K. A. Nelson, Nat. Photonics **7**, 680 (2013).
[4] C. Kealhofer, W. Schneider, D. Ehberger, A. Ryabov, F. Krausz, and P. Baum, Science **352**, 429 (2016).
[5] S. Baierl, M. Hohenleutner, T. Kampfrath, A. K. Zvezdin, A. V. Kimel, R. Huber, and R. V. Mikhaylovskiy, Nat. Photonics **10**, 715 (2016).
[6] V. Jelic, K. Iwaszczuk, P. H. Nguyen, C. Rathje, G. J. Hornig, H. M. Sharum, J. R. Hoffman, M. R. Freeman, and F. A. Hegmann, Nat. Phys. **13**, 591 (2017).
[7] E. A. Nanni, W. R. Huang, K.-H. Hong, K. Ravi, A. Fallahi, G. Moriena, R. J. Dwayne Miller, and F. X. Krtner, Nat. Commun. **6**, 8486 (2015).
[8] D. A. Walsh, D. S. Lake, E. W. Snedden, M. J. Cliffe, D. M. Graham, and S. P. Jamison, Nat. Commun. **8**, 1 (2017).
[9] K. Sengupta, T. Nagatsuma, and D. M. Mittleman, National electronics review **1**, 622 (2018).
[10] J. Zhang, X. Chen, S. Mills, T. Ciavatti, Z. Yao, R. Mescall, H. Hu, V. Semenenko, Z. Fei, H. Li, V. Perebeinos, H. Tao, Q. Dai, X. Du, and M. Liu, ACS Photonics **5**, 2645 (2018).
[11] L. Olivieri, J. S. T. Gongora, A. Pasquazi, and M. Peccianti, ACS Photonics **5**, 3379 (2018).
[12] L. Olivieri, J. S. T. Gongora, L. Peters, V. Cecconi, A. Cutrona, J. Tunesi, R. Tucker, A. Pasquazi, and M. Peccianti, Optica **7**, 186 (2020).
[13] C. Vicario, A. V. Ovchinnikov, S. I. Ashitkov, M. B. Agranat, V. E. Fortov, and C. P. Hauri, Opt. Lett. **39**, 6632 (2014).
[14] C. Vicario, B. Monoszlai, and C. P. Hauri, Phys. Rev. Lett. **112**, 213901 (2014).
[15] T. Seifert *et al.*, Nat. Photonics **10**, 483 (2016).
[16] P. Chevalier, A. Amirzhan, F. Wang, M. Piccardo, S. G. Johnson, F. Capasso, and H. O. Everitt, Science **366**, 856 (2019).
[17] a. Rice, Y. Jin, X. F. Ma, X. C. Zhang, D. Bliss, J. Larkin, and M. Alexander, Appl. Phys. Lett. **64**, 1324 (1994).
[18] H. Hirori, A. Doi, F. Blanchard, and K. Tanaka, Appl. Phys. Lett. **98**, 091106 (2011).
[19] Y. Wu, M. Elyasi, X. Qiu, M. Chen, Y. Liu, L. Ke, and H. Yang, Adv. Mater. **29**, 1603031 (2017).
[20] M. Chen, R. Mishra, Y. Wu, K. Lee, and H. Yang, Adv. Opt. Mater. **6**, 1800430 (2018).
[21] L. Peters, J. Tunesi, A. Pasquazi, and M. Peccianti, Nano Energy **46**, 128 (2018).
[22] V. Apostolopoulos and M. Barnes, J. Phys. D **47**, 374002 (2014).
[23] M. Reid, I. V. Cravetchi, and R. Fedosejevs, Phys. Rev. B **72**, 035201 (2005).
[24] L. Peters, J. Tunesi, A. Pasquazi, and M. Peccianti, Sci. Rep. **7**, 9805 (2017).
[25] A. Tomasino, A. Mazhorova, M. Clerici, M. Peccianti, S.-P. Ho, Y. Jestin, A. Pasquazi, A. Markov, X. Jin, R. Piccoli, S. Delprat, M. Chaker, A. Busacca, J. Ali, L. Razzari, and R. Morandotti, Optica **4**, 1358 (2017).
[26] M. Cazzanelli and J. Schilling, Appl. Phys. Rev. **3**, 011104 (2016).

[27] S. L. Chuang, S. Schmitt-Rink, B. I. Greene, P. N. Saeta, and A. F. J. Levi, Phys. Rev. Lett. **68**, 102 (1992).
[28] M. Reid and R. Fedosejevs, Appl. Phys. Lett. **86**, 011906 (2005).
[29] Z. Zhang, Y. Chen, S. Cui, F. He, M. Chen, Z. Zhang, J. Yu, L. Chen, Z. Sheng, and J. Zhang, Nat. Photonics **12**, 554 (2018).
[30] S. W. Jolly, N. H. Matlis, F. Ahr, V. Leroux, T. Eichner, A.-L. Calendron, H. Ishizuki, T. Taira, F. X. Krtner, and A. R. Maier, Nat. Commun. **10**, 2591 (2019).
[31] M. Clerici, M. Peccianti, B. E. Schmidt, L. Caspani, M. Shalaby, M. Giguere, A. Lotti, A. Couairon, F. Legare, T. Ozaki, D. Faccio, and R. Morandotti, Phys. Rev. Lett. **110**, 253901 (2013).
[32] N. V. Vvedenskii, A. I. Korytin, V. A. Kostin, A. A. Murzanev, A. A. Silaev, and A. N. Stepanov, Phys. Rev. Lett. **112**, 055004 (2014).
[33] P. G. Martinez, I. Babushkin, L. Berge, S. Skupin, E. Cabrera-Granado, C. Kohler, U. Morgner, A. Husakou, and J. Herrmann, Phys. Rev. Lett. **114**, 183901 (2015).
[34] V. Andreeva, O. Kosareva, N. Panov, D. Shipilo, P. Solyankin, M. Esaulkov, P. G. de Alaiza Martinez, A. Shkurinov, V. Makarov, L. Berge, and S. Chin, Phys. Rev. Lett. **116**, 063902 (2016).
[35] V. A. Kostin, I. D. Laryushin, A. A. Silaev, and N. V. Vvedenskii, Phys. Rev. Lett. **117**, 035003 (2016).
[36] Z. Zhang, Y. Chen, M. Chen, Z. Zhang, J. Yu, Z. Sheng, and J. Zhang, Phys. Rev. Lett. **117**, 243901 (2016).
[37] L.-L. Zhang, W.-M. Wang, T. Wu, R. Zhang, S.-J. Zhang, C.-L. Zhang, Y. Zhang, Z.-M. Sheng, and X.-C. Zhang, Phys. Rev. Lett. **119**, 235001 (2017).
[38] A. D. Koulouklidis, C. Gollner, V. Shumakova, V. Y. Fedorov, A. Pugžlys, A. Baltuška, and S. Tzortzakis, Nat. Commun. **11**, 292 (2020).
[39] K. Y. Kim, J. H. Glownia, A. J. Taylor, and G. Rodriguez, Opt. Express **15**, 4577 (2007).
[40] E. Dupont, P. B. Corkum, H. C. Liu, M. Buchanan, and Z. R. Wasilewski, Phys. Rev. Lett. **74**, 3596 (1995).
[41] D. Cote, J. M. Fraser, M. DeCamp, P. H. Bucksbaum, and H. M. van Driel, Appl. Phys. Lett. **75**, 3959 (1999).
[42] J. Gudde, M. Rohleder, T. Meier, S. W. Koch, and U. Hofer, Science **318**, 1287 (2007).
[43] S. Sederberg, F. Kong, F. Hufnagel, C. Zhang, E. Karimi, and P. B. Corkum, Nat. Photonics **14**, 680 (2020).
[44] J. B. Khurgin, J. Nonlinear Opt. Phys. Mater. **04**, 163 (1995).
[45] M. Spasenovic, M. Betz, L. Costa, and H. M. van Driel, Phys. Rev. B **77**, 085201 (2008).
[46] EKSMA BBAR@800 + 400 nm − 310–450 fsec.
[47] K. A. Stankov, V. P. Tzolov, and M. G. Mirkov, Appl. Phys. B **54**, 303 (1992).
[48] Q. Wu, M. Litz, and X. C. Zhang, Appl. Phys. Lett. **68**, 2924 (1996).
[49] D. E. Aspnes and A. A. Studna, Phys. Rev. B **27**, 985 (1983).
[50] Q. Wu and X.-C. Zhang, Appl. Phys. Lett. **70**, 1784 (1997).
[51] J. Dai, X. Xie, and X.-C. Zhang, Phys. Rev. Lett. **97**, 103903 (2006).
[52] N. Bloembergen and P. S. Pershan, Phys. Rev. **128**, 606 (1962).
[53] P. N. Saeta and N. A. Miller, Appl. Phys. Lett. **79**, 2704 (2001).
[54] W. Hubner, K. H. Bennemann, and K. Bohmer, Phys. Rev. B **50**, 17597 (1994).
[55] R. W. Boyd, *Nonlinear Optics*, 3rd ed. (Academic Press, Amsterdam, Boston, 2008).
[56] J. Zhao, Y. E, K. Williams, X.-C. Zhang, and R. W. Boyd, Light Sci. Appl. **8**, 55 (2019).
[57] https://doi.org/10.6084/m9.figshare.13325468.

Appendix B: Generation and Detection in Terahertz Photonics

B.1 Nonlinear Optics in Terahertz Photonics

In this section, I will overview a common physical mechanism regarding the generation and detection in THz Photonics. The primary factor that enables the growth of this vast branch of optics is the development of ultrafast laser sources. Ultrafast pulsed lasers can generate high peak powers within ultrashort durations (sub-picosecond), and this made it possible to observe a broad spectrum of nonlinear phenomena and their temporal dynamics [164–166].

By definition, the "nonlinear regime" is the condition in which the outcome of optical propagation in the medium cannot be described in terms of a linear combination of optical excitations. In other words, the spectral information of an optical system changes with its inputs.

A considerable fraction of nonlinear effects can be derived through a perturbation approach: the expanded polarisation of the medium in response to an applied electric field $\vec{E}$ is given by

$$\overrightarrow{P_{tot}}\,(t) = \epsilon_0 \left[\chi^{(1)}\vec{E} + \chi^{(2)}\overrightarrow{E^2} + \chi^{(3)}\overrightarrow{E^3} + \cdots\right], \tag{B.1}$$

where ϵ_0 is the permittivity of free space and $\chi^{(n)}$is the n^{th} order susceptibility of the medium.

In contrast, in the traditional linear regime, the electric field term $\vec{E}$ is small and consequently the higher order terms become negligible. As the total polarisation acts as a source term in the wave equation,

$$\nabla^2\vec{E} - \frac{n^2}{c^2}\frac{\partial^2\vec{E}}{\partial t^2} = \frac{1}{c^2\epsilon_0}\ \frac{\partial^2\overrightarrow{P_{tot}}}{\partial t^2}, \tag{B.2}$$

the nonlinear field products in Eq. (B.1) become the source of polarisation components oscillating at new frequencies. Noticeably, as $\chi^{(n)}$ becomes exponentially smaller as n increases, their associated terms tend to be relevant only at or above certain electric field magnitudes such as that characteristic of ultrashort pulses [167].

B.2 Optical Rectification

Optical rectification (OR) is the typical nonlinear phenomenon of optical-to-terahertz conversion; it is a difference frequency generation (DFG) generated from ultrashort optical pulses. This mixing (near-DC) leads to frequency components inside the THz band [168]. It is crucial to notice that, in all nonlinear optical effects, the light conversion depends on the field's relative delay (phase), and particularly, we have phase-matching (PM) conditions when the wavevectors components match. In the case of OR, it has been proven that the PM condition is the case when the group velocity of the optical pulse matches the phase velocity of the emitted THz radiation. When using Ti: Sapphire regenerative amplified ultrafast lasers, a common THz source that functions with the OR mechanism is Zinc Telluride ($ZnTe$). Indeed, in $ZnTe$ the group velocity at central wavelength $\lambda = 800nm$ roughly matches the phase velocity between $0.1 \rightarrow 3\,THz$ [169]. However, we need to consider that the velocity matching condition cannot be precisely taken, and as the phase error rises, some frequencies become negligible. This feature is because of the relative broadband spectrum. A tool to quantify the efficiency of transferring the optical pump to the generated field is the 'coherent length', which is why (usually) the interaction length in a nonlinear crystal should be smaller than the coherent length of the frequency band generated.

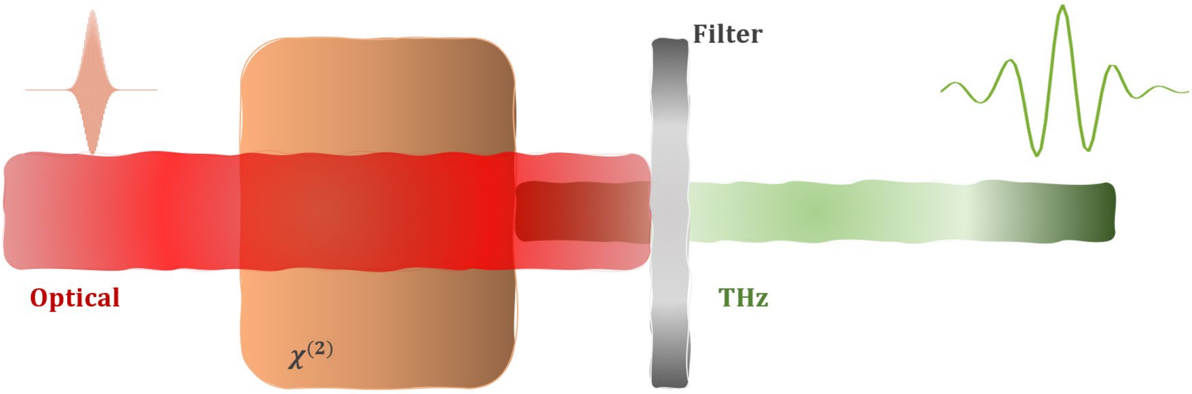

Figure B.1 Illustrative figure of the excitation scheme for Optical Rectification (OR) of ultrashort pulses in a $\chi^{(2)}$ nonlinear medium.

Therefore, in general, the bandwidth converted will be greater by decreasing the thickness of the nonlinear crystal. Notably, in the case of the $ZnTe$ another fundamental limitation occurs as the optical phonon absorption becomes considerable at around $5.3\,THz$ [170]. Hence, in general, the $ZnTe$ output bandwidth can be increased by decreasing the thickness of the crystal used. Other crystals based on OR, such as GaP or $GaAs$, have different trade-offs, and recent work has been orientated to find novel nonlinear materials for THz sources, for instance in organic crystals such as dimethyl amino 4–N–methylstilbazolium tosylate (DAST) [171,172]. In peculiar cases, longitudinal PM is impossible, and alternative illumination geometries are needed to overcome the problem. For instance, by using Lithium Niobate (LiN_bO_3) prism as a THz source, scientists had to use diffraction grating to apply a spatial tilt prior to the non-collinear THz emission [172,173].

In the following, I will illustrate the fundamental mechanism of OR in terms of the second-order polarisation, see Eq. (B.1). Assuming two electric fields with a frequency ω_1 and ω_2 the nonlinear frequency mixing within the crystal is given by

$$\vec{E}(t) = \overrightarrow{E_1}(t)e^{-i\omega_1 t} + \overrightarrow{E_2}(t)e^{-i\omega_2 t} + c.c. \tag{B.3}$$

Inserting this expression inside the polarization relation Eq. (B.1), at this point, the complete second-order polarisation becomes

$$\vec{P}^{(2)} = \epsilon_0 \chi^{(2)} \left[\overrightarrow{E_1^2}\ e^{-i2\omega_1 t} + \overrightarrow{E_2^2}\ e^{-i2\omega_2 t} + 2\,\overrightarrow{E_1}\,\overrightarrow{E_2}\ e^{-i(\omega_1+\omega_2)t} + 2\,\overrightarrow{E_1^*}\,\overrightarrow{E_2}\ e^{-i(\omega_1-\omega_2)t} + c.c. \right] + 2\epsilon_0\chi^{(2)}\left[\overrightarrow{E_1^*}\,\overrightarrow{E_1} + \overrightarrow{E_2^*}\,\overrightarrow{E_2}\right]. \tag{B.4}$$

Note, provided that the phase matching is achieved, $\vec{P}^{(2)}$ then acts as a driving term in the wave equation resulting in the emission of electromagnetic emission [174].

We must notice that in the case of optical pulses, we do not have a monochromatic light to emit THz; therefore, the OR (namely, the zero-frequency term) arises as to the difference between the fundamental frequencies contained within the optical pulse. Considering the emission of light with a frequency equal to the difference $\omega_{DFG} = \omega_1 - \omega_2$, the polarisation terms become

$$\vec{P}_{DFG}^{(2)} = 2\epsilon_0\chi^{(2)}\,\overrightarrow{E_1^*}\,\overrightarrow{E_2}\left[e^{-i(\omega_1-\omega_2)t} + c.c.\right]. \tag{B.5}$$

And by defining $\omega_1 = \omega$ and $\omega_2 = \omega - \Omega$, the term Ω is the frequency that oscillated in the THz range [175]. Collinear OR schemes are typically how broadband THz pulses are generated, as shown in Fig. B.1. However, this is not the only mechanism that allows the generation of ultrafast THz waves; mechanisms such as surface optical rectification (SOR) and Photo-Dember (PD) are other typical ways to generate THz radiation. The desire to find better and more efficient THz sources is often discussed in the literature, and many scientists are still pursuing this as their leading research today [65].

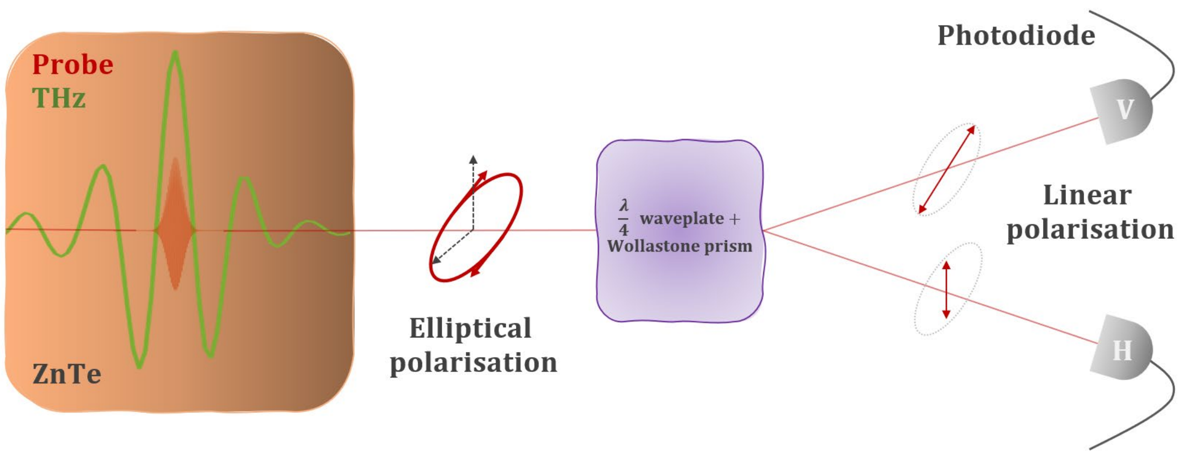

Figure B.2 The experimental setup for an electro-optic sampling of a THz (green) pulse. The input optical (red) pulse is linearly polarised before the ZnTe, after which is a quarter wave plate, Wollaston prism (all included in a purple box for simplicity) and a pair of balanced photodiodes.

B.3 Electro-Optical Sampling

One of the most popular methods to detect ultrafast THz waves is Electro-optic sampling (EOS) [176,177], and the mechanism relies on the birefringence of the THz field induced within a nonlinear crystal of the second order $\chi^{(2)}$. Essentially, it induces a polarization rotation of the ultrashort optical probe (basically, the reverse process of OR) that is collinearly propagated with a THz pulse inside the EO crystal, such as $ZnTe$, see Fig. B.2. When an electric field is present in the EO crystal, its refractive index changes along a particular crystallographic axis [178]. This fact makes it possible to encode a phase delay onto a polarisation axis of the co-propagating optical pulse (probe pulse), resulting in a polarisation rotation.

In a standard THz scheme, the applied electric field is given by the emitted THz pulse, which is then sent to a $< 110 >$ zincblende EO crystal such as ZnTe and therefore, this phase shift Γ is given by [9]

$$\Gamma = E_{THz} \frac{\pi d n_0^3 \gamma_{41}}{\lambda} \sqrt{1} + \sin^2(\phi) \, , \tag{B.6}$$

where E_{THz} is the propagating THz electric field, d is the thickness of the crystal, n_0 is the intrinsic refractive index (with no external field), γ_{41} is the EO coefficient, λ is the central wavelength of the probe pulse, and ϕ is the angle between the optical polarisation and the refractive index ellipsoid's long-axis. The optical probe can then be detected by combining a quarter-wave plate (QWP), a Wollaston prism (WP), and a pair of balanced photodiodes to detect the change in polarisation. The QWP transforms the elliptically polarised pulse back into a superposition of horizontal and vertical polarisations. These are then separated by the WP, with each component detected separately by the pair of balanced photodiodes. The resultant difference signal is detected by two photodiodes which directly read the value proportional to the phase shift given in Eq. B.6, with the signal S being given by

$$S = I_0 \sin(\Gamma) \sin(2\phi) \sim I_0 \Gamma \sin(2\phi) \tag{B.7}$$

where I_0 is the optical pulse intensity, and assuming a small value of Γ, it can be approximated as shown in Eq. (B.7). The signal S is proportional to the THz field emitted, which can be measured in time by delaying the optical probe with respect to the THz waveform (using a standard optical translation stage).

Appendix C: MATLAB Code for the Pulse-Retrieval

In this section, I will overview the MATLAB code of the Genetic algorithm used in the Open Research Europe paper to retrieve the THz pulse after propagating in the scattering medium. In Fig. C.1, I show the flowchart of a genetic algorithm.

C.1 GA Flowchart

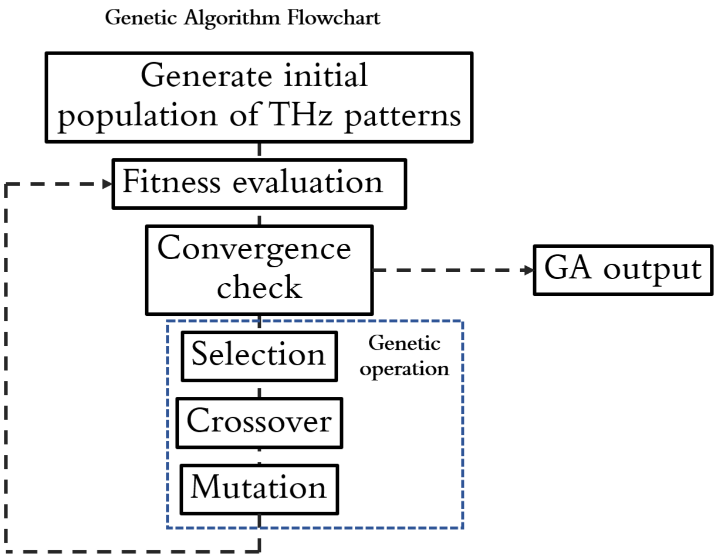

Figure C.1 Flowchart of the Genetic Algorithm.

C.2 MATLAB code

```
clear;
close all;
clc;
% % poolobj = gcp('nocreate'); % If no pool, do not create new one.
% % if is empty(poolobj)
% %     parpool;
% %     poolobj = gcp('nocreate');
% %     poolsize = poolobj.NumWorkers
% % else
% %     poolsize = poolobj.NumWorkers
% % end

% TM Generation // First Run TM_gen=1
TM_gen=1;                                % 1: Generate TM slices;  0: GA
dirname='TM_juan';
mkdir(dirname);

tic
%% ================================== Constants
c0=299792458;                           % speed of light (m/s)
eta0=377;                               % [Ohm]

%% ================================== Parameters
==================================
rng(12334);                             % rand seed for reproducibility
pow=3; %5                               % power of 2 used for sizes
Lx=0.34e-2;                             % physical size of pattern (m)
```

```
Nx=2^pow+1;                             % number of pixels per side (+ 1 to
center the focus)
Nx2=Nx*Nx;                              % Nx^2

P0=100e-6;                              % incident power W
A0=1;
fc= Lx/Nx;                              % desired focal size [mm]

h=0.5;                                  % average disorder
nu=0;
pow=1;

%% ================================== Temporal parameters
Nt=2^9;  % 9                            % N of points in time/freq
dt=80e-15;                              % step size (s) 50 e-15
t0=0;                                   % center of pulse in time (s)
Dt=.3e-12;
wl0=300e-6;                             % central wavelength (m)
cl_f=0.250e12;                          % spectral correlation length

%% ================================== GA Parameters
Np=10;                                  % number of patterns per generation
Ng=10;                                  % number of generations
G=round(Np/2);                          % new generation size
R0=Nx2/2;                               % Initial mutation rate
Rend=Nx2/1000;                          % final mutation rate
lambda=Ng*0.25;                         % mutation decay time
costf=zeros(Np,1);                      % cost function array

%% ==================================
Variables==================================
x=linspace(0,Lx,Nx);
y=linspace(0,Lx,Nx);
dx=x(2)-x(1);
[xx,yy]=meshgrid(x-mean(x),y-mean(y));
r2=xx.^2+yy.^2;
%% ================================== Create temporal profile
t=(1:Nt)*dt; t=t-mean(t);               % time vector (centred in 0)
om0=2*pi*c0/wl0;                        % angular frequency
tt=(t-t0)/Dt/2;                         % gaussian exp

%% TEMPORAL PROFILE
ft=exp(1i*(om0*t)).*(exp(-tt.^2));        % pulse profile (+i\omega t
convention) % pulse profile (+i\omega t convention)
[f,sp]=spectr(ft,dt);                   % create spectrum and frequencies

df=f(2)-f(1);                           % frequency sampling (Hz)
f1=min(f);                              % min freq
f2=max(f);                              % max freq
[mm,idf]=max(abs(sp).^2);

[E0,mu,std0,skew]=compute_moment(ft(:),t(:));

figure(1);
subplot(2,1,1);
plot(t,ft);
title('incident pulse');
subplot(2,1,2);
plot(f,abs(sp));
```

```
drawnow;


%% ================================== Spatial Pinhole
Wsp=round(Nx2/2);                           % focus position

%% ================================== Create TM(x,y,w)
if TM_gen==1

    ph_Tmf=TM_f(Nx2,Nx2,Nt,f1,f2,h,cl_f);    % build phases matrix
    TM=single(exp(-1i*2*pi*ph_Tmf))./ Nx2;

    TMsq= squeeze(TM(Wsp,:,:)).';
    TM_idf= TM(:,:,idf);
    TM_Wsp= TM(Wsp,:,:);

    savefile = [dirname,'/TMsq.mat'];          % save TM slices
    save(savefile, 'TMsq');
    savefile = [dirname,'/TMidf0.mat'];
    save(savefile, 'TM_idf');
    savefile = [dirname,'/TMWsp.mat'];
    save(savefile, 'TM_Wsp');
    clear TM; clear ph_Tmf;
    toc
else
    A= load([dirname,'/TMsq']);
    C= load([dirname,'/TMWsp']);
    E= load([dirname,'/TMidf0']);

    TMsq=A.TMsq;
    TM_Wsp= C.TM_Wsp;
    TM_idf= E.TM_idf;
end

%% ================================== Create first distribution of patterns
fprintf('initial population\n');
P_xy= round(rand(Nx2, 1, Np));
tmp1=repmat(P_xy, [1, Nt, 1]);       % spatial pattern repeated along all
spectral dimensions

P_xy=squeeze(P_xy);
tmp2=repmat(sp,[Nx2,1, Np]);  % incident spectrum repeated along all spatial
dimensions

Em_w=tmp1.*tmp2;

% jst: this should be 1D in space
Ep_w=single(zeros(Nt, Np));                    %Ep initialisation
tmp=zeros(size(Ep_w));

for ii=1:Np
    for ww=1:Nt                                % generate initial population
        Ep_w(ww,ii)=TMsq(ww,:)*Em_w(:, ww, ii);
    end
end

costf=compute_cf(Ep_w,std0,t(:));
[costf,idx]=sort(costf,  'descend');           % sort in descending rank
toc
```

```
Em_w= Em_w(:,:,idx);                            % reorder the incident
patterns
Ep_w= Ep_w(:,idx);                              % reorder the output patterns
P_xy=P_xy(:,idx);                               % reorder the spatial
patterns
Z=P_xy;

Ep_t_start=ifft(Ep_w(:,1),[],1);

figure(2);
subplot(2,1,1);
plot(t,Ep_t_start);
title('non-optimised pulse');
subplot(2,1,2);
plot(f,abs(fft(Ep_t_start)));
drawnow;

% note: what do you need this for?
Epp1=TM_idf* Em_w(:, idf, 1);

%% ================================== Genetic Algorithm ====================
fprintf('GA optimisation\n');
Rs=zeros(Ng,1);                         % mutation vector
delta=1;
opt_res=zeros(Ng,1);
eta=zeros(Ng, 1);
phase_IFFT= zeros(Ng, 1);

sigma_plot=zeros(Ng,1);
tmp_Em_w=zeros(Nx2,Nt,G);
tmp_Ep_w=zeros(Nt,G);
tmp_Z=zeros(Nx2, G);
tmp_P_xy=zeros(Nx2, 1, G);

% these vectors are required to find the permutations at each generation
(mapa = datasample...)
% population to select the random pairs
popul=1:Np;
% these are the probability weights to select a pair
% decreasing linearly as we want to have a higher probability to select
% better performing patterns
p_weights=Np:-1:1;

% matrix with repeated spectrum to speed-up calculations
tmp2= repmat(sp,[Nx2,1, G]);
%%
for n=1:Ng                                  % cycle over generations
    % compute number of mutated pixels
    R=round((R0-Rend)*exp(-n/lambda)+Rend);
    % save current mutation rate
    Rs(n)=R;
    % create a breeding template
    T=randi([0,1],Nx2,1);

    % cycle over mutated patterns (G is the number of new patterns)
    % to generate the new patterns to be tested
    for g=1:G
        % select pairs of parents
```

```
        mapa = datasample(popul, 2, 'Replace',false, 'Weights',p_weights);
        % create offspring
        off=T.*Z(:,mapa(1))+(1-T).*Z(:, mapa(2));
        % mutated pixels
        mymut= round(rand(R,1));
        % select the random pixels to be mutated and replace them in the
        % offspring
        idx=randperm(Nx2,R);
        off(idx)= mymut;
        tmp_Z(:,g)=off;
    end
    % at the end of the cycle, the spatial distribution of new patterns is
    % collected in tmp_Z. Now we need to add the incident spectra
    tmp_P_xy(:,1,:)=tmp_Z;
    tmp1=repmat(tmp_P_xy, [1, Nt, 1]);       % spatial pattern repeated along
all spectral dimensions
    tmp_Em_w=tmp1.*tmp2;

    for g = 1:G
        for ww = 1:Nt
            tmp_Ep_w(ww,g)=TMsq(ww, :)*tmp_Em_w(:, ww, g);
        end
    end
    tmp_costf=compute_cf(tmp_Ep_w,std0,t(:));
    costf(end-G+1:end)=tmp_costf;
    Em_w(:,:, end-G+1:end)=tmp_Em_w;
    Ep_w(:,end-G+1:end)=tmp_Ep_w;
    Z(:,end-G+1:end)= tmp_Z;

    [costf,idx]=sort(costf,  'descend')       % sort in descending rank

    Em_w=Em_w(:,:,idx);                        % reorder the incident patterns
    Ep_w=Ep_w(:,idx);
    Z(:, :)=Z(:,idx);

    Ep_t=ifft(Ep_w(:,1));
    [E0,mu,sig,skew]=compute_moment(Ep_t,t(:));

    sigma_plot(n)=sig;
    opt_res(n)= costf(1);
    eta(n)= Ep_w(idf , 1);

    if(mod(n,10)==0)
        fprintf('current generation: %d / %d\n',n,Ng);
        figure(3);
        subplot(2,1,1);
        plot(t,Ep_t);
        title('optimised pulse');
        subplot(2,1,2);
        plot(f,abs(fft(Ep_t)));
        drawnow;
        toc

    end

    if(mod(n,50)==0)
        figure(4)
        plot(1:Ng,sigma_plot/1e-12);
        xlabel('generations');
```

```
        ylabel('sigma (ps)');
        %  figbel('sigma (ps)');
    end

end
toc


Ep= TM_idf* Em_w(:, idf , 1);
Ep_t_end=ifft(Ep_w(:,1),[],1);

%%
figure(5);
subplot(2,1,1);
plot(t,Ep_t_end);
title('optimised pulse');
subplot(2,1,2);
plot(f,abs(fft(Ep_t_end)));
drawnow;


%%
figure(6);
subplot(3,1,1);
plot(1:Ng,100*Rs/Nx2);
xlabel('generations')
ylabel('mutation rate (% pixels)');

subplot(3,1,2);
plot(1:Ng,opt_res);
xlabel('generations');
ylabel('cost function');

subplot(3,1,3);
plot(1:Ng,sigma_plot/1e-12);
xlabel('generations');
ylabel('sigma (ps)');


%%
figure(7)

subplot(2, 2, 1)
Z_patt=reshape(Z(:,1),Nx,Nx);
pcolor(x,y,Z_patt);
shading flat;
axis equal;axis tight;
colormap('erdc_fireice_h');
colorbar;
title('Best Pattern')


subplot(2, 2, 2)
%Epp= TM_idf*Em_w(:, idf, 1);
qq= reshape(Epp1,[Nx, Nx]);
pcolor(abs(qq).^2);
shading interp;
colormap('fireice');
colorbar;
```

```
title('Intensity focus unoptimised')

subplot(2, 2, 3)
Epp= TM_idf*Em_w(:, idf, 1);
qq= reshape(Epp,[Nx, Nx]);
pcolor(abs(qq).^2);
shading interp;
colormap('fireice');
colorbar;
title('Intensity focus optimised')

subplot(2, 2, 4)
surf(x,y,abs(qq).^2);
shading interp;
dd=daspect;
daspect([dd(1) dd(1) dd(3)]);
colormap('erdc_fireice_h');
title('Intensity focus optimised')


return


%% Cost Function

% CF: Pulse Flip
% function costf=compute_cf(Ep_w,std0,t)
%
% Ep_t= ifft(Ep_w,[],1);
% peaks= min(real(Ep_t),[],1);
% [E0,mu,sig,skew]=compute_moment(Ep_t,t);
%
% costf= (-peaks)./sig;
%
% end


% CF pulse retrieval
function costf=compute_cf(Ep_w,std0,t)

    Ep_t= ifft(Ep_w,[],1);
    peaks= max(real(Ep_t),[],1);
    [E0,mu,sig,skew]=compute_moment(Ep_t,t);

    costf= peaks./sig;

end



%% Transfer Matrix function

function [TM,f]=TM_f(Nx,Ny,Nf,f1,f2,h,clf)
% [TM,f]=TM_f(Nx,Ny,Nf,f1,f2,h,clw)
% generates a random transfer matrix with gaussian correlation in frequency
% Nx, Ny, Nf : number of points in x, y and frequency
% f1, f2 : starting and final frequency (to compute the frequency span)
% clf    : frequency correlation
% f      : vector of frequencies
```

```
f=linspace(f1,f2,Nf);
TM=zeros(Nx,Ny,Nf);

% TM= qr(rand(Nx,Ny));
% TM = repmat (TM, [1, 1, Nf]);

% for ii=1:Nx
%     for jj=1:Ny
%         % [f,x] = rsgeng1D(N,rL,h,cl)
%         TM(ii,jj,:)=rsgeng1D(Nf,f2-f1,h,clf);
%     end
% end

parfor jj=1:Ny
    %disp(Ny-jj);
    t = getCurrentTask();
    if (t.ID)==1
        disp(Ny-jj);
    end
    for ii=1:Nx
        % [f,x] = rsgeng1D(N,rL,h,cl)
        TM(ii,jj,:)=rsgeng1D(Nf,f2-f1,h,clf);
    end
end


%% Rough surface generation & analysis
Link: Surface Generation & Analysis - MySimLabs


function [f,x] = rsgeng1D(N,rL,h,cl)

% [f,x] = rsgeng1D(N,rL,h,cl)

% generates a 1-dimensional random rough surface f(x) with N surface points.
% The surface has a Gaussian height distribution function and a Gaussian
% autocovariance function, where rL is the length of the surface, h is the
% RMS height and cl is the correlation length.

% Input:    N   - number of surface points
%           rL  - length of surface
%           h   - rms height
%           cl  - correlation length

% Output:   f   - surface heights
%           x   - surface points
%
% Last updated: 2010-07-26 (David Bergström).
%

format long;

x = linspace(-rL/2,rL/2,N);

Z = h.*randn(1,N); % uncorrelated Gaussian random rough surface distribution
                     % with mean 0 and standard deviation h

% Gaussian filter
```

```
F = exp(-(x).^2/(cl^2/2));   % filtro delle frequenze

% correlation of surface using convolution (Faltung), inverse
% Fourier transform and normalizing prefactors
f = sqrt(2/sqrt(pi))*sqrt(rL/N/cl)*ifft(fft(Z).*fft(F));
```